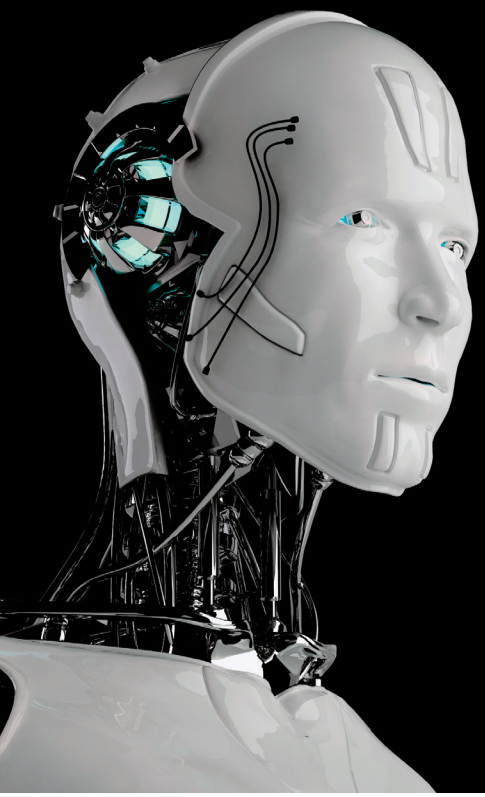

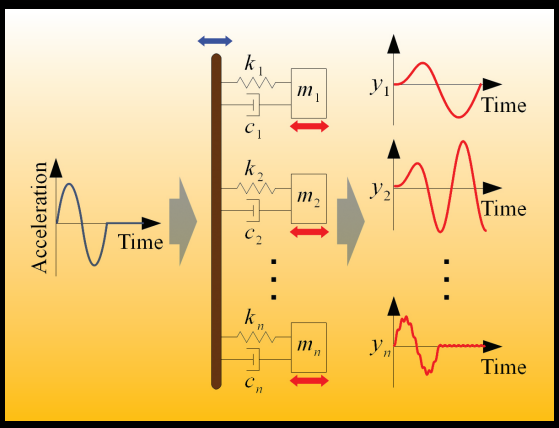

Advances in

High-Performance Motion Control of Mechatronic Systems

Edited by
Takashi Yamaguchi
Mitsuo Hirata
Chee Khiang Pang

CRC Press
Taylor & Francis Group

Advances in

High-Performance Motion Control of Mechatronic Systems

Advances in

High-Performance Motion Control of Mechatronic Systems

Edited by
Takashi Yamaguchi
Mitsuo Hirata
Chee Khiang Pang


CRC Press
Taylor & Francis Group
Boca Raton London New York

CRC Press is an imprint of the
Taylor & Francis Group, an **informa** business

CRC Press
Taylor & Francis Group
6000 Broken Sound Parkway NW, Suite 300
Boca Raton, FL 33487-2742

Version Date: 20130619

International Standard Book Number-13: 978-1-4665-5571-6 (eBook - PDF)

To my family, and my colleagues who have worked with us for continuous improvements in mechatronics servo control.

T. Yamaguchi

To my parents, my wife, and my two sons.

M. Hirata

To those who believe in me, and those who look down on me.

C. K. Pang

Contents

List of Figures

List of Tables

Preface

Mechatronic systems—the synergetic integration of mechanical, electrical, computational, and control systems—have pervaded consumer products ranging from large-scale braking systems in vehicular agents to small-scale integrated sensors in portable mobile phones. To boost sales and increase revenue in competitive consumer electronics industries, continuous improvements in servo evaluation and position control of mechatronic systems are essential. The subject of this book is advanced control topics for mechatronic applications, and in particular, control systems design for ultra-fast and ultra-precise positioning of mechanical actuators in mechatronic systems.

Currently, most precise mechatronic systems, e.g., scanner carriage assembly in facsimiles, photocopy machines, and flatbed scanners, etc., read/write head-positioning in Hard Disk Drives (HDDs), or X-Y tables for steppers used in semiconductor or liquid crystal manufacturing equipment, etc., consist of a (i) high speed point-to-point movement motion mode, (ii) transient motion mode for settling to a target, and (iii) tracking motion mode to remain on desired position. During operations, vibration of the mechanical actuators (excited during acceleration, deceleration, and jerk) remains a significant problem. As such, generation of the desired reference trajectory as well as the corresponding servo control design for transient and steady-state responses are important.

In this book, we propose several state-of-art advanced control techniques to tackle these issues for each the above-mentioned modes of operation based on our latest research activities. This book allows readers to understand the entire process of how to translate control theories and algorithms from a fundamental theoretical viewpoint to actual design and implementation in realistic engineering systems. With the required positioning accuracy in current mechatronic systems in the order of Armstrong levels ($< 1 \times 10^{-9}$ m), readers will also be able to understand what kind of advanced control techniques would provide solutions for the next generation of high-performance mechatronics.

Audience

This book is intended primarily as a bridge between academics in universities, practicing engineers in industries, and scientists working in research institutes. One of the most advanced control technologies has been developed and applied onto HDDs (being classic examples of high-performance mechatronic systems), as ultra-short seek time and ultra-high read/write head positioning accuracy are required for narrower data track width with ever-increasing

areal data storage densities. The developed motion control technologies for precision position control are also widely applicable to various industries such as manufacturing, robotics, home appliances, automobiles, optical drives, etc. For example, an engineer who mounted a piezoelectric actuator on a flexible beam would like to know how to damp the critical resonant modes of the beam using active vibration control in discrete-time. Or a scientist working on robotic systems would like to know how to actuate a two-link robot manipulator from point to point as quickly and accurately as possible in a dual-stage actuation framework. All of the control design methodologies presented have already been applied to various existing high-performance mechatronic systems, so it would be most beneficial to engineers and researchers who are working on control systems and mechatronics.

Learning Outcomes

The desired advanced transient and steady-state position control consist of ultra-high speed precision motion control (seek), control of transient states (settle), and ultra-strong disturbance rejection control (follow) of the single- or dual-stage mechanical actuators in mechatronic systems. This book aims to systematically describe the developed control technologies for the respective modes in detail, and presents the effectiveness of the proposed methodologies which are applied to or verified on various high-performance mechatronic systems. This book can be readily appreciated and used by engineers from industries as well as researchers from research institutes and academia, and will be valuable to researchers and students in translating advanced control theories to other realistic engineering applications.

Supplementary Materials

The following monograph edited by the same team of editors is recommended as a supplementary reading text: T. Yamaguchi, M. Hirata, and C. K. Pang (eds.), *High-Speed Precision Motion Control*, CRC Press, Taylor and Francis, Boca Raton, FL, USA, 2011.

The above-mentioned book covers various track-seeking, track-settling, and track-following control algorithms with actual application or experimentation on commercial HDDs, and proposes the HDD Benchmark Problem for readers to understand and verify the developed schemes. However, the depth of description of the control methodologies was limited due to the coverage of various approaches to motion control design. In this book, we identify one outstanding algorithm for each motion control, e.g., fast motion control, transient control, and precise position control, which are described in detail from theoretical background to actual applications. In particular, dual-stage actuation is currently one of the latest and most widely-researched topics in the area of motion control. While the editors remain the same, the contributing authors in our present monograph are more diversified, working in academia, research institutes and laboratories, as well as industries. As such, readers of our book are expected to understand the theoretical background and engi-

neering issues systematically, and will be able to provide effective solutions for various industrial applications.

Acknowledgments
We would like to express our gratitude to university professors and engineers for their efforts in evolving advanced control techniques for high-performance and high-precision mechatronic systems. We have learned a lot through various technical discussions and communications with all of them.

We would like to take this opportunity to express our gratitude to CRC Press for publishing this book. We would also like to acknowledge our loved ones for their love, understanding, and encouragement throughout the entire course of preparing this research monograph. This book was also made possible with the help of our colleagues, collaborators, as well as students, research staffs, and members of our research teams. This work was supported in part by Singapore MOE AcRF Tier 1 Grants R-263-000-564-133, R-263-000-A44-112, and R-263-000-A52-112.

Last, but not least, we would like to take a moment to send all our best wishes to those who are affected, directly or indirectly, by the 2011 Eastern Japan great earthquake disaster.

Takashi Yamaguchi
Mitsuo Hirata
Chee Khiang Pang

Editors' Biographies

Dr. Takashi Yamaguchi graduated from Tokyo Institute of Technology with an M.S. in 1981. He joined the Mechanical Engineering Research Laboratory (MERL), Hitachi Ltd., in 1981, and has been working on research and development of servo control of Hard Disk Drives (HDDs) from 1987 to 2008. He received his Dr. Eng. in 1998, and the title of his dissertation is "Study of Head Positioning Servo Control for Hard Disk Drives."

Over the past thirty years, Dr. Yamaguchi's main research interests and areas are motion control design, especially fast and precise positioning servo control design for HDDs. He has authored more than 150 publications including 42 journal papers, 4 books, and 28 US Patents. Most of the publications are related to servo control of HDDs.

From 2008, he joined the Core Technology Research Center, Research & Development Group, Ricoh Company Ltd., where he is currently an executive engineer and general manager. He is a fellow of Japan Society of Mechanical Engineers (JSME) and a senior member of the Institute of Electrical Engineers in Japan (IEEJ). He is the chief editor of *Nanoscale Servo Control*, TDU Press, 2007 (which is the first book in Japan regarding the modeling and the control of HDDs), and *High-Speed Precision Motion Control*, CRC Press, 2011. He was also a guest editor for a special issue on "Servo Control for Data Storage and Precision Systems from 17th IFAC World Congress 2008," *Mechatronics*, Vol. 20, No. 1, February 2010. He is a recipient of a technology award from the Society of Instrument and Control Engineers (SICE) in Japan in 1997 for servo control of HDD and from JSME in 2001 for high-speed HDDs. He is also a recipient of a book award from SICE in 2010 for *Nanoscale Servo Control*.

Professor Mitsuo Hirata received his Ph.D. from Chiba University in 1996. From 1996 to 2004, he was a research associate of electronics and mechanical engineering at Chiba University. Currently, he is a professor of electrical and electronic systems engineering at Utsunomiya University.

Professor Hirata has extensive research experience in design and implementation of advanced control algorithms for mechatronic systems. Some past related projects include high-speed and high-precision control of head actuator of HDDs, semiconductor manufacturing systems (a collaboration with CANON Inc.), Galvano scanner (a collaboration with CANON Inc.), and transmission of vehicles (a collaboration with NISSAN Motor Co., Ltd.), etc.

He is the co-author of *Nanoscale Servo Control*, TDU Press, 2007, which is the first book in Japan regarding the modeling and the control of HDDs.

The book includes a HDD benchmark problem in the attached CD-ROM, and he is the chair of a technical working group of the HDD benchmark problem that can also be obtained by the following URL at http://mizugaki.iis.u-tokyo.ac.jp/nss/MSS_bench_e.htm. He has published many international referred journal and conference papers relevant to the scope of this book.

Professor Chee Khiang Pang, **Justin**, received B.Eng.(Hons.), M.Eng., and Ph.D. degrees in 2001, 2003, and 2007, respectively, all in electrical and computer engineering, from National University of Singapore (NUS). In 2003, he was a visiting fellow in the School of Information Technology and Electrical Engineering (ITEE), University of Queensland (UQ), St. Lucia, QLD, Australia. From 2006 to 2008, he was a researcher (tenure) with Central Research Laboratory, Hitachi Ltd., Kokubunji, Tokyo, Japan. In 2007, he was a visiting academic in the School of ITEE, UQ, St. Lucia, QLD, Australia. From 2008 to 2009, he was a visiting research professor in the Automation & Robotics Research Institute (ARRI), University of Texas at Arlington (UTA), Fort Worth, TX, USA. Currently, he is an assistant professor in Department of Electrical and Computer Engineering (ECE), NUS, Singapore. He is a faculty associate of A*STAR Data Storage Institute (DSI) and a senior member of IEEE.

His current research interests include intelligent diagnosis and prognosis of industrial networked systems, systems design of high-performance engineering systems, high-speed precision motion control, energy-efficient manufacturing systems, precognitive maintenance, data analytics, and industrial informatics.

Prof. Pang is an author/editor of three research monographs including *Intelligent Diagnosis and Prognosis of Industrial Networked Systems* (CRC Press, 2011), *High-Speed Precision Motion Control* (CRC Press, 2011), and *Advances in High-Performance Motion Control of Mechatronic Systems* (CRC Press, 2013). He is currently serving as an associate editor for *Journal of Defense Modeling & Simulation* and *Transactions of the Institute of Measurement and Control*, on the editorial board for *International Journal of Advanced Robotic Systems*, *International Journal of Automation and Logistics*, and *International Journal of Computational Intelligence Research and Applications*, and on the conference editorial board for IEEE Control Systems Society (CSS). He also served as a guest editor for *Asian Journal of Control*, *International Journal of Systems Science*, *Journal of Control Theory and Applications*, and *Transactions of the Institute of Measurement and Control*. He was the recipient of The Best Application Paper Award in The 8th Asian Control Conference (ASCC 2011), Kaohsiung, Taiwan, 2011, and the Best Paper Award in the IASTED International Conference on Engineering and Applied Science (EAS 2012), Colombo, Sri Lanka, 2012.

Contributors

Professor Mitsuo Hirata
Utsunomiya University
Japan

Professor Makoto Iwasaki
Nagoya Institute of Technology
Japan

Professor Atsushi Okuyama
Tokai University
Japan

Professor Chee Khiang Pang, Justin
National University of Singapore
Singapore

Dr. Takenori Atsumi
Hitachi, Ltd.
Japan

Dr. Noriaki Hirose
Toyota Central R&D Labs., Inc.
Japan

Dr. Fan Hong
A*STAR Data Storage Institute
Singapore

Dr. Masaki Nagashima
Naval Postgraduate School
USA

Dr. Takashi Yamaguchi
Ricoh Company Ltd.
Japan

1

Introduction to High-Performance Motion Control of Mechatronic Systems

T. Yamaguchi

Ricoh Company Ltd.

CONTENTS

1.1 Concept of Advances in High-Performance Motion Control of Mechatronic Systems

In this chapter, the concept and scope of this edited book are described in detail. The differences and new findings from our previous edited volume in 2011 [1] are also highlighted and explained.

1.1.1 Scope of Book

First we will explain the purpose of editing this book. As depicted in the title, both mechatronics and motion control are well-known terminologies which have been comprehensively defined and explained in various texts, e.g. [2] to describe the design methodologies of most mechatronic products which have dynamics and require motion control. Mechatronics is usually defined as a

synergistic combination of electronics, mechanics, computer, and control. An example of the definition of mechatronics by [3] is shown in Figure 1.1.

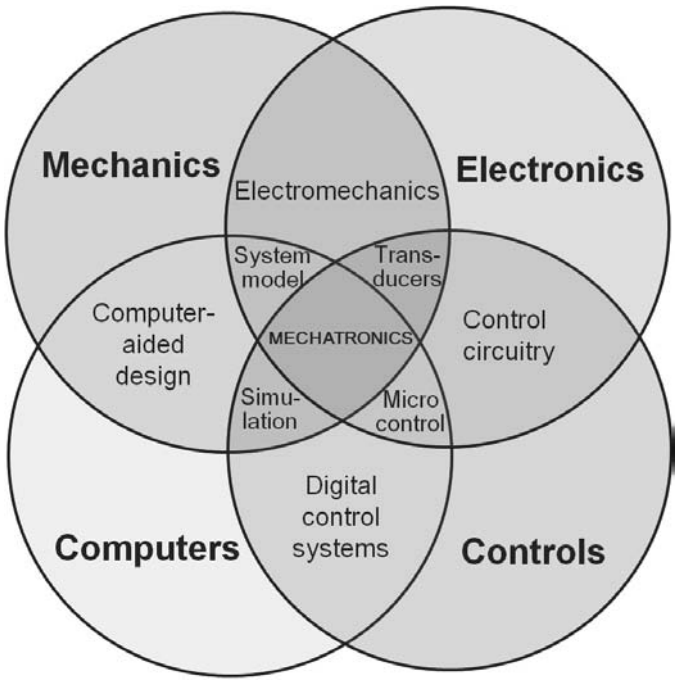

FIGURE 1.1
Definition of mechatronics [3].

Mechatronics is present mainly in systems with dynamical motion, and is an integrated methodology for motion control including the choice of sensors, actuators, processers, and machines to control the dynamics and motion. Mechatronics exists in a wide variety of products which include home and office appliances such as air conditioners, office automation equipment such as printers, precision devices, e.g., wrist watches and digital cameras, etc., and entertainment devices such as electronic musical instruments. On a larger scale, mechatronics also appears in cars, airplanes, machine tools, and robots, etc. On the other hand, motion control is an advanced technology applied to mechatronic systems for achieving desired motions such as fast movement, precise positioning or tracking, profile control, and force control for the above-mentioned products.

In this book, our focus is on specific mechatronics and motion control technologies, i.e., an object is moved from a current position to its target position based on a given performance index such as minimum time, and

target positioning or tracking should be precise enough for the required tasks to be carried out by an end effector or some other mechanical components. Such actions are commonly seen in various mechatronic systems, e.g., robotic arm control, Read/Write (R/W) head-positioning control in Hard Disk Drives (HDDs) and Optical Disk Drives (ODDs), linear or XY table motion control in manufacturing equipment, autofocus control in digital cameras, and servo valve control in electro-hydraulic and pneumatic equipment, etc. Stationary motion control such as speed regulation of the HDD spindle motor under various disturbances can be considered as motion control as well, in which the desired motor speed is the reference that has to be tracked precisely. Hence, even though our focus is on a specific motion control, the domains of application are very broad.

The main concept of this book is on control systems design, and the above-mentioned motion control can be divided into the following four design phases given as [1]:

1. Design of reference trajectory;
2. Design of controllers to track the reference trajectory;
3. Design of transient or settling controller to minimize the tracking error caused by various unmodeled dynamics or unpredicted parametric variations in the plants; and
4. Design of controllers to suppress external disturbances to ensure that the controlled object remains on its target position.

In Phases 1 and 2, the reference trajectory and servo control are designed for fast-motion reference tracking. The reference trajectory should be designed based on the specifications of the overall control system, e.gs., minimum time, minimum energy, low or no harsh grating acoustic noise, etc. The servo control structure for this phase is designed based on Two-Degrees-of-Freedom (TDOF) control, and a key issue in the design of TDOF control is the precise realization of the inverse dynamics of the plant using the feedforward controller. When utilizing the power amplifier saturation for maximum acceleration, it is necessary to convert this nonlinear control action into linear feedback control so that appropriate robust stability and sensitivity characteristics are theoretically guaranteed after settling. Another key issue in these phases is on the handling of the various complicated plant dynamics such as friction and mechanical resonant modes. In this book, both the reference trajectory and controller design with specific considerations of the mechanical resonant modes are described in detail (see Chapter 2).

In Phase 3, a settling controller is designed for transition from fast motion reference tracking in Phases 1 and 2 to precise positioning in Phase 4. In motion control, it is common that a certain amount of tracking error exists when the actuator approaches the target position. This is due to effects of model mismatch, unknown disturbances, and unmodeled plant dynamics, etc., which are common issues in realistic industrial applications. While it is important

for this tracking error to be reduced by the system as quickly as possible, it is generally not easy to handle the corresponding transient responses. In this book, it is shown that the initial values of the controller at mode-switching are design parameters which are independent of other control systems' characteristics such as stability, and can be used to modify the transient response drastically to improve its settling time (see Chapter 3).

In Phase 4, a controller is designed for precise positioning by improving the disturbance suppression capabilities based on precise modeling of both the plant dynamics and disturbance spectra. In this book, controller design with consideration for both plant dynamics and disturbances located below and above the Nyquist frequency is described (see Chapter 4). In addition, the use of dual-stage actuation and multi-sensing servo systems are also powerful approaches for improving the disturbance suppression capabilities in mechatronic systems (see Chapter 5).

1.1.2 Past Studies from *High-Speed Precision Motion Control*

Many of the authors of this book were also involved in the authoring and editing of *High-Speed Precision Motion Control* in 2011 [1]. Control design technologies which are developed and applied to actual HDDs were documented in [1] by ten contributors who are actively engaged in the development of the HDD servo control systems in either academia or industries. The main topics covered include system modeling and identification, basic approach to motion control design, and control technologies for high-speed motion control, precision motion control, as well as energy-efficient and low acoustic noise control. Under the unified approach to high-speed precision motion control, the topics covered include TDOF control which includes Zero Phase Error Tracking Control (ZPETC) for the design of a feedforward controller, Proximate Time Optimal Servomechanism (PTOS)—an access servo control with saturation considerations, Initial Value Compensation (IVC) for settling controller design, classical controller design methods for tracking-following which include the phase compensator, Proportional-Integral (PI) controller, notch filter, observer-based state feedback, etc., as well as multi-rate controller and observer design.

For fast motion control, the control technologies covered are vibration-minimized trajectory designed based on Final-State Control (FSC) theory and Perfect Tracking Control (PTC) theory under multi-rate sampling condition. For precision motion control, the control technologies covered are phase-stable design for high servo bandwidth, robust control using $\mathcal{H}_\infty$ control theory, multi-rate $\mathcal{H}_\infty$ control, repetitive control, and Acceleration Feedforward Control (AFC). For energy-efficient and low acoustic noise control, the control technologies covered are short-track seeking control using TDOF control with IVC, controller design for low acoustic noise seek, and servo control design based on Shock Response Spectrum (SRS) analysis.

As such, a wide variety of control technologies which have been applied to HDDs was covered in [1], with detailed focus on unique designs which are specific to HDDs and newly developed controller designs for HDDs. However, the description of each control technology is less detailed due to the page limit. In this book, the best general control technologies from the high-speed motion, fast settling, and precise-positioning control design phases are chosen and described in greater detail from the theoretical concepts to the application examples. These allow readers to have a better understanding of the basic idea, detailed designed process, as well as effectiveness of the controller designs through simulation/experiment results and actual application examples. In addition, dual-stage actuation and multi-sensing servo systems design are also included since dual-stage actuation has been implemented onto HDD products recently.

1.2 Hard Disk Drives (HDDs) as a Classic Example

In this section, the HDDs are used as a classic example of high-performance mechatronic systems to illustrate the mechanical actuators and their corresponding modeling techniques for simplicity but without loss of generality.

1.2.1 Mechanical Structure

An HDD is shown in Figure 1.2.

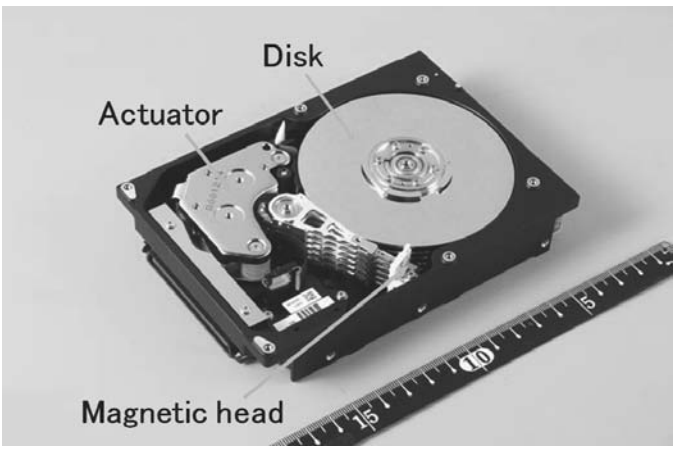

FIGURE 1.2
Schematic apparatus of an HDD.

Typically, one or more disks are stacked on the spindle motor shaft, and are rotated at 15,000 rpm in high-performance HDDs or 5,400–7,200 rpm in mobile or desktop HDDs. Several thousand data tracks are magnetically recorded on the surface of the disk with a track center-to-center spacing of less than 100 nm. The magnetic R/W head is mounted on a slider, which is in turn supported by the suspension and the carriage. The separation between the head and the disk is maintained by a hydrodynamic bearing which is currently less than 5 nm. An electromagnetic actuator, known as the Voice Coil Motor (VCM), rotates the carriage assembly and positions the slider at a desired track. The moving portion of the plant, i.e., the controlled object, consists of the VCM, carriage, suspensions, and sliders. The control algorithms are implemented in a Digital Signal Processor (DSP) or a microprocessor, which is mounted on a circuit board.

1.2.2 Modeling

The basic block diagram of the head-positioning system in HDDs with disturbances is shown in Figure 1.3.

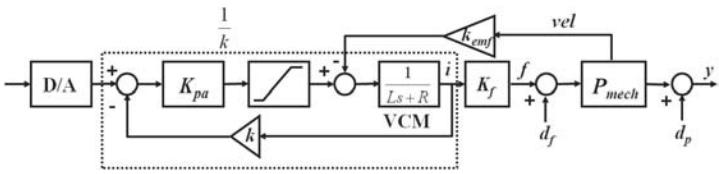

FIGURE 1.3
Block diagram of plant model and disturbances in HDDs.

The control input is calculated in the DSP or microprocessor and passed through a Digital-to-Analog (D/A) converter and a power amplifier. The power amplifier is usually a current-feedback amplifier with a large gain k so that the effects of the back EMF K_{emf} and the first-order dynamics due to inductance and resistance of the VCM coil can be minimized and approximated by $\frac{1}{k}$. A high-gain feedback can be achieved because the first-order dynamics of the coil is absolutely stable. The current i is converted to force f by the force constant of the VCM K_f. The mechanical system P_{mech} which consists of the arm, suspension, and head has very complicated dynamics. In the low-frequency region, pivot friction nonlinearity is observed. In the mid-frequency region, its dynamics are rather similar to that of pure inertia, i.e., double-integrator rigid body characteristics. In the high-frequency region where frequencies are greater than 1 kHz, many mechanical resonant modes can also be observed.

The frequency response of the nominal plant model from input voltage to head position is shown in Figure 1.4. The frequency response of the plant model with parametric variations is shown in Figure 1.5. The mechanical resonant modes are modeled as they are considered by the controller design methods covered in this book. A more comprehensive description of the modeling of the head-positioning control system in HDDs is detailed in Section 2.4.1 and [1].

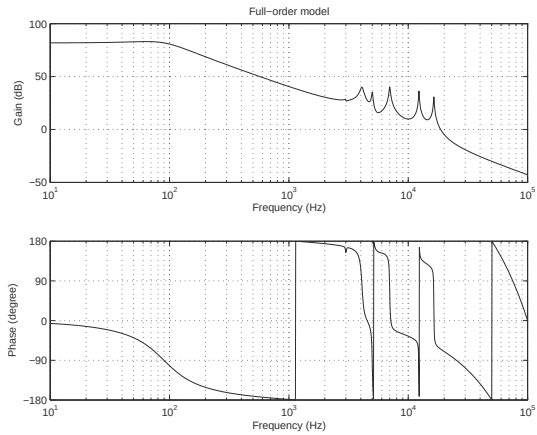

FIGURE 1.4
Frequency response of the nominal model [1].

Besides modeling of the plant dynamics, the modeling of disturbance is also very important. The magnitude of the sensitivity transfer function has to be reduced for improved disturbance suppression. Since the trade-off between sensitivity and robust stability is inevitable, considerable efforts have been made by engineers to shape the characteristics of the servo loop such that a compromise is achieved. When the characteristics and frequency spectra of the disturbances are known, loop-shaping can be carried out easily. An example of the frequency spectrum of the HDD position error in the presence of disturbances and sensor noises is shown in Figure 1.6.

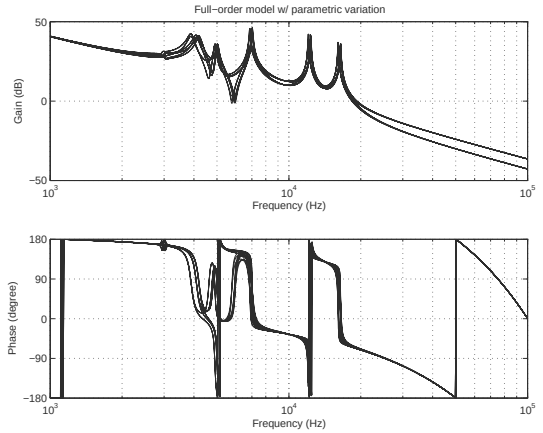

FIGURE 1.5
Frequency response of perturbed plant model [1].

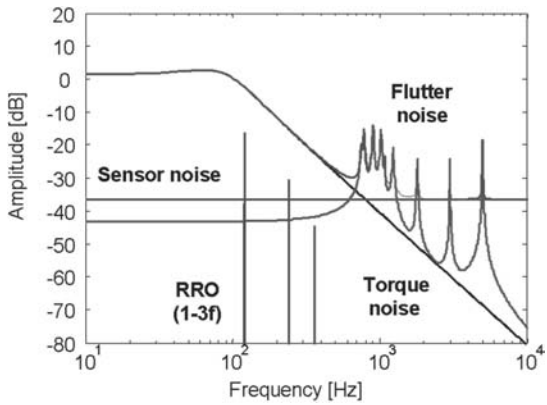

FIGURE 1.6
Spectrum of position error with disturbances and sensor noise [1].

1.3 Brief History of HDD and Its Servo Control

In this section, a brief history of HDDs is covered with specific discussions on the technological advancements in terms of HDD servo control.

1.3.1 Growth in Areal Density

The first shipment of HDDs was from IBM in 1956. The capacity of HDDs was 5 MB then, and an HDD consisted of fifty disks of 24″ in diameter each. The

disk rotational speed was 1,200 revolutions per minute (rpm), and the areal recording density was 2,000 bits/in^2. Today, 3.5″ HDDs have a data storage capacity of 1 TeraByte (TB) per disk, and the latest areal recording density is approaching 1 Tbit/in^2. The trend of HDD areal recording density is shown in Figure 1.7. It can be seen from Figure 1.7 that the areal recording density has increased by more than one hundred million times over the past fifty-five years [4, 5]!

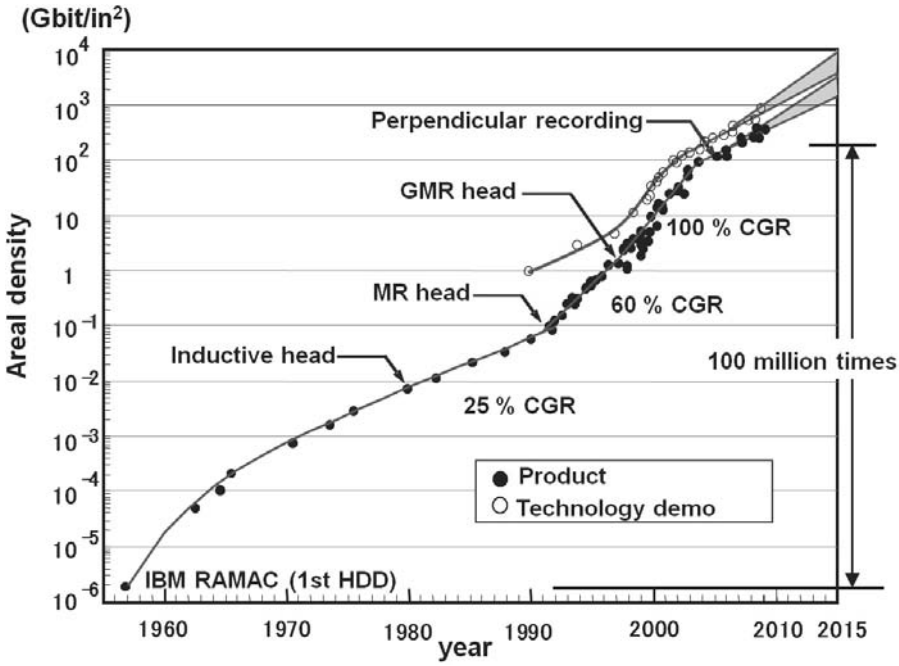

FIGURE 1.7
Trend of HDD areal density [4, 5].

The growth in areal recording density was most rapid from the mid-90s to the early 2000s, where its compound annual growth rate was 100%. This means that the data storage capacity of the shipped HDDs was doubled every year. This rapid growth has placed the HDDs in a distinguished position in the data storage market. The trend of positioning accuracy comprising of both Repeatable Run-Out (RRO) and Non-Repeatable Run-Out (NRRO) is shown in Figure 1.8 [6]. In order to meet such a rapid increase of areal density, the synergistic combination of mechanical, electrical, and control design required to achieve the desired positioning accuracy has been very challenging. From the control design aspect, it should be noted that many control theories have

been applied and improved upon. Many new mechanical structures have also been proposed. These technologies will be briefly discussed in the following section.

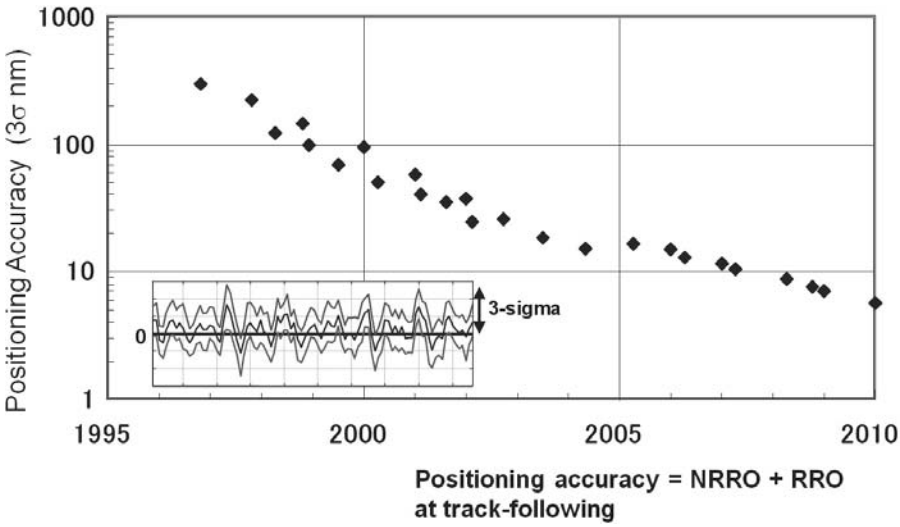

FIGURE 1.8
Trend of positioning accuracy in HDDs [6].

1.3.2 Technological Development in Servo Control

In this section, the technological advancements in servo control of HDDs through advanced control theories and improvements of control topologies are covered.

1.3.2.1 Application of Control Theories

In 1986, the first HDDs using digital control were shipped. Since then, many advanced digital control theories have been proposed and applied to HDDs. Based on the four design phases described in the earlier sections, the application of control theories to HDDs is briefly described as follows:

1. Design of reference trajectory:

   A minimum time or minimum energy trajectory can be derived based on the minimization of time or energy indices, respectively. However, minimum time or energy trajectories have never been applied to HDDs since mechanical resonant modes are present in the

actual servomechanism. In the late 80s, a minimum jerk trajectory was proposed to reduce residual vibrations in [7]. The input-shaping design is a more active approach where a specific resonant frequency is removed from the designed trajectory [8]. Since the early 2000s, the FSC theory has been applied to HDD servo control. The FSC theory is a comprehensive approach for trajectory design and results in less excitation of the mechanical resonant modes [9]. This design method is described in detail in Chapter 2.

2. Design of controllers to track the reference trajectory:

   This servo control design is one of the major areas in control theory, and many methods have been proposed. The PTOS [10] was proposed in the mid-80s and is one of the most popular methods applied to HDDs. For the PTOS, power amplifier saturation is considered for fast access control in the track-seeking mode, and a smooth transfer to the linear feedback loop for precise-positioning control in the track-following mode is provided. The design of the feedforward controller in TDOF control has always been an issue since the realization of the inverse dynamics of the plant model is difficult in many cases. With the ZPETC proposed in the late 80s [11], TDOF control has been applied to HDDs since the 90s. Model-following control [12], sliding mode control, N-delay multi-rate feedforward control [13], and deadbeat control are some other methods which have been proposed for HDDs. The PTC [14] proposed around 2000 is an excellent design that makes use of multi-rate sampling.

3. Design of transient or settling controller to minimize the tracking error caused by various unmodeled dynamics or unpredicted parametric variations in the plants:

   This phase is meant for overcoming settling issues in actual HDD products. The IVC has been applied to the Mode Switching Control (MSC) structure in HDDs since the early 90s [15]. The details of the IVC scheme are described in Chapter 3.

4. Design of controllers to suppress external disturbances to ensure that the controlled object remains on its target position:

   This phase is another very important area in control theory with many methods proposed in the literature. From the perspective of robust stability, Linear Quadratic Gaussian (LQG)/Loop Transfer Recovery (LTR) [16], $\mathcal{H}_\infty$ [17], and $\mathcal{H}_2$ control were proposed in the early 90s. For this design phase, one of the major issues in HDDs is the handling of the complicated mechanical resonant modes under a given sampling frequency for stabilization of the control system. Phase-stable control design has been applied to HDDs since the early 2000s, where even the phase information of the mechanical resonant modes was utilized for stabilization with high servo band-

width [18]. As the mechanical resonant modes are located at both within and above the Nyquist frequency, a comprehensive design and analysis approach has been proposed in [19]. A detailed description of this approach is available in Chapter 4. Dual-stage actuation and multi-sensing servo systems have also been proposed since the early 90s (see Chapter 1.3.2.2). In terms of improving the disturbance rejection capabilities, the disturbance observer [20], AFC for the cancellation of external vibrations [21], as well as repetitive control [22] and learning control [23] for the reduction of RRO have been proposed since the late 80s.

1.3.2.2 Improvement of Control Structure

For the head-positioning system in HDDs, the magnetic R/W head is used as the sensor and the VCM is used as the actuator. The distance between the sensor and the actuator is of several centimeters, and all the mechanical dynamics exist between them. As this structure makes control systems design difficult, dual-stage actuation has been proposed since the early 90s [24]. The three main types of dual-stage actuators are the suspension-driven based, slider-driven based [25], and head-element-driven based [26]. Currently, the suspension-driven based dual-stage actuators have been implemented in commercial HDDs. The MEMS-based slider-driven type and head-element-driven type actuators have been studied for many years and are not commercially available yet.

On the other hand, an additional sensor can be placed on the arm or suspension so that a state-feedback loop can be realized. This so-called multi-sensing systems concept has been proposed since the late 90s [27], and is a fairly standard practice in control engineering. From the control systems perspective, both dual-stage actuation and multi-sensing servo systems are equally difficult to implement. However, both methods have the additional advantage of extending the servo bandwidth, and will be described in detail in Chapter 5.

In addition, interested readers are referred to [28]–[32] and the references therein for a better understanding of the history of HDD servo control from various perspectives.

Bibliography

[1] T. Yamaguchi, M. Hirata, and C. K. Pang (eds.), *High-Speed Precision Motion Control*, CRC Press, Taylor and Francis Group, Boca Raton, FL, USA, 2011.

[2] C. W. de Silva, *Mechatronics: An Integrated Approach*, CRC Press, Taylor and Francis Group, Boca Raton, FL, USA, 2004.

[3] S. Ashley, "Getting a Hold on Mechatronics," *Mechanical Engineering*, Vol. 119, No. 5, pp. 60–63, May 1997.

[4] R. Wood and H. Takano, "Prospects for Magnetic Recording Over the Next 10 Years," in *Digests of the 2006 IEEE INTERMAG Conference*, CA-01, pp. 98, San Diego, CA, USA, May 8–12, 2006.

[5] Y. Shiroishi, K. Fukuda, I. Tagawa, H. Iwasaki, S. Takenoiri, H. Tanaka, H. Mutoh, and N. Yoshikawa, "Future Options for HDD Storage," *IEEE Transactions on Magnetics*, Vol. 45, No. 10, pp. 3816–3822, October 2009.

[6] T. Yamaguchi and T. Atsumi, "Keynote: HDD Servo Control Technologies–What We Have Done and Where We Should Go," in *Proceedings of the 17th IFAC World Congress*, MoA21.1, pp. 821–826, Seoul, Korea, July 6–11, 2008.

[7] E. Cooper, "Minimizing Power Dissipation in a Disk File Actuator," *IEEE Transactions on Magnetics*, Vol. 24, No. 3, pp. 2081–2091, May 1988.

[8] N. Singer and W. Seering, "Preshaping Command Inputs to Reduce System Vibration," *Journal of Dynamic Systems, Measurement, and Control*, Vol. 112, No. 1, pp. 76–82, March 1990.

[9] M. Hirata, T. Hasegawa, and K. Nonami, "Seek Control of Hard Disk Drives Based on Final-State Control Taking Account of the Frequency Components and the Magnitude of Control Input," in *Proceedings of the 7th International Workshop on Advanced Motion Control*, pp. 40–45, Maribor, Slovenia, July 3–5, 2002.

[10] M. Workman, *Adaptive Proximate Time-Optimal Servomechanism*, Ph.D. Dissertation, Stanford University, 1987.

[11] M. Tomizuka, "Zero Phase Error Tracking Algorithm for Digital Control," *Journal of Dynamic Systems, Measurement and Control*, Vol. 109, No. 1, pp. 65–68, March 1987.

[12] M. Iwashiro, M. Yatsu, and H. Suzuki, "Time Optimal Track-to-Track Seek Control by Model Following Deadbeat Control," *IEEE Transactions on Magnetics*, Vol. 35, No. 2, pp. 904–909, March 1999.

[13] S. Takakura, "Design of the Tracking System using N-Delay Two-Degrees-of-Freedom Control and its Application to Hard Disk Drives," *IEEJ Transactions on Industry Applications*, Vol. 119, No. 5, pp. 728–734, 1999 (in Japanese).

[14] H. Fujimoto, Y. Hori, T. Yamaguchi, and S. Nakagawa, "Proposal of Perfect Tracking and Perfect Disturbance Rejection Control by Multirate Sampling and Applications to Hard Disk Drive Control," in *Proceedings of the* 38^{th} *IEEE Conference on Decision and Control*, FrP11, pp. 5277–5282, Phoenix, AZ, USA, December 7–10, 1999.

[15] T. Yamaguchi, S. Shishida, H. Hirai, K. Tsuneta, and M. Sato, "Improvement of Servo Robustness for Digital Sector Servo System," in *Digests of the 1992 IEEE INTERMAG Conference*, GA-12, pp. 332, April 13–16, 1992.

[16] S. Weerasooriya and D. T. Phan, "Discrete-Time LQG/LTR Design and Modeling of a Disk Drive Actuator Tracking Servo System," *IEEE Transactions on Industrial Electronics*, Vol. 42, No. 3, pp. 240–247, June 1995.

[17] M. Hirata, K. Liu, T. Mita, and T. Yamaguchi, "Head Positioning Control of a Hard Disk Drive Using $\mathcal{H}_\infty$ Theory," in *Proceedings of the* 31^{st} *IEEE Conference on Decision and Control*, TP13, pp. 2460–2461, Tucson, AZ, USA, December 16–18, 1992.

[18] T. Atsumi, T. Arisaka, T. Shimizu, and H. Masuda, "Head-Positioning Control Using Resonant Modes in Hard Disk Drives," *IEEE/ASME Transaction on Mechatronics*, Vol. 10, No. 4, pp. 378–384, August 2005.

[19] T. Atsumi, "Disturbance Suppression beyond Nyquist Frequency in Hard Disk Drives," in *Proceedings of the* 17^{th} *IFAC World Congress*, pp. 827–832, Seoul, Korea, July 6–11, 2008.

[20] M. T. White, M. Tomizuka, and C. Smith, "Rejection of Disk Drive Vibration and Shock Disturbances with a Disturbance Observer," in *Proceedings of the American Control Conference*, pp. 4127–4131, San Diego, CA, USA, June 2–4, 1999.

[21] M. T. White and M. Tomizuka, "Increased Disturbance Rejection in Magnetic Disk Drives by Acceleration Feedforward Control," in *Proceedings of the* 13^{th} *IFAC World Congress*, pp. 489–494, San Francisco, CA, USA, June 30–July 5, 1996.

[22] K. Chew and M. Tomizuka, "Digital Control of Repetitive Errors in Disk Drive Systems," *IEEE Control Systems Magazine*, Vol. 10, No. 1, pp. 16–19, January 1990.

[23] Y. Chen, K. L. Moore, J. Yu, and T. Zhang, "Iterative Learning Control and Repetitive Control in Hard Disk Drive Industry–A Tutorial," in *Proceedings of the* 45^{th} *Conference on Decision and Control*, WeTT3.1, pp. 2338–2351, San Diego, CA, USA, December 13–15, 2006.

[24] K. Mori, T. Munemoto, H. Otsuki, Y. Yamaguchi, and K. Akagi, "A Dual-Stage Magnetic Disk Drive Actuator Using a Piezoelectric Device for High Track Density," *IEEE Transactions on Magnetics*, Vol. 27, No. 6, pp. 5298–5302, November 1991.

[25] T. Hirano, L. Fan, T. Semba, W. Y. Lee, J. Hong, S. Pattanaik, P. Webb, W. Juan, and S. Chan, "High-Bandwidth HDD Tracking Servo by a Moving-Slider Microactuator," *IEEE Transactions on Magnetics*, Vol. 35, No. 5, pp. 3670–3672, September 1999.

[26] H. Toshiyoshi, M. Mita, and T. Fujita, "A MEMS Piggyback Actuator for Hard Disk Drives," *IEEE Journal of Microelectromechanical Systems*, Vol. 11, No. 6, pp. 648–654, December 2002.

[27] F. Huang, W. Imaino, T. Semba, and F. Lee, "Rotary Actuator Dynamics with Active Damping," in *Proceedings of the* 11^{th} *Annual Symposium on Information Storage and Processing System*, Session 8, Santa Clara, CA, June 21–23, 2000.

[28] D. Abramovitch and G. Franklin, "A Brief History of Disk Drive Control," *IEEE Control System Magazine*, Vol. 22, No. 3, pp. 28–42, June 2002.

[29] W. Messner and R. Ehrlich, "A Tutorial on Controls for Disk Drives," in *Proceedings of the American Control Conference*, pp. 408–420, Arlington, VA, USA, June 25–27, 2001.

[30] T. Yamaguchi, "Review Paper: Modelling and Control of a Disk File Head-Positioning System," *Proceedings of the Institution of Mechanical Engineers, Part I: Journal of Systems and Control Engineering*, Vol. 215, No. 6, pp. 549–568, September 2001.

[31] A. Al Mamun, G. Guo, and C. Bi, *Hard Disk Drive Mechatronics and Control*, CRC Press, Taylor and Francis Group, Boca Raton, FL, USA, 2006.

[32] T. Yamaguchi, "Guest Editorial Special Issue: 'Servo Control for Data Storage and Precision Systems,' from 17^{th} IFAC World Congress 2008," *Mechatronics*, Vol. 20, No. 1, pp. 1–5, February 2010.

2

Fast Motion Control Using TDOF Control Structure and Optimal Feedforward Input

M. Hirata

Utsunomiya University

CONTENTS

2.1 TDOF Control Structure

2.1.1 One-Degree-Of-Freedom Control System

Let us consider the feedback system as shown in Figure 2.1, where P and K are the transfer functions of the plant and the controller, respectively, and u is a control input, y is a output, r is a reference input, d is a disturbance, n is a measurement noise, and $e = r - y$ is an error. It is assumed that the plant is a Single-Input-Single-Output (SISO) system for simplicity.

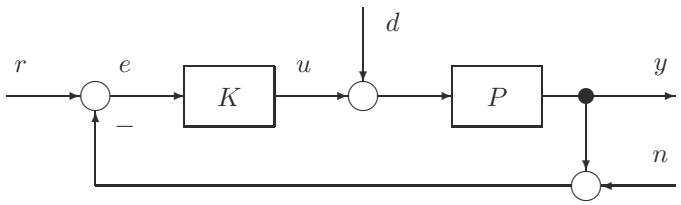

FIGURE 2.1
One-degree-of-freedom control system.

The transfer matrix from all the exogenous signals r, d, and n to the internal signals y, u, and e are

$$\begin{bmatrix} y \\ u \\ e \end{bmatrix} = \begin{bmatrix} \frac{PK}{1+PK} & \frac{P}{1+PK} & \frac{-PK}{1+PK} \\ \frac{K}{1+PK} & \frac{-PK}{1+PK} & \frac{-K}{1+PK} \\ \frac{1}{1+PK} & \frac{-1}{1+PK} & \frac{-1}{1+PK} \end{bmatrix} \begin{bmatrix} r \\ d \\ n \end{bmatrix}. \tag{2.1}$$

The transfer matrix in (2.1) has nine elements consisting of four different transfer functions

$$\frac{1}{1+PK}, \quad \frac{P}{1+PK}, \quad \frac{K}{1+PK}, \quad \frac{PK}{1+PK}. \tag{2.2}$$

All the transfer functions in (2.2) are determined by the feedback controller K only. As such, the control system in Figure 2.1 is referred to as the *One-Degree-Of-Freedom* (ODOF) control system as it has only one degree of freedom.

For instance, the transfer function from the reference input r to the output y is

$$y = \frac{PK}{1+PK} r, \tag{2.3}$$

and the transfer function from the measurement noise n to the output y is

$$y = -\frac{PK}{1+PK} n. \tag{2.4}$$

Both properties are determined by the same transfer function $PK/(1+PK)$.

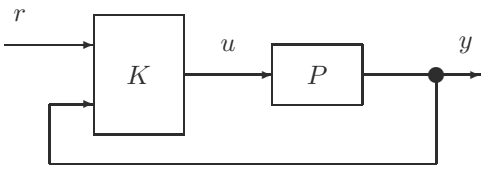

FIGURE 2.2
General formulation of two-degrees-of-freedom control system.

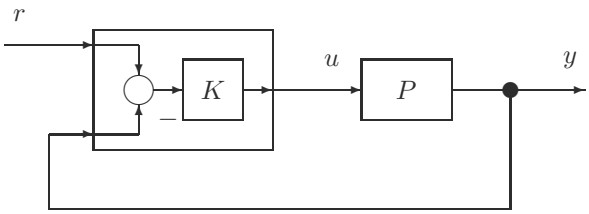

FIGURE 2.3
ODOF controller in TDOF controller structure.

As such, it is impossible to reduce the influence of the measurement noise while the reference input response is kept unchanged. The design of the ODOF controller hence requires severe trade-off among various control properties.

2.1.2 Two-Degrees-Of-Freedom Control System

As for the reference input, a filter F can be introduced[1] such as

$$r = F\tilde{r}. \tag{2.5}$$

Using the filter F, the reference input response can be improved while the other feedback properties are kept intact. In this way, control performance can be determined by not only the feedback controller K but also by the filter F. This control system is referred to as the *Two-Degrees-Of-Freedom* (TDOF) control system since it has two degrees of design freedom.

The general formulation of the TDOF control system is shown in Figure 2.2, where the TDOF controller uses the reference input r and the output y *separately*, while the ODOF controller uses the error $e = r - y$ only. The ODOF control system can be regarded as a special case of the TDOF control system as shown in Figure 2.3.

There are many types of the TDOF control system, and the typical TDOF configurations of control systems are shown in Figure 2.4. It should be noted

[1] Other than the reference input such as disturbance and measurement noise, the introduction of the filter is physically impossible.

that the control system of Figure 2.4(a) has a TDOF control structure though it has no feedforward controller.

Among these TDOF control systems, the design of Figure 2.4(c) is relatively easy and straightforward because the reference response property and the other feedback properties can be determined separately. The TDOF control system of Figure 2.4(c) is referred to as the *Model-Matching Two-Degrees-Of-Freedom* (MMTDOF) control system.

In the MMTDOF control system, M is referred to as *the reference model*, and the feedforward controller G_{FF} is determined so that the transfer function from r to y becomes M. This can be achieved by setting

$$G_{FF} = \frac{M}{P}, \tag{2.6}$$

as

$$\begin{aligned} y &= \left[\frac{PK}{1+PK}M + \frac{P}{1+PK}G_{FF}\right] r \qquad (2.7)\\ &= \left[\frac{PK}{1+PK}M + \frac{P}{1+PK}\frac{M}{P}\right] r \\ &= \left[\frac{PK}{1+PK} + \frac{1}{1+PK}\right] M\, r \\ &= M\, r. \qquad (2.8) \end{aligned}$$

The reference model M must be selected so that M and M/P are stable and proper. If P has unstable zeros, M must have the same zeros to cancel in M/P.

Equation (2.8) shows that the reference response property can be determined solely by M independently of the feedback properties in the ideal case, i.e., the plant has no uncertainties. This is the distinctive feature of the TDOF control system.

If the plant has uncertainties, the reference response property may be degraded. Let us show the effect of the plant uncertainties when the plant has a multiplicative uncertainty as

$$\tilde{P} = (1+\Delta)P.$$

The transfer function from r to y is

$$\begin{aligned} y &= \left[\frac{\tilde{P}K}{1+\tilde{P}K}M + \frac{(1+\Delta)P}{1+\tilde{P}K}\frac{M}{P}\right] r \\ &= \left[\frac{\tilde{P}K}{1+\tilde{P}K} + \frac{(1+\Delta)}{1+\tilde{P}K}\right] M\, r \\ &= \left[\frac{\tilde{P}K}{1+\tilde{P}K} + \frac{1}{1+\tilde{P}K} + \frac{\Delta}{1+\tilde{P}K}\right] M\, r \\ &= \left[1+\Delta\frac{1}{1+\tilde{P}K}\right] M\, r. \qquad (2.9) \end{aligned}$$

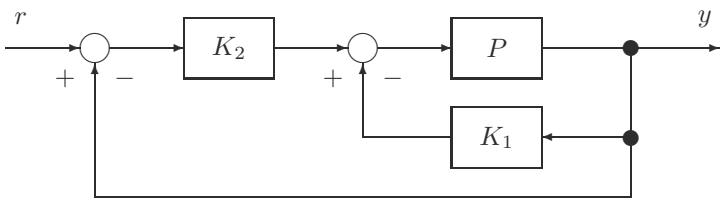

(a) Feedback type TDOF

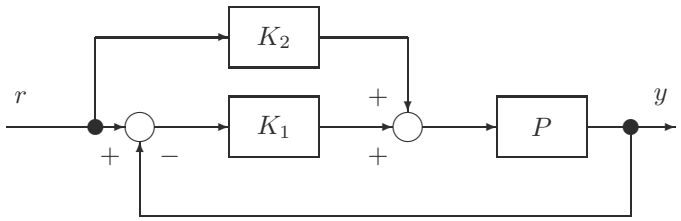

(b) Feedforward type TDOF

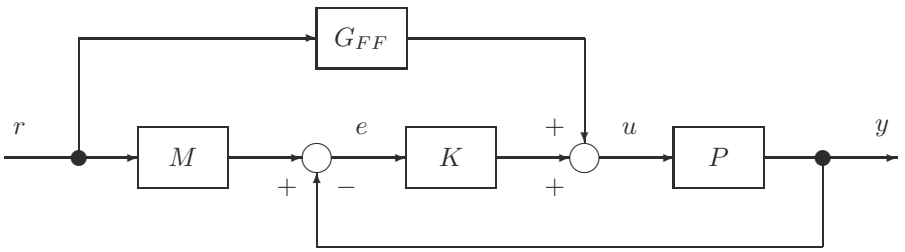

(c) Model-matching TDOF

FIGURE 2.4
Examples of TDOF control systems.

In (2.9), the effect of the multiplicative uncertainty Δ appears as

$$\Delta \frac{1}{1+\tilde{P}K},$$

where $1/(1+\tilde{P}K)$ is the sensitivity function of the actual feedback control system. As such, the robustness of the reference response can be improved by designing the sensitivity function of the control system to be small at the frequencies where the plant has uncertainties.

2.1.3 Implementation of Feedforward Input by TDOF Control Structure

As shown in the previous section, the reference response can be determined by selecting the reference model M in the MMTDOF control system. For example, if $P = 1/s^2$, the reference model can be selected as

$$M = \frac{\omega_n^2}{s^2 + 2\zeta\omega_n s + \omega_n^2}.$$

The design parameters ζ and ω_n are adjusted so that the reference model M has a good step response. However, it is unclear whether the selected values are optimal or not. Moreover, it is difficult to take into account the input saturation and/or the constraints on some state variables of the plant using this framework.

An optimal feedforward input obtained by minimizing a cost function subjected to constraints may solve this problem. This optimal feedforward input plays an important role to achieve high-performance motion control. Such feedforward inputs must be implemented with a feedback controller because feedforward control has no robustness against disturbances and plant uncertainties. The feedforward input u_{FF} can be implemented by the TDOF control structure as shown in Figure 2.5. In Figure 2.5, the transfer function from u_{FF} to y is P if $P = \tilde{P}$. When $P \neq \tilde{P}$ or disturbances exist, the feedback controller K minimizes the error between the actual output $y(t)$ and the output $y_m(t)$ of the nominal model.

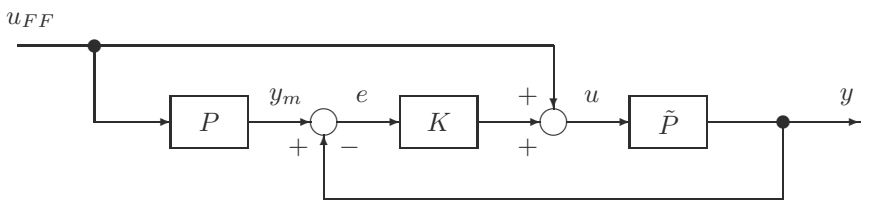

FIGURE 2.5
Implementation of feedforward input by the TDOF control structure.

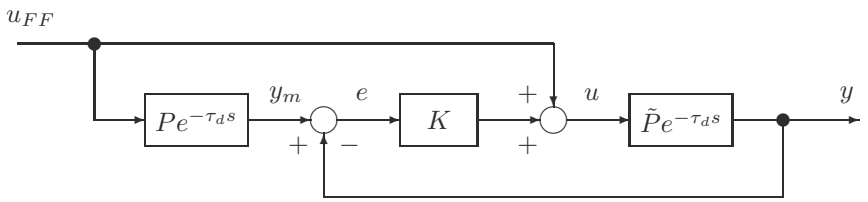

FIGURE 2.6
Implementation of feedforward input when plant has input delay.

When the plant has an input delay τ_d and becomes $\tilde{P}e^{-\tau_d s}$, the TDOF control structure of Figure 2.6 can be used instead of Figure 2.5. When $P = \tilde{P}$, the transfer function from u_{FF} to y becomes $Pe^{-\tau_d s}$. This means that the feedforward input u_{FF} can be designed to the nominal plant P without input delay, and the input delay is taken into account when u_{FF} is implemented to the TDOF control system.

2.2 Optimum Feedforward Input Design

2.2.1 Minimum Time Control

The use of the optimal feedforward input is very effective to achieve fast and precise motion control. Theoretically, the minimum time control can achieve also minimum time positioning [1].

The minimum time control input can be obtained by minimizing the cost function

$$J(T) = \int_0^T 1\, dt,$$

subject to the boundary conditions

$$y(0) = 0, \quad y(T) = r, \quad \dot{y}(0) = 0, \quad \dot{y}(T) = 0,$$

and the input limitation

$$|u(t)| \le u_{max}.$$

When the plant is a rigid-body system

$$y = \frac{1}{s^2}u,$$

the optimal solution is

$$u(t) = \begin{cases} +u_{max} & (0 \le t < T_{opt}/2) \\ -u_{max} & (T_{opt}/2 \le t < T_{opt}) \\ 0 & (t < 0,\ T_{opt} \le t) \end{cases}, \tag{2.10}$$

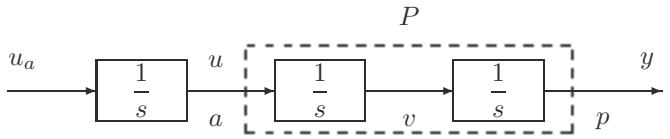

FIGURE 2.7
Augmented system for minimum jerk input.

where

$$T_{opt} = 2\sqrt{\frac{r}{u_{max}}}.$$

The optimum input (2.10) is referred to as *bang-bang* input.

The minimum time control input achieves minimum positioning time if the plant is an ideal rigid-body system. However, all mechanical systems have resonant modes at high frequencies, and the residual vibrations generated by these mechanical vibration modes extend the positioning time. The bang-bang input has maximum deceleration after maximum acceleration which excites these vibration modes easily. In order to reduce the residual vibrations, a smooth acceleration profile is required.

2.2.2 Minimum Jerk Input

A smooth feedforward input does not excite the mechanical vibration modes of the plant easily. One method to obtain the smooth feedforward input is to minimize the square integral of the *jerk*, which is the derivative of the acceleration [2].

When the plant is a rigid-body system as $P = 1/s^2$, the input $u(t)$ is the acceleration. As such, the minimum jerk input can be obtained by minimizing the cost function

$$J = \int_0^T \left(\frac{d}{dt}u(t)\right)^2 dt.$$

In order to evaluate the jerk, P is augmented with an integrator as shown in Figure 2.7, and the state-space equation of the augmented system is given by

$$\begin{aligned}\begin{bmatrix} \dot{p}(t) \\ \dot{v}(t) \\ \dot{a}(t) \end{bmatrix} &= \underbrace{\begin{bmatrix} 0 & 1 & 0 \\ 0 & 0 & 1 \\ 0 & 0 & 0 \end{bmatrix}}_{A} \underbrace{\begin{bmatrix} p(t) \\ v(t) \\ a(t) \end{bmatrix}}_{x} + \underbrace{\begin{bmatrix} 0 \\ 0 \\ 1 \end{bmatrix}}_{B} u_a(t) \\ &= Ax(t) + Bu_a(t),\end{aligned}$$

where $p(t)$, $v(t)$, and $a(t)$ are position, velocity, and acceleration, respectively.

With this augmented system, the cost function becomes a simple form of

$$J = \int_0^T \left(\frac{d}{dt}u(t)\right)^2 dt = \int_0^T u_a^2(t)\, dt.$$

At the initial time $t = 0$ and the final time $t = T$, the velocity and the acceleration should be zero. The position of the actuator moves from the origin to the target position r. The boundary conditions are given by

$$x(0) = \begin{bmatrix} 0 \\ 0 \\ 0 \end{bmatrix}, \quad x(T) = \begin{bmatrix} r \\ 0 \\ 0 \end{bmatrix}.$$

In order to obtain the optimal solution, the Hamiltonian H is defined as

$$H \quad = \quad u_a^2 + \lambda^T(Ax + Bu_a).$$

The costate equation

$$-\dot{\lambda} = \frac{\partial H}{\partial x} = A^T\lambda$$

becomes

$$-\begin{bmatrix} \dot{\lambda}_1 \\ \dot{\lambda}_2 \\ \dot{\lambda}_3 \end{bmatrix} = \begin{bmatrix} 0 & 0 & 0 \\ 1 & 0 & 0 \\ 0 & 1 & 0 \end{bmatrix} \begin{bmatrix} \lambda_1 \\ \lambda_2 \\ \lambda_3 \end{bmatrix}. \tag{2.11}$$

From the stationary condition

$$\frac{\partial H}{\partial u_a} = 2u_a + B^T\lambda = 0,$$

we have

$$u_a = -\frac{1}{2}B^T\lambda = -\frac{1}{2}\lambda_3. \tag{2.12}$$

From (2.11), we have

$$\begin{aligned} \lambda_1 &= c_1' \\ \lambda_2 &= -c_1't + c_2' \\ \lambda_3 &= \frac{c_1'}{2}t^2 - c_2't + c_3'. \end{aligned} \tag{2.13}$$

From (2.12) and (2.13), we have

$$u_a(t) = -\frac{1}{2}\left\{\frac{c_1'}{2}t^2 - c_2't + c_3'\right\}.$$

Since

$$a(t) = \int_0^t u_a(t)dt,$$

and $a(0) = 0$, the acceleration can be described as

$$a(t) = c_1 \left(\frac{t}{T}\right)^3 + c_2 \left(\frac{t}{T}\right)^2 + c_3 \left(\frac{t}{T}\right).$$

From $v(0) = 0$ and $y(0) = 0$, we can obtain

$$\begin{aligned} v(t) &= T\left\{\frac{c_1}{4}\left(\frac{t}{T}\right)^4 + \frac{c_2}{3}\left(\frac{t}{T}\right)^3 + \frac{c_3}{2}\left(\frac{t}{T}\right)^2\right\}, \\ p(t) &= T^2\left\{\frac{c_1}{20}\left(\frac{t}{T}\right)^5 + \frac{c_2}{12}\left(\frac{t}{T}\right)^4 + \frac{c_3}{6}\left(\frac{t}{T}\right)^3\right\}. \end{aligned}$$

With $u(T) = 0$, $v(T) = 0$, and $p(T) = r$, the following simultaneous equation must hold

$$\begin{bmatrix} 1 & 1 & 1 \\ 3 & 4 & 6 \\ 3 & 5 & 10 \end{bmatrix} \begin{bmatrix} c_1 \\ c_2 \\ c_3 \end{bmatrix} = \begin{bmatrix} 0 \\ 0 \\ 1 \end{bmatrix} \frac{60}{T^2} r,$$

and the unique solution is

$$\begin{bmatrix} c_1 \\ c_2 \\ c_3 \end{bmatrix} = \begin{bmatrix} 10 & -5 & 2 \\ -12 & 7 & -3 \\ 3 & -2 & 1 \end{bmatrix} \begin{bmatrix} 0 \\ 0 \\ 1 \end{bmatrix} \frac{60}{T^2} r = \begin{bmatrix} 2 \\ -3 \\ 1 \end{bmatrix} \frac{60}{T^2} r.$$

Finally, we have the minimum jerk input and the trajectories of $p(t)$, $v(t)$, $a(t)$ as

$$\begin{aligned} p(t) &= 60r\left\{\frac{1}{10}\left(\frac{t}{T}\right)^5 - \frac{1}{4}\left(\frac{t}{T}\right)^4 + \frac{1}{6}\left(\frac{t}{T}\right)^3\right\}, \\ v(t) &= \frac{30r}{T}\left\{\left(\frac{t}{T}\right)^4 - 2\left(\frac{t}{T}\right)^3 + \left(\frac{t}{T}\right)^2\right\}, \\ a(t) &= \frac{60r}{T^2}\left\{2\left(\frac{t}{T}\right)^3 - 3\left(\frac{t}{T}\right)^2 + \left(\frac{t}{T}\right)\right\}. \end{aligned}$$

The minimum jerk input $u_{mjc}(t)$ for the rigid-body system $P = 1/s^2$ becomes

$$\begin{aligned} u_{mjc}(t) = a(t) &= \frac{60r}{T^2}\left\{2\left(\frac{t}{T}\right)^3 - 3\left(\frac{t}{T}\right)^2 + \left(\frac{t}{T}\right)\right\} \qquad (2.14) \\ &= \frac{60r}{T^2}\, t_n(2t_n - 1)(t_n - 1), \qquad (2.15) \end{aligned}$$

where $t_n = t/T$. The time response of the minimum jerk input and the trajectories $v(t)$ and $p(t)$ are shown in Figure 2.8.

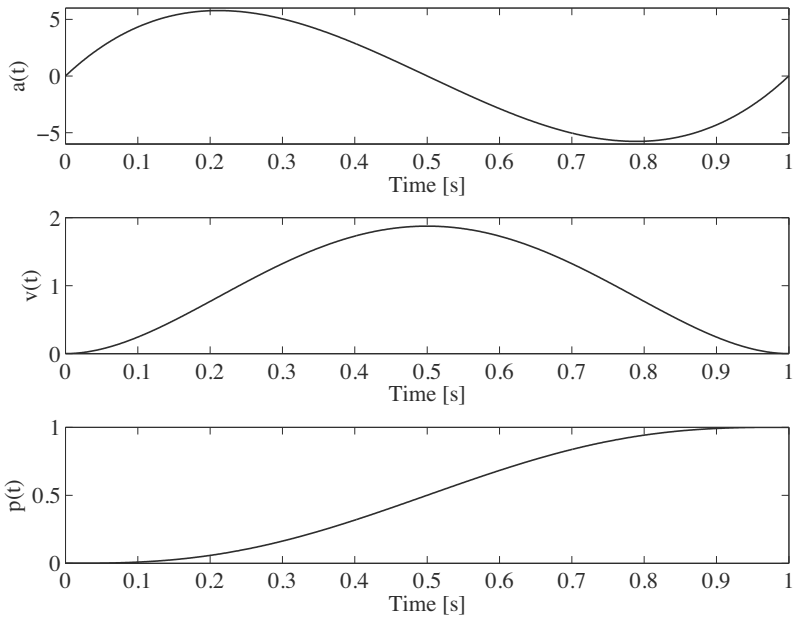

FIGURE 2.8
Minimum jerk input.

2.2.3 Digital Implementation of Minimum Jerk Input

Recently, positioning control algorithms in mechatronic products are implemented by microprocessor in most cases. As such, the minimum jerk input $u_{mjc}(t)$ (which is a continuous-time signal) must be implemented by using a sampler-and-hold as shown in Figure 2.9. In this figure, ZOH is the Zero-Order Hold and τ is a sampling period. In this case, the output $y(t)$ of the plant may not go to the target position if the sampling period cannot be chosen arbitrarily small enough.

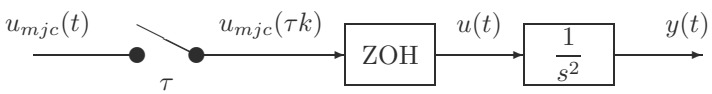

FIGURE 2.9
Digital implementation of $u_{mjc}(t)$.

As an example, the output response $y(t)$ in Figure 2.9 is calculated for different sampling periods. The final time T and the target position r in (2.14) are assumed to be $T = 1$ and $r = 1$. The outputs $y(t)$ are shown in Figure 2.10 when $\tau = 10$ ms and $\tau = 100$ ms. Figure 2.10 shows that the

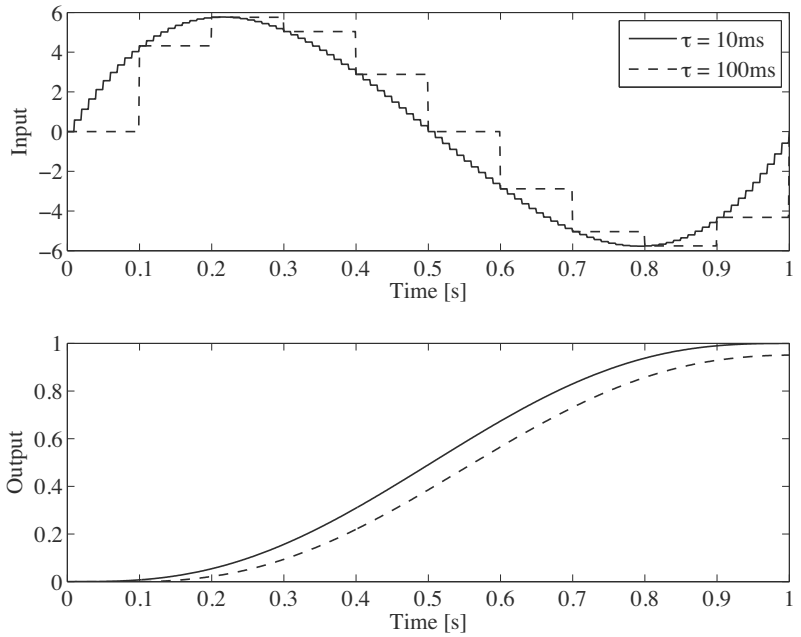

FIGURE 2.10
Minimum jerk control for different sampling periods.

positioning error at $t = T$ becomes large if the sampling period is not small enough as $\tau = 100$ ms.

An approach to avoid the positioning error at the final time $t = T$ is to obtain the feedforward input by taking into account the effects of the ZOH. The details of this approach will be presented in the next section.

2.2.4 Sampled-Data Polynomial Input

A feedforward input generated by a polynomial taking account of the effect of the ZOH is referred to as the *sampled-data polynomial* input [3].

Similarly, the plant $P(s)$ is assumed to be a rigid-body system as

$$P(s) = \frac{1}{s^2}.$$

The state-space representation of $P(s)$ can be given as

$$\begin{bmatrix} \dot{p}(t) \\ \dot{v}(t) \end{bmatrix} = \begin{bmatrix} 0 & 1 \\ 0 & 0 \end{bmatrix} \begin{bmatrix} p(t) \\ v(t) \end{bmatrix} + \begin{bmatrix} 0 \\ 1 \end{bmatrix} u(t), \tag{2.16}$$

where $p(t)$ is the position, $v(t)$ is the velocity, and $u(t)$ is the input.

It is assumed that the input $u(t)$ is generated by a discrete-time signal $u[n]$ $(n = 0, 1, 2, \ldots)$ through the ZOH as

$$u(\tau n + \theta) = u[n], \quad \theta \in [0, \tau).$$

As such, (2.16) can be discretized as

$$\begin{bmatrix} p[n+1] \\ v[n+1] \end{bmatrix} = \begin{bmatrix} 1 & \tau \\ 0 & 1 \end{bmatrix} \begin{bmatrix} p[n] \\ v[n] \end{bmatrix} + \begin{bmatrix} \frac{1}{2}\tau^2 \\ \tau \end{bmatrix} u[n], \tag{2.17}$$

where $p[n] = p(\tau n)$ and $v[n] = v(\tau n)$.

When the initial values of $p[0]$, $v[0]$, and $u[0]$ are set as zero, it is straightforward to show that $v[n]$ and $p[n]$ are given by

$$v[n] = \begin{cases} 0 & (n \le 1) \\ \tau \displaystyle\sum_{i=1}^{n-1} u[i] & (2 \le n) \end{cases}, \tag{2.18}$$

$$p[n] = \begin{cases} 0 & (n \le 1) \\ \dfrac{1}{2}\tau^2 \displaystyle\sum_{i=1}^{n-1} \left[\{2(n-i)-1\}\, u[i]\right] & (2 \le n) \end{cases}. \tag{2.19}$$

Similar to the minimum jerk input, the discrete-time feedforward input $u[n]$ is assumed to be a polynomial of order three as

$$u[n] = An^3 + Bn^2 + Cn + D, \tag{2.20}$$

where the coefficient A, B, C, and D must satisfy the initial conditions

$$u[0] = 0, \quad v[0] = 0, \quad p[0] = 0,$$

and the final conditions

$$u[N] = 0, \quad v[N] = 0, \quad p[N] = r,$$

where N is a final step.

From $u[0] = 0$, we have

$$D = 0.$$

From $u[N] = 0$, we have

$$u[N] = N^3 A + N^2 B + NC = 0. \tag{2.21}$$

From $v[N] = 0$, we have

$$\begin{aligned} v[N] &= \tau \sum_{i=1}^{N-1} u[i] \\ &= \tau \sum_{i=1}^{N-1} (Ai^3 + Bi^2 + Ci) \\ &= X_A A + X_B B + X_C C = 0, \end{aligned} \tag{2.22}$$

where

$$\begin{aligned} X_A &= \tau \sum_{i=1}^{N-1} i^3 = \frac{\tau}{4} N^2 (N-1)^2, \\ X_B &= \tau \sum_{i=1}^{N-1} i^2 = \frac{\tau}{6} N(N-1)(2N-1), \\ X_C &= \tau \sum_{i=1}^{N-1} i = \frac{\tau}{2} N(N-1). \end{aligned}$$

From $p[N] = r$, we have

$$\begin{aligned} p[N] &= \frac{1}{2}\tau^2 \sum_{i=1}^{N-1} \left[\{2(N-i)-1\}\, u[i]\right] \\ &= Y_A A + Y_B B + Y_C C = r, \end{aligned} \tag{2.23}$$

where

$$\begin{aligned} Y_A &= \frac{\tau^2}{2} \sum_{i=1}^{N-1} \left\{(2N-1)i^3 - 2i^4\right\} = \frac{\tau^2}{120} N(N-1)(2N-1)(3N^2-3N+4), \\ Y_B &= \frac{\tau^2}{2} \sum_{i=1}^{N-1} \left\{(2N-1)i^2 - 2i^3\right\} = \frac{\tau^2}{12} N(N-1)(N^2-N+1), \\ Y_C &= \frac{\tau^2}{2} \sum_{i=1}^{N-1} \left\{(2N-1)i - 2i^2\right\} = \frac{\tau^2}{12} N(2N-1)(N-1). \end{aligned}$$

By solving (2.21), (2.22), and (2.23) simultaneously, we have

$$\begin{aligned} A &= \frac{120r}{\tau^2} \frac{1}{N(N^2-1)(N^2-4)}, \\ B &= -\frac{180r}{\tau^2} \frac{1}{(N^2-1)(N^2-4)}, \\ C &= \frac{60r}{\tau^2} \frac{N}{(N^2-1)(N^2-4)}, \end{aligned}$$

and the sampled-data polynomial of (2.20) becomes

$$u[n] = \frac{60r}{\tau^2} \frac{n(n-N)(2n-N)}{N(N^2-1)(N^2-4)}. \tag{2.24}$$

In order to compare the minimum jerk input (2.15) and the sampled-data polynomial (2.24), the normalized step $n_n = n/N$ and the final time $T = \tau N$ are introduced. Equation (2.24) becomes

$$u[n] = \frac{60r}{T^2} n_n (2n_n - 1)(n_n - 1) g, \tag{2.25}$$

where

$$g = \frac{1}{(1 - 1/N^2)(1 - 4/N^4)}.$$

It follows from (2.15) and (2.25) that the sampled-data polynomial (2.25) approaches the minimum-jerk input (2.15) as $N \to \infty$. This implies that the sampled-data polynomial can be used as a substitute of the minimum jerk input.

In this example, we have obtained the sampled-data polynomial of order three, although higher order polynomials can also be obtained. However, additional boundary conditions are required for all the coefficients of the polynomial to be uniquely determined. From fourth- to eight-order polynomials under appropriate boundary conditions, the results are shown in Table 2.1 [3]. A high-order polynomial tends to generate a smoother control input which is effective to reduce the residual vibrations at the target position. As such, the order of the polynomials can be selected by considering the tradeoff between the computational load and the residual vibrations.

The calculation of the solutions to the simultaneous equations will be computationally intensive when the order of the polynomial is high. For such cases, the use of computational softwares such as Mathematica or Maple will be a good choice. MATLAB can also handle symbolic calculations by using Symbolic Math Toolbox. An example of a MATLAB script used to obtain the solution of (2.24) is shown below.

```
%% Initialize
clear all
syms A B C N tau n r

%% Define input polynomial
u = A * n^3 + B * n^2 + C * n;

%% Boundary condtion for n = N
uN = subs(u,n,N);
vN = tau*symsum(u,n,1,N-1);
pN = (1/2)*tau^2*symsum((2*(N-n)-1)*u,n,1,N-1) - r;

%% Solve simultaneous equations
S = solve(uN,vN,pN,A,B,C)

%% Solutions A, B, and C
A_  = factor(S.A)
B_  = factor(S.B)
C_  = factor(S.C)

%% Sampled-data polynomial (solution)
U_ff = factor(subs(u,{A,B,C},{A_,B_,C_}))
```

TABLE 2.1
Acceleration Sampled-Data Polynomials

Order	Boundary conditions and polynomial $u[n]$
Fourth	$p[0] = v[0] = u[0] = 0, p[N] = r,$ $v[N] = u[N] = \frac{d}{dn}u[N] = 0$ $u[n] = \frac{-60n(n-N)^2(5nN - 2(1+N^2))r}{(N-2)(N-1)N(N+1)(N+2)(1+N^2)\tau^2}$
Fifth	$p[0] = v[0] = u[0] = \frac{d}{dn}u[0] = 0, p[N] = r,$ $v[N] = u[N] = \frac{d}{dn}u[N] = 0$ $u[n] = \frac{-420n^2(n-N)^2(2n-N)r}{(N-2)(N-1)N(N+1)(N+2)(5+N^2))\tau^2}$
Sixth	$p[0] = v[0] = u[0] = \frac{d}{dn}u[0] = 0, p[N] = r,$ $v[N] = u[N] = \frac{d}{dn}u[N] = \frac{d^2}{dn^2}u[N] = 0$ $u[n] = \frac{840n^2(n-N)^3(-10 + (7n-3N)N(1+N^2))r}{N(N^2-4)(N^2-1)(N^2+5)(10+3(N^2+N^4))\tau^2}$
Seventh	$p[0] = v[0] = u[0] = \frac{d}{dn}u[0] = \frac{d^2}{dn^2}u[0] = 0, p[N] = r,$ $v[N] = u[N] = \frac{d}{dn}u[N] = \frac{d^2}{dn^2}u[N] = 0$ $u[n] = \frac{2520n^3(n-N)^3(2n-N)r}{(N-2)(N-1)N(N+1)(N+2)(42+5N^2+N^4)\tau^2}$
Eighth	$p[0] = v[0] = u[0] = \frac{d}{dn}u[0] = \frac{d^2}{dn^2}u[0] = 0, p[N] = r,$ $v[N] = u[N] = \frac{d}{dn}u[N] = \frac{d^2}{dn^2}u[N] = \frac{d^3}{dn^3}u[N] = 0$ $u[n] = \frac{-1260n^3(n-N)^4}{(N-2)(N-1)N(N+1)(N+2)(3+N^2)}$ $\times \frac{(-84 + 30nN - 4N^2 + 9nN^3 - 4N^4 + 9nN^5 - 4N^6)r}{(7-2N^2+N^4)(42+5N^2+N^4)\tau^2}$

2.3 Final-State Control

2.3.1 Problem Formulation

A Final-State Control (FSC) is a method to obtain a profile for the feedforward input that drives an initial state to a final state in N sampling steps [4]. In fact, such a problem can be formulated into a classical optimal control problem with two boundary conditions [1]. If the minimum control input norm problem is assumed in the discrete-time domain, it can be easily solved with mathematical methods in the current literature [4, 5].

The state-space representation of an m^{th}-order discrete-time controllable system is given by

$$x[k+1] = Ax[k] + Bu[k]. \tag{2.26}$$

For this system, we would like to obtain a control input $u[k]$ that drives the initial state $x[0]$ to the final-state $x[N]$ in $N \geq m$ sampling steps. Since such an input is generally not unique, and the cost function to be minimized is defined as

$$J = U^T Q U, \tag{2.27}$$

where $Q > 0$ and

$$U := \begin{pmatrix} u[0], & u[1], & \dots & u[N-1] \end{pmatrix}^T. \tag{2.28}$$

By calculating (2.26) from $k = 0$ to N recursively, we have

$$x[N] - A^N x[0] = \Sigma U, \tag{2.29}$$

where

$$\Sigma = \begin{bmatrix} A^{N-1}B, & A^{N-2}B, & \dots, & B \end{bmatrix}. \tag{2.30}$$

It follows from the controllability of (A, B) and $N \geq m$ that Σ is a matrix of full row rank, and it can be shown that a control input U which satisfies (2.29) always exists. In order to obtain a minimum solution of (2.27) subjected to (2.29), a *Lagrange multiplier* 2λ is included and the cost function J becomes

$$J = U^T Q U + 2\lambda(X - \Sigma U), \tag{2.31}$$

where $X := x[N] - A^N x[0]$. It follows from $Q > 0$ that there is a unique solution, and the minimum solution U must satisfy

$$\frac{\partial J}{\partial U} = 2QU - 2\Sigma^T \lambda^T = 0. \tag{2.32}$$

Since $Q > 0$ and Q^{-1} exists, we have

$$U = Q^{-1}\Sigma^T\lambda^T. \tag{2.33}$$

Furthermore, it follows from $X - \Sigma U = 0$ and (2.33) that $X - \Sigma Q^{-1}\Sigma^T\lambda^T = 0$ is satisfied. Since Σ is a matrix of full row rank by the controllability of (A, B), $|\Sigma Q^{-1}\Sigma^T| \neq 0$ is also satisfied. As such, we have

$$\lambda^T = (\Sigma Q^{-1}\Sigma^T)^{-1}X. \tag{2.34}$$

Finally, it follows from (2.33) and (2.34) that [5]

$$U = Q^{-1}\Sigma^T(\Sigma Q^{-1}\Sigma^T)^{-1}(x[N] - A^N x[0]). \tag{2.35}$$

The optimal feedforward input U can now be easily obtained using simple algebra for given $x[0]$, $x[N]$, Q, and N.

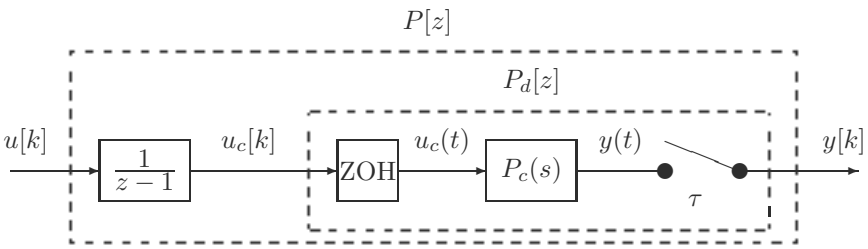

FIGURE 2.11
Augmented system with a discrete-time integrator.

2.3.2 Minimum Jerk Input Design by FSC

The minimum jerk input in discrete-time domain can be easily solved by using the proposed FSC method. Similar to the minimum jerk input design in continuous-time domain as shown in Section 2.2.2, an augmented system with a discrete-time integrator $1/(z-1)$ as shown in Figure 2.11 is considered. In Figure 2.11, $P_c(s)$ is a continuous-time plant whose input is acceleration (or force or the same dimension of those) and $P_d[z]$ is a discretized plant of $P_c(s)$.

Since the input of the augmented system corresponds to jerk, the minimum jerk input can be obtained by minimizing the cost function

$$J = \sum_{k=0}^{\infty} u^T[k]u[k]. \tag{2.36}$$

The state-space representation of $P_c(s)$ which is of m^{th}-order is given by

$$\dot{x}_c(t) = A_c x_c(t) + B_c u_c(t), \quad y(t) = C_c x_c(t), \tag{2.37}$$

and the state-space representation of the discrete-time model $P_d[z]$ with ZOH is given by

$$x_d[k+1] = A_d x_d[k] + B_d u_c[k], \quad y[k] = C_d x_d[k], \tag{2.38}$$

where

$$\begin{aligned} A_d &= e^{A_c \tau}, \quad B_d = \int_0^\tau e^{A_c t} B_c dt, \quad C_d = C_c, \\ x_d[k] &= x_c(k\tau), \quad y[k] = y(k\tau), \end{aligned}$$

and τ is the sampling period. Since the ZOH is used, we have

$$u_c(k\tau + \theta) = u_c[k], \quad \theta \in [0, \tau). \tag{2.39}$$

The state-space representation of the augmented system is thus given by

$$x[k+1] = Ax[k] + Bu[k], \quad y[k] = Cx[k], \tag{2.40}$$

where $x[k] := [x_d^T[k], u_c^T[k]]^T$ and

$$A = \begin{bmatrix} A_d & B_d \\ 0 & 1 \end{bmatrix}, \quad B = \begin{bmatrix} 0 \\ 1 \end{bmatrix}, \quad C = \begin{bmatrix} C_d & 0 \end{bmatrix}. \tag{2.41}$$

In this case, both (A_c, B_c) and (A_d, B_d) are assumed to be controllable.

Now, a smooth input is obtained by applying the FSC method to the augmented system in (2.40) via minimizing the cost function in (2.36) subjected to both initial and final state constraints. It should be noted that the initial and final states of the augmented system have to be given by

$$x[0] = \begin{bmatrix} x_d[0] \\ u_c[0] \end{bmatrix} = 0_{(m+1)\times 1}, \quad x[N] = \begin{bmatrix} x_d[N] \\ u_c[N] \end{bmatrix} = \begin{bmatrix} x_d[N] \\ 0 \end{bmatrix}, \tag{2.42}$$

so that the actual input u_c satisfies $u_c[0] = 0$ and $u_c[N] = 0$. The feedforward input obtained by this method is referred to as the *FSC input* and the trajectory generated by the FSC input is referred to as the *FSC trajectory*.

2.3.3 Vibration Minimized Input Design by FSC

A smooth input is desired to reduce the residual vibrations after positioning. However, such an input may extend beyond the *total* positioning time. In order to achieve both high-speed positioning and vibration suppression, we consider minimizing the *spectrum of the control input* at the frequencies where resonant modes of the plant exist [5].

The Fourier transform $\hat{U}_c(\omega)$ of $u_c(t)$ is defined as

$$\hat{U}_c(\omega) = \int_0^{N\tau} u_c(t) e^{-j\omega t} dt, \tag{2.43}$$

and its gain $|\hat{U}_c(\omega)|$ is minimized at the desired frequency points $\omega_i (i = 1, \ldots, \ell)$. For this purpose, the following cost function is introduced as

$$J_w = \sum_{k=0}^{N-1} u^2[k] + \sum_{i=1}^{\ell} q_i |\hat{U}_c(\omega_i)|^2. \tag{2.44}$$

The first term of the right-hand side of (2.44) evaluates the smoothness of the control input, and the second term evaluates the frequency components of the control input. By choosing ω_i to cover the frequencies of the resonant modes of the plant, the frequency components around these frequencies are reduced. The weighting parameter q_i is selected to be a positive real number, and a larger q_i achieves a larger reduction in frequency components.

In order to obtain the closed-form of U which minimizes (2.44), the state-space representation of the discrete-time integrator is given by

$$\frac{1}{z-1} = \{1, 1, 1, 0\} =: \{A_w, B_w, C_w, 0\}. \tag{2.45}$$

Assuming $u_c[0] = 0$, the actual control input $u_c[k]$ can be described by

$$U_c = \Omega_w U, \tag{2.46}$$

where

$$U_c = \left[\; u_c[0], \ldots, u_c[N-1] \; \right]^T, \tag{2.47}$$

and

$$\Omega_w = \begin{bmatrix} 0 & 0 & \cdots & \cdots & 0 \\ C_w B_w & 0 & \ddots & & \vdots \\ C_w A_w B_w & C_w B_w & \ddots & \ddots & \vdots \\ \vdots & \ddots & \ddots & 0 & 0 \\ C_w A_w^{N-2} B_w & \cdots & C_w A_w B_w & C_w B_w & 0 \end{bmatrix}. \tag{2.48}$$

Since $u_c(t)$ is the output of the ZOH, we have

$$u_c(t) = \sum_{i=0}^{N-1} P_i(t) u_c[k], \tag{2.49}$$

where

$$P_i(t) := \begin{cases} 1, & i\tau \le t < (i+1)\tau \\ 0, & t < i\tau \;\text{ or }\; t \ge (i+1)\tau \end{cases}. \tag{2.50}$$

The Fourier transform $\hat{U}_c(\omega)$ of $u_c(t)$ can be given by

$$\begin{aligned}\hat{U}_c(\omega) &= \int_0^{N\tau} u_c(t)e^{-j\omega t}dt \\ &= \sum_{k=0}^{N-1}\int_{k\tau}^{(k+1)\tau} u_c[k]e^{-j\omega t}dt \\ &= \frac{2\sin(\omega\tau/2)}{\omega}e^{-j\omega\tau/2}\sum_{k=0}^{N-1} u_c[k]e^{-j\omega\tau k} \\ &= \hat{U}_1(\omega)\hat{U}_2(\omega)e^{-j\omega\tau/2}, \end{aligned} \tag{2.51}$$

where

$$\hat{U}_1(\omega) := \frac{2\sin(\omega\tau/2)}{\omega}, \quad \hat{U}_2(\omega) := \sum_{k=0}^{N-1} u_c[k]e^{-j\omega\tau k}. \tag{2.52}$$

It is easy to show that

$$\mathrm{Re}\left[\hat{U}_2(\omega)\right] = \sum_{k=0}^{N-1} u_c[k]\cos(k\omega\tau) = S_R(\omega)U_c, \tag{2.53}$$

$$\mathrm{Im}\left[\hat{U}_2(\omega)\right] = \sum_{k=0}^{N-1} u_c[k]\sin(k\omega\tau) = S_I(\omega)U_c, \tag{2.54}$$

where

$$S_R(\omega) := \left[\cos(0),\ \cos(\omega\tau),\ \ldots,\ \cos((N-1)\omega\tau)\right], \tag{2.55}$$

$$S_I(\omega) := \left[\sin(0),\ \sin(\omega\tau),\ \ldots,\ \sin((N-1)\omega\tau)\right]. \tag{2.56}$$

As such,

$$|\hat{U}_2(\omega)|^2 = U_c^T(S_R^T S_R(\omega) + S_I^T S_I(\omega))U_c. \tag{2.57}$$

From (2.57) and $U_c = \Omega_z U$, we have

$$|\hat{U}_c(\omega)|^2 = |\hat{U}_1(\omega)|^2 U^T\Omega_z^T(S_R^T S_R(\omega) + S_I^T S_I(\omega))\Omega_z U. \tag{2.58}$$

Finally, J_w in (2.44) can be represented as a quadratic form of U as

$$J_w = U^T Q_w U, \tag{2.59}$$

where

$$Q_w = I_N + \sum_{i=1}^{\ell} q_i Q_U(\omega_i), \tag{2.60}$$

$$Q_U(\omega_i) = |\hat{U}_1(\omega_i)|^2\Omega_z^T(S_R^T S_R(\omega_i) + S_I^T S_I(\omega_i))\Omega_z. \tag{2.61}$$

The FSC input obtained by minimizing (2.59) is referred to as *Frequency-shaped Final State Control* (FFSC) input and the trajectory generated by the FFSC input is referred to as the *FFSC trajectory*.

2.3.4 Final-State Control with Constraints

In actual control problems, the maximum absolute value of the control input is limited due to saturation. Moreover, the minimum or maximum value of velocity, acceleration, and current may also be limited. In this case, the feedforward input must be designed so as to satisfy these constraints. In order to incorporate the constraints into the FSC design, the constraint variable $z[k]$ is introduced as

$$z[k] = C_z x[k] + D_z u[k], \tag{2.62}$$

and the control input $u[k]$ which minimizes (2.27) is obtained subjected to

$$|z[k]| < z_{max} \quad (k = 0, \ldots, N-1), \tag{2.63}$$

for a given z_{max}.

This problem can be formulated as a Quadratic Programming (QP) problem [6]. The QP is a problem to obtain a solution $U \in \mathcal{R}^N$ minimizing the cost function

$$J = U^T Q U, \tag{2.64}$$

with $Q > 0$ and subjected to one or more constraints of the form

$$A_{EQ} U = b_{EQ} \quad \text{(equality constraint)}, \tag{2.65}$$

$$A_{INEQ} U \leq b_{INEQ} \quad \text{(inequality constraint)}, \tag{2.66}$$

where A_{EQ} and A_{INEQ} are arbitrary matrices, and b_{EQ} and b_{INEQ} are arbitrary vectors. The notation $A_{INEQ}U \leq b_{INEQ}$ means that every entry of the vector $A_{INEQ}U$ is less than or equal to the corresponding entry of the vector b_{INEQ}.

In the FSC method, the equality constraint in (2.29) corresponds to (2.65), and the cost function (2.27) corresponds to (2.64). In addition, constraints on the state variables and/or the input of the plant can easily be handled by utilizing the inequality constraints in (2.66).

Without loss of generality, $z[k]$ is assumed to be a scalar variable, and $z[0], \ldots, z[N-1]$ are calculated as

$$\begin{cases} z[0] = C_z x[0] + D_z u[0] \\ z[1] = C_z A x[0] + C_z B u[0] + D_z u[1] \\ \qquad \vdots \\ z[N-1] = C_z A^{N-1} x[0] + \cdots + D_z u[N-1] \end{cases}. \tag{2.67}$$

Equation (2.67) can be represented collectively in a matrix form as

$$Z = \Phi_z x[0] + \Omega_z U, \tag{2.68}$$

where

$$Z = \left[\; z[0], \quad \cdots, \quad z[N-1] \; \right]^T, \tag{2.69}$$

$$\Phi_z = \begin{bmatrix} C_z \\ C_z A \\ \vdots \\ C_z A^{N-1} \end{bmatrix}, \tag{2.70}$$

$$\Omega_z = \begin{bmatrix} 0 & 0 & \dots & \dots & 0 \\ C_z B & 0 & \ddots & & \vdots \\ C_z AB & C_z B & \ddots & \ddots & \vdots \\ \vdots & \ddots & \ddots & 0 & 0 \\ C_z A^{N-2} B & \dots & C_z AB & C_z B & 0 \end{bmatrix}. \tag{2.71}$$

As such, the constraint in (2.63) can be represented as an inequality as

$$\begin{bmatrix} \Omega_z \\ -\Omega_z \end{bmatrix} U \leq \begin{bmatrix} Z_{max} - \Phi_z x[0] \\ Z_{max} + \Phi_z x[0] \end{bmatrix}, \tag{2.72}$$

where $Z_{max} = z_{max}[1, \dots, 1]^T$. Since (2.72) corresponds to (2.66), the FSC and FFSC problems with constraints can be reformulated as QP problems.

2.4 Industrial Application: Hard Disk Drives

The FSC and FFSC inputs are designed for the plant of the Hard Disk Drive (HDD) Benchmark Problem [7], and the control performance is evaluated by simulations.

2.4.1 HDD Benchmark Problem and the Plant Model

Various control methods have been proposed for HDD servo problems so far. However, it is difficult to compare and evaluate these control methods fairly because they have been developed for a specific control objective and on different HDDs. As such, the demand for the benchmark problem of HDD control has been tremendously increased.

To realize these purposes, the "Investigation R&D Committee for Next Generation Servo Control Technology for Mass-Storage System," the Chair being Dr. Takashi Yamaguchi, at the Institute of Electrical Engineers of Japan (IEEJ) set up a working group to develop the HDD Benchmark Problem together. In September 2005, the working group released Version 1 of the HDD Benchmark Problem, in which plant parameters are optimized for the

TABLE 2.2
Plant Parameters

i	f_i [Hz]	ζ_i	A_i
1	0	0	1.0
2	3000	0.01	−0.01
3	4100	0.03	−1.0
4	5000	0.01	0.3
5	7000	0.01	−1.0
6	12300	0.005	1.0
7	16400	0.005	−1.0

TABLE 2.3
Parameter Variations

Variable	min (%)	max (%)
f_2	−2 %	+1 %
f_3	−5 %	+2.5 %
$f_{4,5,6,7}$	−2 %	+0.5 %
$A_{2,4}$	−200 %	+0 %
A_3	−0 %	+20 %
$\zeta_{5,6,7}$	−50 %	+100 %

track-following controller design. In the following year, the plant model was updated to reflect more realistic properties of actual HDDs, and Version 2 of the HDD Benchmark Problem was released. Finally in 2010, the plant models in Versions 1 and 2 were unified in the latest version or Version 3 of the HDD Benchmark Problem, where both models can now be used by selecting the corresponding parameter files [8, 9]. In this section, the parameter set in Version 2 of the HDD Benchmark Problem is used.

The transfer function of the plant model is defined as

$$P_f(s) = K_p \left(\sum_{i=1}^{N} \frac{A_i}{s^2 + 2\zeta_i \omega_i s + \omega_i^2} \right) e^{-sT_d}, \tag{2.73}$$

where $\omega_i = 2\pi f_i$, $K_p = 3.93 \times 10^9$, and $T_d = 1 \times 10^{-5}$s. The control input is the acceleration [m/s^2] of the voice coil motor and the measurement output is the head position [track]. The parameters A_i, ζ_i, and f_i of the resonant modes are shown in Table 2.2, and the frequency response of the nominal model is shown in Figure 2.12. The HDD Benchmark Problem also includes a model of parameter variation of the mechanical resonant mode. The upper and lower bounds of the parameters are shown in Table 2.3, and the frequency responses of the perturbed models are shown in Figure 2.13. The change in loop gain of ±10% is also assumed.

In the HDD Benchmark Problem for track-seeking, the following assumptions are made:

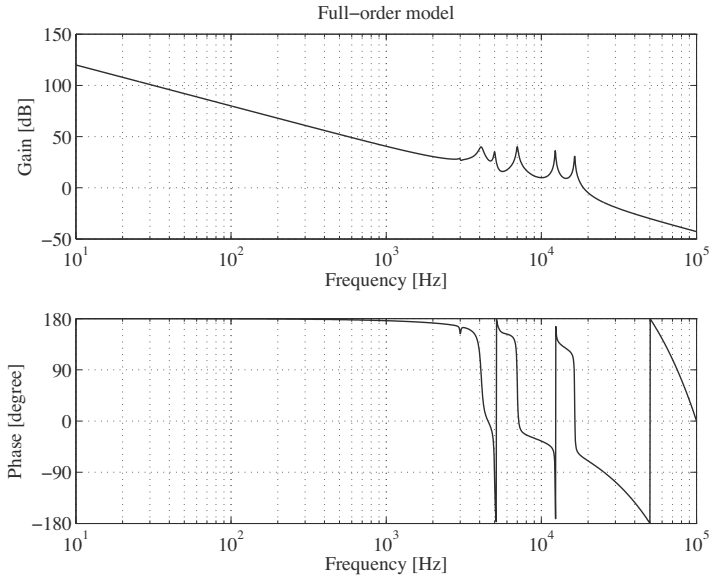

FIGURE 2.12
Bode plot of the nominal model.

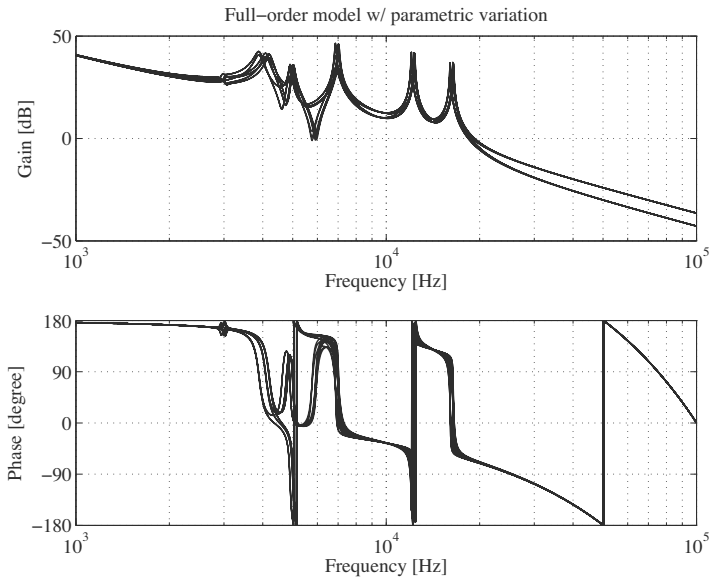

FIGURE 2.13
Bode plots of the perturbed plants.

1. no disturbances are taken into account;
2. the magnitude of the control input is not limited;
3. two seek distances of one track and ten tracks are considered; and
4. the seeking time is defined as the time in which the head position settles within ±0.1 of the track width at the target track for all the nominal and perturbed models.

The main object of the track-seeking control problem is to design a track-seeking control system which achieves the shortest seeking time for both one and ten track-seeks. The controller parameters can be optimized for both one and ten track-seeks as long as the same control method is used.

This section focuses on the design of the feedforward input that reduces the residual vibrations. As such, a feedback controller is not used. In the HDD Benchmark Problem, a plant gain change of ±5% is included. For our simulations, the gain change is not considered because the gain change cannot be compensated for without the feedback controller.

2.4.2 FSC and FFSC Inputs Design

Design 1

In Design 1, a minimum jerk input for a rigid-body mode model was obtained using the FSC method. The step number N was determined by trial and error so that the maximum seeking times for all the plant model are minimized. As a result, $N = 12$ achieved the minimum seeking time for one track-seek. The corresponding time response and the spectrum of the obtained minimum jerk input are shown in Figure 2.14.

Track-seeking simulations were then carried out, and the time responses and the spectra of the head positions for all the plant models are shown in Figure 2.15. The worst-case seek time was 0.333 ms.

As for ten track-seek, $N = 26$ achieves the minimum seeking time. The corresponding time response and the spectrum of the obtained minimum jerk input is shown in Figure 2.16. The time responses and the spectra of the head position for all the plant models are shown in Figure 2.17. The worst-case seek time was 0.879 ms.

In both one and ten track-seek, it was difficult to further decrease the seek time since the head position varies beyond ±10% of the track width due to residual vibrations.

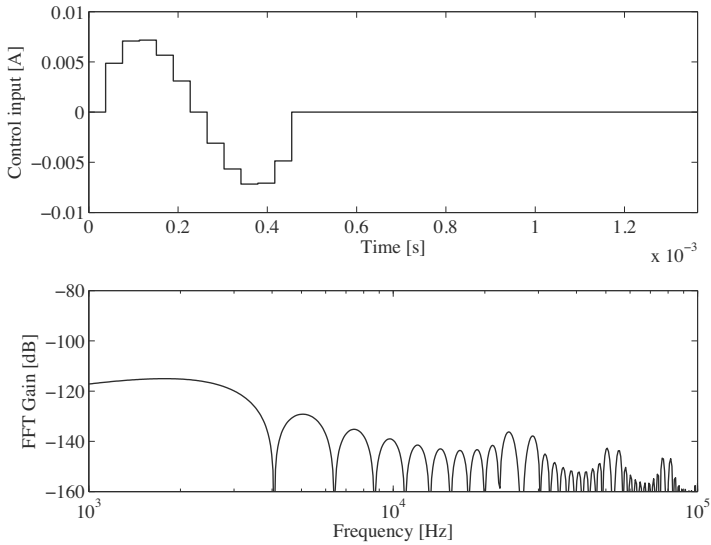

FIGURE 2.14
Design 1: Feedforward input for one track-seek.

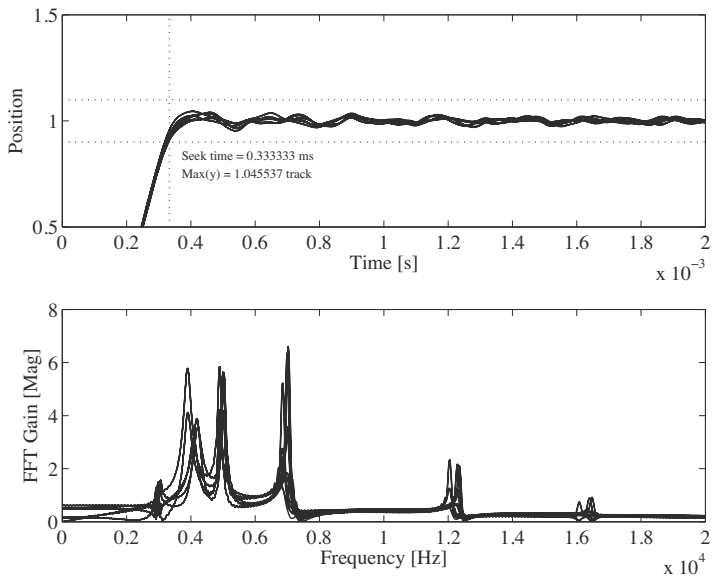

FIGURE 2.15
Design 1: Output response for one track-seek.

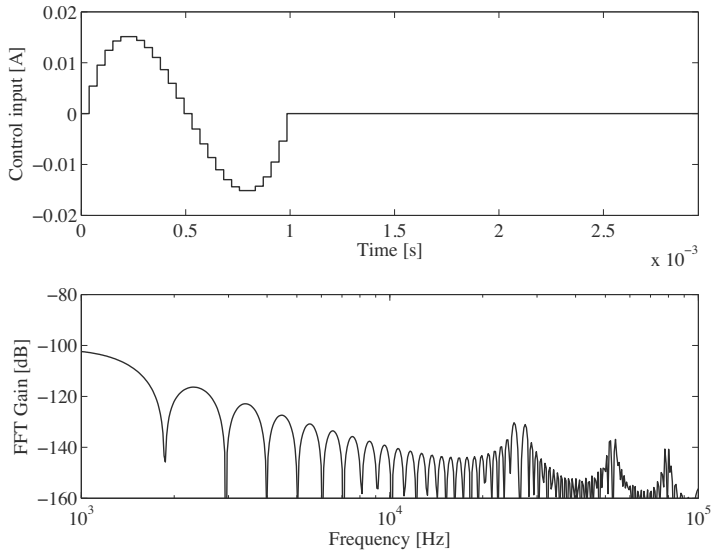

FIGURE 2.16
Design 1: Feedforward input for ten track-seek.

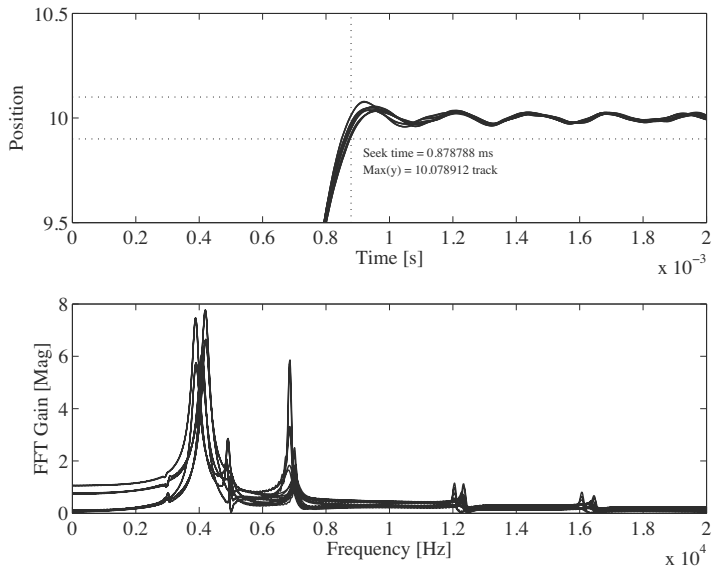

FIGURE 2.17
Design 1: Output response for ten track-seek.

Design 2

In Design 2, the FFSC method was applied to minimize the residual vibrations. In the FFSC method, the selections of the frequencies $\omega_i = 2\pi f_i$ and the weights q_i in (2.44) are very important to reduce the residual vibrations without extending the seek time.

In the HDD Benchmark Problem, the lower- and upper-bound of the frequency changes of the resonant modes are defined for each vibration mode as shown in Table 2.3. As such, the cost function is modified so that the design parameters can easily be tuned for each vibration mode separately as [7]

$$J_w = \frac{1}{N}\sum_{k=0}^{N-1} u^2[k] + \sum_{i=3}^{7}\sum_{j=1}^{\ell_i} q_i |\hat{U}_c(2\pi f_{ij})|^2, \tag{2.74}$$

where

$$f_{ij} = f_{\ell i} + \frac{f_{ui} - f_{\ell i}}{\ell_i - 1} j, \quad (j = 1 \cdots \ell_i). \tag{2.75}$$

The plant in the HDD Benchmark Problem has six vibration modes at 3 kHz, 4.1 kHz, 5 kHz, 7 kHz, 12.3 kHz, and 16.4 kHz. The FFSC input was designed so that the spectra at 4.1 kHz, 5 kHz, 7 kHz, and 12.3 kHz are well reduced for one track-seek as these modes cause large residual vibrations. The parameters of (2.74) and (2.75) are shown in Table 2.4. Note that $\ell_i = 60$ for all i.

TABLE 2.4
Design Parameters for Design 2

i	$f_{\ell i}$ (Hz)	f_{hi} (Hz)	q_i (1 track)	q_i (10 tracks)
3	3895	4305	5×10^9	5×10^9
4	4900	5050	2×10^8	2×10^8
5	6860	7070	1×10^{10}	5×10^{10}
6	12054	12423	2×10^9	1×10^9
7	16072	16564	0	1×10^8

On the other hand, for ten track-seek, the FFSC input was designed so that the spectra at 4.1 kHz, 5 kHz, 7 kHz, 12.3 kHz, and 16.4 kHz are well reduced. The design parameters are also shown in Table 2.4. The seek step N was chosen so that the worst-case seek time is minimized for all the plant models. $N = 10$ for one track-seek and $N = 17$ for ten track-seek were determined. The time responses and the spectra of the FFSC inputs are shown in Figure 2.18 and Figure 2.20. The time responses and the spectra of the head position are shown in Figure 2.19 and Figure 2.21. The seek time was 0.280 ms for one track-seek and 0.538 ms for ten track-seek, resulting in 16% and 39% improvements of seek time, respectively.

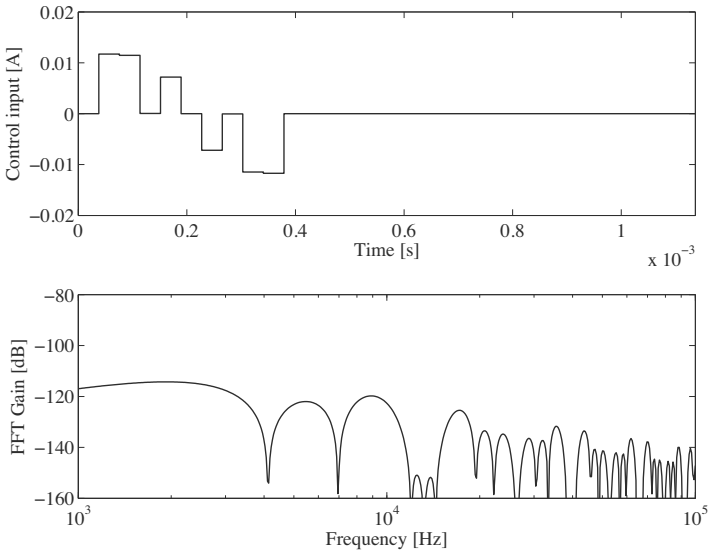

FIGURE 2.18
Design 2: Feedforward input for one track-seek.

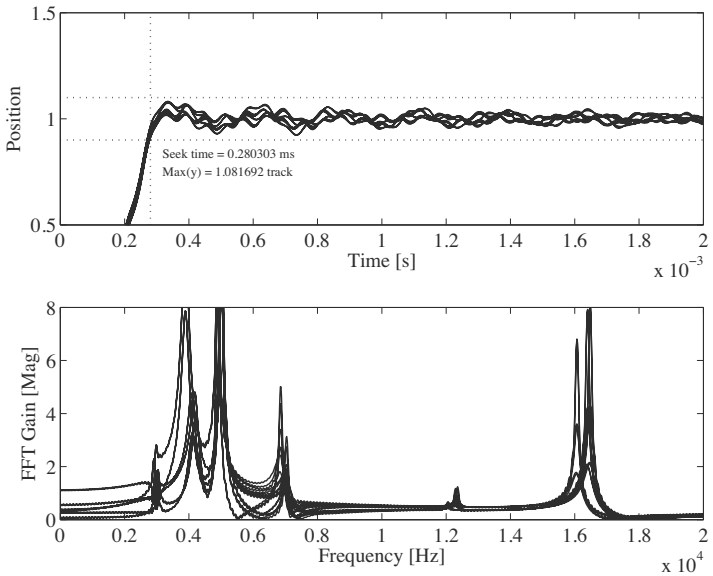

FIGURE 2.19
Design 2: Output response for one track-seek.

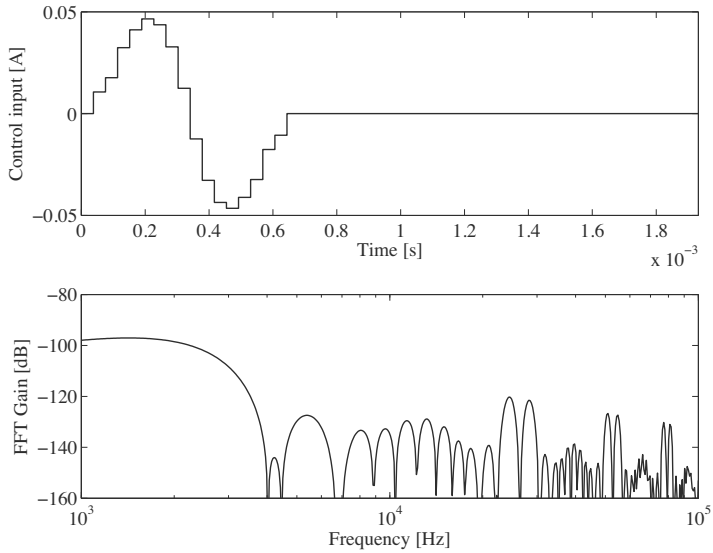

FIGURE 2.20
Design 2: Feedforward input for ten track-seek.

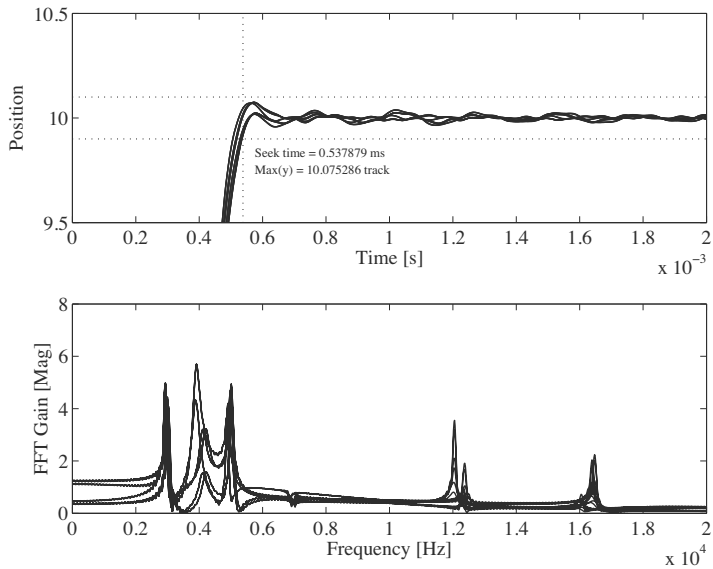

FIGURE 2.21
Design 2: Output response for ten track-seek.

2.5 Industrial Application: Galvano Scanner I

The laser-drilling machine for printed wiring boards is required to process smaller diameter holes with higher precision and throughput. The galvano scanner is a key component in the laser processing machine, and it has a mirror to control the direction of the laser beam. The angle of the mirror must be controlled as quickly and precisely as possible.

In this section, the FSC and FFSC inputs are designed for the galvano scanner, and the obtained feedforward inputs are implemented using the TDOF control structure. The effectiveness of the proposed method is verified with simulations and experiments [10].

2.5.1 Plant Model

The control system of the galvano scanner is shown in Figure 2.22.

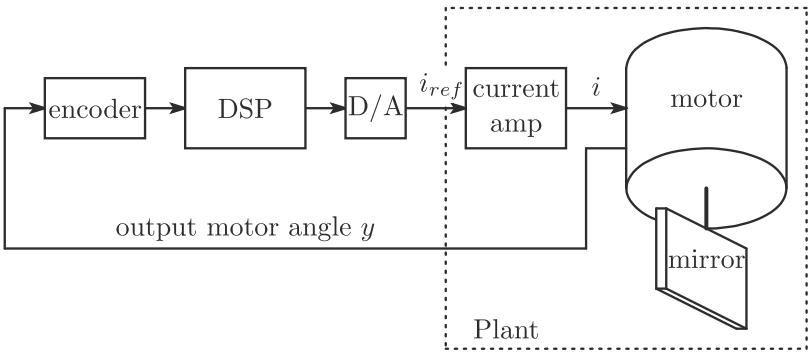

FIGURE 2.22
Control system of galvano scanner.

In Figure 2.22, i is a motor current, i_{ref} is a reference to the motor current, and y is a motor angle. The measured frequency response from i_{ref} to y is shown in Figure 2.23 by the solid line. Note that the unit [Hz/unit] is a normalized frequency where the frequency of the first resonant mode is unity. As shown in Figure 2.23, the plant has two large resonant modes at high frequencies.

To fit the measured frequency response, the transfer function of the galvano scanner is modeled as a system having a rigid-body mode and two vibration modes with an input delay as

$$P(s) = P_{mech}(s)e^{-\tau_d s},$$

where P_{mech} is defined as

$$P_{mech}(s) = P_n(s) + P_1(s) + P_2(s), \tag{2.76}$$

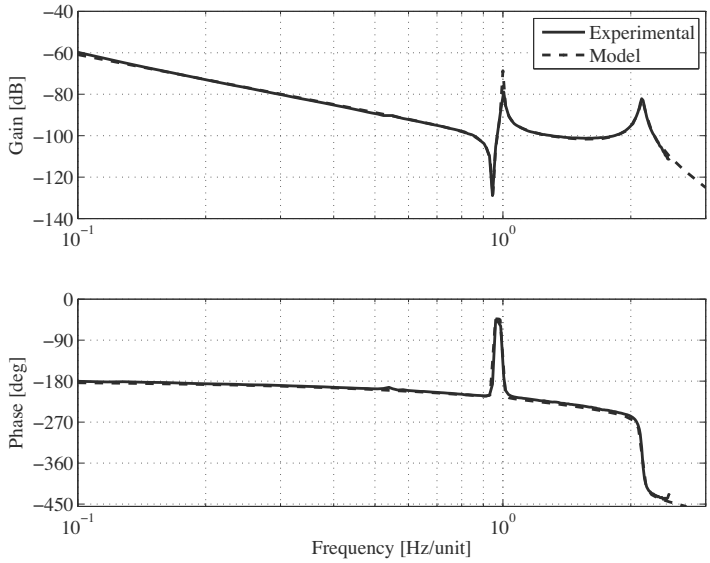

FIGURE 2.23
Frequency responses of galvano scanner.

where

$$P_n(s) = \frac{k_0}{s^2}, \tag{2.77}$$

$$P_i(s) = \frac{k_i}{s^2 + 2\zeta_i\omega_{ni}s + \omega_{ni}^2} \quad (i = 1,\ 2). \tag{2.78}$$

The Bode plot of P is shown by the dashed line in Figure 2.23.

2.5.2 FSC and FFSC Inputs Design

The proposed FSC and FFSC inputs are designed for the galvano scanner. In the FSC input design, a feedforward input is designed for P_{mech} which includes two vibration modes. The input delay $e^{-\tau_d s}$ is not taken into account in the feedforward input design, and it is considered when the obtained feedforward input is implemented in the TDOF control structure.

In the FFSC design, it is desired to reduce the spectrum of the feedforward input around the vibration modes to increase the robustness to the variation of the resonant frequencies while the other design condition is the same as that of the FSC design.

The continuous-time systems $P_n(s)$, $P_1(s)$, and $P_2(s)$ are discretized using

the ZOH method, and their state-space representations are given as

$$P_n[z]: \left\{ \begin{array}{rcl} x_n[k+1] & = & A_n x_n[k] + B_n u_c[k] \\ y_n[k] & = & C_n x_n[k] \end{array} \right. , \tag{2.79}$$

$$P_1[z]: \left\{ \begin{array}{rcl} x_1[k+1] & = & A_1 x_1[k] + B_1 u_c[k] \\ y_1[k] & = & C_1 x_1[k] \end{array} \right. , \tag{2.80}$$

$$P_2[z]: \left\{ \begin{array}{rcl} x_2[k+1] & = & A_2 x_2[k] + B_2 u_c[k] \\ y_2[k] & = & C_2 x_2[k] \end{array} \right. , \tag{2.81}$$

where the state vectors are defined as

$$x_n[k] = \left[\begin{array}{c} x_{np} \\ x_{nv} \end{array} \right], \; x_1[k] = \left[\begin{array}{c} x_{1p} \\ x_{1v} \end{array} \right], \; x_2[k] = \left[\begin{array}{c} x_{2p} \\ x_{2v} \end{array} \right].$$

Note that the subscripts $_p$ and $_v$ of the state variables denote the position and the velocity of each mode, respectively.

Under these definitions, the discrete-time state-space representation of P_{mech} is given as

$$P_{mech}[z]: \left\{ \begin{array}{rcl} x_d[k+1] & = & A_d x_d[k] + B_d u_c[k] \\ y[k] & = & C_d x_d[k] \end{array} \right. , \tag{2.82}$$

where

$$A_d = \left[\begin{array}{ccc} A_n & 0 & 0 \\ 0 & A_1 & 0 \\ 0 & 0 & A_2 \end{array} \right], \quad B_d = \left[\begin{array}{c} B_n \\ B_1 \\ B_2 \end{array} \right], \quad C_d = \left[\begin{array}{ccc} C_n & C_1 & C_2 \end{array} \right],$$

$$x_d[k] = \left[\begin{array}{c} x_n[k] \\ x_1[k] \\ x_2[k] \end{array} \right].$$

To design the FSC input, the augmented system of Figure 2.24 is considered which corresponds to the augmented system of Figure 2.11. The state vector of the augmented system is defined as

$$x[k] = \left[\begin{array}{c} x_d[k] \\ u_c[k] \end{array} \right],$$

and the initial and the final states are given as

$$x[0] = \left[\begin{array}{c} x_d[0] \\ u_c[0] \end{array} \right] = \left[\begin{array}{c} x_n[0] \\ x_1[0] \\ x_2[0] \\ \hdashline u_c[0] \end{array} \right] = \left[\begin{array}{c} \mathbf{0} \\ \mathbf{0} \\ \mathbf{0} \\ \hdashline 0 \end{array} \right],$$

$$x[N] = \left[\begin{array}{c} x_d[N] \\ u_c[N] \end{array} \right] = \left[\begin{array}{c} x_n[N] \\ x_1[N] \\ x_2[N] \\ \hdashline u_c[N] \end{array} \right] = \left[\begin{array}{c} \left[\begin{array}{c} r \\ 0 \end{array} \right] \\ \mathbf{0} \\ \mathbf{0} \\ \hdashline 0 \end{array} \right],$$

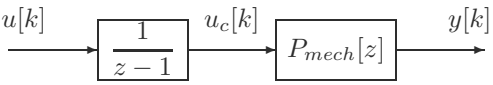

FIGURE 2.24
Augmented system to design the FSC and FFSC inputs for the galvano scanner.

where r is the target position. The step number N is determined as $N = 79$ so that the feedforward input does not saturate. The obtained FSC input and its spectrum are shown in Figure 2.25 and Figure 2.26 by the dashed line, respectively. In Figure 2.25, the unit [s/unit] of the horizontal axis is a normalized time so that the final time is one second and the unit [A/unit] is a unit when the target position is normalized to $r = 1$. In Figure 2.26, the vertical dashed line of the left-hand side represents the primary resonant frequency, and that of the right-hand side represents the secondary resonant frequency. From Figure 2.26, it is confirmed that the spectra at the resonant frequency are well reduced, and the width of the notch of each frequency is very narrow.

Next, the FFSC input was obtained by reducing the spectra around the primary and the secondary resonant modes. The parameter ω_i in the cost function (2.44) is selected to cover the resonant frequency variation of $\pm 6\%$ of the primary and secondary vibration modes as

$$\omega_i = \begin{cases} 0.94\omega_{n1} + \dfrac{1.06\omega_{n1} - 0.94\omega_{n1}}{50} \times (i-1), & (i = 1, \ldots, 50) \\ 0.94\omega_{n2} + \dfrac{1.06\omega_{n2} - 0.94\omega_{n2}}{50} \times (i-51), & (i = 51, \ldots, 100) \end{cases}$$

where ω_{n1} and ω_{n2} are the resonant frequencies of the primary and secondary vibration modes, respectively. The weighing parameter q_i is selected to be

$$q_i = \begin{cases} 1 \times 10^9, & (i = 1, \ldots, 50) \\ 5 \times 10^7, & (i = 51, \ldots, 100) \end{cases}.$$

The weight q_i for the primary vibration mode is selected to be larger than that of the secondary vibration mode because the frequency change of the primary vibration mode easily increases the residual vibrations as compared to that of the secondary vibration mode in this system.

The obtained FFSC input and its spectrum are shown in Figure 2.25 and Figure 2.26 by the solid line, respectively. From Figure 2.26, it is confirmed that the spectrum of the input is well reduced not only at the resonant frequencies but also over the frequency interval where the frequency varies. As such, the robustness to the frequency changes of the resonant modes is expected to increase.

Note that the maximum absolute value of the FFSC input is larger than that of the FSC input. The design parameters must be selected so as not to exceed the maximum value of the control input.

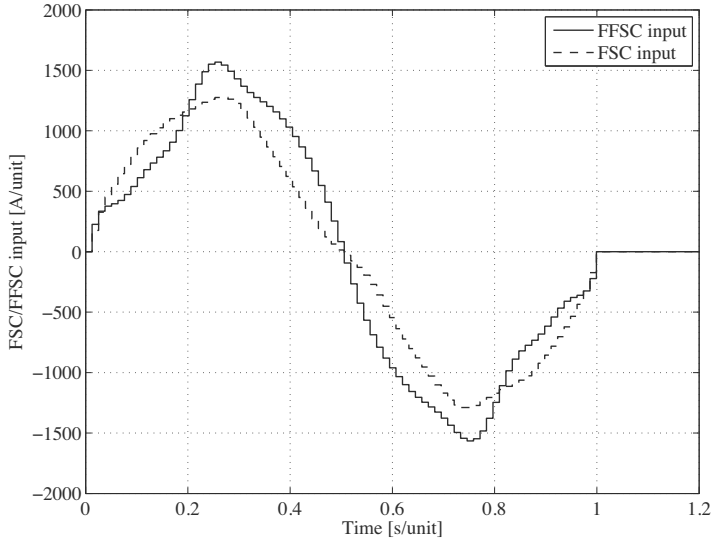

FIGURE 2.25
Time responses of FSC and FFSC inputs.

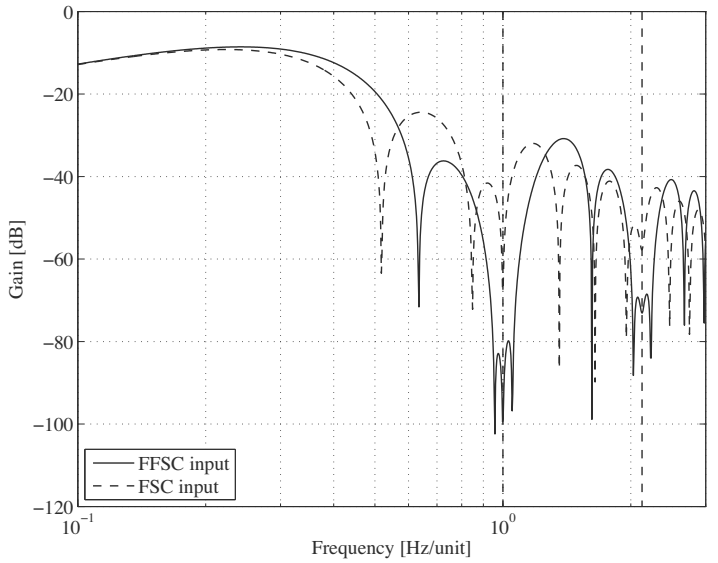

FIGURE 2.26
Spectra of FFSC and FSC inputs.

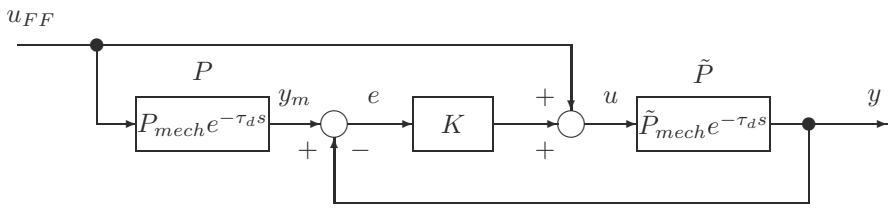

FIGURE 2.27
MMTDOF control system for galvano scanner control system.

2.5.3 Simulation Results

The robustness to the resonant frequency variation is evaluated by simulations. Since the plant has an input delay $e^{-\tau_d s}$, the MMTDOF control system taking into account the input delay as explained in Section 2.1.3 was used. The block diagram of the MMTDOF control system is shown in Figure 2.27, and the feedback controller in commercial products was used.

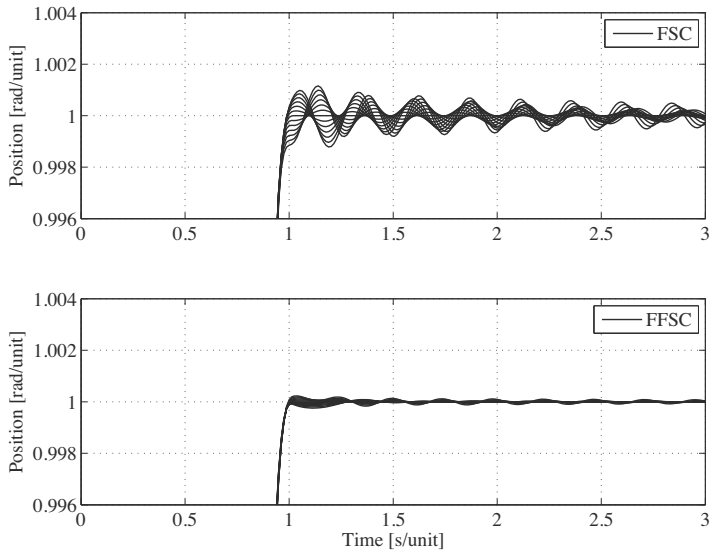

FIGURE 2.28
Simulated time responses of output when the frequency of the primary vibration mode is changed from −6% to +6%.

The upper figure in Figure 2.28 shows the output response y of the FSC input at the target position when the primary resonant mode of the plant was changed from −6% to +6% at 1% intervals. Note that [rad/unit] is the normalized unit so that the target position is equal to unity.

The bottom figure of Figure 2.28 shows the output response of the FFSC input under the same condition to the FSC input simulation. By comparing the results of the FSC and FFSC inputs, the FFSC input achieves smaller residual vibrations. The effectiveness of the frequency shaping using the FFSC method has been confirmed.

2.5.4 Experimental Results

Experiments were conducted by using the same TDOF control structure as the simulations. The output response of the FSC input is shown in Figure 2.30 by the dashed line. The output converged to the target position with an overshoot. Since the allowable positioning error of this galvano scanner is ±0.08% of the target position, the positioning time is approximately 1.33 s/unit. Note that the 1 rad/unit corresponds to several hundreds μrad, and the tolerable positioning error is the nano-scale.

The output response of the FFSC input is shown by the solid line. The overshoot and undershoot are larger than the results of the FSC input. The positioning time is 1.39 s/unit, which is also slower than the FSC input. The residual vibrations of both methods are almost the same. As such, the FSC input achieves good nominal performance than the FFSC input.

Next, the robustness to the frequency variations of the resonant modes is evaluated. However, it is difficult to change the resonant frequency of the actual system arbitrarily. The resonant frequency of the plant model to design the FSC and FFSC inputs was changed instead. The FSC and FFSC inputs were designed by changing the primary resonant frequency to +6% of the nominal frequency. The spectra of the obtained FSC and FFSC inputs are shown in Figure 2.29. From Figure 2.29, it can be observed that the frequency where the magnitude of the spectrum is reduced around the primary vibration mode is shifted to the higher frequencies.

The output responses obtained by experiments are shown in Figure 2.31. In Figure 2.31, a large residual vibration is observed in the output response of the FSC input and the performance degradation is significant. The positioning time is also extended from 1.33 s/unit to 1.94 s/unit. The FSC input has poor robustness to the frequency changes of the vibration modes.

On the other hand, the output of the FFSC input maintains lower residual vibrations as shown in Figure 2.31 by the solid line. The positioning time is extended from 1.39 s/unit to 1.44 s/unit, but the extension is quite small compared with that obtained by the FSC input. These results are supported by the spectrum of the FFSC input as shown in Figure 2.29 by the solid line. The spectrum around the primary resonant mode is still reduced even if the design frequency of the primary resonant mode is shifted to +6% of the nominal frequency. As such, the FFSC input has good robustness to the frequency change of the resonance modes.

Finally, in order to evaluate the residual vibrations quantitatively, the spectrum of the residual vibration was calculated as shown in Figure 2.32.

Figure 2.32 shows that the peak of the spectrum obtained by the FSC input around 1 Hz/unit is drastically reduced by the FFSC input.

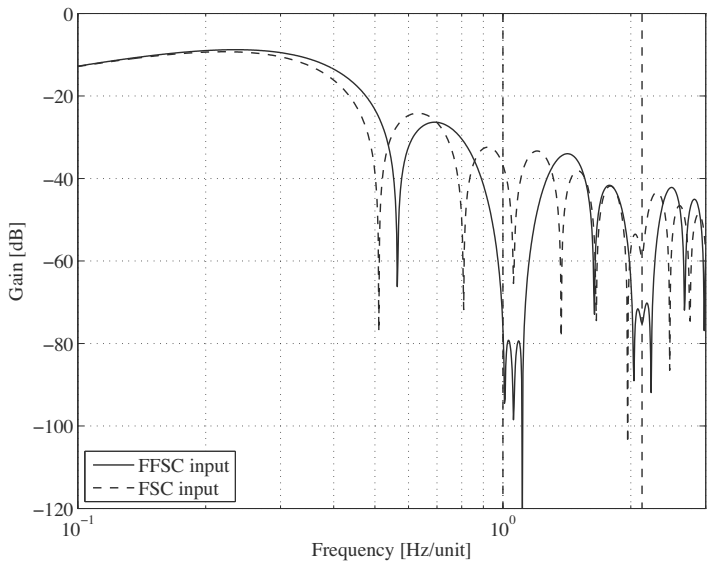

FIGURE 2.29
Spectra of FSC and FFSC inputs when nominal frequency of primary vibration mode is perturbed to +6% of the nominal frequency in both FSC and FFSC designs.

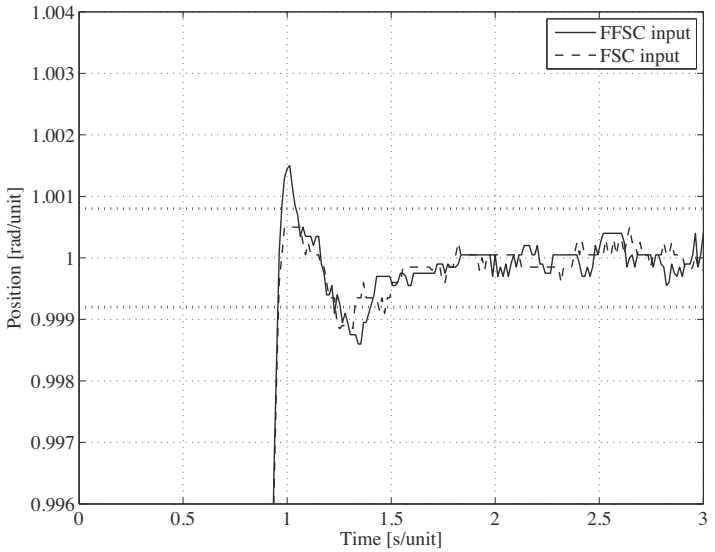

FIGURE 2.30
Experimental time responses of outputs.

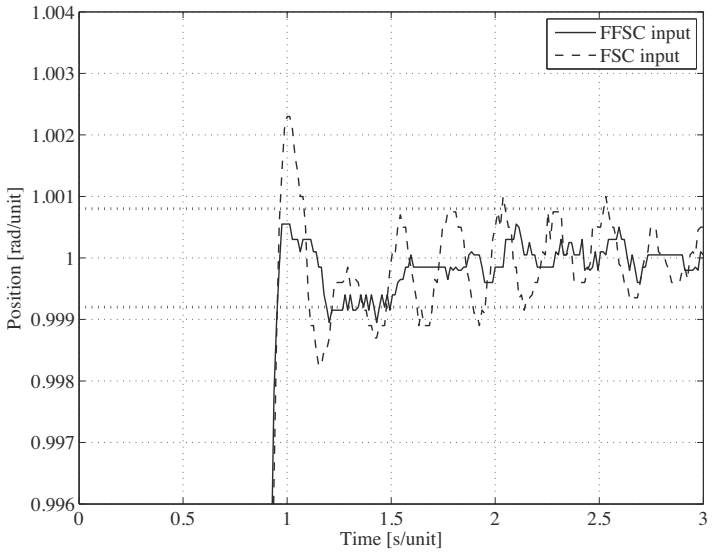

FIGURE 2.31
Experimental time responses of outputs when nominal frequency of primary vibration mode is perturbed to +6% of the nominal frequency in both FSC and FFSC designs.

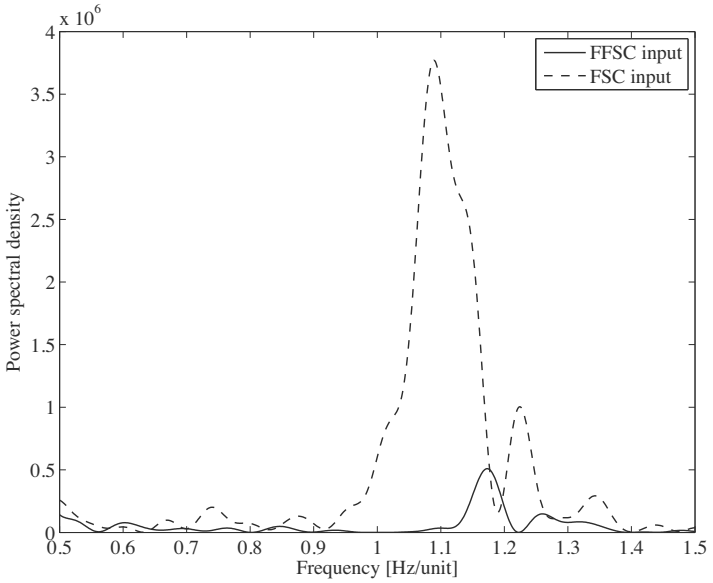

FIGURE 2.32
Spectra of residual vibrations when nominal frequency of primary vibration mode is perturbed to +6% of the nominal frequency.

2.6 Industrial Application: Galvano Scanner II

In order to control the galvano mirror as quickly and precisely as possible, the bandwidth of the current amplifier must be increased. To respond to these requirements, the maximum voltage of the current amplifier is also increased. However, further increase of the voltage may be difficult to achieve as the heat generated at the current amplifier will be unacceptable. Although a Pulse Width Modulation (PWM) amplifier may resolve the heat problem, it is difficult to achieve the required control accuracy. As such, linear amplifiers are still used for galvano scanners in order to achieve high-speed and high-precision positioning.

In recent years, several studies have examined trajectory design methods that constrain control input and/or some state variables [11, 12, 13]. However, few studies have considered the voltage constraint of the current amplifier. An anti-windup method can be applied when the voltage is saturated, although performance degradation is inevitable. The feedforward input should be designed so as not to saturate in advance.

In this section, a FFSC design method that can take into account the voltage constraint of the current amplifier is introduced [6]. By constraining the applied voltage to the motor, the power supply voltages of the current amplifier is lowered. The energy consumption and heat generated by the current amplifier can also be reduced.

2.6.1 Voltage Saturation in Current Amplifier

In order to explain the FFSC methods considering the voltage constraint of the current amplifier, the control system of Figure 2.33, where a rigid-body system (with no friction) driven by an ideal electromagnetic actuator is considered. As shown in Figure 2.33, current feedback is realized by analog circuit to achieve a higher bandwidth in most cases. In Figure 2.33, $P_c(s)$ is the rigid-body system, K_t is the torque constant, J is the moment of inertia, $x_p(t)$ is the position, $x_v(t)$ is the velocity, R is the armature resistance, L is the armature inductance, K_e is the back electromotive force coefficient, and $K(s)$ is the current feedback controller. It is assumed that the current feedback controller $K(s)$ is designed so that the actual current $i(t)$ follows the reference current $i_{ref}(t)$ over wide frequency range. The applied voltage $V_M(t)$ to the armature is limited by the power supply voltage V_p. Voltage saturation occurs when the output of $K(s)$ exceeds V_p.

If the controller $K(s)$ of the current amplifier is known, the applied voltage $V_M(t)$ can be represented by the state variables of the closed-loop system. The voltage constraint problem can then treated by the FSC or FFSC methods with constraints. However, this may be difficult for the following reasons:

1. The parameters of the current feedback controller $K(s)$ are required

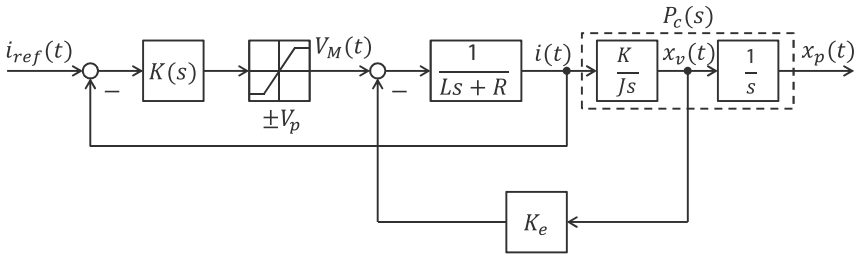

FIGURE 2.33
Control system with current amplifier.

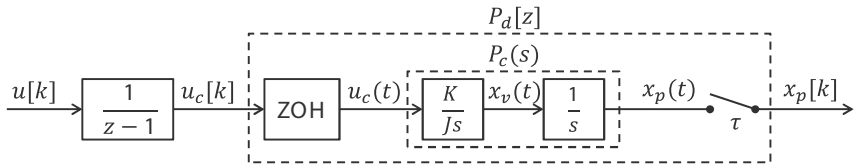

FIGURE 2.34
Augmented system for rigid-body mode model.

in order to design the FSC or FFSC input. As such, the trajectory must be redesigned when the current amplifier is replaced; and

2. Obtaining information about the current feedback controller $K(s)$ is often difficult in the case of commercially available current amplifiers.

A method that does not depend on the current feedback controller $K(s)$ is required.

2.6.2 FSC Design Considering Voltage Saturation in Current Amplifier

Generally, the reference input $i_{ref}(t)$ to the current amplifier is followed by the actual current $i(t)$ with a sufficiently small tracking error because the bandwidth of the current feedback loop is designed to be high. $i(t) = i_{ref}(t)$ almost always holds, and the augmented system of Figure 2.34 can be used for FSC and FFSC input design by ignoring the current amplifier and assuming that the current $i(t)$ is the control input $u_c(t)$. In Section 2.5, it has been shown that the FSC and FFSC inputs designed by using the augmented system of Figure 2.24 achieve good control performances when the input voltage is not saturated. If the FSC and FFSC inputs could be designed based on the augmented system of Figure 2.34 to satisfy the input voltage constraint, the control performances are expected to be satisfactory.

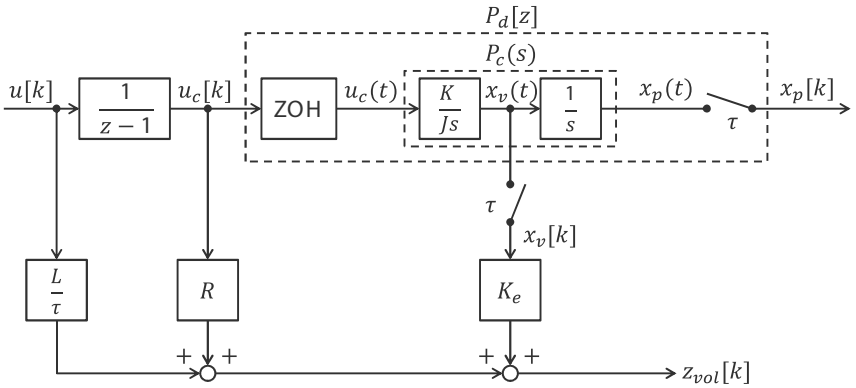

FIGURE 2.35
Augmented system for voltage constraint.

The applied voltage $V_M(t)$ is described as

$$V_M(t) = Ri(t) + L\frac{di(t)}{dt} + K_e x_v(t), \tag{2.83}$$

and a discretized approximation of $V_M(t)$ is

$$z_{vol}[k] = Ru_c[k] + L\frac{u_c[k+1] - u_c[k]}{\tau} + K_e x_v[k], \tag{2.84}$$

where $x_v[k] = x_v(\tau k)$. Note that the input $u[k]$ to the augmented system of Figure 2.34 is the forward difference of $u_c[k]$. As such, we have

$$\begin{aligned} z_{vol}[k] &= Ru_c[k] + \frac{L}{\tau}u[k] + K_e x_v[k] && (2.85)\\ &= C_{vol}x[k] + D_{vol}u[k], && (2.86) \end{aligned}$$

where

$$\begin{aligned} C_{vol} &= [0,\ K_e,\ R], \quad D_{vol} = L/\tau,\\ x[k] &= [x_p[k],\ x_v[k],\ u_c[k]]^T. \end{aligned}$$

The augmented system with $z_{vol}[k]$ is shown in Figure 2.35. This method is very simple because the constraint of (2.86) is only added to the conventional augmented system in Figure 2.34. It should be noted that $z_{vol}[k]$ is the approximation of $V_M(t)$, and the effectiveness of this approximation must be verified experimentally.

In addition to the voltage constraint, the current and the velocity constraints can also be introduced as

$$\begin{aligned} z_{cur}[k] &= C_{cur}x[k] + D_{cur}u[k], && (2.87)\\ z_{vel}[k] &= C_{vel}x[k] + D_{vel}u[k], && (2.88) \end{aligned}$$

where

$$\begin{aligned} C_{cur} &= [0,0,1], \quad D_{cur} = 0, \\ C_{vel} &= [0,1,0], \quad D_{vel} = 0. \end{aligned}$$

When $z_{vol}[k]$, $z_{cur}[k]$, and $z_{vel}[k]$ are constrained simultaneously, $z[k]$ in (2.62) and z_{max} in (2.63) are selected to be

$$\begin{aligned} z[k] &= [z_{vol}[k],\ z_{cur}[k],\ z_{vel}[k]]^T \\ z_{max} &= [z_{vol}^{max},\ z_{cur}^{max},\ z_{vel}^{max}]^T, \end{aligned}$$

where the superscript ^{max} denotes the maximum value of each constraint state variable.

2.6.3 Application to Galvano Scanner Control Problem

The FFSC input is designed for the model P_{mech} of (2.76). As P_{mech} consists of the rigid-body mode and two vibration modes, the constraint variables of voltage, current, and velocity are redefined as z_{vol}, z_{cur}, and z_{vel}, respectively, by using the state variables of P_{mech} and transformation T as

$$\begin{aligned} z_{vol}[k] &= C_{vol}Tx[k] + D_{vol}u[k], \\ z_{cur}[k] &= C_{cur}Tx[k] + D_{cur}u[k], \\ z_{vel}[k] &= C_{vel}Tx[k] + D_{vel}u[k], \end{aligned}$$

where

$$T = \left[\begin{array}{cccccc:c} 1 & 0 & 1 & 0 & 1 & 0 & 0 \\ 0 & 1 & 0 & 1 & 0 & 1 & 0 \\ 0 & 0 & 0 & 0 & 0 & 0 & 1 \end{array}\right], \quad x[k] = \left[\begin{array}{c} x_d[k] \\ u_c[k] \end{array}\right],$$

and $x_d[k]$ is the state vector of $P_{mech}[z]$ defined in (2.82).

In the control system of the galvano scanner, the current is limited to less than 12 A due to the limitation of the current amplifier. The velocity is limited to less than 5 m/s due to the limitation of the bandwidth of the encoder. As for the limitation of the applied voltage to the motor, three types of conditions are provided, i.e., no constraint, less than 72 V, and less than 36 V.

The trajectory of a 1 mm step control was designed under these constraints. The 1 mm step is commonly used to evaluate the control performance of the galvano scanner. The step number $N = 73$ is selected such that the residual vibrations are sufficiently small when the voltage is not saturated.

To design the FFSC input, ω_i and q_i in (2.44) were set to the same values as used in Section 2.5, where the voltage constraint was not considered. The time responses of the voltage, current, and velocity of the obtained trajectories are shown in Figure 2.36. Figure 2.36 shows that the trajectories satisfy the constraints.

In the experiments, the obtained FFSC inputs were applied to the galvano

scanner by using the MMTDOF control system as shown in Figure 2.27 taking into account the input delay. First, the control performance of the FFSC input which does not introduce the voltage constraint is evaluated. Figure 2.37 shows the position responses for three different power supply voltages of $V_p = 162$ V, 76 V, and 72 V. Since the maximum value of V_M was 146 V and the voltage drop of the current amplifier was 16 V, the voltage of the current amplifier must have been saturated, except for the case in which $V_p = 162$ V. From Figure 2.37, there is no difference between the position responses of $V_p = 162$ V and 76 V. However, the settling performance of the result of $V_p = 72$ V is degraded. Since the required positioning accuracy of the galvano scanner is $\pm 3\mu m$ in this case, the positioning time of $V_p = 72$ V is extended.

Next, two different FFSC inputs were designed with the constraints of $z_{vol}^{max} = 72$ V and 36 V. Since there is a voltage drop of 16 V in the current amplifier, the power supply voltage can be reduced to $V_p = 88$ V and 52 V for the FFSC inputs designed under the constraints of $z_{vol}^{max} = 72$ V and 36 V, respectively. Figure 2.38 shows the experimental results for the case in which the solid, dashed, and dotted lines show the results without the voltage constraint ($V_p = 162$ V), with the voltage constraint of $V_p = 88$ V ($z_{vol}^{max} = 72$ V), and that of $V_p = 52$ V ($z_{vol}^{max} = 36$ V), respectively. Figure 2.38 shows that a significant performance degradation cannot be seen even for the result for the case where $V_p = 52$ V. As such, the FFSC input design with the voltage constraint is very effective in reducing the power supply voltage without performance degradation.

Since all the energy consumption in the current amplifier is transferred into heat losses, the heat is evaluated by the amount of energy consumption. The energy consumption in the current amplifier in the ideal condition can be calculated by

$$P_{amp} = \frac{1}{N\tau} \int_0^{N\tau} |i(t)|(V_p - |V_M(t)|)dt, \tag{2.89}$$

where $V_M(t)$ is the voltage of the motor, and V_p is the supply voltage.

In order to compare the energy consumption, the FFSC inputs of the 0.1 mm step and 10 mm step were also obtained. The step numbers N for 0.1 mm and 10 mm step controls were selected to be 37 and 351, respectively. The other parameters were selected to be the same as that of 1 mm step control.

The results are shown in Figure 2.39. Note that the result without input constraint is indicated as the constraint voltage of 146 V because the maximum voltage was 146 V. When (2.89) was calculated, the voltage V_p was selected to be 52 V, 88 V, and 162 V corresponding to the voltage constraint of 36 V, 72 V, and no constraint, respectively, as the current amplifier has an internal voltage drop of 16 V. As shown in Figure 2.39, the energy consumption is drastically reduced by lowering the constraint voltage.

It should be noted that the energy consumption for a 10 mm step is lower than that for 0.1 mm and 1 mm steps. As P_{amp} in (2.89) is the average power consumption per unit of time and the reference trajectory of 10 mm step has

a constant velocity interval where the current is zero, P_{amp} for the 10 mm is reduced.

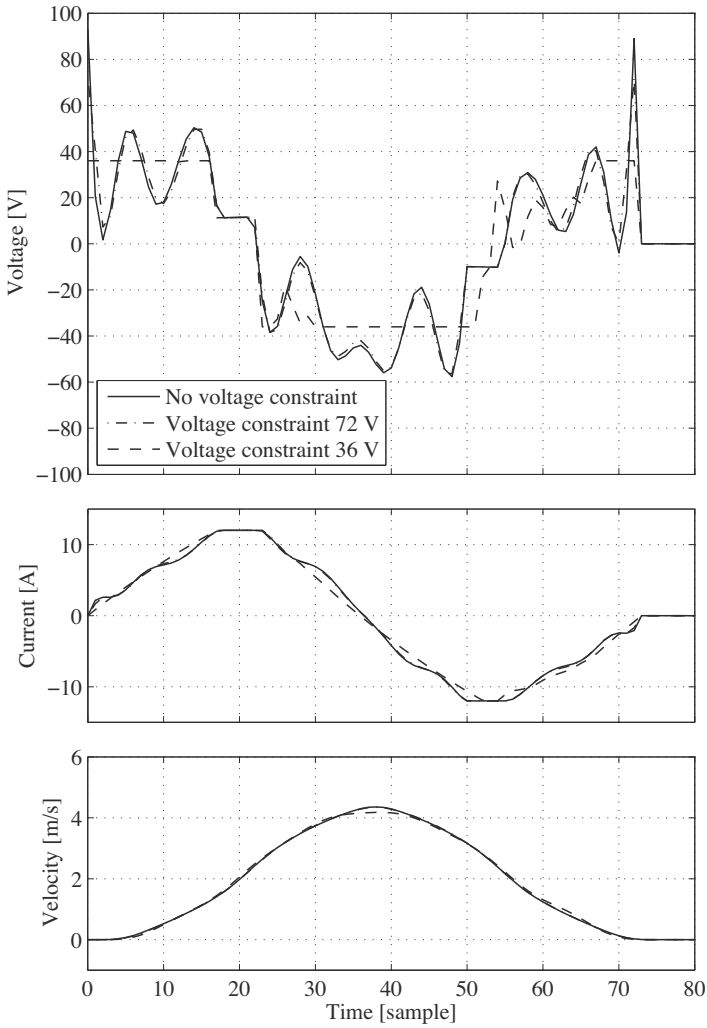

FIGURE 2.36
Trajectory waveforms of 1 mm step.

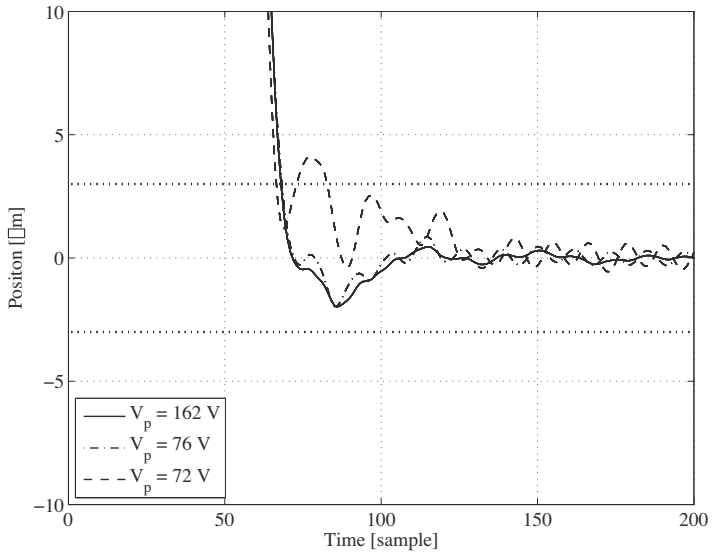

FIGURE 2.37
Position responses of 1 mm step when the FFSC inputs were designed without input voltage constraint.

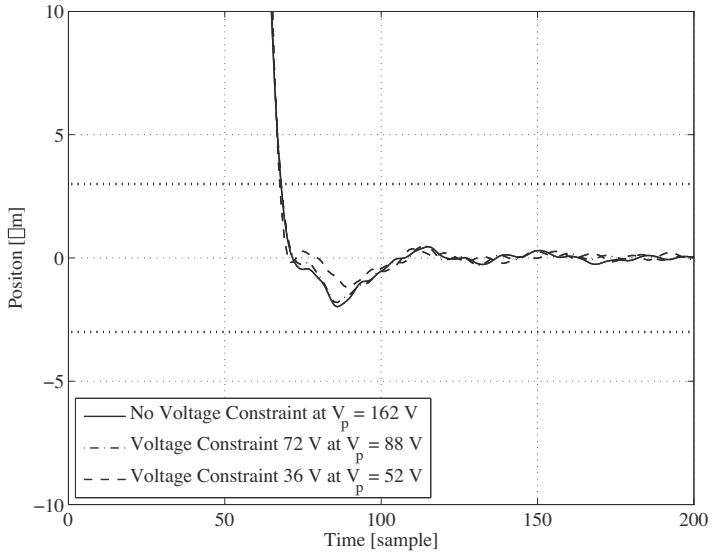

FIGURE 2.38
Position responses of 1 mm step when the FFSC inputs were designed with input voltage constraint.

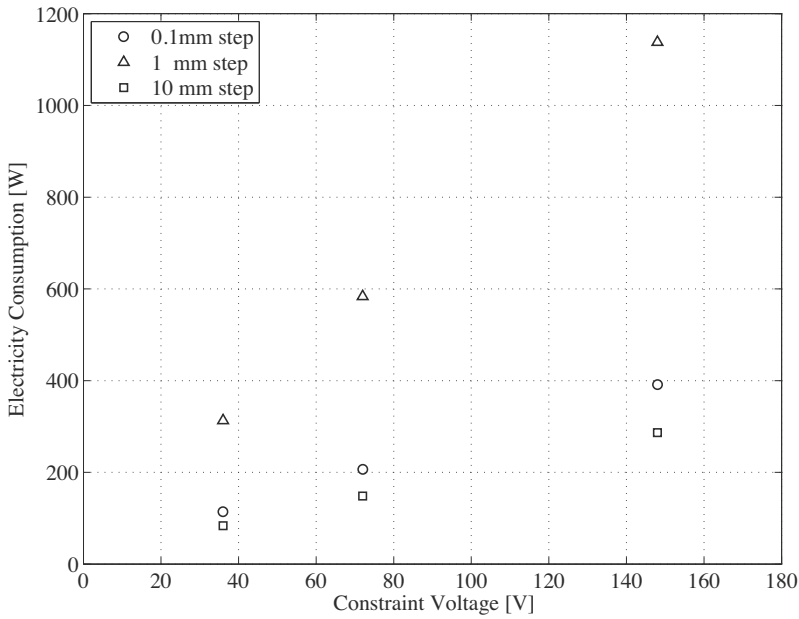

FIGURE 2.39
Energy consumption in the current amplifier.

Bibliography

[1] F. L. Lewis and V. L. Syrmos, *Optimal Control*, John Wiley & Sons, New York, NY, USA, 1995.

[2] Y. Mizoshita and S. Hasegawa, "Vibration Minimized Access Control for Disk Drives," *IEEE Transactions on Magnetics*, Vol. 32, No. 3, pp. 1793–1798, May 1996.

[3] T. Atsumi, "Feedforward Control Using Sampled-Data Polynomial for Track Seeking in Hard Disk Drives," *IEEE Transactions on Industrial Electronics*, Vol. 56, No. 5, pp. 1338–1346, May 2009.

[4] T. Totani and H. Nishimura, "Final-State Control Using Compensation Input," *Transactions of SICE*, Vol. 30, No. 3, pp. 253–260, 1994.

[5] M. Hirata, T. Hasegawa, and K. Nonami, "Short Track-Seeking Control of Hard Disk Drives by Using Final-State Control," *IEEJ Transactions on Industry Applications*, Vol. 125-D, No. 5, pp. 524–529, 2005 (in Japanese).

[6] S. Ueda and M. Hirata, "Trajectory Design Method for Voltage Saturation of a Current Amplifier," in *Proceedings of ASME* 5^{th} *Annual Dynamics Systems and Control Conference joint with the JSME* 11^{th} *Motion and Vibration Control Conference*, 2012.

[7] M. Hirata and Y. Hasegawa, "Vibration Minimized Trajectory Design For Information Devices," in *Proceedings of SICE-ICCAS International Joint Conference 2006*, pp. 2777–2780, 2006.

[8] Hard Disk Drive Benchmark Problem Version 3, Investigation R&D Committee for Next Generation Servo Control Technology for Mass-Storage System, Institute of Electrical Engineers of Japan (IEEJ), http://mizugaki.iis.u-tokyo.ac.jp/mss/benchmark.html.

[9] T. Yamaguchi, M. Hirata, and C. K. Pang (eds.), *High-Speed Precision Motion Control*, CRC Press, Boca Raton, FL, USA, 2011.

[10] M. Hirata, T. Kidokoro, and S. Ueda, "Nanoscale Servo Control for Galvano Scanner Using Final-State Control," *IEEJ Transactions on Industry Applications*, Vol. 129-D, No. 9, pp. 43–48, 2009 (in Japanese).

[11] M. Hirata, T. Hasegawa, and K. Nonami, "Seek Control of Hard Disk Drives Based on Final-State Control Taking Account of the Frequency Components and the Magnitude of Control Input," in *Proceedings of IEEE International Workshop on Advanced Motion Control 2002*, pp. 40–45, 2002.

[12] T. Sugie and H. Yamamoto, "Reference Management for Closed Loop Systems with State and Control Constraints," *Transactions of SICE*, Vol. 37, No. 9, pp. 849–855, 2001 (in Japanese).

[13] N. Hirose, M. Iwasaki, and H. Hirai, "Feedforward Compensation by Specified Step Settling Considering Constraint on Control Input," *IEEJ Transactions on Industry Applications*, Vol. 130-D, No. 6, pp. 785–792, 2010 (in Japanese).

3

Transient Control Using Initial Value Compensation

A. Okuyama

Tokai University

N. Hirose

Toyota Central R&D Labs., Inc.

T. Yamaguchi

Ricoh Company Ltd.

M. Iwasaki

Nagoya Institute of Technology

CONTENTS

3.1 Introduction

3.1.1 Background

In motion control of many mechatronic products, e.g., motion control of robot arms, magnetic head-positioning control in Hard Disk Drives (HDDs), lens focus control in optical disk drives, galvano scanner control in laser drilling equipment, and XY-stage control in semiconductor or LCD manufacturing equipment, their motion from a steady state to the next steady state can be divided into two modes. The movement from the current position to a target position is one mode, and keeping its position or trajectory in order to begin the tasks is another mode. In the case of robot arm control, its motion control is to move the arm from the current position to a target position, after which an end effector attached to the arm does some tasks such as assembling or welding while the controller keeps the end effector on the right position or trajectory. In HDDs, a magnetic head is moved from the current track to a target data track, and the head reads or writes data to the target track while the position of the head is kept on the track precisely. Although these two modes are acted continuously, the first mode is required for very fast or minimum time movement to a target position, and the second mode is required to keep the end effector on a target position or trajectory very precisely. Thus, during one servo action from a steady state to the next steady state, the purpose of these two modes is different from each other in terms of their motion control design. In this book, a servo control design that is applied to the above-mentioned motion control that has multiple control purposes is proposed.

This motion control might certainly be a general servo control. However, the controller of the first mode may be designed utilizing the saturation of the power amplifier so that maximum power can be applied to realize a fast movement which is the control purpose of the first mode. On the other hand, it may be desired that linear robust control theory is applied to the designing of the controller of the second mode so that it is capable of precise positioning. In other words, disturbance suppression capability can be designed quantitatively while maintaining robust stability. It is quite a natural idea to design different types of controllers to meet the control purpose for each mode optimally. One way to implement this idea is that the structure of the motion control system has multiple controllers and a switching function which ensures that each controller hands over to another controller smoothly. In fact, engineers in various industries have already designed multiple controllers independently.

However, these controllers tend to be switched from one to another after reaching a steady state, which may result in longer time.

Consequently, a feature of the servo control system picked up in this chapter is that there are multiple controllers and switching functions so that the whole servo control system can meet multiple control purposes, and each controller can be designed specifically to meet a control purpose. During one servo control action, which means the movement from a steady state to the next steady state, the control purpose is changed from fast movement to precise positioning or stopping. Hence, the controller should also be switched from a controller optimally designed for fast movement to another controller optimally designed for precise positioning or stopping, while the servo system is in unsteady state. This servo control system is called Mode Switching Control (MSC). The design issue of MSC is regarding how well a controller can be handed over to the next controller. In other words, controllers can be switched from one to another.

One of the most important constraints for designing MSC is that this switching does not influence the design of each controller. It would be meaningless if the design of mode switching interfered with each controller design, since one of the biggest benefits of MSC is to allow each controller to be designed optimally. The second issue is that the transient response caused by mode switching should be minimal. In most mechatronic systems, response time is key. Hence, a very smooth transient from the first mode to the second mode is strongly required.

It is necessary to find out new free parameters for designing the mode switching so that the design is independent from other controller designs. While the state variables of the plant should be continuous at mode switching since they are governed by physical laws, it is possible to hand over controllers with discontinuous state variables since MSC includes a discrete event which is the mode switching. This means that the initial values of the controller state variables just after mode switching can be independently set. Thus, the initial values are new free design parameters when using MSC.

Even though MSC is a nonlinear control because of its switching functions, control design after mode switching is just linear control design with non-zero initial values, since the mode is switched during unsteady-state conditions. It is well-known that non-zero initial state variables strongly affect the transient responses. As such, the initial values of the controller state variables at mode switching are quite effective design parameters for controlling the transient responses after mode switching. Besides, the initial values are design parameters which are completely independent from fundamental control characteristics such as robust stability, sensitivity, and disturbance suppression capability. In this chapter, several methods for designing the initial values are described in detail.

Another important aspect of MSC is that the same situation may occur when the reference target is changed before the states of the former transient response are settled. This situation should also be treated as servo design

with non-zero initial values. In general, in cases where discrete events such as controller mode switching or reference target changing occur under unsteady-state conditions, undesired transient responses may occur after the events. Thus, one of the methods for improving the transient responses after such discrete events is to manipulate the initial values of the controllers, and its design is proposed here as the Initial Value Compensation (IVC).

In summary:

1. Many servo control systems in mechatronic industries accomplish multiple control purposes such as fast movement and precise positioning during one servo action from a steady state to the next steady state. MSC has been widely applied to meet these purposes, where multiple controllers are designed to meet each control purpose optimally, and the controllers are handed over from one to another. While switching control is generally more broadly defined, the meaning of MSC is limited to the above-mentioned usage in this book.

2. One of the issues of MSC is the transient response after mode switching. Mode switching occurs during unsteady state. For example, as the magnetic head is approaching a target track with some amount of displacement, velocity, and acceleration, its controller is switched from the fast movement servo controller for seek mode to the precise positioning controller for track-following mode. Since this mode switching has to be done with non-zero initial states, undesired transient responses may occur. Thus, the design issue of MSC is to improve the transient responses after mode switching. This kind of undesired transient response may also occur when a reference target is changed during the unsteady state of the control system. As such, it is necessary to take into account the improvement of the transient response for any discrete events that occur during the unsteady state.

3. MSC is the design of switching functions, but the characteristics of the servo control system such as robust stability and sensitivity are not affected. This means that it is necessary to find out new design parameters which are independent from the control structure. In MSC, initial values of the controller state variables are used as new design parameters.

4. Since it is well known that the initial values of the control system state variables strongly affect the transient response, the above-mentioned free design parameters may be good design parameters for handling the above-mentioned issue of MSC. This design approach is called IVC and its design algorithm will be described in detail.

3.1.2 Initial Value Compensation (IVC)

In this section, the basic idea of IVC is described. In IVC, the initial values of the controller state variables after mode switching are design parameters. Using the initial state of the plant, the initial state of the controller can be calculated as

$$x_c[0] = Kx_p[0], \tag{3.1}$$

where $x_c[0]$ is the initial state of the controller after mode switching, $x_p[0]$ is the initial state of the plant after mode switching, and K is a coefficient matrix.

Assume that the relation between the control variable $y[z]$, such as the head position, and the initial variables of the control system $[x_p[0], x_c[0]]$ is written as

$$y[z] = \frac{N_r[z]}{D[z]}r[z] + \frac{N_p[z]}{D[z]}x_p[0] + \frac{N_c[z]}{D[z]}x_c[0], \tag{3.2}$$

where $D[z]$ and $N_r[z]$ are scalar polynomials, and $N_p[z]$ and $N_c[z]$ are $1 \times n$ and $1 \times m$ polynomials, respectively. Substituting (3.1) into (3.2), (3.2) can be transformed as

$$y[z] = \frac{N_r[z]}{D[z]}r[z] + \frac{N_p[z] + N_c[z]K}{D[z]}x_p[0]. \tag{3.3}$$

It is shown by (3.3) that the zeros of the transfer function from $x_p[0]$ to $y[z]$ can be shifted to the desired values by selecting appropriate values of K so that the transient response can be improved. There have been several known design methods for calculating K. As this method is easy to implement in an actual controller, this idea has been widely applied to actual products such as HDD head-positioning servo control [1]–[4].

An extended idea of (3.1) is that K is not just a coefficient matrix, but a transfer function matrix given as

$$r'[k] = \frac{n[z]}{d[z]}x_p[0], \quad x_c[0] = 0, \tag{3.4}$$

where $r'[z]$ is a time sequential data superimposed on the output of the controller. This idea provides a much wider design flexibility to shape the transient response [5],[7]–[12].

It is shown by (3.3) that IVC is a method of shifting the zeros of the transfer function from $x_p[0]$ to $y[z]$ to appropriate values. Although the poles of the transfer functions of a servo system are designed based on various kinds of linear control theory to achieve appropriate closed-loop characteristics, these poles are not always appropriate for transient responses.

The Two-Degrees-of-Freedom (TDOF) controller is a quite well-known structure for servo control systems, where a feedforward controller $F[z]$ can be designed independently from the closed-loop characteristics. The transfer

function from reference $r[z]$ to control variable $y[z]$ is given as

$$y[z] = \frac{PF + PC}{1 + PC} r[z], \tag{3.5}$$

where P is the plant model, C is a feedback controller, and F is a feedforward controller. If F can be realized as an approximate P^{-1}, all the zeros will approach the poles.

Both TDOF and IVC move the zeros of the transfer function to appropriate values so that the transient response can be improved. For example, zeros are assigned to cancel the undesirable poles in terms of transient response. This can be realized by adding a feedforward path in the case of TDOF, and by adding initial values in the case of IVC under the structure of MSC. When designing a servo control system, it will be interesting to look for different structures for moving its zeros.

In terms of IVC applications to industries, there are many proposals and reports for HDD applications [1]–[5][7, 8][13]–[17][21, 22][24]–[26][28, 29]. Most of the referred papers show the application of IVC to the settling mode of head-positioning servo control, and some of them show the application of IVC to the design of the short track seek mode which is a step response from steady state within saturation limits [24-26]. Other applications of IVC include optical lens focus servo control in an optical disk drive application [30]–[32] and galvano scanner control for laser drilling equipment [9, 10][34]–[37]. Recently, an application to a personal mobility robot was proposed [33], and there seem to be many other potential applications of IVC in mechatronic systems. In this chapter, the methods for designing IVC are described in detail in Section 3.3. This is followed by the description of two kinds of IVC applications to industries in Section 3.4 and Section 3.5. The application of IVC to mode switching in HDDs, an optical disk drive, and a personal mobility robot is described in Section 3.4, and the application of IVC to reference switching for a laser drilling machine is described in Section 3.5. The application to short track seek control in HDDs may be another application of the latter case, although IVC is applied at steady state. A concise description of this design is shown in [38].

3.2 Overview of Switching Control

This section gives an outline of switching control which is equivalent to the generalization of MSC.

There have been increasing research interests in the study of hybrid systems. A hybrid system is a dynamic system that is described using a mixture of continuous/discrete dynamics and logic-based switching. A switching control system is positioned as a special case of a hybrid system and it consists

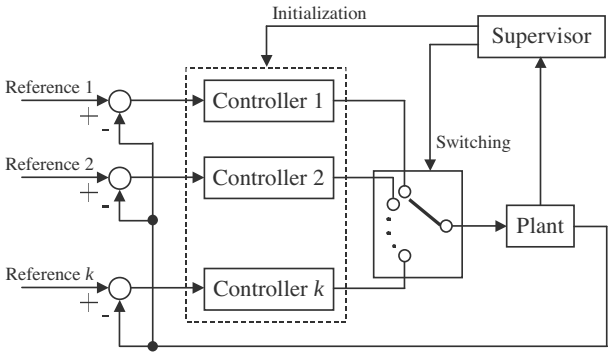

FIGURE 3.1
Block diagram of a switching control system.

of the following subsystems, namely, a plant to be controlled, a family of controllers, and a supervisor. The block diagram of a switching control system is shown in Figure 3.1. Each controller can be designed optimally according to the prior information of the plant. On the other hand, a supervisor can determine a controller according to the subsequent information from the online data during operation. Therefore, switching control is positioned between robust control and adaptive control. Indeed, a switching control scheme provides an effective mechanism when faced with a control system which contains nonlinear elements such as physical constraints, state variable constraints, and saturation limits.

Constraints on the control inputs and the state variables are common in practical control systems. Violations of such constraints drastically degrade system performances and lead to instability in worst-case scenarios. To avoid these reductions in performance, switching control strategies have been proposed. The purpose of a switching control strategy is to meet the performance objectives, such as fast response and good disturbance rejection, while satisfying the specified state and control constraints.

In synthesizing the switching control strategies, utilizing a maximal output admissible set is important for ensuring the safe operation of the system for the given state and control constraints. The maximal output admissible set is a set of all closed-loop initial states, which is guaranteed to satisfy the given constraints. An example of a constrained system is shown in Figure 3.2. Next, the maximal output admissible set O_∞ as shown in Figure 3.3 is obtained, where x_a and x_b are the states of the closed-loop system, and it is assumed that O_∞ includes the origin. When x_a is included in O_∞, controller C can converge x_a to the origin without violating the specified constraints. On the other hand, when x_b is not included in the maximal output admissible set O_∞, the specified constraints will be violated in the process of using controller C to converge x_b to the origin. The maximal output admissible set O_∞ can be

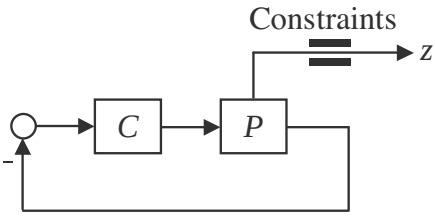

FIGURE 3.2
Constrained control system.

expressed as a convex polyhedron in state space, and it can be obtained by repetition calculation of a limited time.

A controller switching strategy based on the maximal output admissible set is explained. The roles of the supervisor are the selection of the controller, the deciding of the switching condition of the controller, and the initialization of the controller.

First, the selection of the controller as a supervisory role is explained. It is assumed that each controller C_i where $i = 1, 2, \cdots, k$ has already been designed so that control performance improves in ascending order of the index i. The maximal output admissible set corresponding to each controller C_i is set to O_∞^i where $i = 1, 2, \cdots, k$, and it is assumed that the inclusive relations given by

$$O_\infty^k \subset \cdots \subset O_\infty^1 \tag{3.6}$$

are fulfilled. As shown in Figure 3.4, this means that O_∞^i becomes small as the index i becomes large. Here, it is considered that the present state $x(t)$ is contained in O_∞^i, but not in O_∞^{i+1}. In this case, the equation given by

$$x(t) \in O_\infty^i \subset O_\infty^{i-1} \subset \cdots \subset O_\infty^1 \tag{3.7}$$

is obtained. This means that the controller C_i corresponding to O_∞^i is the controller with the highest performance in the family of controllers which can converge $x(t)$ to the origin without violating the specified constraints. Therefore, the controller with the highest performance can be determined by choosing the controller C_i which satisfies

$$x(t) \in O_\infty^i \wedge x(t) \notin O_\infty^{i+1} \tag{3.8}$$

for all time without violating the specified constraints.

Second, the deciding of the switching condition as a supervisory role is explained. It is assumed that the controller is switched from C_{i-1} to C_i at $t = 0$. The state $x(t)$ of a closed-loop system consists of the state $x_p(t)$ of the plant and the state $x_{ci}(t)$ of the controller. Therefore, the deciding of the switching condition as a supervisory role means the deciding of $x_p(0)$ and $x_{ci}(0)$. The deciding of $x_p(0)$ is the problem of finding an optimal combination

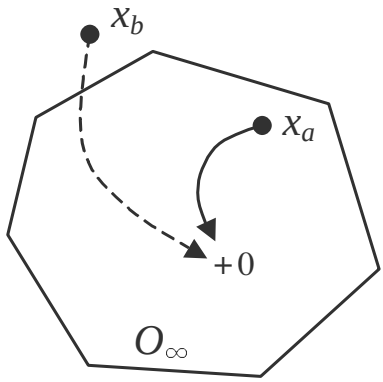

FIGURE 3.3
Maximal output admissible set.

of the state variables of the plant such as position, velocity, acceleration, etc. However, the question of how $x_{ci}(0)$ can be determined remains a problem of the initialization of the controller which will be mentioned below. Since the value of these initial states is related to the transient response after a switching, a suitable design is needed.

Third, the initialization of the controller as a supervisory role is explained. Two methods for calculating $x_{ci}(0)$ have been proposed, namely, the offline calculation method, and the online calculation method based on the detected $x_p(0)$.

For the offline calculation method, the method which minimizes an error system index representing the steady-state of the closed-loop response after switching has been proposed. In addition, the conventional bumpless control is also usually included in the offline calculation method.

For the online calculation method, the IVC method has been proposed to calculate $x_{ci}(0)$ using the product of the detected $x_p(0)$ and a predefined real matrix K, which is given as

$$x_{ci}(0) = Kx_p(0). \tag{3.9}$$

Moreover, in order that the constraints are taken into consideration, the equation given by

$$x(0) = \begin{bmatrix} x_p(0) \\ x_{ci}(0) \end{bmatrix} \in O_\infty^i \tag{3.10}$$

needs to be held so that the control system after a switching satisfies the given constraints. However, $x_{ci}(0)$ which satisfies (3.10) is generally not unique.

It is possible to find $x_{ci}(0)$ that minimizes a square norm of $x(0)$ in the above equation. When the IVC method is applied, the initialization of the controller is not needed as a role of the supervisor. In this case, (3.10) can be

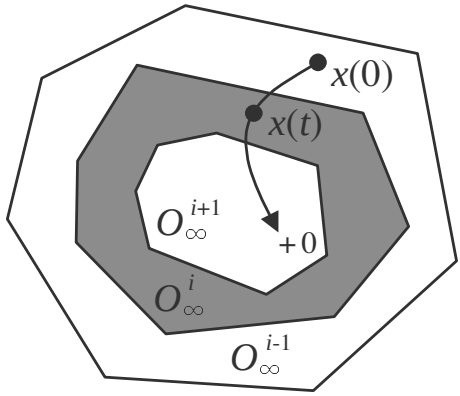

FIGURE 3.4
Inclusive relationship of maximal output admissible sets.

expressed as

$$x(0) = \begin{bmatrix} I \\ K \end{bmatrix} x_p(0) \in O_\infty^i. \tag{3.11}$$

Therefore, the problem of finding the safe switching condition so that the given constraints are fulfilled can result in the problem of finding $x_p(0)$.

Finally, the relation between switching control and MSC is described. In an HDD servo system, MSC has been commonly used. There are two modes, namely, seeking mode and following mode. The seeking mode rapidly moves the head to the target track, and the following mode accurately maintains the head along the center of the target track. Occasionally, a settling mode for smooth settling onto a target track is added. Each servo mode is designed independently to satisfy a certain cost function. MSC is a type of switching control system. However, the order of the switching of the controllers is decided beforehand. In other words, the controller is switched in the order of seeking, settling, and following. Therefore, for MSC, the selection of the controller is not needed as a role of the supervisor. The roles of the supervisor are the deciding of the switching condition of the controller and the initialization of the controller. In particular, when the IVC method is applied to MSC, the initialization of the controller is also not needed as a role of the supervisor.

3.3 Design of IVC

In this section, the methods for the design of IVC are described in detail. At the end of each design method, simulation and experimental results based

on HDD head-positioning servo control are used to show how the transient responses can be improved with the application of IVC.

3.3.1 Design of Initial Values on Feedback Controller

The discrete-time state-space equations of a plant $P[z]$ and a controller $C[z]$ are represented as

$$P[z]: \begin{cases} x_p[k+1] = A_p x_p[k] + B_p u[k] \\ y[k] = C_p x_p[k] \end{cases}, \tag{3.12}$$

$$C[z]: \begin{cases} x_c[k+1] = A_c x_c[k] + B_c(r[k] - y[k]) \\ u[k] = C_c x_c[k] + D_c(r[k] - y[k]) \end{cases}, \tag{3.13}$$

where $x_p \in \mathcal{R}^{n\times 1}$ is a state vector of the plant, $x_c \in \mathcal{R}^{m\times 1}$ is a state vector of the controller, $u \in \mathcal{R}$ is the control input, $y \in \mathcal{R}$ is the control variable, $r \in \mathcal{R}$ is a reference, A_p, B_p, and C_p are real matrices of the plant with appropriate dimensions, and A_c, B_c, C_c, and D_c are real matrices of the controller with appropriate dimensions. The expression $k = 0$ represents the time during mode switching.

It is assumed that the state $x_p[k]$ of the plant can be measured. According to the initial state $x_p[0]$ of the plant, IVC produces the initial state $x_c[0]$ of the controller using

$$x_c[0] = K x_p[0], \tag{3.14}$$

where $K \in \mathcal{R}^{m\times n}$ is the real coefficient matrix to be designed. Two IVC approaches are explained.

First, the method of designing IVC by minimizing a cost function is explained. This method is also known as J-min-type IVC. From (3.12) and (3.13), the state-space equation of the closed-loop system $\Sigma[z]$ is represented as

$$\Sigma[z]: \begin{cases} x[k+1] = Ax[k] + Br[k] \\ y[k] = Cx[k] \end{cases}, \tag{3.15}$$

where

$$x[k] = \begin{bmatrix} x_p[k] \\ x_c[k] \end{bmatrix}, \tag{3.16}$$

$$A = \begin{bmatrix} A_p - B_p D_c C_p & B_p C_c \\ -B_c C_p & A_c \end{bmatrix}, \quad B = \begin{bmatrix} B_p D_c \\ B_c \end{bmatrix}, \quad C = \begin{bmatrix} C_p & 0 \end{bmatrix}. \tag{3.17}$$

In J-min-type IVC, the cost function is defined as

$$J = \sum_{k=0}^{\infty} x^T[k] Q x[k], \quad Q > 0, \tag{3.18}$$

where $Q \in \mathcal{R}^{(n+m)\times(n+m)}$ is a square weighting matrix. (3.18) can be transformed as

$$\begin{aligned} J &= x^T[0]Px[0] \\ &= \begin{bmatrix} x_p^T[0] & x_c^T[0] \end{bmatrix} \begin{bmatrix} p_{11} & p_{12} \\ p_{12}^T & p_{22} \end{bmatrix} \begin{bmatrix} x_p[0] \\ x_c[0] \end{bmatrix}, \end{aligned} \tag{3.19}$$

where P is a positive definite matrix which satisfies a discrete Lyapunov equation given by

$$A^T PA - P = -Q. \tag{3.20}$$

J is a second-order polynomial in $x_c[0]$. Thus, there exists a minimum value of J for $x_c[0]$, and it is obtained by differentiating J with respect to $x_c[0]$ and using

$$\frac{\partial J}{\partial x_c[0]} = 2p_{11}x_c[0] + 2p_{12}x_p[0] = 0. \tag{3.21}$$

Therefore,

$$x_c[0] = -p_{11}^{-1}p_{12}x_p[0]. \tag{3.22}$$

During mode switching, the initial state of the controller is set as $x_c[0]$ in (3.22). Using IVC, the transient response of the closed-loop system after mode switching can be minimized in the sense that J can be minimized.

Next, the method of designing IVC by pole-zero cancellation is explained. This method is also known as pole-zero-type IVC. From (3.12) and (3.13), a transfer function of the closed-loop system $\Sigma[z]$ is represented as

$$y[z] = \frac{N_r[z]}{D[z]}r[z] + \frac{N_p[z]}{D[z]}x_p[0] + \frac{N_c[z]}{D[z]}x_c[0], \tag{3.23}$$

where $D[z]$ and $N_r[z]$ are scalar polynomials given by

$$D[z] = det(zI - A), \tag{3.24}$$

$$N_r[z] = Cadj(zI - A)B, \tag{3.25}$$

and $N_p[z]$ and $N_c[z]$ are respectively $1\times n$ and $1\times m$ polynomials concatenated as

$$\begin{bmatrix} N_p[z] & N_c[z] \end{bmatrix} = Cadj(zI - A)z. \tag{3.26}$$

Substituting (3.14) into (3.23), (3.23) can be transformed as

$$y[z] = \frac{N_r[z]}{D[z]}r[z] + \frac{N_p[z] + N_c[z]K}{D[z]}x_p[0]. \tag{3.27}$$

It is shown by (3.27) that the zeros of the transfer function from $x_p[0]$ to $y[z]$ can be shifted to the desired values by selecting appropriate values of K. This suggests that the transient characteristics after mode switching can be improved by shifting the zeros to cancel the undesirable poles in (3.27).

Here, the method for designing K for the pole-zero-type IVC is explained. Equation (3.27) can be represented in each element as

$$y[z] = \frac{N_r[z]}{D[z]} r[z] + \sum_{i=1}^{n} \frac{N_{pi}[z] + N_{ci}[z]K_i}{D[z]} x_{pi}[0], \tag{3.28}$$

where

$$N_p[z] = \begin{bmatrix} N_{p1}[z] & N_{p2}[z] & \cdots & N_{pn}[z] \end{bmatrix}, \tag{3.29}$$

$$N_c[z] = \begin{bmatrix} N_{c1}[z] & N_{c2}[z] & \cdots & N_{cm}[z] \end{bmatrix}, \tag{3.30}$$

$$K = \begin{bmatrix} K_1 & K_2 & \cdots & K_n \end{bmatrix}, \tag{3.31}$$

$$K_i = \begin{bmatrix} K_{1i} \\ K_{2i} \\ \vdots \\ K_{mi} \end{bmatrix} \quad (i = 1, 2, \cdots, n), \tag{3.32}$$

$$x_p[0] = \begin{bmatrix} x_{p1}[0] & x_{p2}[0] & \cdots & x_{pn}[0] \end{bmatrix}^T. \tag{3.33}$$

The undesirable closed-loop poles to be canceled are represented by λ_j, where $j = 1, 2, \cdots, r$. Substituting $z = \lambda_j$ into the numerator polynomial in (3.27), r simultaneous equations are thus given as

$$\Sigma K_i = \Gamma_i \quad (i = 1, 2, \cdots, n), \tag{3.34}$$

where

$$\Sigma = \begin{bmatrix} N_{c1}[\lambda_1] & N_{c2}[\lambda_1] & \cdots & N_{cm}[\lambda_1] \\ N_{c1}[\lambda_2] & N_{c2}[\lambda_2] & \cdots & N_{cm}[\lambda_2] \\ \vdots & \vdots & \vdots & \vdots \\ N_{c1}[\lambda_r] & N_{c2}[\lambda_r] & \cdots & N_{cm}[\lambda_r] \end{bmatrix}, \tag{3.35}$$

$$\Gamma_i = \begin{bmatrix} -N_{pi}[\lambda_1] \\ -N_{pi}[\lambda_2] \\ \vdots \\ -N_{pi}[\lambda_r] \end{bmatrix}. \tag{3.36}$$

When the number r of poles to be canceled is equal to the degree m of the controller, Σ in (3.35) becomes nonsingular and it has an inverse matrix. Therefore, the real coefficient matrix K can be calculated as

$$K_i = \Sigma^{-1}\Gamma_i \quad (i = 1, 2, \cdots, n). \tag{3.37}$$

The block diagram of a simplified case of the HDD head-positioning servo system is shown in Figure 3.5. In this case, a second-order lead-lag filter is applied as the controller, and the plant model is a simple second-order system. The open loop crossover frequency of this closed-loop system is 250 Hz. In this simulation, J-min-type IVC is applied. Since both the orders of the plant model

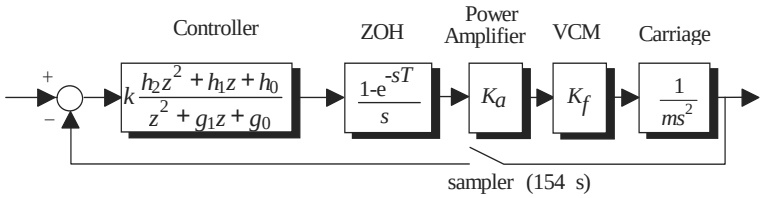

FIGURE 3.5
Block diagram of a simplified case of the HDD head-positioning servo system.

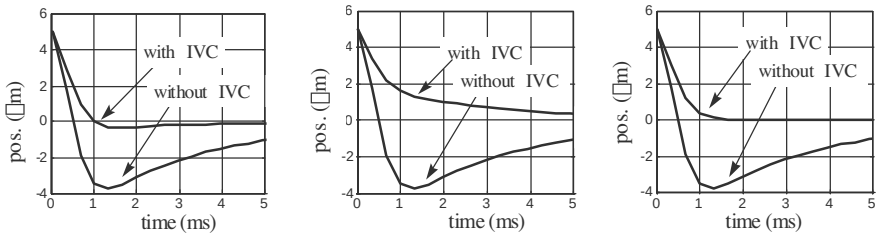

(1) γ=0 (2) γ=1.0e-6 (3) γ=1.55e-7

FIGURE 3.6
Transient responses with and without IVC (simulation).

and controller are two, all the initial values of the controller are calculated based on (3.22). The transient time responses with and without IVC are shown in Figure 3.6. In this case, the state variables of the plant are position and velocity, and their initial values are 5 μm and –5 mm/s, respectively. Three cases of different weighting coefficients Q are shown. In (1), the weighting coefficient for velocity is 0, and the weighting coefficient for position is 1. In (2) and (3), the weighting coefficients for velocity are 1.0e-6 and 1.55e-7, respectively, while the weighting coefficient for position is kept 1 for both cases. It is shown by every case that the transient response is very much improved by the use of IVC, and it is also shown that Q can be selected based on the desired type of of transient response. If overshoot is not desired, case (2) will be appropriate. If it is required that a certain region around a target point is reached in minimum time, case (1) which has a slight overshoot may be better.

Figure 3.7 shows the block diagram of an HDD head-positioning servo system considering a time delay which includes the processor execution time delay and the approximate filter delay. In this case, a second-order lead-lag filter is applied as the controller, and the plant model is a simple third-order system when the time delay is modeled as a first-order transfer function based on *Pade approximation*. In this simulation, pole-zero-type IVC is applied. The transient time responses with and without IVC are shown in Figure 3.8. The

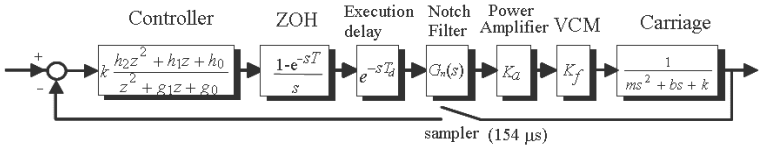

FIGURE 3.7
Block diagram of HDD head-positioning servo system with time delay considered.

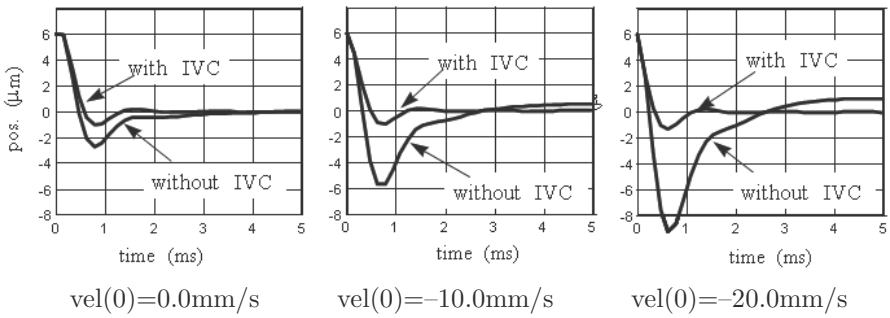

FIGURE 3.8
Transient responses with and without IVC (simulation).

poles of this closed-loop are at $z = -0.335, 0.555 \pm j0.416, 0.905, 0.954$. Since the order of controller is two, two zeros of the closed-loop can be moved to the desired values by calculating K using (3.37). In this case, since the slow transient response occurs due to the two poles at $z = 0.905$ and $z = 0.954$, two zeros should be shifted to cancel these poles. Hence, in this case, the zeros of the transfer function from the initial position to the displacement are at $z = 0.954, 0.905, -0.390, 0.169$. The zeros of the transfer function from the initial velocity to the displacement are $z = 0.954, 0.905, -0.291$.

The transient time responses with and without IVC are shown in Figure 3.8. Even though the initial velocity is changed, there are little changes in the transient responses with the use of IVC because of the cancellation of the slow modes.

In practice, it is difficult to detect $x_p[k]$ and hence, velocity, acceleration, and other undetected states are approximately calculated using a state observer or an appropriate filter. This basic idea of shaping transient response by IVC has been applied to HDDs for years [38]. A more sophisticated application is described in Section 3.4.1.

3.3.2 Design of Additional Input to Controller

In the IVC design described in Section 3.3.1, the presented IVC approach gives designed initial values to the feedback controller to improve the transient responses of the switching control system. In the previous approach, the design freedom depends on the order of the feedback compensation. Since the number of poles that can be canceled by the IVC are the same as the number of poles of the feedback controller, there are some cases where the previous IVC in Section 3.3.1 may not provide the desired transient responses. Therefore, in this section, IVC using an additional input r' shown in Figure 3.9 is introduced to cancel the undesirable poles and achieve the desired transient responses.

With the additional input r' shown in Figure 3.9, the discrete state-space equation of the control system can be expressed as

$$\begin{aligned} x[k+1] &= Ax[k] + Br[k] + B_u r'[k], \\ y[k] &= Cx[k], \end{aligned} \tag{3.38}$$

where B_u for r' is given by

$$B_u = \begin{bmatrix} B_p \\ 0 \end{bmatrix}. \tag{3.39}$$

By performing z-transformation of (3.38) with consideration for the initial values $x_p[0]$ and $x_c[0]$, $y[z]$ can be given as

$$\begin{aligned} y[z] &= C(zI - A)^{-1}Br[z] + C(zI - A)^{-1}B_u r'[z] \\ &\quad + C(zI - A)^{-1} z \begin{bmatrix} x_p[0] \\ x_c[0] \end{bmatrix} \\ &= \frac{N_r[z]}{D[z]} r[z] + \frac{N_{ru}[z]}{D[z]} r'[z] + \frac{N_{pr}[z]}{D[z]} x_p[0] + \frac{N_{cr}[z]}{D[z]} x_c[0]. \end{aligned} \tag{3.40}$$

The transient responses that deteriorate the positioning performance correspond to the initial value responses for $x_p[0]$ which appears in the third term on the right-hand side of (3.40). In order to suppress these initial value responses, the following r' is superimposed to the control input u and, as a result, the initial value of the feedback controller $x_c[0]$ can be cleared [5] as follows.

$$\begin{aligned} r'[z] &= \frac{n[z]}{d[z]} x_p[0] \\ x_c[0] &= 0 \end{aligned} \tag{3.41}$$

By substituting (3.41) into (3.40), $y[z]$ is redefined as

$$y[z] = \frac{N_r[z]}{D[z]} R[z] + \frac{N_{pr}[z]d[z] + N_{ru}[z]n[z]}{D[z]d[z]} x_p[0]. \tag{3.42}$$

Here, the k^{th} component in $x_p[0]$ is defined as the initial value $x_{pk}[0]$, which

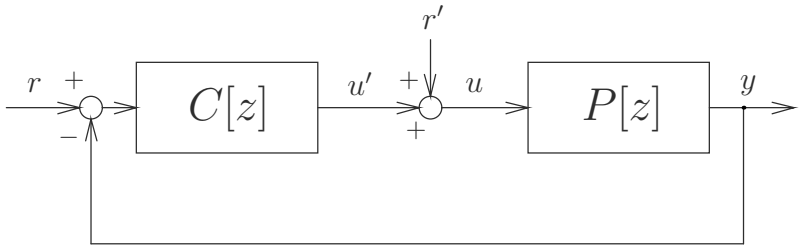

FIGURE 3.9
Block diagram of control system with additional input r'.

should be suppressed by the IVC. The corresponding output $y_{0k}[z]$ for $x_{pk}[0]$ can be extracted as

$$y_{0k}[z] = \frac{N_{pk}[z]d[z] + N_{ru}[z]n_k[z]}{D[z]d[z]} x_{pk}[0], \tag{3.43}$$

where $N_{pk}[z]$ and $n_k[z]$ are the k^{th} polynomials of $N_p[z]$ and $n[z]$, respectively. In IVC using r', all roots of $D[z]$ can be canceled by designing $n_k[z]$, while the desired poles are assigned by $d[z]$ to allow the initial value responses $y_{0k}[z]$ to converge to zero by the desired time constant. Therefore, $n_k[z]$ can be designed under the conditions given by

$$N_{pk}[\lambda_i]d[\lambda_i] + N_{ru}[\lambda_i]n_k[\lambda_i] = 0, \tag{3.44}$$

where λ_i with $i = 1, 2, \ldots, n+m$ is the i^{th} root of $D[z]$. Here, $n_k[z]$ is assumed to be represented by the polynomial given by

$$n_k[z] = a_g z^g + a_{g-1} z^{g-1} + \ldots + a_1 z + a_0, \tag{3.45}$$

where a_k with $k = 0, 1, 2, \ldots, g$ are the undetermined real coefficients. The equation derived from the combination of (3.44) and (3.45) is given by

$$\begin{bmatrix} \lambda_1^g & \lambda_1^{g-1} & \cdots & \lambda_1 & 1 \\ \lambda_2^g & \lambda_2^{g-1} & \cdots & \lambda_2 & 1 \\ \vdots & \vdots & \vdots & \vdots & \vdots \\ \lambda_{n+m}^g & \lambda_{n+m}^{g-1} & \cdots & \lambda_{n+m} & 1 \end{bmatrix} \begin{bmatrix} a_g \\ a_{g-1} \\ \vdots \\ a_0 \end{bmatrix} = \begin{bmatrix} -N_{ru}[\lambda_1]^{-1} N_{pk}[\lambda_1]\, d[\lambda_1] \\ -N_{ru}[\lambda_2]^{-1} N_{pk}[\lambda_2]\, d[\lambda_2] \\ \vdots \\ -N_{ru}[\lambda_{n+m}]^{-1} N_{pk}[\lambda_{n+m}]\, d[\lambda_{n+m}] \end{bmatrix}. \tag{3.46}$$

Equation (3.46) can be redefined as

$$\Sigma a = \Gamma. \tag{3.47}$$

The equality constraint of (3.47) to cancel all the roots of $D[z]$ can be defined as an affine function of the free parameter a. The free parameter a can be determined by solving (3.47) under the assumptions that $D[z]$ does not include multiple roots and g is selected as $n+m-1$.

On the other hand, the additional input r' may cause saturation of the control input u when faster responses are required, which excites the uncertain vibration modes in the high frequency range. Therefore, an optimization approach for the control input has been developed to design the initial value compensator $\frac{n_k[z]}{d[z]}$ [14]. In order to optimize the input, the cost function J that is to be minimized under the equality constraint of (3.47) is given by [12]

$$J = a^T Q_x a + 2Q_y a + Q_z, \tag{3.48}$$

where Q_x, Q_y, and Q_z are weighting matrices to suppress the amplitude of the control input and its jerk component. The control input $u[k]$ in Figure 3.9 can be expressed as

$$\begin{aligned} u[k] &= \begin{bmatrix} -D_c C_p & C_c \end{bmatrix} \begin{bmatrix} x_p[k] \\ x_c[k] \end{bmatrix} + D_c r[k] + r'[k] \\ &= C_u \begin{bmatrix} x_p[k] \\ x_c[k] \end{bmatrix} + D_c r[k] + r'[k]. \end{aligned} \tag{3.49}$$

From (3.15) and (3.49), and by performing z-transformation, $u[z]$ is given as

$$\begin{aligned} u[z] &= C_u(zI-A)^{-1}Br[z] + (C(zI-A)^{-1}B_u + 1)r'[z] \\ &\quad + C_u(zI-A)^{-1}z \begin{bmatrix} x_p[0] \\ x_c[0] \end{bmatrix} \\ &= \frac{N_u[z]}{D[z]} r[z] + \frac{N_{uu}[z]}{D[z]} r'[z] + \frac{N_{pu}[z]}{D[z]} x_p[0] + \frac{N_{cu}[z]}{D[z]} x_c[0]. \end{aligned} \tag{3.50}$$

By substituting (3.41) into (3.50), $u[z]$ is given as

$$u[z] = \frac{N_u[z]}{D[z]} r[z] + \frac{N_{uu}[z]}{D[z]} \frac{n[z]}{d[z]} x_p[0] + \frac{N_{pu}[z]}{D[z]} x_p[0]. \tag{3.51}$$

Using the second and third terms on the right-hand side of (3.51), the corresponding control input $u_{0k}[z]$ for $x_{pk}[0]$ can be extracted as

$$u_{0k}[z] = \frac{N_{uu}[z]}{D[z]} \frac{n_k[z]}{d[z]} x_{pk}[0] + \frac{N_{puk}[z]}{D[z]} x_{pk}[0]. \tag{3.52}$$

In order to define the cost function J of (3.48), $u_{0k}[z]$ should be expressed as a time series vector $U_{0k} \in \mathcal{R}^{N\times 1}$. Using a controllable canonical form, the corresponding additional input $r'[z]$ for $x_{pk}[0]$ can be redefined as

$$r'[z] = C_r(zI - A_r)^{-1} B_r x_{pk}[0], \tag{3.53}$$

where A_r, B_r, and C_r are defined as

$$A_r = \begin{bmatrix} 0 & 1 & \dots & 0 \\ 0 & 0 & \ddots & 0 \\ 0 & 0 & \dots & 1 \\ -b_0 & -b_1 & \dots & -b_h \end{bmatrix}, B_r = \begin{bmatrix} 0 \\ \vdots \\ 0 \\ 1 \end{bmatrix}, C_r = a^T. \tag{3.54}$$

Here, $(zI - A_r)^{-1}B_r$ is a $g \times 1$ transfer function vector. The unit impulse response of the i-th transfer function of $(zI - A_r)^{-1}B_r$ is defined as $V_{0i} \in \mathcal{R}^{N\times 1}$. As a result, the time series vector $R' \in \mathcal{R}^{N\times 1}$ of (3.41) can be expressed as an affine function of a, which is given by

$$\begin{aligned} R' &= \begin{bmatrix} V_{01} & V_{02} & \dots & V_{0g} \end{bmatrix} a x_{pk}[0] \\ &= V_0 a x_{pk}[0]. \end{aligned} \tag{3.55}$$

In addition, the unit impulse response $H_{uu} \in \mathcal{R}^{N\times 1}$ of the transfer function $\frac{N_{uu}[z]}{D[z]}$ in (3.52) can be defined as

$$H_{uu} := \begin{bmatrix} h_{uu}(0) & h_{uu}(1) & \dots & h_{uu}(N-1) \end{bmatrix}^T. \tag{3.56}$$

A convolution matrix M_u of H_{uu} is defined as [14]

$$M_u := \begin{bmatrix} h_{uu}(0) & 0 & \cdots & 0 \\ h_{uu}(1) & h_{uu}(0) & \cdots & 0 \\ \vdots & \vdots & \ddots & \vdots \\ h_{uu}(N_x-1) & h_{uu}(N_x-2) & \cdots & h_{uu}(0) \end{bmatrix}. \tag{3.57}$$

Moreover, the unit impulse response of the transfer function $\frac{N_{puk}[z]}{D[z]}$ is defined as $U_i \in \mathcal{R}^{N\times 1}$. As a result of the definitions, a time series matrix U_{0k} for $u_{0k}[k]$ can be expressed by M_u, V_0, a, and U_i as

$$U_{0k} = (M_u V_0 a_k + U_i) x_{pk}[0]. \tag{3.58}$$

On the other hand, a differentiation matrix $M_d \in \mathcal{R}^{N\times N}$ is defined as

$$M_d := \begin{bmatrix} 1 & 0 & \cdots & 0 & 0 \\ -1 & 1 & \cdots & 0 & 0 \\ \cdots & \cdots & \cdots & \cdots & \cdots \\ 0 & 0 & \cdots & -1 & 1 \end{bmatrix} \tag{3.59}$$

in order to consider the jerk component in J. A delta matrix J_{0k} for U_{0k} can be expressed by M_d as

$$\begin{aligned} J_{0k} &= M_d U_{0k} \\ &= M_d (M_u V_0 a + U_i) x_{pk}[0]. \end{aligned} \tag{3.60}$$

In order to suppress the amplitude of the control input and its jerk component, J can be designed as a quadratic form of U_{0k} and J_{0k}, which is given by

$$J = q_1 U_{0k}^T U_{0k} + q_2 J_{0k}^T J_{0k}. \tag{3.61}$$

Over here, q_1 and q_2 are weighting coefficients for the amplitude of the control input and its jerk component, respectively. By substituting (3.58) and (3.60) into (3.61), the weighting matrices Q_x, Q_y, and Q_z in (3.48) can be formulated as

$$\begin{aligned} Q_x &= q_1 V_0^T M_u^T M_u V_0 + q_2 V_0^T M_u^T M_d^T M_d M_u V_0, \\ Q_y &= 2q_1 V_i^T M_u V_0 + 2q_2 V_i^T M_d^T M_d M_u V_0, \\ Q_z &= q_1 U_i^T U_i + q_2 U_i^T M_d^T M_d U_i. \end{aligned} \tag{3.62}$$

According to the Lagrange multiplier, the free parameter a can be optimized by minimizing J under the equality constraint $\Sigma a = \Gamma$. Hence, a is given by

$$a = Q_x^{-1}\Sigma^T \lambda^T - Q_x^{-1} Q_y, \tag{3.63}$$

where λ^T is given as

$$\lambda^T = (\Sigma Q_x^{-1} \Sigma^T)^{-1}(\Gamma + \Sigma Q_x^{-1} Q_y). \tag{3.64}$$

The order g of the initial value compensator should be preliminarily designed to satisfy the inequality $g+1 > n+m$ under J. The designed additional input can ensure complete cancellation of all the roots of $D[z]$ to obtain the desired transient response, and can suppress the amplitude and discontinuity of the control input.

In this simulation, the controller is also a conventional second-order lead-lag filter, and the plant model is a third-order system which includes a second-order mechanical model and a time delay modeled by Padé approximation. The closed-loop system has five poles which are at $z = -0.323, 0.550 \pm j0.497, 0.904, 0.955$. The transfer function from the additional input $r'[z]$ to the controlled variable $y[z]$ has four zeros which are at $z = -56.79, 0.999, -0.416, -0.235$.

Since there are five closed-loop poles, all the poles can be canceled by calculating (3.46) in the case where the numerator (3.45) is of fourth-order. Over here, the desired pole is set to $z = 0.6$.

After deriving the additional input, the poles and zeros of the transfer function between the initial state variables and the controlled variable are as follows:

1. Poles: $z = 0.550 \pm j0.497, 0.999, 0.955, 0.904, -0.416, -0.323, -0.234, 0.600$.
2. Zeros of transfer function between initial position and $y[z]$: $z = 0.550 \pm j0.497, 0.999, 0.955, 0.904, -0.416, -0.323, -0.234, -0.393$.
3. Zeros of transfer function between initial velocity and $y[z]$: $z = 0.550 \pm j0.497, 0.999, 0.955, 0.904, -0.416, -0.323, -0.234$.

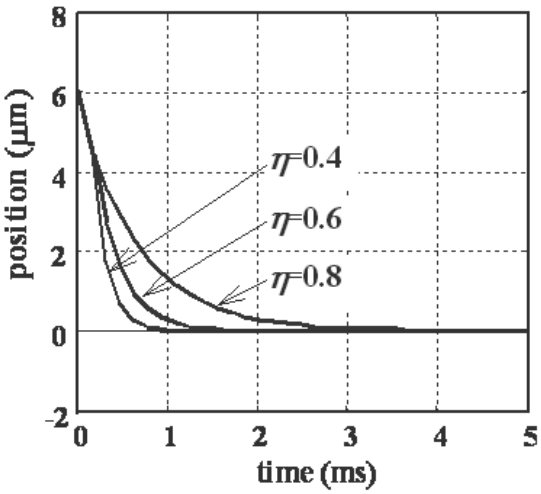

FIGURE 3.10
Transient waveforms for various desired eigenvalues (simulation).

All poles except the assigned pole at $z = 0.6$ are canceled by the zeros. Consequently, the transient response is governed by the assigned pole. Here, the design for initial position and velocity are described in detail. The procedure is the same for designing other state variables and references.

Figure 3.10 shows the simulation results for the free responses of three assigned desired poles at $z = 0.4$, $z = 0.6$, and $z = 0.8$. The trajectories of the responses in the phase plane are shown in Figure 3.11, where 'o' denotes the responses of the system, and the solid lines denote the responses of the first-order systems with their corresponding poles. The trajectories show that the responses are exactly the same as those of the first-order systems.

Figure 3.12 shows the transient responses from both simulations and experiments using the HDD head-positioning system. The switching condition is 6 μm before the target track center, and the velocity is about –10 mm/s. In Figure 3.12, the time responses of the systems, whose individual assigned poles are respectively $z = 0.8$, $z = 0.6$, $z = 0.4$, and $z = 0.2$, are shown. It should be noted that the transient response can be appropriately designed by assigning a dominant pole. As a result, these figures show that by selecting an appropriate pole, the IVC method improves the settling time by about 2 ms.

3.3.3 Design of Optimal Switching Condition

In this section, a design method for optimizing the mode switching condition is described. As mentioned in the previous sections, IVC is a method for improving the characteristics from the initial values at mode switching to

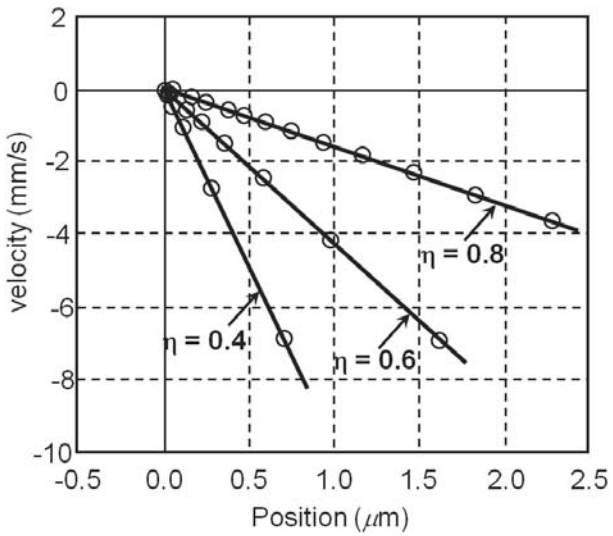

FIGURE 3.11
Trajectories on phase plane (simulation).

the control variable such that they are desirable characteristics. However, this does not mean the realization of the desired transient time responses, because the transient responses depend on the initial values such as displacement, velocity, and acceleration during mode switching, even though the characteristics between the initial values and the control variable can be shaped ideally. Thus, it is necessary to design an optimal mode switching condition such as an optimal set of initial values during mode switching. By applying IVC, the initial values during mode switching are only the initial values of the plant model. The design of the optimal mode switching condition is the definition of an index to evaluate a transient time response, and finding a set of initial values that minimizes the index. Here, the $\mathcal{H}_2$-norm of the displacement response after mode switching and the $\mathcal{H}_2$-norm of the control input response after mode switching are defined. It is then necessary to design a reference trajectory which passes through the designed optimal set of initial values.

The discrete-time state-space equations of a plant $P[z]$ and a controller $C[z]$ are represented as

$$P : \begin{cases} x_p[k+1] = A_p x_p[k] + B_p u[k] \\ y[k] = C_p x_p[k] \end{cases}, \tag{3.65}$$

$$C : \begin{cases} x_c[k+1] = A_c x_c[k] + B_c(-y[k]) \\ u[k] = C_c x_c[k] + D_c(-y[k]) \end{cases}, \tag{3.66}$$

where x_p is a state vector of the plant, x_c is a state vector of the controller, u is the control input, y is the control variable, A_p, B_p, and C_p are real matrices

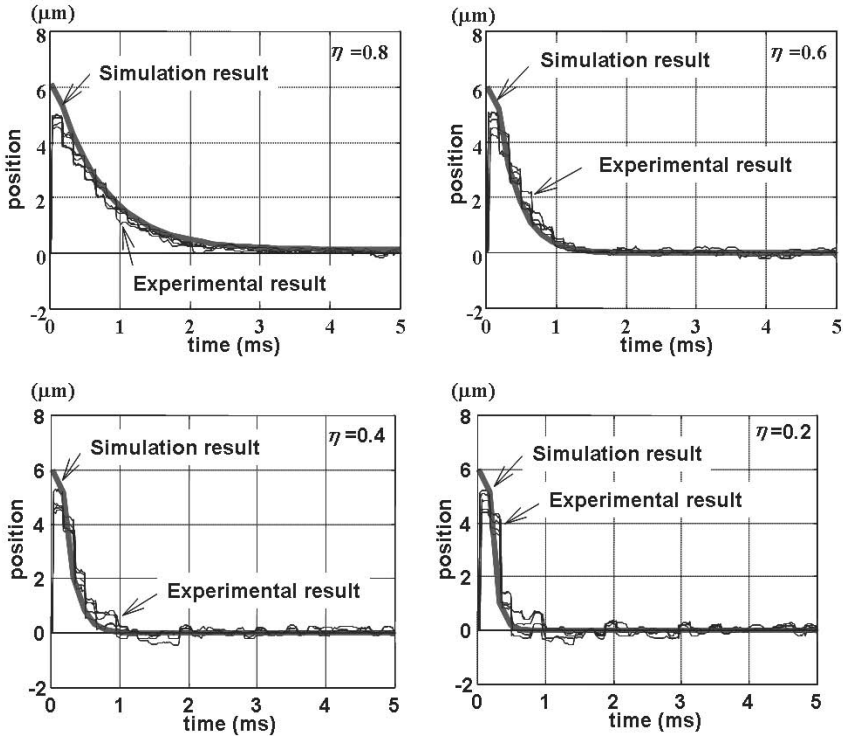

FIGURE 3.12
Transient waveforms with IVC compensation (simulations and experiments).

of the plant with appropriate dimensions, and A_c, B_c, C_c, and D_c are real matrices of the controller with appropriate dimensions.

Since the $\mathcal{H}_2$-norm of the transfer function is a root-mean-square of the impulse response, the $\mathcal{H}_2$-norm is suitable as a performance index for evaluating transient responses. As it is necessary to check if the unmodeled mechanical resonant modes in an actual system are excited by a large control input, the $\mathcal{H}_2$-norm of the control input response is also considered here. From (3.65) and (3.66), the transfer function between the plant initial values and the control variable, and the transfer function between the initial values and the control input are obtained as

$$z \begin{bmatrix} x_p \\ x_c \end{bmatrix} - z \begin{bmatrix} x_p[0] \\ x_c[0] \end{bmatrix} = \begin{bmatrix} A_p - B_p D_c C_p & B_p C_c \\ -B_c C_p & A_c \end{bmatrix} \begin{bmatrix} x_p \\ x_c \end{bmatrix} \tag{3.67}$$

$$\therefore zx - zx[0] = A \cdot x,$$

where $x = [x_p^T \;\; x_c^T]^T$, and as a result,

$$x = \begin{bmatrix} zI - (A_p - B_p D_c C_p) & -B_p C_c \\ B_c C_p & zI - A_c \end{bmatrix}^{-1} zx[0], \tag{3.68}$$

$$u = \begin{bmatrix} -D_c C_c & C_c \end{bmatrix} x, \tag{3.69}$$

$$y = \begin{bmatrix} C_p & 0 \end{bmatrix} x. \tag{3.70}$$

Next, the IVC is applied to this system. This means that the initial values of the controller $x_c[0]$ can be replaced by the multiplication of $x_p[0]$ with K which can be derived from the IVC algorithm, and where it is assumed that the initial values $x_p[0]$ of the plant can be measured or estimated. Hence, $x_c[0]$ is given by

$$x_c[0] = K x_p[0]. \tag{3.71}$$

Substituting equation (3.71) into equation (3.68) gives

$$x = \begin{bmatrix} zI - (A_p - B_p D_c C_p) & -B_p C_c \\ B_c C_p & zI - A_c \end{bmatrix}^{-1} z \begin{bmatrix} I \\ K \end{bmatrix} x_p[0]. \tag{3.72}$$

As a result, after using IVC, the transfer function between the plant initial values and the control variable, and the transfer function between the plant initial values and the control input after are

$$\begin{aligned} u &= \begin{bmatrix} -D_c C_c & C_c \end{bmatrix} \begin{bmatrix} zI - (A_p - B_p D_c C_p) & -B_p C_c \\ B_c C_p & zI - A_c \end{bmatrix}^{-1} z \begin{bmatrix} I \\ K \end{bmatrix} x_p[0] \\ &\equiv G \cdot x_p[0], \end{aligned} \tag{3.73}$$

$$\begin{aligned} y &= \begin{bmatrix} C_p & 0 \end{bmatrix} \begin{bmatrix} zI - (A_p - B_p D_c C_p) & -B_p C_c \\ B_c C_p & zI - A_c \end{bmatrix}^{-1} z \begin{bmatrix} I \\ K \end{bmatrix} x_p[0] \\ &\equiv H \cdot x_p[0]. \end{aligned} \tag{3.74}$$

The performance indices are defined as

$$J_u = \| \, G \cdot x_p[0] \, \|_2^2, \tag{3.75}$$

$$J_y = \| \, H \cdot x_p[0] \, \|_2^2 \, . \tag{3.76}$$

Next, from the definition of the $\mathcal{H}_2$-norm, $\| \, G \cdot x_p[0] \, \|_2^2$ becomes

$$\begin{aligned} \| \, G \cdot x_p[0] \, \|_2^2 &= trace\{(x_p[0]D)^T (D x_p[0]) + (x_p[0]B)^T L_o (B x_p[0])\} \\ &= trace\{x_p[0]^T (D^T D + B^T L_o B) x_p[0]\}, \end{aligned} \tag{3.77}$$

where L_o is the solution of the Lyapunov equation in discrete-time domain which is given as

$$A^T L_o A - L_o + C^T C = 0. \tag{3.78}$$

For simplicity, the matrices of the state-space equation of $G(z)$ are described as A, B, C, and D. From (3.77), the optimal combination of the plant state variables $x_p(0)$ can then be calculated by minimizing

$$x_p[0]^T(D^TD + B^TL_oB)x_p[0]. \tag{3.79}$$

Since (3.77) is a linear quadratic equation with m variables and the $\mathcal{H}_2$-norm is positive, the minimum value exists. For example, the state variables of the plant are assumed to be position, velocity, and acceleration, and the initial values of the state variables are represented as $x_p[0] \equiv [x_{pos}\ \ x_{vel}\ \ x_{acc}]^T$. Hence,

$$\begin{aligned} J_u &= x_p[0]^T(D^TD + B^TL_oB)x_p[0] \\ &\equiv x_p[0]^TKx_p[0] \\ &= \begin{bmatrix} x_{pos} & x_{vel} & x_{acc} \end{bmatrix} \begin{bmatrix} k_{11} & k_{12} & k_{13} \\ k_{21} & k_{22} & k_{23} \\ k_{31} & k_{32} & k_{33} \end{bmatrix} \begin{bmatrix} x_{pos} \\ x_{vel} \\ x_{acc} \end{bmatrix}. \end{aligned} \tag{3.80}$$

The optimal initial condition can then be calculated by solving

$$\frac{\partial J_u}{\partial x_{vel}} = 0, \quad \frac{\partial J_u}{\partial x_{acc}} = 0. \tag{3.81}$$

The model used in the simulation has open loop characteristics which are a crossover frequency of 500 Hz and a phase margin of 36°. The plant model is of third-order and the compensator is a conventional second-order lead-lag filter with a sampling rate of 150 μs.

The $\mathcal{H}_2$-norm of $u - x[0]$ for various initial velocities and accelerations is shown in Figure 3.13. It is practical to find a condition with smaller initial values, and which does not very much increase the $\mathcal{H}_2$-norm.

The experimental setup uses a 3.5″ HDD. The track-seeking distance is about 7.5 mm which is one-third of the full stroke, and the mode switching condition is 15 μm from the target track center. During mode switching, pole-zero-type IVC is applied. The experimental and corresponding simulation results for the transient response of the head position after mode-switching at $t = 0$ are shown in Figure 3.14. In each figure, the experimental data are obtained from many sets of experiments and drawn on the same figure. In Figure 3.14, Condition A represents the responses with a designed mode-switching condition given by an initial velocity of 60 mm/s and an acceleration of 150 m/s^2. For comparison, Conditions B and C in Figure 3.14 represent worse mode-switching conditions given by initial velocities of 90 mm/s and 25 mm/s, respectively. Each condition is plotted in Figure 3.13. It is shown that the designed mode-switching condition produces the best transient response. The experimental results for the transient responses of the current for the same mode-switching conditions shown in Figure 3.14 are shown in Figure 3.15. It is obvious that the designed mode-switching condition shown

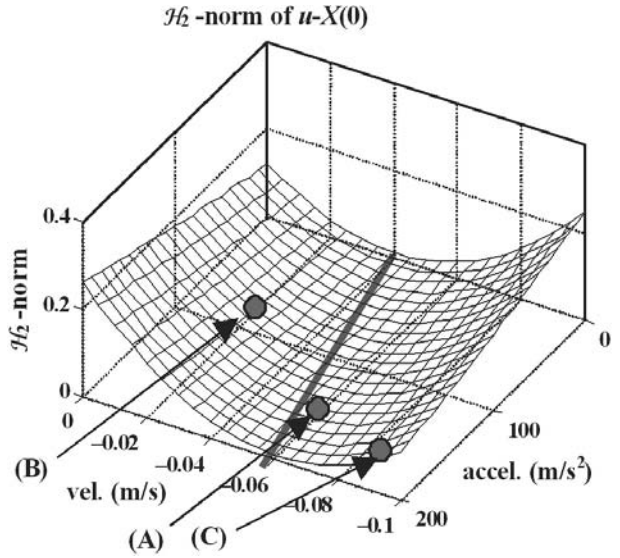

FIGURE 3.13
$\mathcal{H}_2$-norm plane for initial velocity and acceleration.

in Condition A is the most desirable. From the experimental results of both position and current transient responses, it is clear that the proposed mode-switching conditions are appropriate.

Next, the design of the switching condition in consideration of constraints is explained [2, 3]. The discrete-time state-space equations of a plant P and a controller C are represented as (3.65) and (3.66), respectively. To ensure that bumpy switching does not occur, the constraint imposed on the control input u after switching is given by

$$-0.02 \leq u[k] \leq 0.02, \quad k \geq 0, \tag{3.82}$$

where the control input u refers to current in the case of the Voice Coil Motor (VCM). The vector signal to be constrained is expressed as z which is equal to u. Z represents the set of z which satisfies the specified constraints and is given by

$$Z = \{z|\ M_z z \leq m_z\}, \tag{3.83}$$

where

$$M_z = \begin{bmatrix} -1 \\ 1 \end{bmatrix}, \quad m_z = \begin{bmatrix} 0.02 \\ 0.02 \end{bmatrix}, \tag{3.84}$$

and where it is assumed that Z includes the origin. The state-space equation of the closed-loop system is expressed as

$$\begin{cases} x[k+1] = Ax[k] \\ y[k] = Cx[k] \\ z[k] = C_z x[k] \end{cases}, \tag{3.85}$$

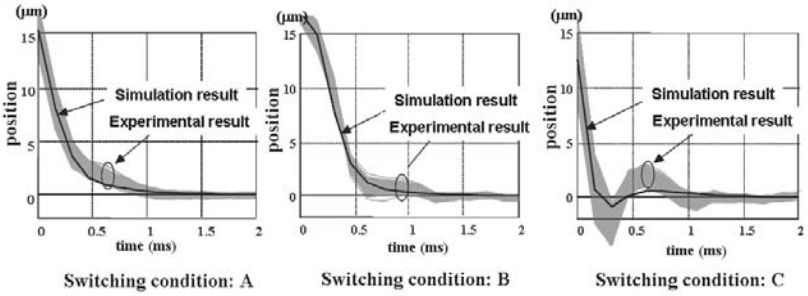

FIGURE 3.14
Transient response of head position after mode switching (experimental results).

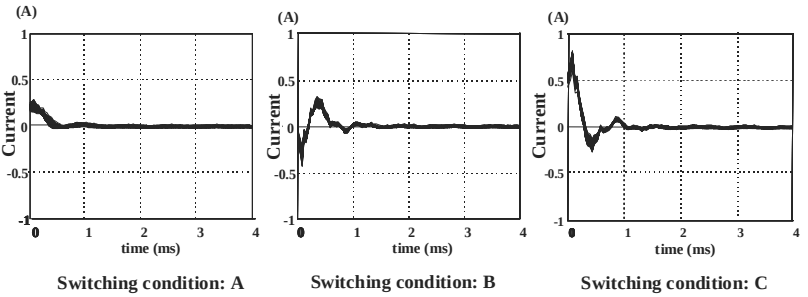

FIGURE 3.15
Transient response of current after mode switching (experimental results).

where

$$x[k] = \begin{bmatrix} x_p[k] \\ x_c[k] \end{bmatrix}, \quad A = \begin{bmatrix} A_p - B_p D_c C_p & B_p C_c \\ -B_c C_p & A_c \end{bmatrix}, \tag{3.86}$$

$$C = \begin{bmatrix} C_p & 0 \end{bmatrix}, \quad C_z = \begin{bmatrix} -D_c C_p & C_c \end{bmatrix}. \tag{3.87}$$

The vector signal z to be constrained at time k can be expressed as

$$z[k] = C_z A^k x[0] = C_z A^k \begin{bmatrix} x_p[0] \\ x_c[0] \end{bmatrix}. \tag{3.88}$$

Thus, the maximal output admissible set O_∞ is defined as

$$O_\infty = \left\{ x[0] = \begin{bmatrix} x_p[0] \\ x_c[0] \end{bmatrix} \mid z[k] \in Z, \ k \geq 0 \right\}. \tag{3.89}$$

The maximal output admissible set O_∞ is a set of all closed-loop initial states

which can be converged to the origin without violating the specified constraints defined in (3.83). In order to improve the transient response after switching, J-min-type IVC is applied as

$$x_c[0] = Kx_p[0], \tag{3.90}$$

where $K \in \mathcal{R}^{m\times n}$ is the real coefficient matrix to be designed. To prevent bumpy switching, the cost function of IVC is defined as

$$J = \sum_{k=0}^{\infty} u[k]^2. \tag{3.91}$$

By using IVC, (3.89) can be tranformed as

$$O_\infty = \left\{ x[0] = \begin{bmatrix} I \\ K \end{bmatrix} x_p[0] |\ z[k] \in Z,\ k \geq 0 \right\}. \tag{3.92}$$

The safe switching condition so that the given constraints are fulfilled can be designed by calculating the maximal output admissible set O_∞.

The calculated maximal output admissible set is shown in Figure 3.16. The solid line is where the initial state of the controller is initialized by the IVC technique, and the dashed line is where the initial state of the controller is set to zero. The horizontal axis represents the head position normalized by the track-pitch which is denoted as Tp, and the vertical axis represents the head velocity. The origin of the horizontal axis represents the target track position. For instance, –10 on the horizontal axis represents the position of 10 tracks ahead of the target track. The safe region where the constraints are fulfilled is expanded using the IVC technique.

The simulation results for initializations using IVC and zero reset case are shown in Figures 3.17 and 3.18, respectively. The four switching conditions listed in Table 3.1 are evaluated for the simulation. The relation between the maximal output admissible set and the four switching conditions is shown in Figure 3.16. For the initialization using IVC, it is shown in Figure 3.17 that the constraint on the control input is fulfilled when the switching conditions are contained within the maximal output admissible set. For all switching conditions, the transient response of the positioning error is good. On the other hand, only switching condition 1 is contained within the maximal output admissible set for initialization using zero reset, and the results in Figure 3.18 show that the constraint on the control input is fulfilled only for switching condition 1. However, even when the switching condition is contained within the maximal output admissible set, the positioning error does not have a good transient response, i.e., an overshoot occurs.

The experimental results for the initialization using IVC are shown in Figure 3.19. Switching condition 2 listed in Table 1 is used. Figure 3.19(a) is a plot of the entire control input waveform, Figure 3.19(b) is a close-up of Figure 3.19(a), and Figure 3.19(c) is a plot of the positioning error waveform

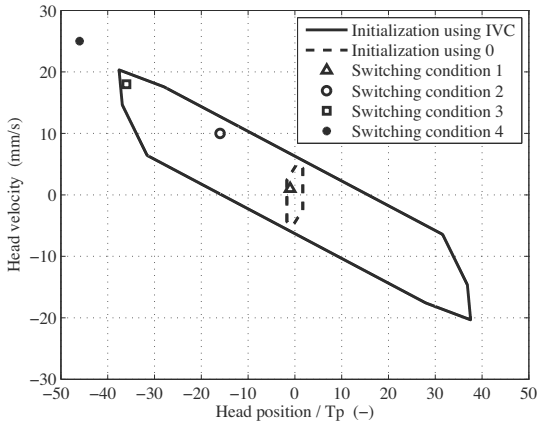

FIGURE 3.16
Maximal output admissible sets.

after switching from the seeking mode to the settling mode. The average, maximum, and minimum positioning error waveforms in a 200-times experiment are plotted. The constraint on the control input is fulfilled and the transient response of the positioning error is good.

TABLE 3.1
Switching Conditions

Switching conditions	Head position (Track)	Head velocity (mm/s)
1	–1	1
2	–16	10
3	–36	18
4	–46	25

3.4 Industrial Applications 1 (IVC for Mode Switching)

3.4.1 HDD (Reduction of Acoustic Noise)

In an HDD, the importance of acoustic-noise reduction has been increasing. Acoustic noise in an HDD can be categorized into two major components, namely, idle noise and seek noise. Seeking noise occurs intermittently during seeking operation. The driving force which moves the head is generated by

supplying a current to the VCM. When the VCM moves the head, mechanical vibrations may occur in the HDD depending on the waveform of the VCM force. These vibrations spread to the top cover. It is considered that the vibration of the top cover in contact with external air is the main cause of seeking noise. Therefore, to reduce the seeking noise, it is necessary to optimize the seeking current. In particular, discontinuous switching from mode switching control excites the mechanical resonant modes and increases the acoustic noise. Thus, an example of switching condition design which is based on the IVC method and reduces seek noise is explained [2, 3].

The block diagram of the model-following control system for the settling mode is shown in Figure 3.20. P is the plant, P_0 is the plant model, C is a following controller, C_0 is a settling controller, $u_0 \in \mathcal{R}$ is the control input, $y_0 \in \mathcal{R}$ is the controlled variable which is the head position, and $r \in \mathcal{R}$ is the reference. The discrete-time state-space equations of the plant model P_0 and the settling controller C_0 are represented as

$$P_0 : \begin{cases} x_{p0}[k+1] = A_{p0}x_{p0}[k] + B_{p0}u_0[k] \\ y_0[k] = C_{p0}x_{p0}[k] \end{cases}, \tag{3.93}$$

$$C_0 : \begin{cases} x_{c0}[k+1] = A_{c0}x_{c0}[k] + B_{c0}(r[k] - y_0[k]) \\ u_0[k] = C_{c0}x_{c0}[k] + D_{c0}(r[k] - y_0[k]) \end{cases}, \tag{3.94}$$

where $x_{p0} \in \mathcal{R}^{n\times 1}$ is a state vector of the plant, $x_{c0} \in \mathcal{R}^{m\times 1}$ is a state vector of the settling controller, A_{p0}, B_{p0}, and C_{p0} are real matrices of the plant model with appropriate dimensions, and A_{c0}, B_{c0}, C_{c0}, and D_{c0} are real matrices of the settling controller with appropriate dimensions. During mode switching from seeking mode to settling mode, the model-following control operates as follows: (1) IVC is applied to the settling controller C_0; (2) The initial state of the following controller C is set to zero; and (3) The initial state of the plant model P_0 is set to the initial state $x_p[0]$ of the actual plant. Consequently, when the mode switches from settling mode to following mode, the controller remains switched on. Therefore, mode switching is carried out once from the seeking mode to the settling mode.

To reduce the seeking noise, it is necessary to reduce the impulse-like current at mode switching. Therefore, a cost function for the J-min-type IVC is defined as

$$\begin{aligned} J &= \sum_{k=0}^{\infty} u_0^2[k] \\ &= \sum_{k=0}^{\infty} \begin{bmatrix} x_{p0}^T[k] & x_{c0}^T[k] \end{bmatrix} Q \begin{bmatrix} x_{p0}[k] \\ x_{c0}[k] \end{bmatrix}, \end{aligned} \tag{3.95}$$

where

$$Q = \begin{bmatrix} -D_{c0}C_{p0} & C_{c0} \end{bmatrix}^T \begin{bmatrix} -D_{c0}C_{p0} & C_{c0} \end{bmatrix}. \tag{3.96}$$

In order to achieve the effects of the IVC method, the design of switching

conditions is also carried out. By using the IVC method, the initial state of the settling controller is produced by the initial state of the plant. Thus, the state of the closed-loop system only becomes the state of the plant and therefore, the switching conditions are simple. In addition, velocity control is performed so that the acceleration may be set to zero at the termination of the seeking mode. As a result, in terms of the state variables of the plant, the deciding of the switching condition from seeking mode to settling mode is the problem of finding an optimal combination of position and velocity.

The design of the switching conditions is performed using the following procedures: (1) The index for evaluating the control purpose is set up. The trade-off between the peak value of operation current (which is an important factor in the reduction of acoustic noise during seek), the overshoot of the head position, and the settling-time after mode switching is considered; (2) The initial states which are guaranteed to satisfy the constraints given to each evaluation index are calculated; and (3) According to the calculated initial state sets, the switching conditions are determined with consideration for the trade-off of each evaluation index.

The initial state sets that meet their individual constraint condition on the current peak value *cp* are shown in Figure 3.21. Figure 3.21(a) is a plot for the pole-zero-type IVC for comparison, and Figure 3.21(b) is a plot for the J-min-type IVC. The horizontal axis represents the head position normalized by the track-pitch which is denoted as Tp, and the vertical axis represents the head velocity. The origin of the horizontal axis represents the target track position. For instance, –10 of the horizontal axis shows the position of 10 tracks forward from the target track. By using the J-min-type IVC technique, the safe region where the current peak value is reduced is expanded. The switching conditions can be chosen from within the safe region.

The initial state sets that meet their individual constraint condition on the overshoot *os* are shown in Figure 3.22. Both the pole-zero-type IVC and the J-min-type IVC have a large safe region where the overshoot of the head position is reduced to 10% or less of the track pitch.

Figure 3.23 shows the initial state sets that meet their individual constraint condition on the settling time *st* which is defined as the time required for the positioning error to converge to less than 10% of the track pitch. The safe region where the constraint on the settling time is fulfilled is small for both the pole-zero-type IVC and the J-min-type IVC. From the perspective of reducing acoustic noise, J-min type IVC may have broader alternatives in designing IVC.

The experimental results for the pole-zero-type IVC and the J-min-type IVC are shown in Figures 3.24 and 3.25, respectively. Figures 3.24(a) and 3.25(a) are plots of operation current, and Figures 3.24(b) and 3.25(b) are plots of sound pressure normalized by its maximum value. The switching condition is determined in consideration of the calculated initial state sets, which is given by a position of 16 tracks forward from the target track and a velocity of 10 mm/s. By using the J-min-type IVC with the optimal switching

condition, the impulse-like current at mode switching is reduced and therefore, the sound pressure is also reduced.

3.4.2 Robot (Personal Mobility Robot)

3.4.2.1 Introduction

Recently, several types of Personal Mobility Robot (PMR) for our aging society are being developed to travel a short distance [39]. The PMR shown in Figure 3.26 is a wheeled inverted pendulum type mobility robot which can travel and control its posture using two driven wheels. Also, there is a joystick as a human-machine interface, a gyro sensor to control its posture, a seat, a pair of assist wheels, and a footrest. Wheeled inverted pendulum type mobility has various advantages in traveling performance as compared to electric wheelchair type mobility whose four wheels are always in contact with the ground. For example, the PMR can turn about a point and can maintain the same seat posture even on a slope. However, the PMR also has its disadvantages. Wheeled inverted pendulum type mobility must be stabilized by a feedback controller in order to maintain the posture of the body. Furthermore, the body is easily swung, no matter what the controller is. Therefore, the PMR must be steadied by additional assist wheels on the ground when a driver mounts, dismounts, or works from the PMR. In order to accomplish both of the above tasks, the traveling mode of the PMR must be switched between the four-wheel mode and the wheeled inverted pendulum mode depending on the situations [40].

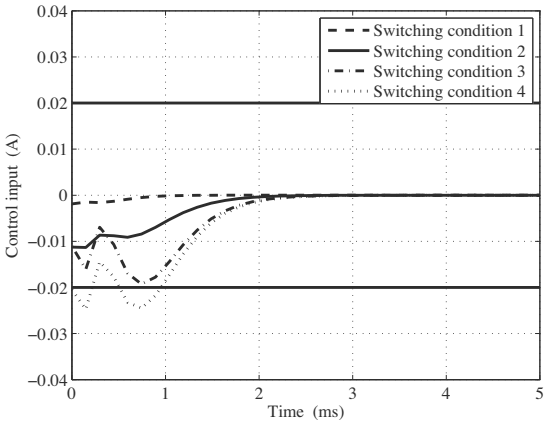

(a) Control input

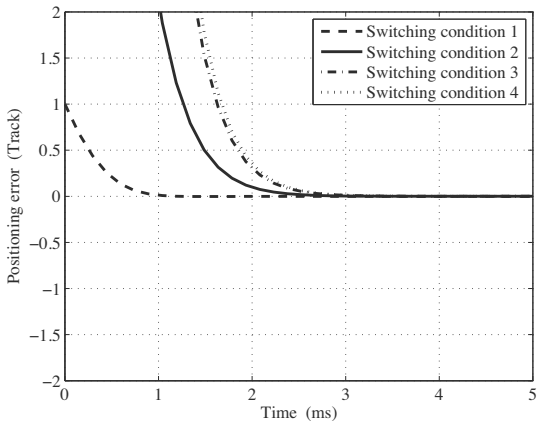

(b) Positioning error

FIGURE 3.17
Simulations results for initialization using IVC.

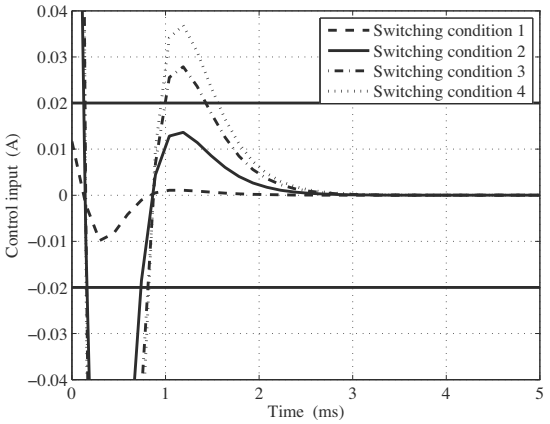

(a) Control input

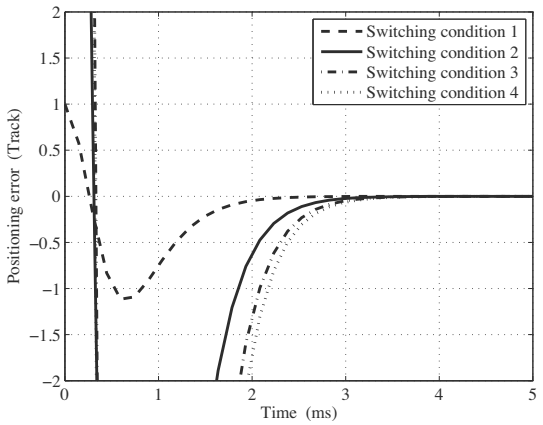

(b) Positioning error

FIGURE 3.18
Simulation results for initialization using zero reset.

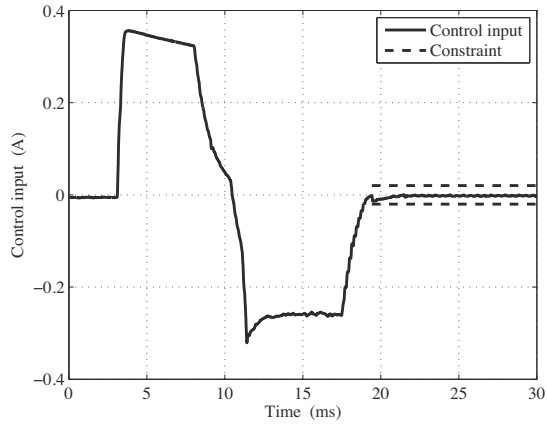

(a) Control input

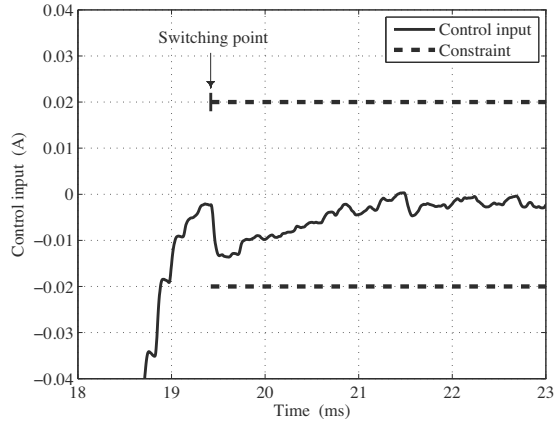

(b) Close-up of (a)

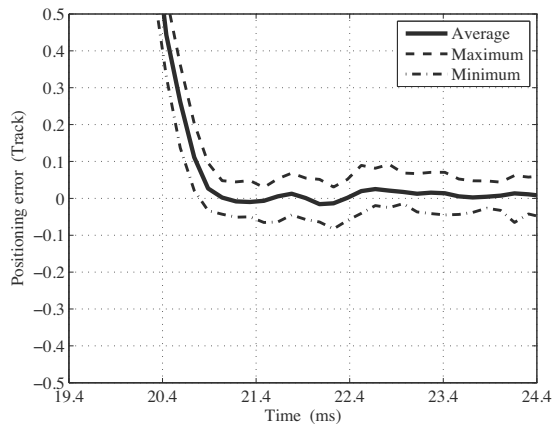

(c) Positioning error after switching

FIGURE 3.19
Experimental results for initialization using IVC.

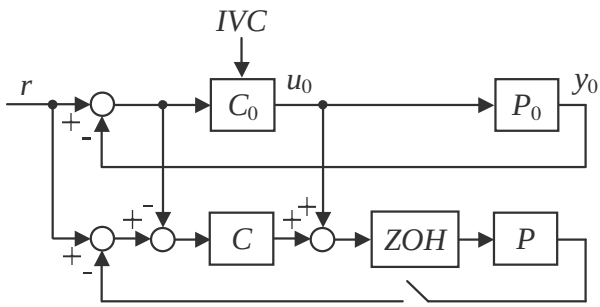

FIGURE 3.20
Block diagram of model-following control system with IVC.

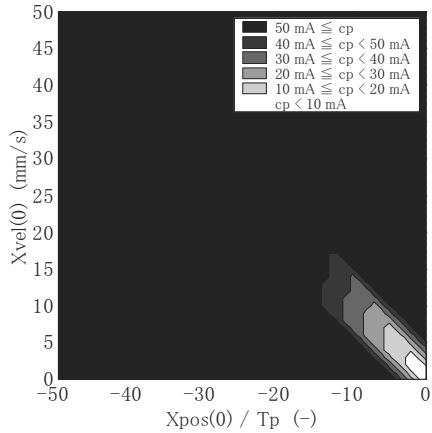

(a) pole-zero-type IVC

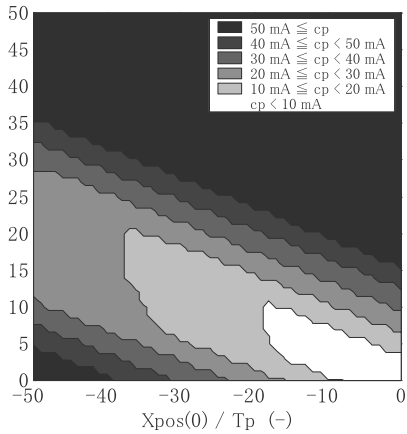

(b) J-min-type IVC

FIGURE 3.21
Initial state sets that meet their individual constraint condition on the current peak value *cp*.

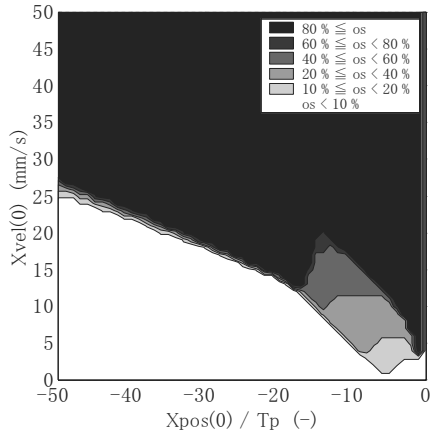

(a) pole-zero-type IVC

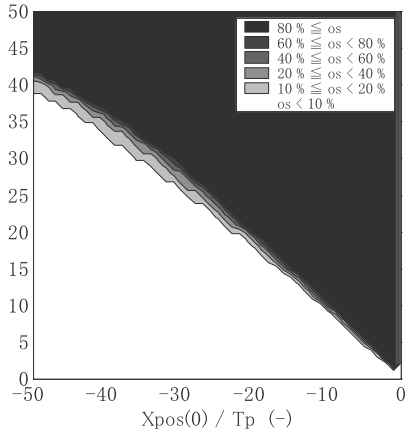

(b) J-min-type IVC

FIGURE 3.22
Initial state sets that meet their individual constraint condition on the overshoot *os*.

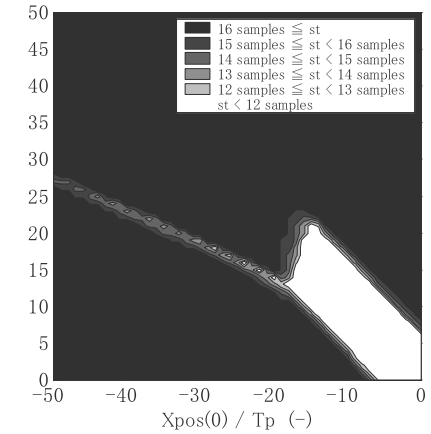

(a) pole-zero-type IVC

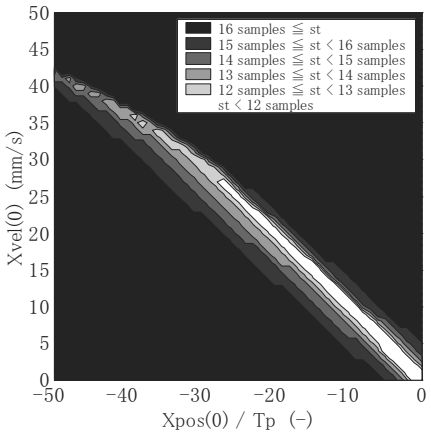

(b) J-min-type IVC

FIGURE 3.23
Initial state sets that meet their individual constraint condition on the settling time *st*.

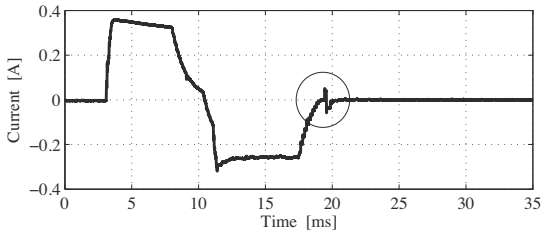

(a) Current

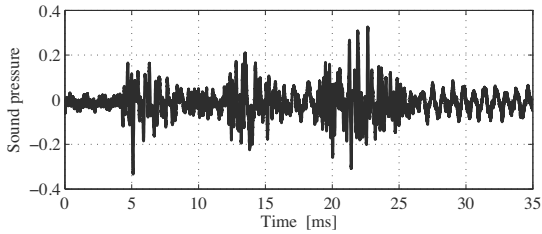

(b) Sound pressure

FIGURE 3.24
Experimental results for pole-zero-type IVC.

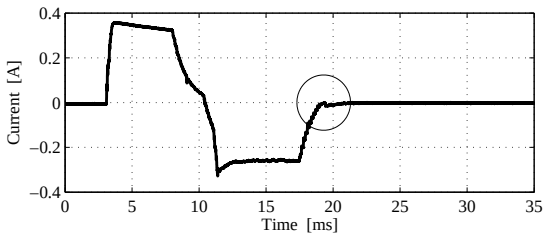

(a) Current

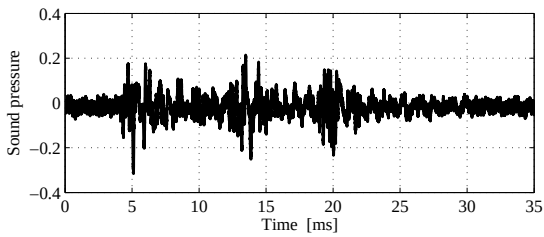

(b) Sound pressure

FIGURE 3.25
Experimental results for J-min-type IVC.

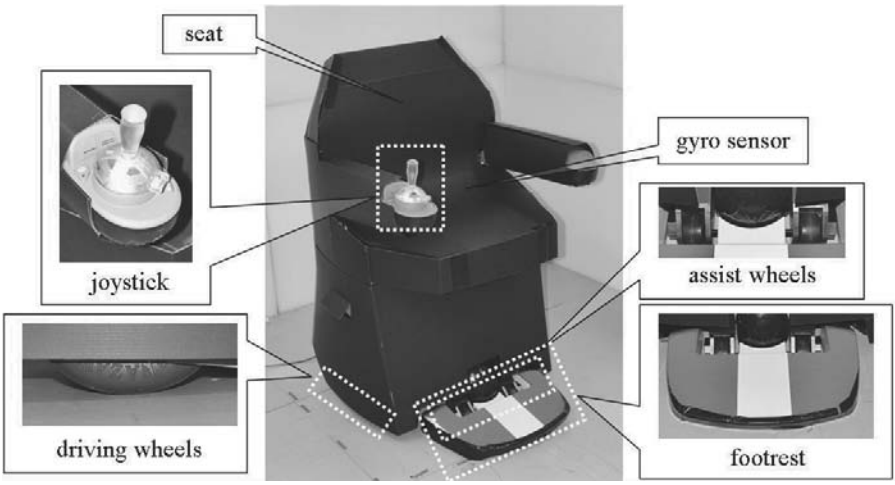

FIGURE 3.26
Configuration of prototype PMR.

An example of a transition from the four-wheel mode to the wheeled inverted pendulum mode is shown in Figure 3.27. In Figure 3.27(a), the PMR rests on four wheels to allow mounting, dismounting, or work to be carried out safely while sitting down. In this transition example, the PMR accelerates to raise the two front assistant wheels as shown in Figure 3.27(b). Next, its wheelie-like state is detected by the internal gyroscope. Based on this detection, the feedback controller for the wheeled inverted pendulum mode stabilizes its posture. As a result, the PMR can travel safely. From the above examinations, the three important issues that should be solved to realize the transition are as follows:

(a) To design an acceleration pattern to raise the assistant wheels;

(b) To distinguish whether the assistant wheels are in contact with the ground or not; and

(c) To smoothly switch to the feedback controller.

For (c), an appropriate initial value of the feedback controller for the wheeled inverted pendulum mode should be designed and given to improve the ride quality during switching. Therefore, the IVC presented in Section 3.3.1 is applied to achieve the required specifications. In addition, simple solutions are given for (a) and (b) in this section. For (a), a stepwise torque reference is generated. Its amplitude is given as a sufficient value to raise the assistant wheels independent of the driver. For (b), the state of the PMR is determined by the threshold of inclination angle $\eta = 0.05$ rad for the PMR.

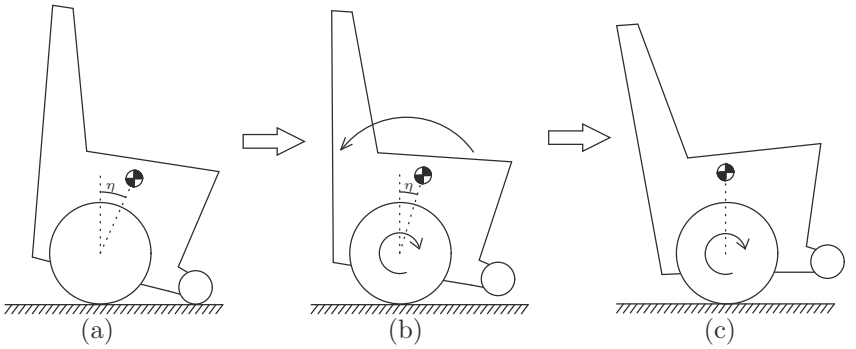

FIGURE 3.27
Transition from four-wheel mode to wheeled inverted pendulum mode.

3.4.2.2 Mathematical Model

The basic model for the wheeled inverted pendulum mode is shown in Figure 3.28. Using the Lagrange equation of motion, the mathematical model for the wheeled inverted pendulum mode can be formulated as

$$\begin{aligned}(M_b l^2 + J_b + n^2 J_m)\ddot{\eta}(t) &+ (M_b r_w l - n^2 J_m)\ddot{\theta}(t) \\ -M_b g l \sin\eta(t) &+ f_r(\dot{\eta}(t) - \dot{\theta}(t)) = -n\tau(t), \\ \\ (M_b r_w l - n^2 J_m)\ddot{\eta}(t) &+ ((M_b + M_w)r_w^2 \\ +J_w + n^2 J_m))\ddot{\theta}(t) &- M_b l r_w \dot{\eta}(t)^2 \sin\eta(t)\eta(t) \\ &- f_r(\dot{\eta}(t) - \dot{\theta}(t)) = n\tau(t),\end{aligned} \tag{3.97}$$

where M_w, J_w, and r_w are the weight, inertia, and radius of each driven wheel, respectively, J_m is the inertia of the motor, n is the gear ratio, M_b and J_b are the total weight and total inertia of the human and the PMR without the driven wheels, respectively. The human together with the PMR without the driven wheels is referred to as the upper body, and l in (3.97) is the distance between the axle and the center of gravity of the upper body, θ is the angle of the driven wheel, η is the inclination angle of the upper body, f_r is the viscosity coefficient, and g is acceleration of gravity. In order to apply IVC to this system, (3.97) can be linearized under the assumption of $\eta(t) \ll 1$, and it is given by

$$\begin{aligned}(M_b l^2 + J_b + n^2 J_m)\ddot{\eta}(t) &+ (M_b r_w l - n^2 J_m)\ddot{\theta}(t) \\ -M_b g l \eta(t) &+ f_r(\dot{\eta}(t) - \dot{\theta}(t)) = -n\tau(t), \\ \\ (M_b r_w l - n^2 J_m)\ddot{\eta}(t) &+ ((M_b + M_w)r_w^2 \\ +J_w + n^2 J_m))\ddot{\theta}(t) &- f_r(\dot{\eta}(t) - \dot{\theta}(t)) = n\tau(t).\end{aligned} \tag{3.98}$$

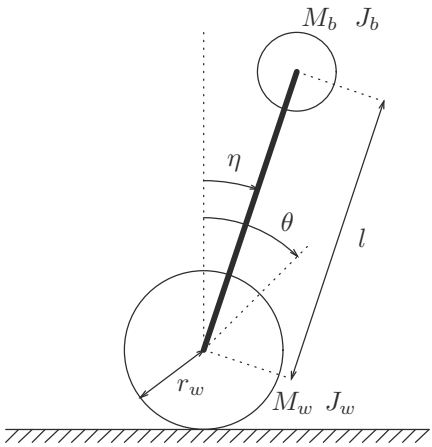

FIGURE 3.28
Model of wheeled inverted pendulum mode of PMR.

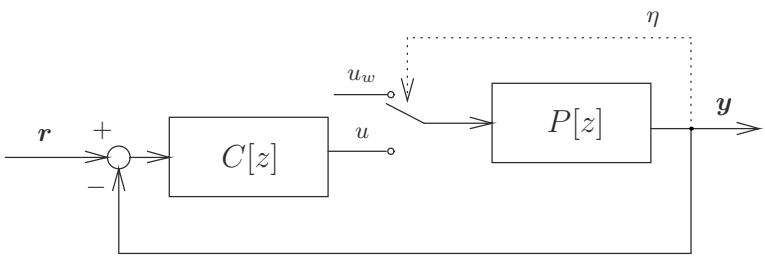

FIGURE 3.29
Block diagram of switching control system for making transition between the four-wheel mode and the wheeled inverted pendulum mode.

The block diagram of the switching control system for making the transition from the four-wheel mode to the wheeled inverted pendulum mode is shown in Figure 3.29. Over here, $P[z]$ is the transfer function from torque input $u = n\tau$ for the driving wheels to $y = [\eta[k]\ \dot{\eta}[k]\ \dot{\theta}[k] - \dot{\eta}[k]]^T$, $C[z]$ is a fifth-order feedback compensator designed by H_∞ control framework to stabilize the unstable plant system $P[z]$, r is the reference for y, and u_w is the torque input for the four-wheeled mode.

3.4.2.3 Design of IVC

The order of the feedback compensator $C[z]$ is enough to improve the transient responses by mode switching with the IVC in Section 3.3.1. The initial value $x_c[0]$ for the feedback compensator $C[z]$ can be optimized by the minimization

of the following cost function J given by [33]

$$J = J_s + q_u J_u + q_j J_j, \tag{3.99}$$

where J_s is a cost function for converging the state values to those at steady state, J_u is a cost function for decreasing the amplitude of the control input, J_j is a cost function for suppressing the jerk component, and q_u and q_j are the weighting coefficients for each cost function. This cost function can be derived as the square of $x_c[0]$. The appropriate initial value $x_c[0]$ can be given as

$$x_c[0] = K_a x_p[0] + K_b r + K_c u_w, \tag{3.100}$$

where $x_p[0]$ is the initial value of $P[z]$, and K_a, K_b, and K_c are the matrix coefficients designed by minimizing J. As a result, the transient responses can be improved only by providing the designed $x_c[0]$ for the feedback compensator $C[z]$ during switching [33].

3.4.2.4 Experimental Results

The experimental results with and without the IVC are shown in Figure 3.30, in which a driver actually mounts a prototype of the PMR. Figure 3.30(a) shows the waveforms of motor velocity $\dot{x} = \dot{\theta} - \dot{\eta}$, Figure 3.30(b) shows the waveforms of inclination angle η, Figure 3.30(c) shows the waveforms of inclination angular velocity $\dot{\eta}$, and Figure 3.30(d) shows the waveforms of control input τ. The horizontal dotted line in Figure 3.30(a) indicates the target value of the motor velocity which corresponds to 1.0 km/h. In Figures 3.30(a)–(d), the vertical dashed lines indicate the switching time of the feedback controller, which is defined as 0 s. Before switching, a stepwise control input is given to accelerate the PMR and lift the assist wheels. Therefore, the inclination angle η shown in Figure 3.30(b) decreases and reaches the threshold value $\eta = 0.05$ which is used to determine whether the assist wheels are in contact with the ground or not. After switching, the gray lines in Figures 3.30(a)–(c) indicate that without IVC, there are large overshoot and undershoot in the responses of the motor velocity, the inclination angle, and the inclination angular velocity. In addition, the control input τ suddenly decreases and reaches -20 Nm just after switching, after which τ increases to $+20$ Nm with an oscillatory response.

On the other hand, it is shown by the solid lines that with IVC, all transient responses converge smoothly to their steady states without overshoot or undershoot, while the amplitude and jerk component of the control input are suppressed.

In order to evaluate the ride quality of the proposed approach, the accelerations of the driver's head in both horizontal and vertical directions are detected by acceleration sensors. The waveforms of the acceleration in both horizontal and vertical directions are shown in Figure 3.31. Figure 3.31(a) shows that the maximum value of acceleration in the horizontal direction is 7.0 m/s^2 without IVC, while acceleration in the horizontal direction is suppressed to within

± 2.0 m/s^2 with IVC. Furthermore, the acceleration in the vertical direction can also be improved by IVC. These experimental results demonstrate that IVC can provide a more comfortable transition for the driver.

3.4.3 Optical Disk Drive

The optical disk drive shown in Figure 3.32 is a disk drive that uses laser light for reading or writing data to or from the optical disk. The optical disk drive structure includes an optical pickup head, a sled to carry the head, a sled motor to move the sled, and a spindle motor to rotate the optical disk. There are two servo controls. One of the servo controls is known as the focus servo, and it maintains a correct distance between the lens and the disk, and ensures that the laser beam is focused on a small laser spot on the disk. The other servo control is known as a tracking servo, and it moves the optical pickup head onto a target track of the optical disk.

As optical disk drives have been widely used in various applications, their servo systems must be made more robust. Various control technologies have been studied [43, 44], and one of the simple and effective controllers is the high-gain servo controller with complex zeros [42], which is the same second-order controller as the conventional controller. The high-gain servo controller can realize a much higher gain with the same servo bandwidth, and contributes to making the servo system more robust. The controller has been applied to the focus servo of Blu-ray disc drives, and it has been verified to decrease the servo error and improve the resistance to vibration. IVC has also been applied to this high-gain servo controller to suppress the overshoot in initial value responses. This design and application was done by Yoshiyuki Urakawa [31, 32].

Using the state-space expression of the entire servo system, the initial responses are expressed as

$$y(t) = L^{-1}[C(sI - A)^{-1}]x(0), \tag{3.101}$$

where A and C are coefficient matrices of the state equation of the servo control system. The initial value of the state variable $x(0)$ is expressed as $[x_{c1}(0)x_{c2}(0)y(0)v(0)]^T$, where $x_{c1}(0)$ and $x_{c2}(0)$ are the initial values of the controller, $y(0)$ is the initial value of the position of the actuator of the servo system, and $v(0)$ is the initial value of the velocity of the actuator. This means that the initial values $x_{c1}(0)$ and $x_{c2}(0)$ of the controller affect the initial response. Therefore, if the initial values $x_{c1}(0)$ and $x_{c2}(0)$ of the controller are set as

$$\begin{bmatrix} x_{c1}(0) \\ x_{c2}(0) \end{bmatrix} = \alpha \begin{bmatrix} y(0) \\ v(0) \end{bmatrix}, \tag{3.102}$$

where α matrix is calculated using

$$Cadj(sI - A) \begin{bmatrix} \alpha \\ I \end{bmatrix}_{s=s_1,s_2} = 0, \tag{3.103}$$

the zeros of the initial response can be assigned to s_1 and s_2 which are identical to the undesirable poles of the closed-loop system by applying the pole-zero-type IVC.

The IVC is applied to the focus servo system of the experimental setup, which is shown in Figure 3.33. The α matrix is set as

$$\alpha = \begin{bmatrix} 1.6940e4 & 1.0276e{-}1 \\ 3.1543e5 & -8.4265 \end{bmatrix} \tag{3.104}$$

to assign zeros at $z = 0.96416$ and $z = 0.95975$ which are undesirable poles of the closed-loop system. Experimental and simulation data are shown in Figures 3.34 and 3.35 for six initial position conditions which are ±78 nm, ±39 nm, and 0 nm. The initial responses of the focus error signals without IVC are shown in Figure 3.34. These data are measured without rotating the disk so that noise from disk rotation can be removed. The initial responses with IVC are shown in Figure 3.35, where it can be observed that overshoots are well suppressed by IVC.

3.5 Industrial Applications 2 (IVC for reference switching)

3.5.1 Galvano Mirror for Laser Drilling Machine

3.5.1.1 Introduction

In the case of a repetitive positioning process with a short interval, the controller should be designed with consideration for initial value responses, since the initial state values still remain in the feedback control system at the beginning of the next positioning and deteriorate the settling performance.

Galvano scanner for laser drilling machines is an example of industrial positioning devices that require the fast and precise positioning properties of the galvano mirror for repetitive motion with a short interval. The configuration of the galvano scanner which comprises of a servo motor with a galvano mirror is shown in Figure 3.36. The galvano scanner for laser drilling machines reflects laser pulses to the desired position on printed circuit boards by positioning the angle of the mirror. In order to control the galvano scanner, the detected sensor angle is transferred to a DSP controller through an interface with a sampling period of 20 μs. The servo motor is driven by a current controlled amplifier with the current reference i_{ref} generated by the position controller. In the system, as stated above, the next position reference is given although the initial state values such as the residual vibration components during the settling of the previous positioning still remain, especially when the positioning interval is shortened.

Therefore, in this section, the IVC using additional input presented in

Section 3.3.2 is applied to improve the positioning accuracy of the repetitive motion with the shortened interval period.

3.5.1.2 Mathematical Model

The galvano scanner can be modeled by a multi-mass body system whose frequency response characteristic from the current reference i_{ref} to the motor angle y_s is shown by the solid lines in Figure 3.37. From the figure, it can be observed that the mechanism includes the first vibration mode at 3020 Hz, the second vibration mode at 6240 Hz, other vibration modes in the high-frequency range, and a dead-time component due to the current control delay, thus affecting the positioning performance. The nominal plant model $P(s)$ consists of a rigid mode, vibration modes up to $k = 2$, and the dead-time component. $P(s)$ is formulated as a polynomial given by

$$P(s) = \frac{y_s(s)}{i_{ref}(s)} = e^{-Ls} \cdot K_p \left(\frac{1}{s^2} + \sum_{k=1}^{2} \frac{K_k}{s^2 + 2\zeta_{nk}\omega_{nk}s + \omega_{nk}^2} \right), \tag{3.105}$$

where K_p is a gain which includes the moment of inertia and torque constant of the motor, ω_{nk}, ζ_{nk}, K_k are the natural angular frequency, damping coefficient, and gain of the k^{th} vibration mode, respectively, and L is the equivalent dead time which is 15.5 μs. The frequency response characteristic of the nominal model $P(s)$ is shown by the dashed lines in Figure 3.37. From the figure, it can be observed that the dashed line coincides well with the measured solid line for both gain and phase characteristics.

The desired control specification is given as a point-to-point positioning with a settling time of 0.9 ms for a typical position reference amplitude of 1.5 mm which is the equivalent displacement on the printed circuit board for the motor angle. This settling time corresponds to the achievement of a higher servo bandwidth that is above one-third of the frequency of the first vibration mode, and requires a fast and precise positioning performance with resonant vibration suppression, robust system stabilization, and dead-time compensation. In order to realize the above specification, the feedback controller is designed as an Integral-Proportional-Derivative (I-PD) compensator with two notch filters to attenuate the first and second vibration modes [35]. The waveform of the experimental position error $(x_r - y_s)$ is shown by the solid line in Figure 3.38, where a position reference with amplitude of x_r =1.5 mm is given. The I-PD controller with the two notch filters achieves the desired positioning with the specified settling-time performance of 0.9 ms, while the experimental waveform of the position error includes a residual vibration after reaching the target position, which depends on the first vibration mode. On the other hand, a numerical simulated waveform for the same motion is shown in Figure 3.38. These two waveforms coincide well, proving the effectiveness of the mathematical plant model $P(s)$ in (3.105) for the following IVC design.

It is important for the galvano scanner to provide the desired fast and precise positioning performance for arbitrary repetitive position references with short interval periods. Although the waveform for a single-reference motion can satisfy the control specification as shown in Figure 3.38, the expansion of the servo bandwidth excites the residual vibration corresponding to the first vibration mode, which directly affects the initial values and hence the settling characteristics of the next motion. Over here, the positioning performance is examined for a sequential back-and-forth positioning motion between 0 and 1.5 mm. An example of the experimental position error waveforms for the repetitive reference with the typical interval period of 1.5 ms is shown in Figure 3.39, where Figure 3.39(b) shows eight superimposed trials of the back-and-forth waveform. In Figure 3.39(b), the left waveforms correspond to the responses of the forward motion, and the right waveforms after 1.5 ms correspond to the responses of the backward motion. It should be noted that the thick line among the left waveforms in Figure 3.39(b) represents the response of the first motion with zero initial values, which satisfies the desired positioning. On the other hand, other waveforms in Figure 3.39(b) include scattered residual vibrations due to the undesirable initial values corresponding to the first vibration mode, which deteriorate the positioning accuracy. In addition, the experimental results with a shorter interval period of 1.16 ms are also shown in Figure 3.40. In the same way as that shown in Figure 3.39, the undesirable initial values lead to scattered residual vibrations after the second positioning.

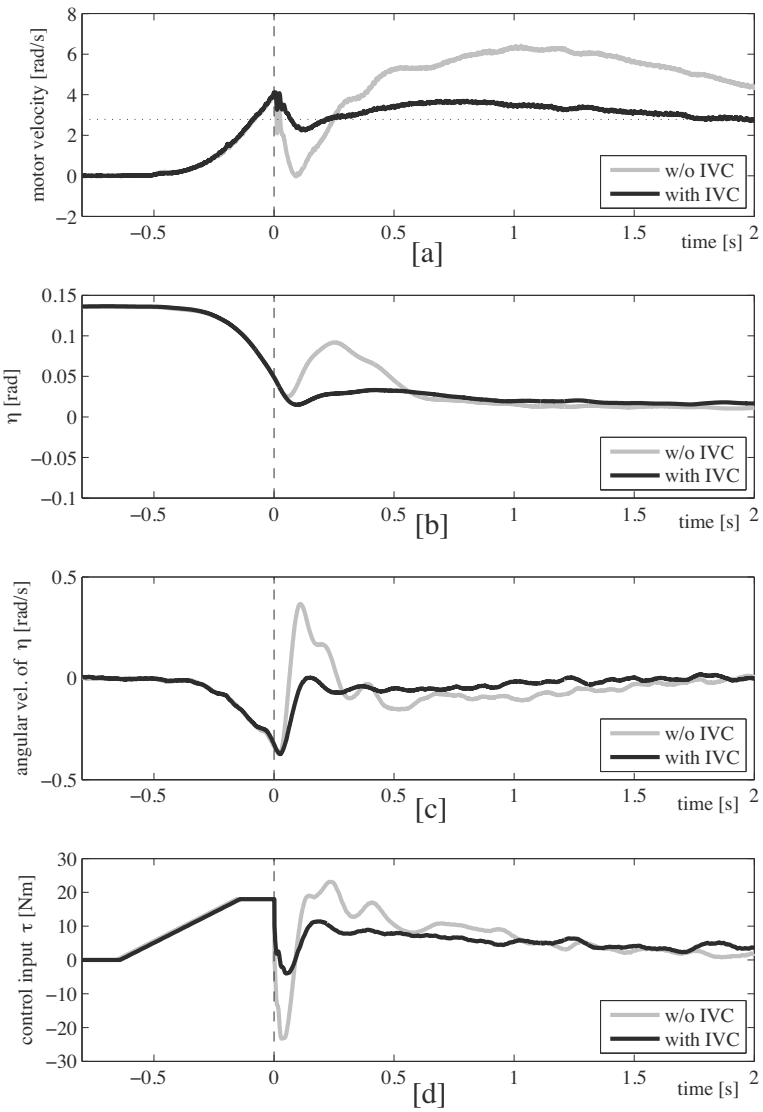

FIGURE 3.30
Experimental results with and without IVC.

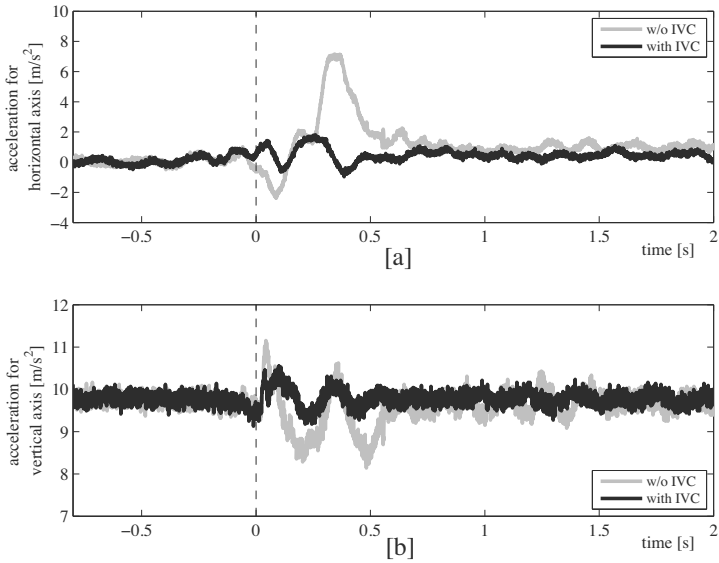

FIGURE 3.31
Experimental results for acceleration of driver's head.

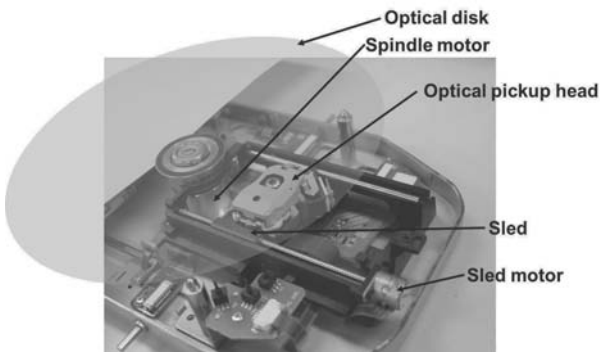

FIGURE 3.32
Schematic apparatus of an optical disk drive.

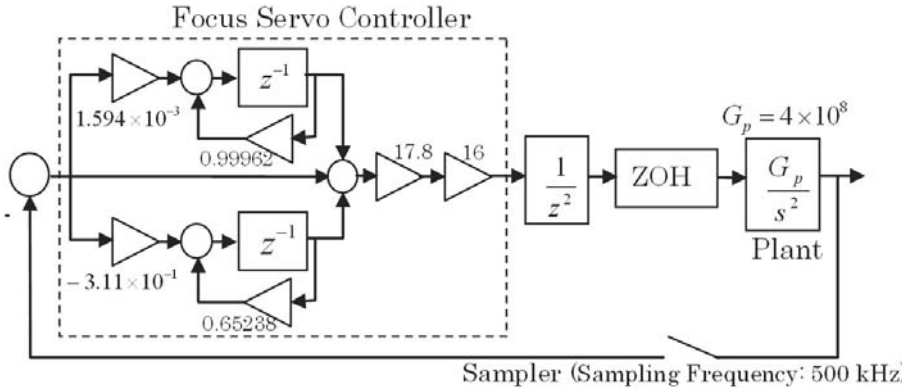

FIGURE 3.33
Focus servo system of the experimental setup with the high-gain servo controller [32].

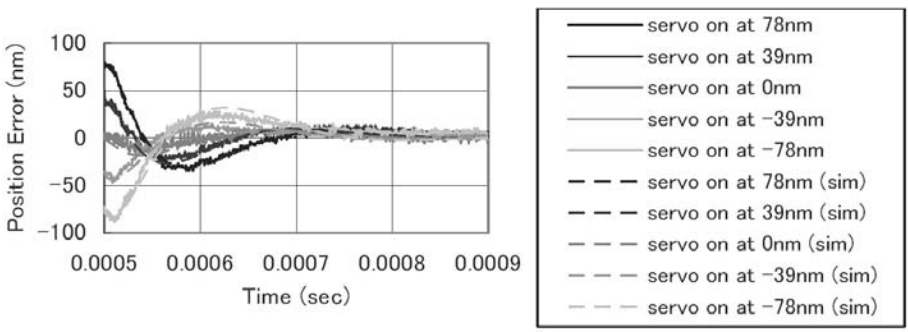

FIGURE 3.34
Initial responses of the focus servo system of the experimental setup without IVC [32].

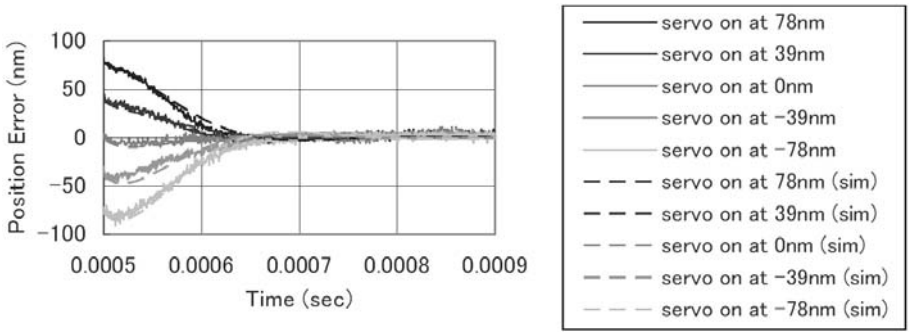

FIGURE 3.35
Initial responses of the focus servo system of the experimental setup with IVC [32].

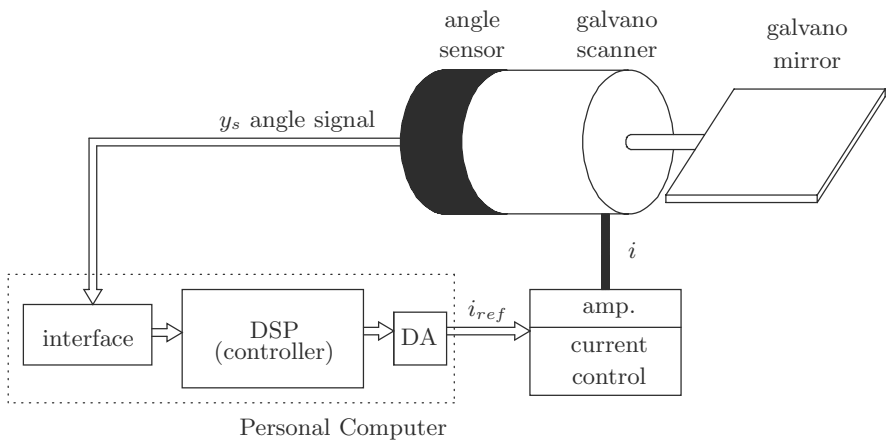

FIGURE 3.36
Configuration of experimental setup.

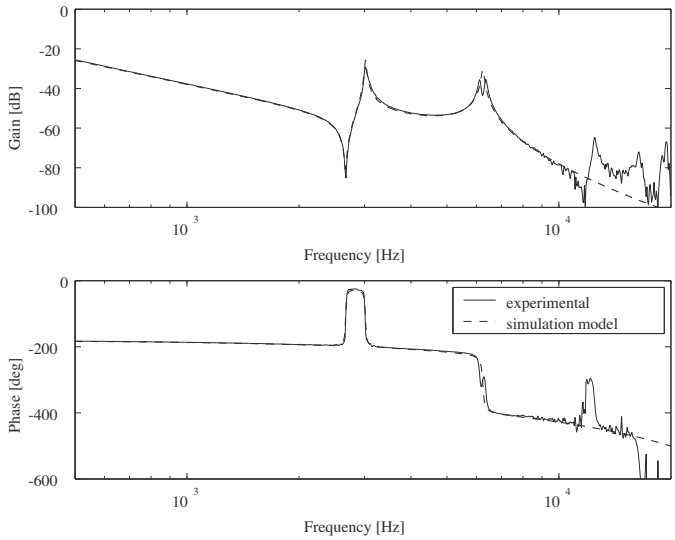

FIGURE 3.37
Frequency response of plant system from i_{ref} to y_s.

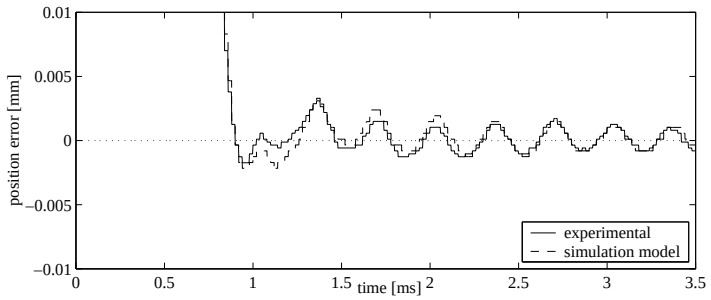

FIGURE 3.38
Experimental position error responses.

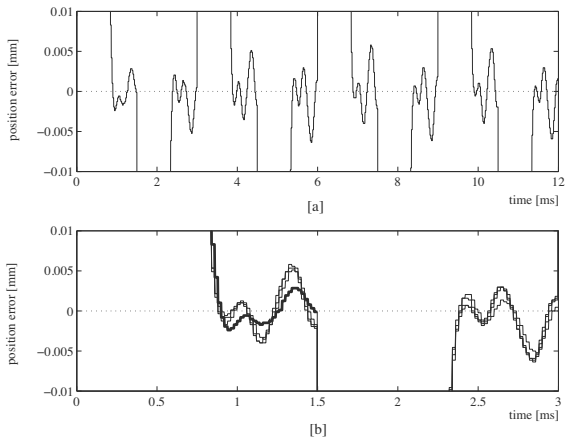

FIGURE 3.39
Experimental position error responses for a reference with an interval period of 1.50 ms.

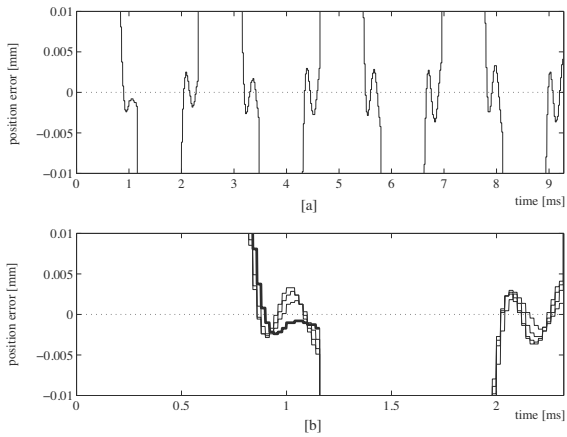

FIGURE 3.40
Experimental position error responses for a reference with an interval period of 1.16 ms.

3.5.1.3 Design of IVC

In order to suppress the residual vibration in the positioning of this setup, two initial values of position $x_{\theta 1}[0]$ and velocity $x_{\omega 1}[0]$ corresponding to the first vibration mode are selected to be compensated. Based on IVC, the additional input r' that is to be superimposed is given by

$$r'[z] = \frac{n_\theta[z]}{d[z]} x_{\theta_1}[0] + \frac{n_\omega[z]}{d[z]} x_{\omega_1}[0]. \tag{3.106}$$

Here, the initial value compensators $\frac{n_\theta[z]}{d[z]}$ and $\frac{n_\omega[z]}{d[z]}$ are designed using the IVC approach presented in Section 3.3.2. The design process of the polynomials $n_\theta[z]$, $n_\omega[z]$, and $d[z]$ is as follows.

The feedback control system includes 13 roots which should be canceled by the compensations. The compensators are designed as 12^{th}-order transfer functions to cancel the 13 roots by designing polynomials $n_\theta[z]$ and $n_\omega[z]$. In addition, $d[z]$ can be designed to assign alternative poles at 0.5, which correspond to frequencies higher than the inverse of the settling time which is 0.9 ms. According to Section 3.3.2, the polynomials $n_\theta[z]$ and $n_\omega[z]$ with 13 undetermined real coefficients can be determined to cancel all the roots of the control system.

The original poles and zeros in the transfer functions that relate the initial values $x_{\theta 1}[0]$ and $x_{\omega 1}[0]$ to the motor angle are shown in Figure 3.41. In this figure, '$\circ$' indicates a zero and '$\times$' indicates a pole. On the other hand, the assigned poles and zeros by applying the additional input r' in (3.106) are shown in Figure 3.42. The original poles are completely canceled by the reassignment of zeros, and the new desirable poles can be assigned by $d[z]$.

3.5.1.4 Experimental Results

The experimental position error waveforms with IVC for the same repetitive reference as shown in Figures 3.39 and 3.40 are shown in Figures 3.43 and 3.44. The ideal positioning performance can be achieved for all back-and-forth positioning without scattered responses. This performance improvement verifies the effectiveness of IVC.

3.6 Conclusion

Various kinds of motion control systems in mechatronic products including robots, HDDs, optical disk drives, laser drilling machines, and semiconductor/LCD manufacturing equipment, have in one continuous operation, several control objectives such as minimum time movement and precise stopping or positioning. Many control structures for achieving this motion control have been proposed, including a single-mode structure and a multi-mode structure

with switching. They have been applied to actual products to meet specific requirements of the products. Hence, it cannot be said which structure is superior in general. A multi-mode structure with switching is called MSC, and the detailed design methodology and application examples are shown in this chapter. The switching control theory is well known as a general theory. The focus of this chapter has been on the MSC which has a handover function from one mode to another, and which has been widely used in various industries that are mentioned above. It should be noted that state variables of the servo system are non-zero during mode switching in MSC. In general, when discrete events occur when a system is under an unsteady-state condition, an undesirable transient response is often observed after the occurrence of the discrete event when the system is designed based on the steady-state condition. The discrete events are not only mode switching, but also reference signal switching. Many control designs assume this steady-state condition as an initial condition. In this chapter, the IVC technique has been proposed for MSC to enhance the conventional control design based on steady state in order to improve the transient response.

Since the proposed IVC design has already been widely applied to HDDs, optical disk drives, laser drilling machines, and a personal mobility robot, the IVC is one of the quite effective design methods for controlling transient responses.

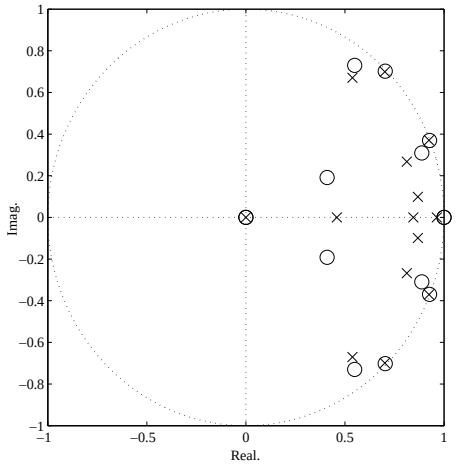

(a) initial value $x_{\theta_1}[0] \sim$ motor angle y_s

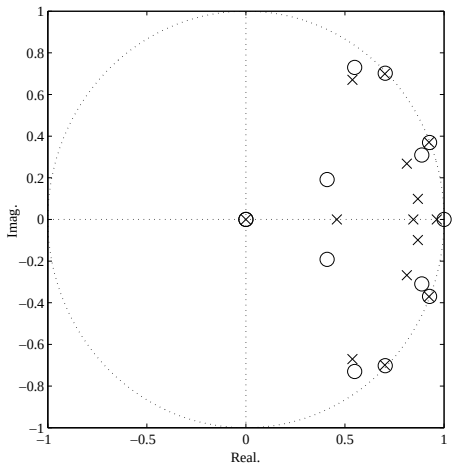

(b) initial value $x_{\omega_1}[0] \sim$ motor angle y_s

FIGURE 3.41
Pole-zero plots without IVC.

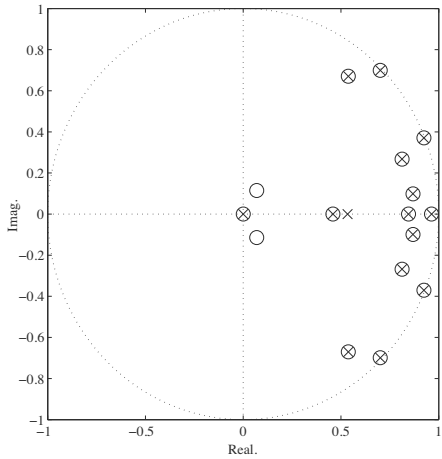

(a) initial value $x_{\theta 1}[0] \sim$ motor angle y_s

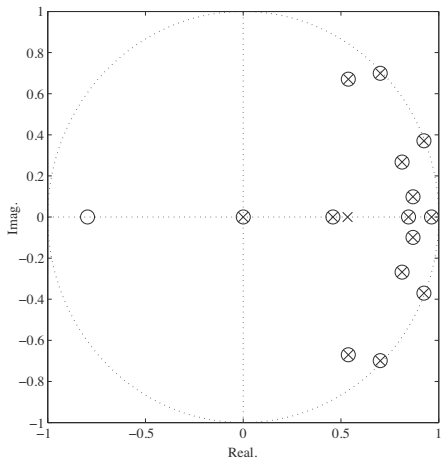

(b) initial value $x_{\omega 1}[0] \sim$ motor angle y_s

FIGURE 3.42
Pole-zero plots with IVC.

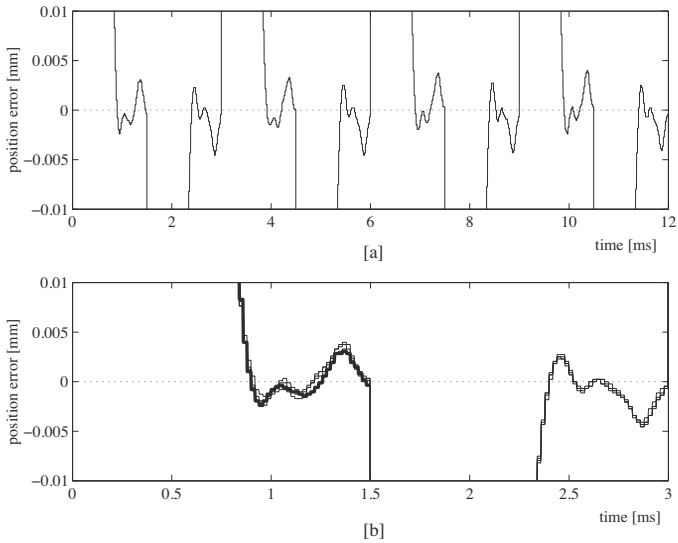

FIGURE 3.43
Experimental position error responses with IVC for a reference with an interval period of 1.50 ms.

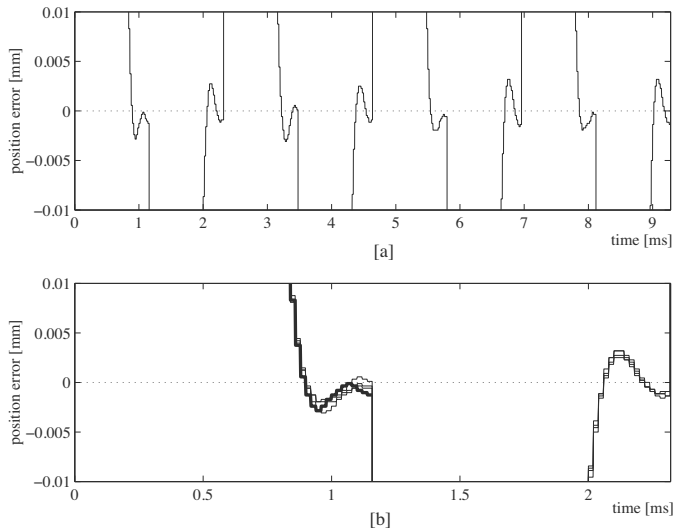

FIGURE 3.44
Experimental position error responses with IVC for a reference with an interval period of 1.16 ms.

Bibliography

[1] T. Yamaguchi, K. Shishida, H. Hirai, K. Tsuneta, and M. Sato, "Improvement of Servo Robustness for Digital Sector Servo System," *IEEE Transactions on Magnetics*, Vol. 28, No. 5, pp. 2910–2912, September 1992.

[2] A. Okuyama and T. Yamaguchi, "Controller Switching Strategy for Constrained Systems and its Application to Hard Disk Drives," in *Proceedings of the* 9^{th} *IEEE International Workshop on Advanced Motion Control*, pp. 143-148, Istanbul, Turkey, March 27–29, 2006.

[3] A. Okuyama and M. Kobayashi, "Controller-Switching Strategy for HDD Servo Systems with Measurement Errors and Constraints on State and Control Variables," in *Proceedings of the 2006 IEEE International Conference on Control Applications*, pp. 249–254, Munich, Germany, October 4–6, 2006.

[4] T. Yamaguchi, K. Shishida, S. Tohyama, and H. Hirai, "Mode Switching Control Design with Initial Value Compensation and its Application to Head Positioning Control on Magnetic Disk Drives," *IEEE Transactions on Industrial Electronics*, Vol. 43, No. 1, pp. 65–73, February 1996.

[5] T. Yamaguchi, Y. Soyama, H. Hosokawa, K. Tsuneta, and H. Hirai, "Improvement of Settling Response of Disk Drive Head Positioning Servo Using Mode Switching Control with Initial Value Compensation," *IEEE Transactions on Magnetics*, Vol. 32, No. 3, pp. 1767–1772, May 1996.

[6] K. Fuwa, T. Umemura, H. Kando, T. Yamaguchi, and H. Hirai, "Optimization Method of Initial Value Compensation for Mode Switching Control Systems," *IEEJ Transactions on Electronics, Information and Systems*, Vol. 125, No. 12, pp. 1844–1851, 2005 (in Japanese).

[7] T. Yamaguchi, S. Shishida, S. Tohyama, Y. Soyama, H. Hosokawa, H. Ohsawa, H. Numasato, T. Arai, K. Tsuneta, and H. Hirai, "A Mode-Switching Controller with Initial Value Compensation for Hard Disk Drive Servo Control," *Control Engineering Practice*, Vol. 5, No. 11, pp. 1525–1532, November 1997.

[8] T. Yamaguchi and H. Hirai, "Control of Transient Response on Servo System Using Mode-Switching Control and its Application to Magnetic

Disk Drives," *Control Engineering Practice*, Vol. 6, No. 9, pp. 1117–1123, September 1998.

[9] Y. Maeda, M. Wada, M. Iwasaki, and H. Hirai, "Improvement of Settling Performance by Mode Switching Control with Split Initial Value Compensation Based on Input Shaper," in *Proceedings of the 2011 IEEE International Symposium on Industrial Electronics (ISIE)*, pp. 905–910, Gdansk, Poland, June 27–30, 2011.

[10] N. Hirose, M. Iwasaki, M. Kawafuku, and H. Hirai, "Improvement of Computational Load in Initial Value Compensation with Additional Input," in *Proceedings of the 2007 IEEE International Symposium on Industrial Electronics (ISIE)*, pp. 3096–3101, Vigo, Spain, June 4–7, 2007.

[11] Y. Maeda, M. Wada, M. Iwasaki, and H. Hirai, "Improvement of Settling Performance by Mode-Switching Control with Split Initial-Value Compensation Based on Input Shaper," *IEEE Transactions on Industrial Electronics*, Vol. 60, No. 3, pp. 979–987, March 2013.

[12] N. Hirose, Y. Terachi, M. Kawafuku, M. Iwasaki, and H. Hirai, "Initial Value Compensation with Additional Input Considering Optimization of Control Input," *Electrical Engineering in Japan*, Vol. 175, No. 2, pp. 63–73, January 2011.

[13] M. Johansson, "Optimal Initial Value Compensation for Fast Settling Times in Mode-Switching Control Systems," in *Proceedings of the 39th IEEE Conference on Decision and Control*, Vol. 5, pp. 5137–5142, Sydney, Australia, December 12–15, 2000.

[14] Y. Li, Y. Sun, C. Smith, L. Guo, and W. Guo, "Optimization of Initial Value Compensation for Settle Control in Hard Disk Drives," *IEEE Transactions on Magnetics*, Vol. 41, No. 2, pp. 797–801, February 2005.

[15] T. Y. Doh and J. R. Ryoo, "A Linear Matrix Inequality Approach to Initial Value Compensation for Mode Switching Control in Hard Disk Drive Servo Systems," *IEEE Transactions on Magnetics*, Vol. 45, No. 9, pp. 3362–3364, September 2009.

[16] T. Yamaguchi, H. Numasato, and H. Hirai, "A Mode-Switching Control for Motion Control and its Application to Disk Drives, Design of Optimal Mode-Switching Conditions," *IEEE/ASME Transactions on Mechatronics*, Vol. 3, No. 3, pp. 202–209, September 1998.

[17] K. Eddy, J. Steele, and W. Messner, "Bias in Disk Drive Rotary Actuators, Characterization, Prediction, and Compensation," *IEEE Transactions on Magnetics*, Vol. 33, No. 3, pp. 2424–2436, May 1997.

[18] Y. Maeda and M. Iwasaki, "Improvement of Settling Performance by Initial Value Compensation Considering Rolling Friction Characteristic," in

Proceedings of the 36th Annual Conference on IEEE Industrial Electronics (IECON), pp. 1902–1907, Glendale, AZ, USA, November 7–10, 2010.

[19] Y. Maeda and M. Iwasaki, "Improvement of Settling Performance by Mode Switching Feedback Compensation in Fast and Precise Positioning," in *Proceedings of the 37th Annual Conference on IEEE Industrial Electronics (IECON)*, pp. 3406–3411, Melbourne, Australia, November 7–10, 2011.

[20] M. Iwasaki, M. Kawafuku, and H. Hirai, "2DOF Control-Based Fast and Precise Positioning Using Disturbance Observer," in *Proceedings of the 32nd Annual Conference on IEEE Industrial Electronics (IECON)*, pp. 5234–5239, Paris, France, November 7–10, 2006.

[21] Y. Huang and W. Messner, "A Novel Robust Time-Optimal Algorithm for Servo Systems with Bias Disturbance," *IEEE Transactions on Magnetics*, Vol. 34, No. 1, pp. 7–12, January 1998.

[22] R. Oboe and M. Federico, "Initial Value Compensation Applied to Disturbance Observer-Based Servo Control in HDD," in *Proceedings of the 7th International Workshop on Advanced Motion Control*, pp. 34–39, Maribor, Solvenia, July 3–5, 2002.

[23] Y. Maeda and M. Iwasaki, "Initial Friction Compensation by Disturbance Observer Based on Rolling Friction Model," in *Proceedings of the 35th Annual Conference on IEEE Industrial Electronics (IECON)*, pp. 3124–3129, Porto, Portugal, November 3–5, 2009.

[24] M. Hirata and M. Tomizuka, "Short Track Seeking of Hard Disk Drives Under Multirate Control-Computationally Efficient Approach Based on Initial Value Compensation," *IEEE/ASME Transactions on Mechatronics*, Vol. 10, No. 5, pp. 535–545, October 2005.

[25] M. Hirata and M. Tomizuka, "Multi-Rate Short Track-Seeking Control of Hard Disk Drives for Computation Saving," in *Proceedings of the 42nd IEEE Conference on Decision and Control*, Vol. 4, pp. 3420–3425, Maui, HI, December 9–12, 2003.

[26] L. Yang and M. Tomizuka, "A Novel Design of Short-Seeking Control for Hard Disk Drives," in *Proceedings of the 2006 American Control Conference*, pp. 588–593, Minneapolis, MN, USA, June 14–16, 2006.

[27] M. Teixeira, N. Silva, E. Assuncao, and E. Machado, "Design of Fuzzy Regulators with Optimal Initial Conditions Compensation," *IEEE International Conference on Fuzzy Systems*, pp. 84–91, Vancouver, BC, Canada, July 16–21, 2006.

[28] L. Guo, J. Chang, and H. Xiaoping, "Track-Following and Seek/Settle Control Schemes for High Density Disk Drives with Dual-Stage Actuators," in *Proceedings of the IEEE/ASME International Conference on Advanced Intelligent Mechatronics*, Vol. 2, pp. 1136–1141, Corno, Italy, July 8–12, 2001.

[29] D. Wu, G. Guo, and T. Chong, "Midfrequency Disturbance Suppression via Micro-Actuator in Dual-Stage HDDs," *IEEE Transactions on Magnetics*, Vol. 38, No. 5, pp. 2189–2191, September 2002.

[30] T. Ashitani, H. Takahashi, and M. Asakura, "Advanced Focus Capture Control for High NA Optical Storage System," in *Proceedings of the 2002 International Symposium on Optical Memory and Optical Data Storage Topical Meeting*, pp. 323–325, Waikoloa, HI, July 7–11, 2002.

[31] Y. Urakawa and Y. Suzuki, "High-Gain Servo Controller for Optical Disk Drives and the Initial Value Compensation," in *Proceedings of the 17th IFAC World Congress*, pp. 3116–3117, Seoul, Korea, July 6–11, 2008.

[32] Y. Urakawa and Y. Suzuki, "Effects of the High Gain Servo Controller and the Initial Value Compensation on Optical Disk Drive," in *Proceedings of the SPIE*, Vol. 6620, pp. 66200X-1–66200X-6, 2007.

[33] N. Hirose, K. Sukigara, H. Kajima, and M. Yamaoka, "Mode Switching Control for a Personal Mobility Robot Based on Initial Value Compensation," in *Proceedings of the 36th Annual Conference on IEEE Industrial Electronics (IECON)*, pp. 1914–1919, Glendale, AZ, USA, November 7–10, 2010.

[34] N. Hirose, M. Iwasaki, M. Kawafuku, and H. Hirai, "Initial Value Compensation Using Additional Input for Semi-Closed Control Systems," in *Proceedings of the 10th IEEE International Workshop on Advanced Motion Control*, pp. 218–223, Trento, Italy, March 26–28, 2008.

[35] N. Hirose, M. Iwasaki, M. Kawafuku, and H. Hirai, "Initial Value Compensation Using Additional Input for Semi-Closed Control Systems," *IEEE Transactions on Industrial Electronics*, Vol. 56, No. 3, pp. 635–641, March 2009.

[36] M. Iwasaki, M. Kawafuku, and H. Hirai, "Residual Vibration Suppression in Repetitive Positioning by Practical Initial Value Compensation," in *Proceedings of the 2005 IEEE/ASME International Conference on Advanced Intelligent Mechatronics*, pp. 1605–1610, Monterey, CA, USA, July 24–28, 2005.

[37] M. Iwasaki, N. Hirose, M. Kawafuku, and H. Hirai, "Residual Vibration Suppression Using Initial Value Compensation for Repetitive Positioning," in *Proceedings of the 8th IEEE International Workshop on Advanced Motion Control*, pp. 571–576, Kawasaki, Japan, March 25–28, 2004.

[38] T. Yamaguchi, M. Hirata, and C. K. Pang (eds.), *High-Speed Precision Motion Control*, CRC Press, Taylor and Francis Group, Boca Raton, FL, USA, 2011.

[39] A. Salerno and J. Angeles, "A New Family of Two-Wheeled Mobile Robots: Modeling and Controllability," *IEEE Transactions on Robotics*, Vol. 23, No. 1, pp. 169–173, February 2007.

[40] S. Jeong and T. Takahashi, "Wheeled Inverted Pendulum Type Assistant Robot: Inverted Mobile, Standing, and Sitting Motions," *in Proceedings of the 2007 IEEE/RSJ International Conference on Intelligent Robots and Systems*, pp. 1932–1937, San Diego, CA, USA, October 29–November 2, 2007.

[41] N. Hirose, M. Iwasaki, M. Kawafuku, and H. Hirai, "Deadbeat Feedforward Compensation with Frequency Shaping in Fast and Precise Positioning," *IEEE Transactions on Industrial Electronics*, Vol. 56, No. 10, pp. 3790–3797, October 2009.

[42] Y. Urakawa and T. Watanabe, "A Study of High-Gain Servo Controller with Complex Zeros for Optical Disk Drives," *Japanese Journal of Applied Physics*, Vol. 44, No. 5B, pp. 3427–3431, May 2005.

[43] T. Miyazaki, K. Ohishi, K. Inomata, K. Kuramochi, D. Koide and H. Tokumaru, "Robust Feedforward Tracking Control Based on Sudden Disturbance Observer and ZPET Control for Optical Disk Recording System," in *Proceedings of the 8th International Workshop on Advanced Motion Control*, pp. 353-358, Kawasaki, Japan, March 25–28, 2004.

[44] K. Takahashi, K. Takeishi, Y. Tomita and S. Ohsawa, "Application of the Sliding Mode Controller to Optical Disk Drives," in *Technical Digest of the 2003 International Symposium on Optical Memory (ISOM)*, pp. 36–37, Nara, Japan, November 3–7, 2003.

4

Precise Positioning Control in Sampled-Data Systems

T. Atsumi

Hitachi, Ltd.

CONTENTS

4.1 Introduction

The wide availability of inexpensive microprocessors has made sampled-data control systems very popular for positioning control in mechatronic products. As a result, the sampled-data control system could be assumed to be the standard control system in these engineering systems. The sampled-data control system is a hybrid system which includes continuous-time and discrete-time signals, implying that the controlled variable is measured only at specific instants. As such, the intersample behavior can degrade the performance and reliability of these systems. For example, in the head-positioning control system of Hard Disk Drives (HDDs), the unobservable head-position may cause destruction of user data stored in HDDs.

There are essentially three different approaches to design controllers for sampled-data control systems. The first approach is *continuous-time control system design*, where discretization errors cannot be avoided and may degrade the control performance and/or stability of the control system. The second approach is *discrete-time control system design*, which can compensate for the discretization errors but does not account for the behaviors of the continuous-time signal between samples. The last approach is *sampled-data control system design*, which can compensate for the discretization errors by considering the intersampling behaviors of the continuous-time signals. Nevertheless, the first and second approaches are more widely employed because of their ease of use, while the last approach is not generally used in the positioning control system of mechatronic products since it is generally more difficult to understand and apply.

To address these concerns, we propose the following calculation methods for

1. sensitivity and complementary sensitivity transfer functions in sampled-data control systems [1];
2. unobservable oscillations in sampled-data positioning systems [2]; and
3. residual vibrations in sampled-data positioning control systems [3].

4.2 Sensitivity and Complementary Sensitivity Transfer Functions in Sampled-Data Control Systems

A main reason why sampled-data control system design is not popular is the difficulty in handling the corresponding frequency responses, since sampled-data control systems are not Linear Time-Invariant (LTI) systems. To overcome these problems, a method based on frequency responses for the calculation of the sensitivity and complementary sensitivity transfer functions of a sampled-data control system is shown. In this method, the gains of the sensitivity and complementary sensitivity transfer functions can be evaluated by the maximum *displacement* of the control variable. As such, infinity norms of signals can be used to define the gain of the sensitivity transfer functions for disturbance suppression in sampled-data positioning control systems.

4.2.1 Relationship Between Continuous- and Discrete-Time Signals

In this section, the relationship between a continuous- and discrete-time signal is defined. For simplicity but without loss of generality, a sinusoidal wave $x_0(t)$ is defined as

$$x_0(t) = e^{j\omega_0 t}. \tag{4.1}$$

The discrete-time signal $x_d(n)$ corresponding to the signal after sampling $x_0(t)$ at a sampling time T_s can be given as

$$\begin{aligned} x_d(n) &= x_0(nT_s) \\ &= e^{j\omega_0 nT_s}. \end{aligned} \tag{4.2}$$

The continuous-time signal $x_c(t)$ which is created from $x_d(n)$ can be given as

$$\begin{aligned} x_c(t) &= \sum_{l=-\infty}^{\infty} \delta(t - lT_s) e^{j\omega_0 t} \\ &= \frac{1}{T_s} \sum_{l=-\infty}^{\infty} e^{j(\omega_0 + \omega_s l)t}, \end{aligned} \tag{4.3}$$

where δ is the Dirac delta function. From (4.2) and (4.3), it can be observed that the discrete-time signal caused by a single complex sinusoid can be represented by a single frequency, while the continuous-time signal caused by the discrete-time signal consists of multiple frequencies.

4.2.2 Sensitivity and Complementary Sensitivity Transfer Functions in Sampled-Data Control Systems

The block diagram of a sampled-data control system is shown in Figure 4.1. In this figure, $\mathcal{S}$ is a sampler, C is a digital controller, $\mathcal{H}$ is a hold, and P_c is a continuous-time plant. r is a reference signal, u_d is an output signal from C, u_c is an output signal from $\mathcal{H}$, d_c is a disturbance signal in continuous time, y_{c0} is an output signal from P_c, y_{d0} is a sampled signal of y_{c0}, y_c is a controlled variable in continuous time, and y_d is a controlled variable in discrete time. In this example, the sampling time T_s is in seconds and the sampling frequency is $\omega_s = \frac{2\pi}{T_s}$ rad/s.

To avoid complex calculations involving matrix algebra, we use frequency responses to analyze the sampled-data control system [1]. The transfer characteristics from u_d to y_d at ω_0 is the controlled object in the discrete-time system denoted as $P_d(j\omega_0)$, and is given as

$$P_d(j\omega_0) = \frac{1}{T_s} \sum_{k=-\infty}^{\infty} \mathcal{H}(j\omega_0 + j\omega_s k) P_c(j\omega_0 + j\omega_s k). \tag{4.4}$$

In this case, the disturbance signal $d_c(t, \omega_0)$ is a single complex sinusoid and is given as

$$d_c(t, \omega_0) = e^{j\omega_0 t}. \tag{4.5}$$

At steady-state with d_c, u_d can be given by

$$u_d(n) = \frac{-C(e^{j\omega_0 T_s})}{1 + P_d(j\omega_0) C(e^{j\omega_0 T_s})} e^{j\omega_0 T_s n}, \tag{4.6}$$

and $u_c(t)$ is given by

$$u_c(t) = \frac{-C(e^{j\omega_0 T_s})}{1 + P_d(j\omega_0) C(e^{j\omega_0 T_s})} \frac{1}{T_s} \sum_{l=-\infty}^{\infty} \mathcal{H}(j\omega_0 + j\omega_s l) e^{j(\omega_0 + \omega_s l)t}. \tag{4.7}$$

$y_{c0}(t)$ is given by

$$y_{c0}(t) = \sum_{l=-\infty}^{\infty} \Gamma(\omega_0, l) e^{j(\omega_0 + \omega_s l)t}, \tag{4.8}$$

where

$$\Gamma(\omega, l) = -\frac{1}{T_s} \frac{C(e^{j\omega T_s}) \mathcal{H}(j\omega + j\omega_s l) P_c(j\omega + j\omega_s l)}{1 + P_d(j\omega) C(e^{j\omega T_s})}, \quad \forall l \in \mathbb{Z}. \tag{4.9}$$

By summing d_c and y_{c0}, $y_c(t)$ can be obtained as

$$y_c(t) = e^{j\omega_0 t} + \sum_{l=-\infty}^{\infty} \Gamma(\omega_0, l) e^{j(\omega_0 + \omega_s l)t}. \tag{4.10}$$

$y_{d0}(n)$ is given by

$$\begin{aligned} y_{d0}(n) &= y_{c0}(nT_s) \\ &= \sum_{l=-\infty}^{\infty} \Gamma(\omega_0, l) e^{j(\omega_0 T_s + 2\pi l)n} \\ &= \left(\sum_{l=-\infty}^{\infty} \Gamma(\omega_0, l) \right) e^{j\omega_0 T_s n} \\ &= \frac{-P_d(j\omega_0)C(e^{j\omega_0 T_s})}{1 + P_d(j\omega_0)C(e^{j\omega_0 T_s})} e^{j\omega_0 T_s n}, \end{aligned} \tag{4.11}$$

and $y_d(n)$ is given by

$$\begin{aligned} y_d(n) &= y_c(nT_s) = e^{j\omega_0 T_s n} + \sum_{l=-\infty}^{\infty} \Gamma(\omega_0, l) e^{j(\omega_0 T_s + 2\pi l)n} \\ &= \left(1 + \sum_{l=-\infty}^{\infty} \Gamma(\omega_0, l) \right) e^{j\omega_0 T_s n} \\ &= \frac{1}{1 + P_d(j\omega_0)C(e^{j\omega_0 T_s})} e^{j\omega_0 T_s n}. \end{aligned} \tag{4.12}$$

y_{c0} and y_c consist of multiple frequencies as shown in (4.8) and (4.10), respectively. This means that the transfer characteristics from d_c to y_{c0} and from d_c to y_c are *not* LTI systems. As such, LTI transfer functions cannot be defined for sampled-data control systems, and the stability of sampled-data control systems should be designed using discrete-time control techniques to make the system stable at the sampled-data points.

In a positioning control system, the performance of the control system can be evaluated by the maximum displacement of the control variable. As such, infinity norms of the signals can be used for defining the gains of the sensitivity and complementary sensitivity transfer functions for performance evaluation in sampled-data positioning control systems.

Using $d_c(t, \omega_0) = e^{j\omega_0 t}$ and y_{c0} which are shown in Figure 4.1 and (4.8), the magnitude response of the complementary sensitivity transfer function $|T_{sd}|$

in a sampled-data control system at ω_0 is given by

$$\begin{aligned} |T_{sd}(j\omega_0)| &= \frac{||y_{c0}(t)||_\infty}{||d_c(t,\omega_0)||_\infty} \\ &= \sup_t |y_{c0}(t)| \\ &= \sum_{l=-\infty}^{\infty} |\Gamma(\omega_0, l)|\,. \end{aligned} \tag{4.13}$$

$|T_{sd}|$ is a periodic function as indicated by (4.13), and is given as

$$|T_{sd}(j\omega_0)| = |T_{sd}(j\omega_0 + j\omega_0 l)|, \quad \forall l \in \mathbb{Z}. \tag{4.14}$$

From (4.11), the complementary sensitivity transfer function T_d of the discrete-time system can be given as

$$\begin{aligned} T_d(j\omega_0) &= \frac{P_d(j\omega_0)C(e^{j\omega_0 T_s})}{1 + P_d(j\omega_0)C(e^{j\omega_0 T_s})} \\ &= -\sum_{l=-\infty}^{\infty} \Gamma(\omega_0, l). \end{aligned} \tag{4.15}$$

The difference between $|T_d|$ and $|T_{sd}|$ is $|T_\Delta|$, and can be given as

$$\begin{aligned} |T_\Delta(j\omega_0)| &= |T_{sd}(j\omega_0)| - |T_d(j\omega_0)| \\ &= \sum_{l=-\infty}^{\infty} |\Gamma(\omega_0, l)| - \left| \sum_{l=-\infty}^{\infty} \Gamma(\omega_0, l) \right|. \end{aligned} \tag{4.16}$$

$|T_\Delta(j\omega_0)|$ indicates the ratio between the amplitude of the intersampling vibrations and the amplitude of the sampled-point vibration caused by the noise at ω_0. As such, the control system must make $|T_\Delta(j\omega_0)|$ small when the control system has a large noise signal at ω_0.

Similarly, using $d_c(t, \omega_0) = e^{j\omega_0 t}$ and y_c which are shown in Figure 4.1 and (4.10), the magnitude response of the sensitivity transfer function in a sampled-data control system at ω_0 is given by

$$\begin{aligned} |S_{sd}(j\omega_0)| &= \frac{||y_c(t)||_\infty}{||d_c(t,\omega_0)||_\infty} \\ &= \sup_t |y_c(t)| \\ &= |1 + \Gamma(\omega_0, 0)| + \sum_{l=-\infty, \neq 0}^{\infty} |\Gamma(\omega_0, l)|. \end{aligned} \tag{4.17}$$

$|S_{sd}|$ is *not* a periodic function like that of discrete-time systems and $|T_{sd}|$,

as can be seen from (4.17). It is also indicated in (4.17) that the control system must satisfy

$$|\Gamma(\omega_0, 0)| > \sum_{l=-\infty, \neq 0}^{\infty} |\Gamma(\omega_0, l)|, \tag{4.18}$$

in order to make

$$|S_{sd}(j\omega_0)| < 1. \tag{4.19}$$

In other words, when the control system achieves (4.19), the control system will have

$$|S_{sd}(j\omega_0 + j\omega_s l)| > 1, \quad \forall l \neq 0, \tag{4.20}$$

because $|\Gamma(\omega_0, l)| < \sum_{k=-\infty, \neq l}^{\infty} |\Gamma(\omega_0, k)|$. In particular, when $|S_{sd}(j\omega_0)| \simeq 0$,

$$|S_{sd}(j\omega_0 + j\omega_s l)| \simeq 2, \quad \forall l \neq 0. \tag{4.21}$$

It should be noted that (4.18) is not a sufficient condition for (4.19).

From (4.12), the sensitivity transfer function S_d of the discrete-time system can be given as

$$\begin{aligned} S_d(j\omega_0) &= \frac{1}{1 + P_d(j\omega_0)C(e^{j\omega_0 T_s})} \\ &= 1 + \sum_{l=-\infty}^{\infty} \Gamma(\omega_0, l). \end{aligned} \tag{4.22}$$

The difference between $|S_d|$ and $|S_{sd}|$ can now be given as

$$\begin{aligned} |S_\Delta(j\omega_0)| &= |S_{sd}(j\omega_0)| - |S_d(j\omega_0)| \\ &= |1 + \Gamma(\omega_0, 0)| + \sum_{l=-\infty, \neq 0}^{\infty} |\Gamma(\omega_0, l)| - \left| 1 + \sum_{l=-\infty}^{\infty} \Gamma(\omega_0, l) \right|. \end{aligned} \tag{4.23}$$

$|S_\Delta(j\omega_0)|$ indicates the ratio between the amplitude of the intersampling vibrations and the amplitude of the sampled-point vibration caused by the disturbance at ω_0. Therefore, the control system must make $|S_\Delta(j\omega_0)|$ small when the control system has a large disturbance at ω_0.

From (4.13) and (4.17), the relationship between $|S_{sd}|$ and $|T_{sd}|$ can be given as

$$|S_{sd}(j\omega_0)| = |T_{sd}(j\omega_0)| - |\Gamma(\omega_0, 0)| + |1 + \Gamma(\omega_0, 0)|. \tag{4.24}$$

$|T_{sd}(j\omega_0)| - |\Gamma(\omega_0, 0)|$ shows that the effects of the aliasing frequencies of ω_0 on $|T_{sd}(j\omega_0)|$. Therefore, the control system needs to make the effects of the aliasing frequencies of ω_0 on $|T_{sd}(j\omega_0)|$ small in order to make $|S_{sd}(j\omega_0)|$ small. Besides, it is also shown by (4.24) that when $|S_{sd}(j\omega_0)| \simeq 0$, $|T_{sd}(j\omega_0)|$ becomes approximately 1.

With these notions, the results for the sensitivity and complementary sensitivity transfer functions of a sampled-data control system can be summarized as follows:

- The relationship between $|S_{sd}|$ and $|T_{sd}|$ are given by (4.24). This implies that the control system needs to make the effects of the aliasing frequencies of ω_0 on $|T_{sd}(j\omega_0)|$ small in order to make $|S_{sd}(j\omega_0)|$ small;
- $|T_{sd}|$ is a periodic function similar to that of discrete-time systems, but $|S_{sd}|$ is not a periodic function;
- When the sampled-data control system achieves $|S_{sd}(j\omega_0)| < 1$, $|S_{sd}(j\omega_0 + j\omega_s l)| > 1$ for all $l \neq 0$;
- When $|S_{sd}(j\omega_0)| \simeq 0$, $|S_{sd}(j\omega_0 + j\omega_s l)| \simeq 2$ $\forall l \neq 0$ and $|T_{sd}(j\omega_0 + j\omega_s l)| \simeq 1$ for all l;
- The control system must make $|T_\Delta(j\omega_0)|$ small when the control system has a large noise signal at ω_0; and
- The control system must make $|S_\Delta(j\omega_0)|$ small when the control system has a large disturbance at ω_0;

4.2.3 Sampled-Data Control System Using a Multi-Rate Digital Filter

In sampled-data control systems, multi-rate filters are often used to improve the control performance. In this section, the focus is on sampled-data control systems using multi-rate filters realized with multi-rate holds and interpolators so that the frequency responses of the multi-rate system can be defined. The block diagram of a sampled-data control system with a multi-rate digital filter is shown in Figure 4.2. In this figure, I_p is an interpolator, F_m is a multi-rate digital filter, and $\mathcal{H}_m$ is a multi-rate hold. The multi-rate number is defined as m.

The transfer characteristics from u_d to y_d at ω_0 is the controlled object in the discrete-time system which includes the multi-rate filter. This is denoted as $P_{dm}(j\omega_0)$, and is given as

$$P_{dm}(j\omega_0) = \frac{1}{T_s} \sum_{k=-\infty}^{\infty} W(j\omega_0 + j\omega_s k) P_c(j\omega_0 + j\omega_s k), \tag{4.25}$$

where

$$W(j\omega) = I_p(e^{\frac{j\omega T_s}{m}}) F_m(e^{\frac{j\omega T_s}{m}}) \mathcal{H}_m(j\omega). \tag{4.26}$$

$y_{c0}(t)$ consists of multiple frequencies and is given by

$$y_{c0}(t) = \sum_{l=-\infty}^{\infty} \Gamma_m(\omega_0, l) e^{j(\omega_0 + \omega_s l)t}, \tag{4.27}$$

where

$$\Gamma_m(\omega, l) = -\frac{1}{T_s} \frac{C(e^{j\omega T_s}) W(j\omega + j\omega_s l) P_c(j\omega + j\omega_s l)}{1 + P_{dm}(j\omega) C(e^{j\omega T_s})}, \quad \forall l \in \mathbb{Z}. \tag{4.28}$$

By adding d_c and y_{c0}, $y_c(t)$ can be given as

$$y_c(t) = e^{j\omega_0 t} + \sum_{l=-\infty}^{\infty} \Gamma_m(\omega_0, l) e^{j(\omega_0+\omega_s l)t}. \tag{4.29}$$

$y_{d0}(n)$ is given by

$$\begin{aligned} y_{d0}(n) &= \left(\sum_{l=-\infty}^{\infty} \Gamma_m(\omega_0, l) \right) e^{j\omega_0 T_s n} \\ &= \frac{-P_{dm}(j\omega_0)C(e^{j\omega_0 T_s})}{1 + P_{dm}(j\omega_0)C(e^{j\omega_0 T_s})} e^{j\omega_0 T_s n}, \end{aligned} \tag{4.30}$$

and $y_d(n)$ is given by

$$\begin{aligned} y_d(n) &= \left(1 + \sum_{l=-\infty}^{\infty} \Gamma_m(\omega_0, l) \right) e^{j\omega_0 T_s n} \\ &= \frac{1}{1 + P_{dm}(j\omega_0)C(e^{j\omega_0 T_s})} e^{j\omega_0 T_s n}. \end{aligned} \tag{4.31}$$

From (4.27), $|T_{sd}(j\omega_0)|$ can be given by

$$|T_{sd}(j\omega_0)| = \sum_{l=-\infty}^{\infty} |\Gamma_m(\omega_0, l)|, \tag{4.32}$$

and from (4.30), T_d can be given as

$$\begin{aligned} T_d(j\omega_0) &= \frac{P_{dm}(j\omega_0)C(e^{j\omega_0 T_s})}{1 + P_{dm}(j\omega_0)C(e^{j\omega_0 T_s})} \\ &= -\sum_{l=-\infty}^{\infty} \Gamma_m(\omega_0, l). \end{aligned} \tag{4.33}$$

The difference between $|T_d|$ and $|T_{sd}|$ can be given as

$$|T_\Delta(j\omega_0)| = \sum_{l=-\infty}^{\infty} |\Gamma_m(\omega_0, l)| - \left| \sum_{l=-\infty}^{\infty} \Gamma_m(\omega_0, l) \right|. \tag{4.34}$$

From (4.29), $|S_{sd}(j\omega_0)|$ can be given by

$$|S_{sd}(j\omega_0)| = |1 + \Gamma_m(\omega_0, 0)| + \sum_{l=-\infty, \neq 0}^{\infty} |\Gamma_m(\omega_0, l)|, \tag{4.35}$$

and from (4.31), S_d can be given as

$$\begin{aligned} S_d(j\omega_0) &= \frac{1}{1 + P_{dm}(j\omega_0)C(e^{j\omega_0 T_s})} \\ &= 1 + \sum_{l=-\infty}^{\infty} \Gamma_m(\omega_0, l). \end{aligned} \tag{4.36}$$

The difference between $|S_d|$ and $|S_{sd}|$ can be given as

$$|S_\Delta(j\omega_0)| = |1 + \Gamma_m(\omega_0, 0)| + \sum_{l=-\infty, \neq 0}^{\infty} |\Gamma_m(\omega_0, l)| - \left| 1 + \sum_{l=-\infty}^{\infty} \Gamma_m(\omega_0, l) \right|. \tag{4.37}$$

From (4.32) and (4.35), the relationship between $|S_{sd}|$ and $|T_{sd}|$ can be given as

$$|S_{sd}(j\omega_0)| = |T_{sd}(j\omega_0)| - |\Gamma_m(\omega_0, 0)| + |1 + \Gamma_m(\omega_0, 0)|. \tag{4.38}$$

The above-mentioned results show that the characteristics of the sensitivity and complementary sensitivity transfer functions of the sampled-data control system with a multi-rate filter are similar to that of the sampled-data control system without a multi-rate filter. As such, the results for a multi-rate sampled-data control system are summarized as follows:

- The relationship between $|S_{sd}|$ and $|T_{sd}|$ are given by (4.38);
- $|T_{sd}|$ is a periodic function similar to that of discrete-time systems, but $|S_{sd}|$ is not a periodic function;
- When the sampled-data control system achieves $|S_{sd}(j\omega_0)| < 1$, $|S_{sd}(j\omega_0 + j\omega_s l)| > 1$ for all $l \neq 0$;
- When $|S_{sd}(j\omega_0)| \simeq 0$, $|S_{sd}(j\omega_0 + j\omega_s l)| \simeq 2$ $\forall l \neq 0$ and $|T_{sd}(j\omega_0 + j\omega_s l)| \simeq 1$ for all l;
- The control system must make $|T_\Delta(j\omega_0)|$ small when the control system has a large noise signal at ω_0; and
- The control system must make $|S_\Delta(j\omega_0)|$ small when the control system has a large disturbance at ω_0.

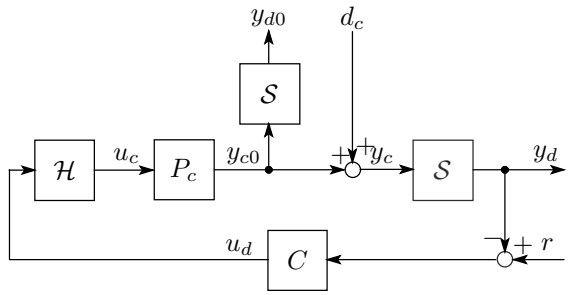

FIGURE 4.1
Block diagram of a sampled-data control system.

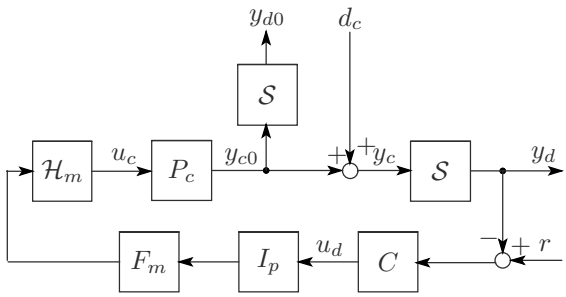

FIGURE 4.2
Block diagram of a sampled-data control system with a multi-rate filter.

4.3 Unobservable Oscillations in Sampled-Data Positioning Systems

The term *unobservable oscillation* refers to the movement of a controlled position variable that occurs between samples, which usually arises from mechanical vibrations. The degree of unobservability depends on the relationship between the sampling frequency and the oscillation frequency. The relationship between the oscillation frequency and the sampling frequency is shown using an index of unobservable magnitude of oscillations based on its Root-Mean-Square (RMS) amplitude. By using this index, the effects of the unobservable oscillations caused by mechanical resonances can be estimated.

4.3.1 Relationship Between Oscillation Frequency and Unobservable Magnitude of Oscillations

The performance of a positioning control system can be evaluated by looking at the maximum displacement of the controlled variable. In the sampled-data positioning control system shown in Figure 4.1, the maximum displacement from y_d is observed by the control system. However, the actual position is y_c. Therefore, the sampled-data control system has an unobservable magnitude which is the difference between the maximum displacement of y_c and the maximum displacement of y_d. When the unobservable magnitude is large, the performance and reliability of the mechatronic products may degrade. Consequently, the control system must ensure that the magnitude of the unobservable signal is small enough for the device to operate with good performance reliably.

4.3.1.1 Definition of Unobservable Magnitude of Oscillations

In this section, the effects of the sampler are studied where the position signal y_c is a sinusoid given by

$$y_c(t) = \sin(\omega_t t), \tag{4.39}$$

and ω_t is the oscillation frequency in rad/s. The discrete-time signal y_d corresponds to the signal after sampling y_c with sampling time τ and is given as

$$\begin{aligned} y_d[n, \Delta_s] &= y_c(\tau(n + \Delta_s)) \\ &= \sin(\omega_t \tau(n + \Delta_s)), \end{aligned} \tag{4.40}$$

where n is the sample number and Δ_s is the timing of the sampling ($0 \leq \Delta_s < 1$) within one sampling period. The unobservable magnitude y_u is defined as

$$y_u[\Delta_s] = \max(|y_{um}[\Delta_s]|, |y_{up}[\Delta_s]|), \tag{4.41}$$

with $y_{um}[\Delta_s] = \inf_t(y_c(t)) - \min_n(y_d[n, \Delta_s])$ and $y_{up}[\Delta_s] = \sup_t(y_c(t)) - \max_n(y_d[n, \Delta_s])$.

The *worst-case* unobservable magnitude y_{uw} is given by

$$y_{uw} = \sup_{\Delta_s \in [0,1)} (y_u[\Delta_s]). \tag{4.42}$$

When $\tau = 25$ μs, the sampling frequency is 40 kHz and the relationship between y_{uw} and ω_t is shown in Figure 4.3. Figure 4.3 shows that y_{uw} depends on the ratio of the oscillation frequency ω_t to the sampling frequency. As such, the focus is on the cases where $\omega_t = 2\pi 40 \times 10^3$ rad/s and coincides with the sampling frequency where $\omega_t = 2\pi 20 \times 10^3$ rad/s and coincides with the Nyquist frequency, and $\omega_t = 2\pi 13.3 \times 10^3$ rad/s and coincides with one-third of the sampling frequency.

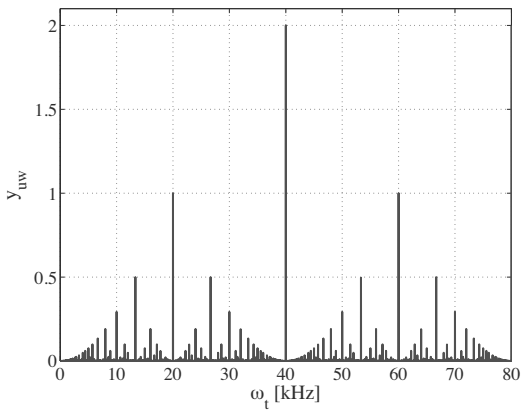

FIGURE 4.3
Relationship between maximum unobservable magnitude y_{uw} and ω_t ($\tau = 25$ μs).

4.3.1.2 Oscillations at the Sampling Frequency

Consider a sinusoid y_c of the same frequency as the sampling frequency and is given by

$$y_c(t) = \sin \frac{2\pi t}{\tau}. \tag{4.43}$$

The unobservable magnitude y_u calculated from (4.41) and is shown in Figure 4.4.

As shown in Figure 4.4, the minimum value of y_u is 1 which occurs when the timing of the sampling Δ_s is 0 or 0.5. The maximum value of y_u is 2, and it occurs when Δ_s is 0.25 or 0.75. The time responses of y_c and y_d for an oscillation at the sampling frequency are shown in Figure 4.5.

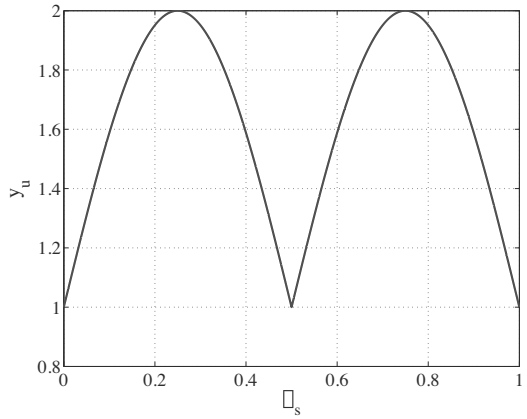

FIGURE 4.4
Dependence of unobservable magnitude y_u on sampling phase $\Delta_s \in [0, 1)$ for an oscillation at the sampling frequency.

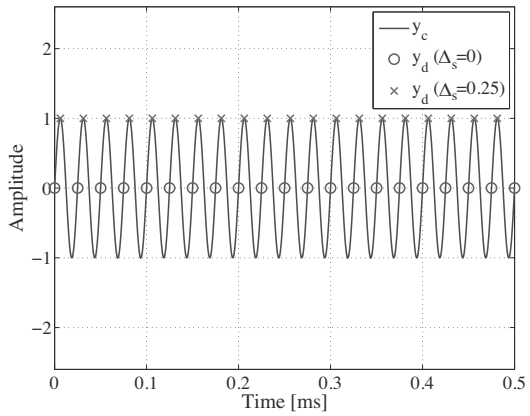

FIGURE 4.5
Time responses of y_c and y_d for an oscillation at the sampling frequency. Solid: y_c. 'o': y_d with $\Delta_s = 0$. 'x': y_d with $\Delta_s = 0.25$.

4.3.1.3 Oscillations at the Nyquist Frequency

Now, consider a sinusoid y_c of the same frequency as the Nyquist frequency and is given by

$$y_c(t) = \sin \frac{\pi t}{\tau}. \tag{4.44}$$

The unobservable magnitude y_u calculated from (4.41) and is shown in Figure 4.6.

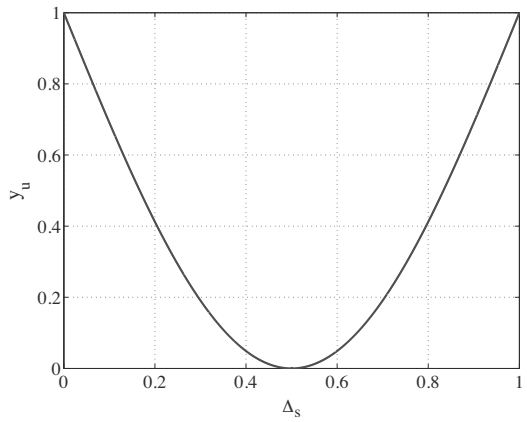

FIGURE 4.6
Unobservable magnitude for an oscillation at the Nyquist frequency.

As shown in Figure 4.6, the minimum unobservable magnitude $y_u = 0$ occurs when the sampling phase $\Delta_s = 0.5$. The maximum unobservable magnitude $y_u = 1$ occurs when $\Delta_s = 0$. The time responses of y_c and y_d for an oscillation at the Nyquist frequency are shown in Figure 4.7.

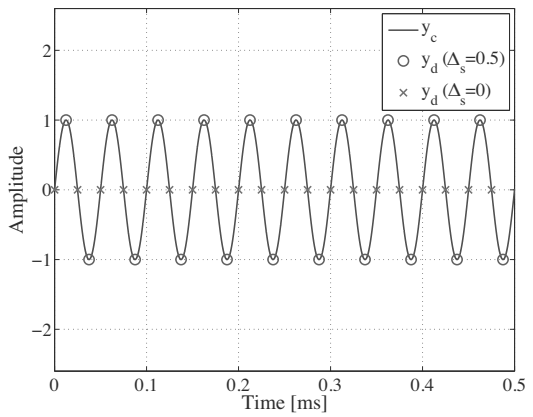

FIGURE 4.7
Time responses of y_c and y_d for an oscillation at the Nyquist frequency. Solid: y_c. 'o': y_d with $\Delta_s = 0.5$. 'x': y_d with $\Delta_s = 0$.

4.3.1.4 Oscillations at One-Third of the Sampling Frequency

The third case considered is a sinusoid y_c of frequency that is one-third of the sampling frequency, and is given by

$$y_c(t) = \sin \frac{2\pi t}{3\tau}. \tag{4.45}$$

The unobservable magnitude y_u calculated from (4.41) is shown in Figure 4.8.

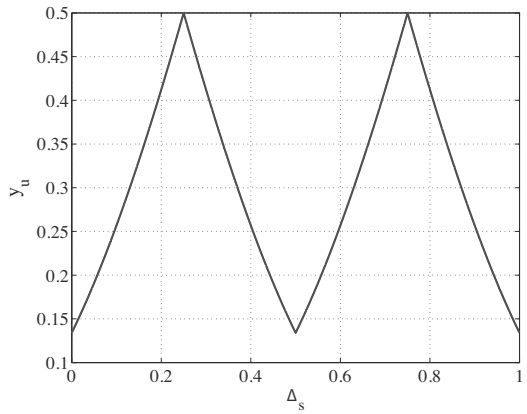

FIGURE 4.8
Unobservable magnitude for an oscillation at one-third of the sampling frequency.

As shown in Figure 4.8, the minimum unobservable magnitude $y_u = 0.134$ occurs when the timing of the sampling $\Delta_s = 0$ or $\Delta_s = 0.5$, and the maximum unobservable magnitude $y_u = 0.5$ occurs when $\Delta_s = 0.25$ or $\Delta_s = 0.75$. The time responses of y_c and y_d for an oscillation at one-third of the sampling frequency are shown in Figure 4.9.

4.3.2 Unobservable Magnitudes of Oscillations with Damping

In this section, we consider and study the effects of unobservable magnitudes of oscillations with positive damping. This is more practical since most oscillations arising from mechanical vibrations are passive in nature and decay with time.

4.3.2.1 Definition of Unobservable Magnitudes of Oscillations with Damping

For a positioning control system in mechatronic products, many of the oscillations in the position signal are caused by damped mechanical resonances.

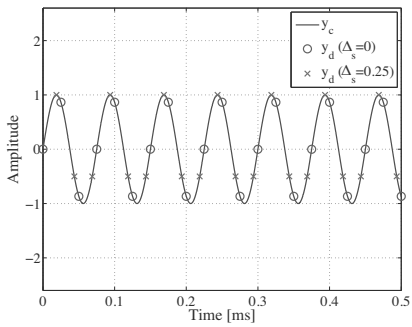

Δ

FIGURE 4.9
Time responses of y_c and y_d for an oscillation at one-third of the sampling frequency. Solid: y_c. 'o': y_d with $\Delta_s = 0$. 'x': y_d with $\Delta_s = 0.75$.

As such, the oscillation signal y_c and measurement data y_d are redefined as

$$y_c(t) = e^{-\zeta\omega_n t}\sin(\omega_d t), \tag{4.46}$$

and

$$\begin{aligned} y_d[n, \Delta_s] &= y_c(\tau(n + \Delta_s)) \\ &= e^{-\zeta\omega_n\tau(n+\Delta_s)}\sin(\omega_d\tau(n + \Delta_s)), \end{aligned} \tag{4.47}$$

where ω_n and ζ are the natural frequency and damping ratio of the resonant mode, respectively, and $\omega_d = \omega_n\sqrt{(1-\zeta^2)}$ is the damped natural frequency.

In general, a positioning control system must estimate the maximum displacement of the control variable from a finite number of samples of the position signal. For example, the head-positioning control system of an HDD must determine the data writability by comparing a finite number of samples of position signal against the write-inhibit condition. Therefore, the unobservable magnitude has to be considered, which is the difference between the maximum displacement of y_c and the maximum displacement of y_d for a finite number of samples. The unobservable magnitude y_u for a finite number of samples can be redefined as

$$y_u[\Delta_s] = \begin{cases} 0 : y_{up}[\Delta_s] \le 0, y_{um}[\Delta_s] \ge 0 \\ |y_{up}[\Delta_s]| : y_{up}[\Delta_s] > 0, y_{um}[\Delta_s] \ge 0 \\ |y_{um}[\Delta_s]| : y_{up}[\Delta_s] \le 0, y_{um}[\Delta_s] < 0 \\ |y_{up}[\Delta_s]| : y_{up}[\Delta_s] \ge -y_{um}[\Delta_s] > 0 \\ |y_{um}[\Delta_s]| : -y_{um}[\Delta_s] > y_{up}[\Delta_s] > 0 \end{cases}, \tag{4.48}$$

where $y_{um}[\Delta_s] = \inf_{t\in[N_s\tau,\infty)}(y_c(t)) - \min_{n\in[1,N_s]}(y_d[n, \Delta_s])$ and $y_{up}[\Delta_s] = \sup_{t\in[N_s\tau,\infty)}(y_c(t)) - \max_{n\in[1,N_s]}(y_d[n, \Delta_s])$, and N_s is the sample number for the judgment of the maximum displacement. An example of the time responses of y_c and y_d with $N_s = 5$ is shown in Figure 4.10. In this case, y_u is equal to $|y_{um}|$ because $y_{up} \le 0$ and $y_{um} < 0$.

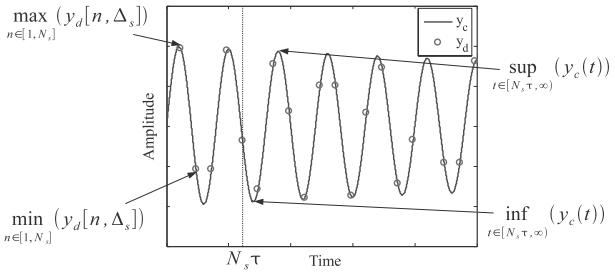

FIGURE 4.10
Example of time responses of y_c and y_d with damping for a finite number of samples ($N_s = 5$).

4.3.2.2 Example of Unobservable Magnitudes for Oscillations with Damping

The first case considered is the case where the damped natural frequency coincides with the sampling frequency with $\tau = 25\ \mu$s, $\zeta = 0.1$, and $N_s = 5$. The relationship between y_u and Δ_s is indicated by Figure 4.11, and the time responses of y_c and y_d for the damped oscillation at the sampling frequency are shown in Figure 4.12.

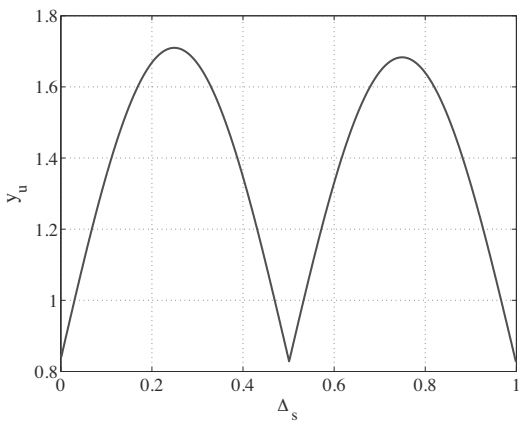

FIGURE 4.11
Unobservable magnitude for a damped oscillation at the sampling frequency ($\tau = 25\ \mu$s, $\zeta = 0.1$, and $N_s = 5$).

The histogram of the event probability of the unobservable magnitude is shown in Figure 4.13. The event probability Ep in % is given by

$$Ep(n) = 100 \times \frac{m_n}{m_a}, \tag{4.49}$$

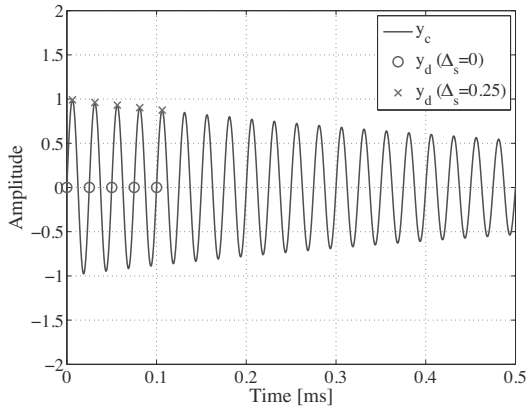

FIGURE 4.12
Time responses of y_c and y_d for a damped oscillation at the sampling frequency ($\tau = 25$ μs, $\zeta = 0.1$, and $N_s = 5$). Solid: y_c. 'o': y_d with $\Delta_s = 0$. 'x': y_d with $\Delta_s = 0.25$.

where m_n counts the number of observations that fall into

$$0.1(n-1) \leq y_u < 0.1n, \tag{4.50}$$

and m_a counts the total number of observations. In this case, most of the magnitudes are more than 140% of the amplitude.

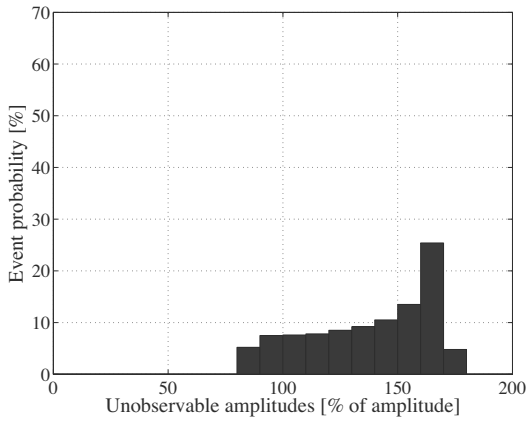

FIGURE 4.13
Histogram of event probability of unobservable magnitude for a damped oscillation at the sampling frequency ($\tau = 25$ μs, $\zeta = 0.1$, and $N_s = 5$).

The second case considered is the case where the damped natural frequency

coincides with the Nyquist frequency with $\tau = 25$ μs, $\zeta = 0.1$, and $N_s = 5$. The relationship between y_u and Δ_s is indicated by Figure 4.14, and the time responses of y_c and y_d for the damped oscillation at the Nyquist frequency are shown in Figure 4.15.

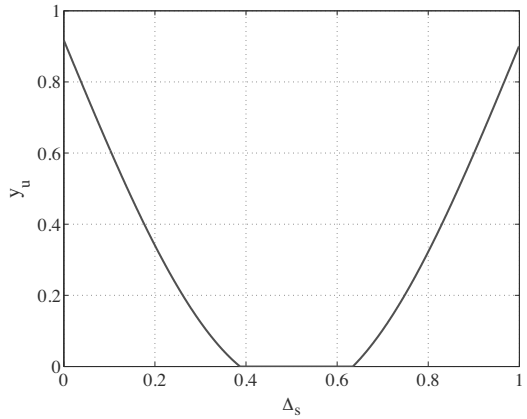

FIGURE 4.14
Unobservable magnitude for a damped oscillation at the Nyquist frequency ($\tau = 25$ μs, $\zeta = 0.1$, and $N_s = 5$).

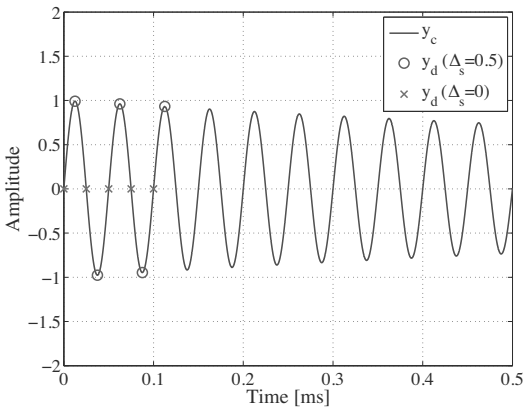

FIGURE 4.15
Time responses of y_c and y_d for a damped oscillation at the Nyquist frequency ($\tau = 25$ μs, $\zeta = 0.1$, and $N_s = 5$). Solid: y_c. 'o': y_d with $\Delta_s = 0.5$. 'x': y_d with $\Delta_s = 0$.

The histogram of the event probability of the unobservable magnitudes is

shown in Figure 4.16. In this case, most of the magnitudes are less than 30% of the amplitude.

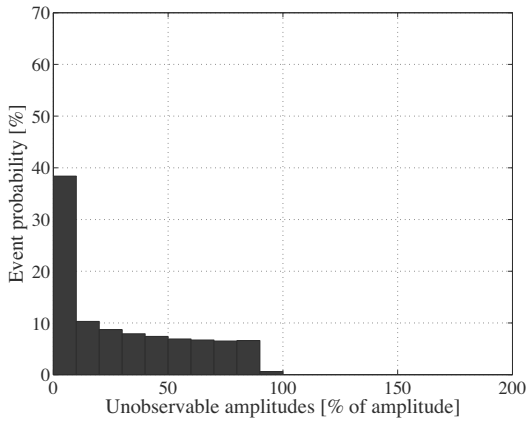

FIGURE 4.16
Histogram of event probability of unobservable magnitude for a damped oscillation at the Nyquist frequency ($\tau = 25$ μs, $\zeta = 0.1$, and $N_s = 5$).

The third case considered is the case where the damped natural frequency coincides with one-third of the sampling frequency with $\tau = 25$ μs, $\zeta = 0.1$, and $N_s = 5$. The relationship between y_u and Δ_s is indicated by Figure 4.17, and the time responses of y_c and y_d for a damped oscillation at one-third of the sampling frequency is shown in Figure 4.18.

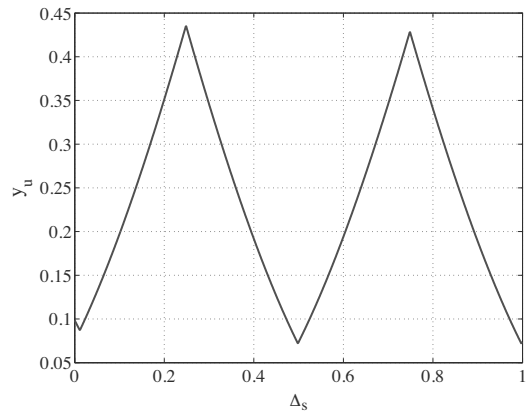

FIGURE 4.17
Unobservable magnitude for a damped oscillation at one-third of the sampling frequency ($\tau = 25$ μs, $\zeta = 0.1$, and $N_s = 5$).

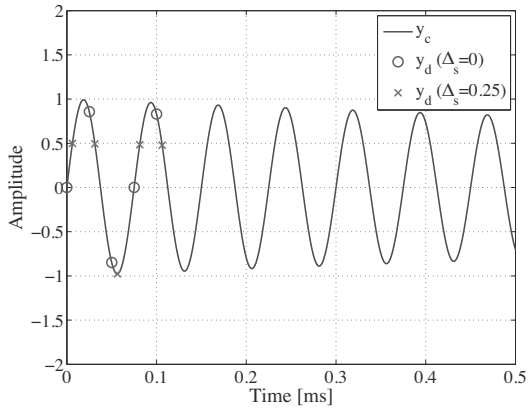

FIGURE 4.18
Time responses of y_c and y_d for a damped oscillation at one-third of the sampling frequency ($\tau = 25$ μs, $\zeta = 0.1$, and $N_s = 5$). Solid: y_c. 'o': y_d with $\Delta_s = 0$. 'x': y_d with $\Delta_s = 0.25$.

The histogram of the event probability of the unobservable magnitude is shown in Figure 4.19. In this case, most of the magnitudes are less than 30% of the amplitude.

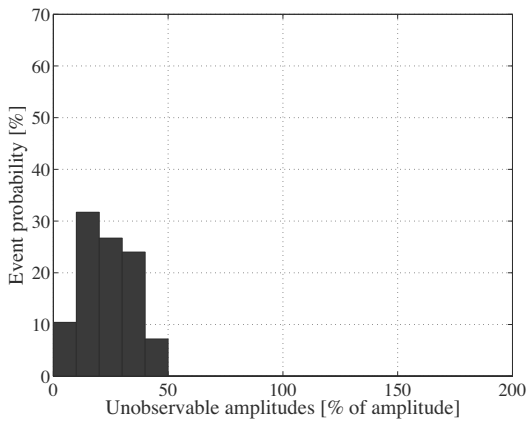

FIGURE 4.19
Histogram of event probability of unobservable magnitude for a damped oscillation at one-third of the sampling frequency ($\tau = 25$ μs, $\zeta = 0.1$, and $N_s = 5$).

4.3.2.3 Index of Unobservable Magnitudes

The *worst-case* unobservable magnitude y_{uw} for a finite number of samples is given by

$$y_{uw} = \sup_{\Delta_s \in [0,1)} (y_u[\Delta_s]). \tag{4.51}$$

The worst-case unobservable magnitude y_{uw} with $\tau = 25$ μs and $\zeta = 0$ is shown in Figure 4.20. Figure 4.21 shows y_{uw} with $\tau = 25$ μs and $\zeta = 0.01$. It can be seen that the areas where y_{uw} is large become wider under finite sample number, especially around the sampling frequency. The widths of the peaks of y_{uw} become narrower as N_s increases. Besides, it can also be seen that y_{uw} becomes smaller as ζ increases. This effect becomes larger as ω_d increases.

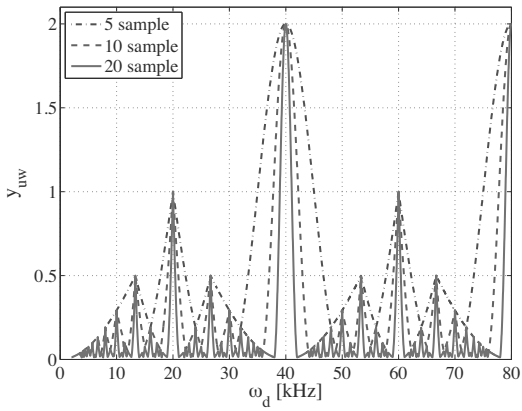

FIGURE 4.20
Relationship between y_{uw} and ω_d ($\tau = 25$ μs and $\zeta = 0$). Dashed: $N_s = 5$. Dashed-dot: $N_s = 10$. Solid: $N_s = 20$.

The worst-case unobservable magnitude and its event probability depend on the relationship between the oscillation frequency and the sampling frequency. This means that the index of unobservable magnitude that includes the worst-case value and its event probability have to be defined. For example, y_{uw} at the sampling frequency is twice that at the Nyquist frequency as shown in Figure 4.3. However, it can be seen from Figures 4.13 and 4.16 that the risk of degradation of performance and reliability caused by the oscillation at the sampling frequency is much higher than that caused by the oscillation at the Nyquist frequency.

As such by using the RMS value of y_u, the index value of unobservable magnitude y_{ui} which includes the effects of the event probability is proposed to be

$$y_{ui} = \sqrt{\int_0^1 y_u[\Delta_s]^2 d\Delta_s}, \tag{4.52}$$

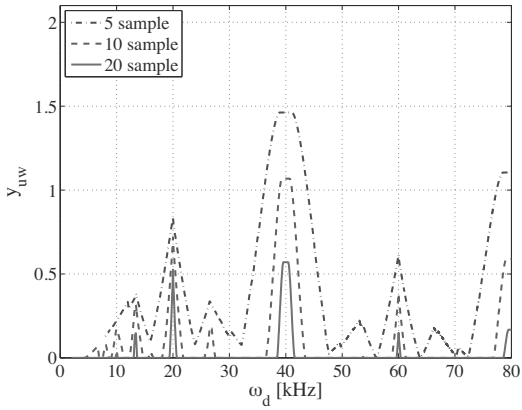

FIGURE 4.21
Relationship between y_{uw} and ω_d ($\tau = 25$ μs and $\zeta = 0.01$). Dashed: $N_s = 5$. Dashed-dot: $N_s = 10$. Solid: $N_s = 20$.

and y_{ui} with $\tau = 25$ μs and $\zeta = 0$ is shown in Figure 4.22, and y_{ui} with $\tau = 25$ μs and $\zeta = 0.01$ is shown in Figure 4.23. It can be seen that y_{ui} is large around the sampling frequency and the widths of the peaks of y_{ui} become narrower as N_s increases.

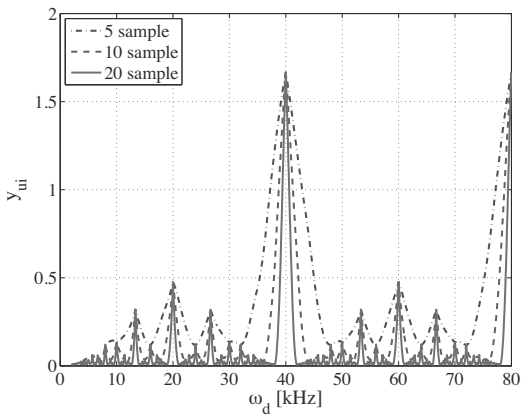

FIGURE 4.22
Relationship between y_{ui} and ω_d ($\tau = 25$ μs and $\zeta = 0$). Dashed: $N_s = 5$. Dashed-dot: $N_s = 10$. Solid: $N_s = 20$.

These results show that the unobservable magnitude for oscillations at the sampling frequency is far larger. Therefore, the positioning control system

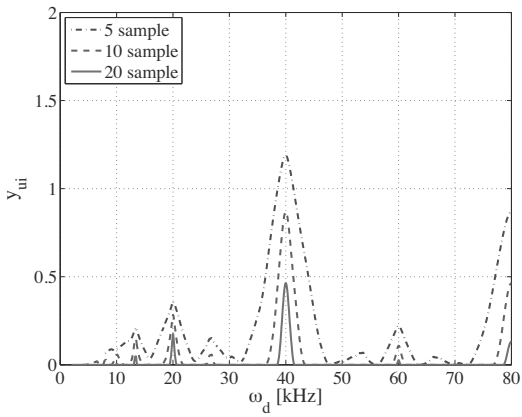

FIGURE 4.23
Relationship between y_{ui} and ω_d ($\tau = 25$ μs and $\zeta = 0.01$). Dashed: $N_s = 5$. Dashed-dot: $N_s = 10$. Solid: $N_s = 20$.

must be designed such that the sampling frequency is away from a mechanical resonant frequency.

These results also show that the sampled-data control system has unobservable magnitudes of oscillations even if the oscillation frequencies are below the Nyquist frequency. This means that the use of the signal y_d alone may result in an underestimation of the true amount of displacement of the controlled position value from a reference value. Consequently, this underestimation should be accounted for by conditions on the controlled position, of which an example is the write-inhibit condition in HDDs. In other words, the estimate of the actual displacement of the controlled variable y_c should use the expected value of y_{ui} found using the method described in this section and as illustrated in Figures 4.22 and 4.23. It is critical to choose a sufficient number of samples of y_d for this estimate.

In some positioning control systems, changing the sampling frequency may be easier than changing the mechanical resonant frequency. Therefore, the relationship between the index of unobservable magnitude y_{ui} and the sampling frequency is shown considering fixed resonant frequency and damping ratio.

The relationship between y_{ui} and sampling frequency $\frac{1}{\tau}$ with damped resonant frequency $\omega_d = 40$ kHz and damping ratio $\zeta = 0.01$ is shown in Figure 4.24. It can be seen that the values of y_{ui} are largest when the sampling frequency is around the damped resonant frequency which is 40 kHz, and second largest when the sampling frequency is around half the resonant frequency which is 20 kHz. By choosing N_s and the acceptable level for the RMS of the unobservable magnitude of the mechanical resonance, the unacceptable sampling frequency for which the value of y_{ui} is larger than the acceptable level can be estimated. For example, the dashed line in Figure 4.24 shows that the

sampling frequency should not be set around 13.3 kHz, 20.0 kHz, 40.0 kHz, and 80.0 kHz, when the acceptable level is 0.2 and $N_s = 10$.

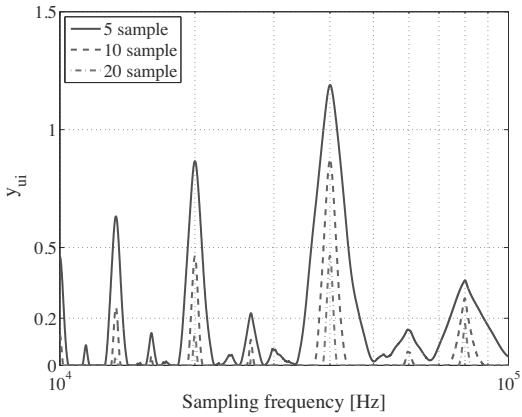

FIGURE 4.24
Relationship between y_{ui} and the sampling frequency, with $\omega_d = 40$ kHz and $\zeta = 0.01$. Solid: $N_s = 5$. Dashed: $N_s = 10$. Dashed-dot: $N_s = 20$.

The dependence of y_{ui} on the measurement time $\tau \times N_s$ for the judgment of the maximum displacement with $\omega_d = 40$ kHz and $\zeta = 0.01$ is shown in Figure 4.25. It can be seen that y_{ui} becomes smaller with increasing $\tau \times N_s$, and the decrease of the ratio of y_{ui} to $\tau \times N_s$ depends on the sampling frequency. When the sampling time and the acceptable level for RMS of the unobservable magnitude of the mechanical resonance is decided, the unacceptable N_s for which the value of y_{ui} is larger than the acceptable level can be estimated. For example, the dashed line in Figure 4.25 shows that $\tau \times N_s$ should be more than 0.26 ms when the acceptable level of $y_{ui} = 0.2$ and $\tau = 23.8$ μs (42 kHz).

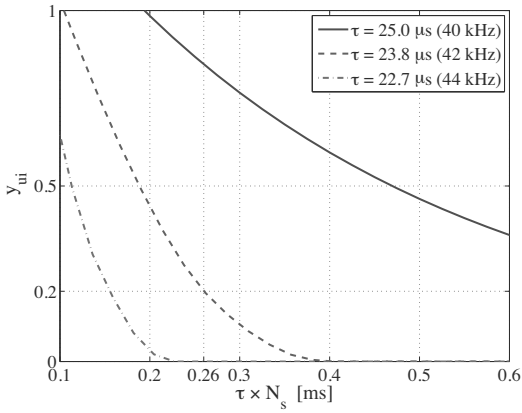

FIGURE 4.25
Relationship between y_{ui} and $\tau \times N_s$, with $\omega_d = 40$ kHz and $\zeta = 0.01$. Solid: $\tau = 25.0$ μs (40 kHz). Dashed: $\tau = 23.8$ μs (42 kHz). Dot-dashed: $\tau = 22.7$ μs (44 kHz).

4.4 Residual Vibrations in Sampled-Data Positioning Control Systems

Positioning systems often have mechanical vibrations with resonant frequencies extending beyond the Nyquist frequency of the control system. As such, the characteristics of the residual vibrations caused by mechanical resonances above the Nyquist frequency have to be analyzed. To analyze the amplitude of mechanical vibrations caused by the acceleration input signal, the Discrete Fourier Transform (DFT) is commonly used as an analysis tool. While DFT analysis is suitable for analyzing the components of a steady-state signal, it is not suitable for analyzing a transient response. In this section, the Shock Response Spectrum (SRS) analysis is used to handle the transient characteristics of the mechanical resonant modes by using their identified modal parameters.

4.4.1 Residual Vibration Analysis Based on SRS Analysis

In this section, the SRS analysis using half-sine wave and polynomial wave is performed on residual vibrations. The effectiveness of the SRS analysis is also compared with traditional DFT techniques.

4.4.1.1 SRS Analysis

The basic concept of the analysis is illustrated in Figure 4.26.

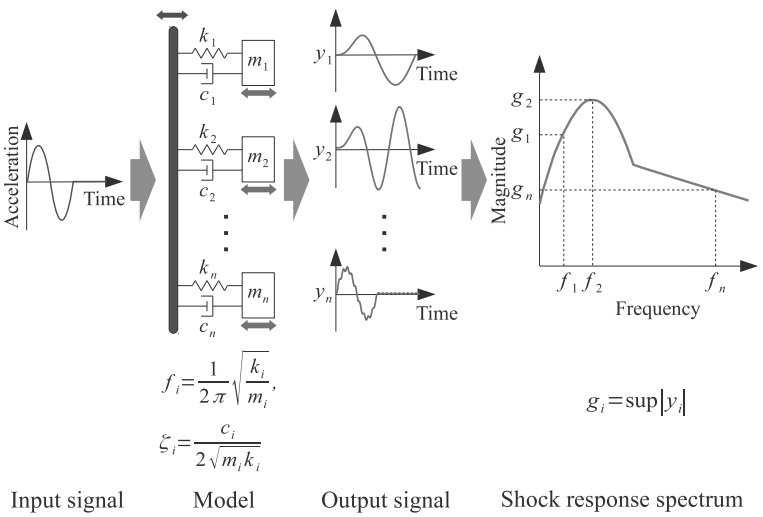

FIGURE 4.26
Basic concept of SRS analysis.

The steps for SRS analysis are as follows:

- Step 1: Determine an input signal for the SRS analysis;
- Step 2: Determine a model for the SRS analysis consisting of spring-mass-damper systems. Each spring-mass-damper system has the same damping ratio and a different resonant frequency;
- Step 3: Calculate the output signal of each spring-mass-damper system with the input signal. This is called the "shock response";
- Step 4: Plot the maximum amplitude of the shock response vs. the resonant frequency of each spring-mass-damper system. This is called the SRS.

The input signal for the SRS analysis is given by

$$u_{srs}(t) = \begin{cases} u_{acc}(t) : 0 \leq t \leq T_{srs} \\ 0 : t > T_{srs} \end{cases}, \tag{4.53}$$

where $u_{acc}(t)$ is the acceleration signal and T_{srs} is the time-width of $u_{acc}(t)$. The SRS analysis model is given by

$$P_{srs}(s) = \frac{s^2}{s^2 + 2\zeta_{srs}(2\pi f_{srs})s + (2\pi f_{srs})^2}, \tag{4.54}$$

where f_{srs} is a specific frequency and ζ_{srs} is the damping ratio. This model is called the *relative acceleration model*, and is suitable for analyzing settling vibrations because mechanical vibrations caused by control inputs depend on the characteristics of relative accelerations. The output signal $y_{srs}(t)$ from the SRS model is given by the convolution

$$y_{srs}(t) = \mathcal{L}^{-1}[P_{srs}(s)] * u_{srs}(t). \tag{4.55}$$

In SRS analysis, there are two kinds of responses. One of them is the *initial shock response,* which is the largest response observed after the start of the shock, and the other is the *residual shock response,* which is the largest response observed after the end of the shock. The magnitude of the initial shock response is defined as

$$g_{srs}(f_{srs}) = \sup_{t \in [0,\infty)} |y_{srs}(t)|, \tag{4.56}$$

and the magnitude of the residual shock response is defined as

$$g_{srs}(f_{srs}) = \sup_{t \in [T_{srs},\infty)} |y_{srs}(t)|. \tag{4.57}$$

The purpose of this section is to analyze residual vibrations. As such, the focus of this chapter from here onwards will be on the residual shock response depicted in (4.57).

4.4.1.2 SRS Analysis Using Half-Sine Wave

To show the characteristics of residual vibrations in sampled-data control systems, SRS analyses are performed using half-sine waves that are widely employed as acceleration signals in SRS analyses. The acceleration signal using the half-sine wave is given by

$$u_c(t) = \sin \frac{\pi t}{T_{srs}}, \quad 0 \le t \le T_{srs}. \tag{4.58}$$

The acceleration signal using the half-sine wave with a Zero-Order-Hold (ZOH) whose sampling time T_{zoh} is given by

$$u_{zoh}(t) = u_c(nT_{zoh}), \quad nT_{zoh} \le t < (n+1)T_{srs}, \tag{4.59}$$

where n is the sample number. The half-sine waves are shown in Figure 4.27. The maximum amount of acceleration is 1 m/s^2, and the width of the $T_{srs} =$ 0.5 ms.

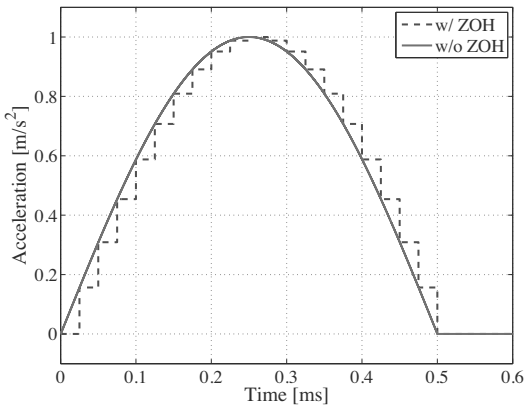

FIGURE 4.27
Time responses of half-sine waves for SRS analysis. Dashed: with ZOH at a sampling time of 25 μs (sampling frequency of 40 kHz). Solid: without ZOH.

A comparison of the results of the SRS analysis with and without the ZOH is shown in Figure 4.28. In this figure, $\zeta_{srs} = 0$. The SRS result without the ZOH shows that residual vibration is large only when the resonant frequency is around 1.4 kHz. In contrast, the SRS result with the ZOH shows that residual vibration is large when the resonant frequencies are around 1.4 kHz, 38.6 kHz, 41.4 kHz, 78.6 kHz, and 81.4 kHz. This means that the large magnitude of the SRS at low frequencies is spread over all of the aliasing frequencies due to the effects of the sampler in the ZOH. Consequently, the magnitude of the SRS around the Nyquist frequency and its integer multiples is small, and the magnitude of the SRS around the sampling frequency and its integer multiples is large.

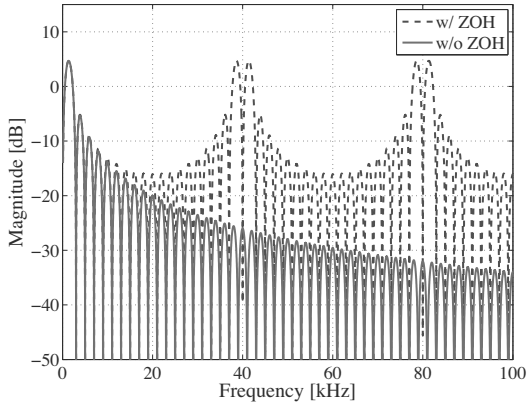

FIGURE 4.28
Comparison of SRS results with and without the ZOH ($\zeta_{srs} = 0$). Dashed: with ZOH. Solid: without ZOH.

To evaluate the effects of the damping ratio, two values of ζ_{srs} given by $\zeta_{srs} = 0$ and $\zeta_{srs} = 0.005$ are used for SRS analysis using the half-sine wave shown by the dashed line in Figure 4.28. In Figure 4.28, the case of $\zeta_{srs} = 0$ means that the mechanical resonance has no damping, and $\zeta_{srs} = 0.005$ means that the mechanical resonance has an average damping ratio.

In Figure 4.29, the SRS result with $\zeta_{srs} = 0$ shows points with nearly zero-magnitude at regular frequency intervals. These points are dependent on the period of the half-sine wave and the ZOH. The SRS result with $\zeta_{srs} = 0.005$ shows that increasing the damping ratio of the resonant mode will result in a decrease in the residual vibration at almost all frequencies, except those near the zero-magnitude frequencies of the case where $\zeta_{srs} = 0$.

Figure 4.30 shows the results of the shock response $y_{srs}(t)$ using $\zeta_{srs} = 0.005$, with the half-sine wave shown by the dashed line in Figure 4.27. In this figure, (a) shows the result with $f_{srs} = 20$ kHz which coincides with the Nyquist frequency of the ZOH, (b) shows the result with $f_{srs} = 40$ kHz which coincides with the sampling frequency of the ZOH, and (c) shows the result with $f_{srs} = 38.6$ kHz. Figure 4.27 also shows that the maximum value of the $y_{srs}(t)$ occurs when $f_{srs} = 38.6$ kHz. In particular, the residual vibration of $y_{srs}(t)$ with $f_{srs} = 38.6$ kHz is far larger than the residual vibrations with $f_{srs} = 20$ kHz, or $f_{srs} = 40$ kHz.

To show the effects of the period of the half-sine wave, two half-sine waves are used for SRS analysis. In Figure 4.31, the dashed line represents the half-sine wave whose period is 0.5 ms, and the solid line represents the half-sine wave whose period is 1 ms. The results of SRS analysis of these half-sine waves with $\zeta_{srs} = 0$ are shown in Figure 4.32. The SRS result with the half-sine wave whose period is 1 ms shows that the residual vibration is largest when

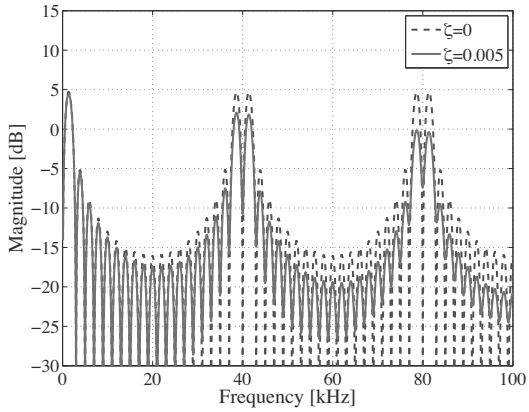

(a) SRS below 100 kHz

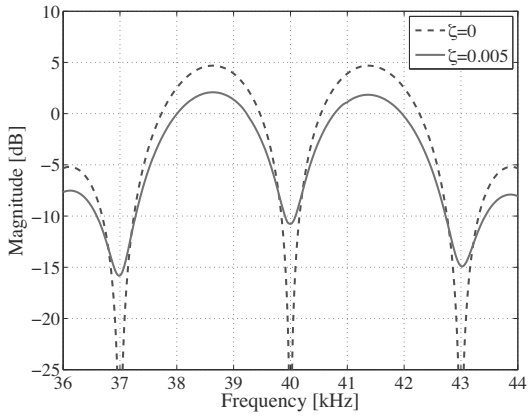

(b) Close-up of SRS around the sampling frequency

FIGURE 4.29
SRS of half-sine wave whose period is 0.5 ms, with ZOH. Solid: $\zeta_{srs} = 0.005$. Dashed: $\zeta_{srs} = 0$.

the resonant frequencies are around 700 Hz, 39.3 kHz, and 40.7 kHz. This is because the distance between the frequency around the sampling frequency where the magnitude of the SRS is largest and the sampling frequency depends on the period of the half-sine wave.

4.4.1.3 SRS Analysis Using Polynomial Wave

The half-sine wave is widely employed as an acceleration signal in SRS analyses. However, feedforward control systems employing time polynomials are widely used in positioning control systems with a controlled object that can be modeled as a rigid-body mode using a double integrator. As such, SRS

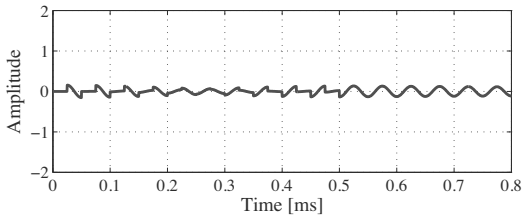

(a) f_{srs}: 20 kHz (the Nyquist frequency)

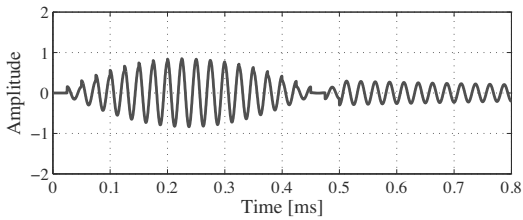

(b) f_{srs}: 40 kHz (the sampling frequency)

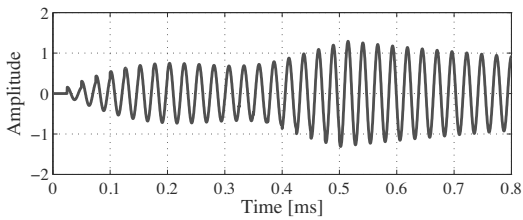

(c) f_{srs}: 38.6 kHz

FIGURE 4.30
Results of shock response $y_{srs}(t)$ using $\zeta_{srs} = 0.005$, with the half-sine waves shown by the dashed line in Figure 4.27.

analyses using acceleration inputs based on polynomials-in-time are described in this section.

A discrete-time acceleration input signal $F_{poly}(n)$ which satisfies the boundary conditions including the characteristics of a ZOH is generated with the sampled-data polynomial given by [4]

$$F_{poly}(n) = \frac{840n^2(n-N)^3(-10+(7n-3N)N(1+N^2))P_t}{N(N^2-4)(N^2-1)(N^2+5)(10+3(N^2+N^4))\tau_{ff}^2}, \qquad (4.60)$$

where N is the period of the acceleration input in terms of samples and P_t is the target of the moving span in meters. In this case, the acceleration signal for SRS analysis is given by

$$u_{acc}(t) = F_{poly}(n), \quad nT_{zoh} \le t < (n-1)T_{zoh}. \qquad (4.61)$$

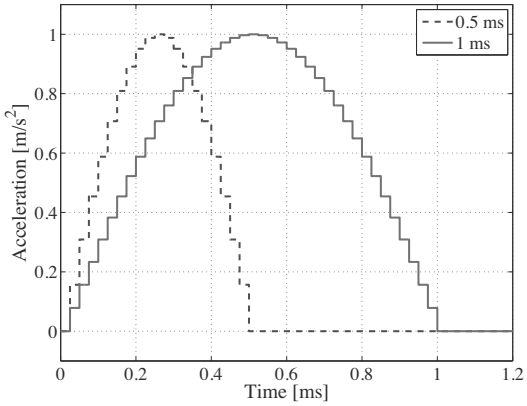

FIGURE 4.31
Time responses of half-sine waves with ZOH for SRS analysis. Dashed: 0.5 ms. Solid: 1 ms.

The acceleration inputs based on polynomials-in-time for SRS analysis are shown in Figure 4.33. The dashed line represents the polynomial wave whose period is 20 samples, and the solid line represents the half-sine wave whose period is 40 samples.

Figure 4.34 shows the SRS results using two different values of damping ratio given by $\zeta_{srs} = 0$ and $\zeta_{srs} = 0.005$, and with the polynomial wave shown by the dashed line in Figure 4.33. Figure 4.35 shows the SRS results using the two polynomial waves of different periods as shown in Figure 4.33. The SRS result with $\zeta_{srs} = 0.005$ which is shown by the solid lines in Figure 4.34 is larger than that using the half-sine waves which is shown by the solid lines in Figure 4.29, because the values of T_{srs} are different in these cases. Otherwise, the SRS results with the polynomial waves are similar to the SRS results with the half-sine waves.

Figure 4.36 shows the results of the shock response $y_{srs}(t)$ using $\zeta_{srs} = 0.005$, with the polynomial wave shown by the solid line in Figure 4.33. In this figure, (a) shows the result with $f_{srs} = 20$ kHz which coincides with the Nyquist frequency of the ZOH, (b) shows the result with $f_{srs} = 40$ kHz which coincides with the sampling frequency of the ZOH, and (c) shows the result with $f_{srs} = 38.7$ kHz. It can be seen that the maximum value of $y_{srs}(t)$ and the residual vibration of $y_{srs}(t)$ are largest when $f_{srs} = 38.7$ kHz.

4.4.1.4 Comparison between SRS and DFT

To analyze the amplitude of the mechanical vibrations caused by the acceleration input signal, the method that is most generally used is DFT analysis with Fast Fourier Transform (FFT). While DFT analysis is suitable for analyzing

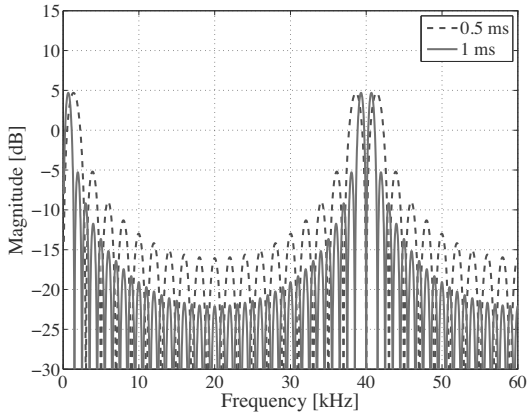

(a) SRS below 60 kHz

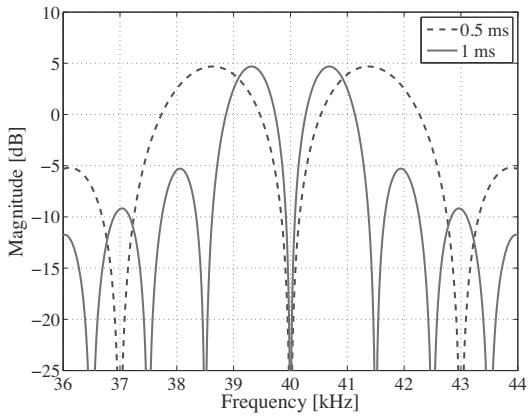

(b) Close-up of SRS around the sampling frequency

FIGURE 4.32
Comparison of SRS results between the half-sine wave having a width of 0.5 ms and the half-sine wave having a width of 1 ms. Dashed: 0.5 ms. Solid: 1 ms.

the contents of steady-state characteristics, it is not suitable for analyzing transient characteristics.

To show the difference between DFT and SRS analyses, a DFT analysis of the acceleration input is performed. Figure 4.37 shows a comparison between the results of the SRS and that of the DFT analysis with the polynomial wave shown by the solid line in Figure 4.33. In this figure, the solid line represents the DFT result shown using an amplitude spectrum, the dashed line represents the SRS result with $\zeta_{srs} = 0$, and the dot-dashed line represents the SRS result with $\zeta_{srs} = 0.005$. These results are normalized so that the maximum magnitude is of 0 dB.

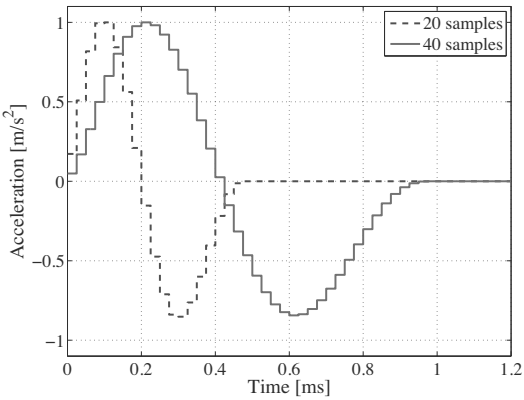

FIGURE 4.33
Acceleration inputs based on polynomials-in-time for SRS analysis. Dashed: 20 samples. Solid: 40 samples.

Figure 4.37 shows that the amplitude of the DFT result decreases as frequency increases. This is caused by the low-pass filter effect of the ZOH on the steady-state behavior. In contrast, the SRS result with $\zeta_{srs} = 0$ shows that for transient-state behavior, the magnitude is not at all decreased by the ZOH as frequency increases.

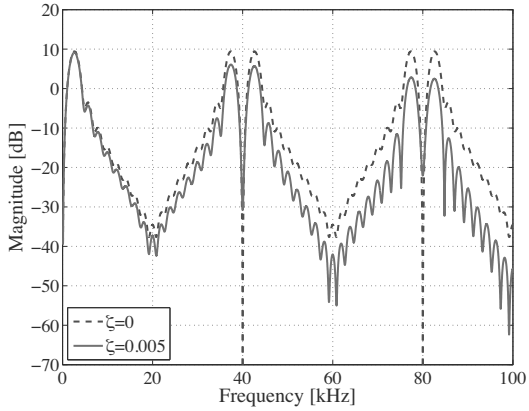

(a) SRS below 100 kHz

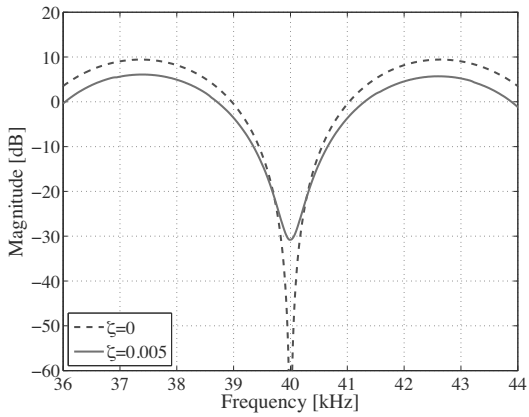

(b) Close-up of SRS around the sampling frequency

FIGURE 4.34
SRS of polynomial wave whose period is 20 samples. Solid: $\zeta_{srs} = 0.005$. Dashed: $\zeta_{srs} = 0$.

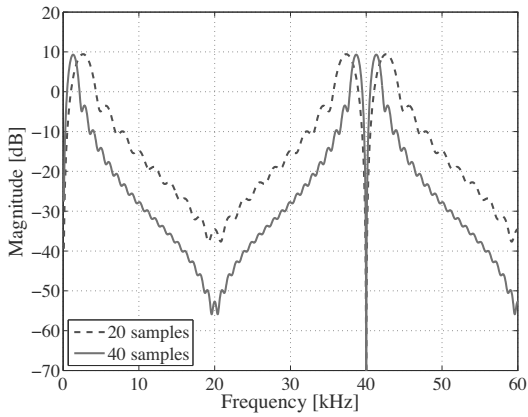

(a) SRS below 60 kHz

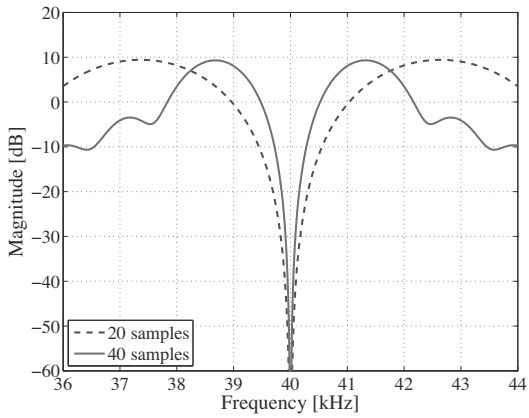

(b) Close-up of SRS around the sampling frequency

FIGURE 4.35
Comparison of SRS results between the polynomial wave with a period of 20 samples and the polynomial wave with a period of 40 samples using $\zeta_{srs} = 0$. Dashed: 20 samples. Solid: 40 samples.

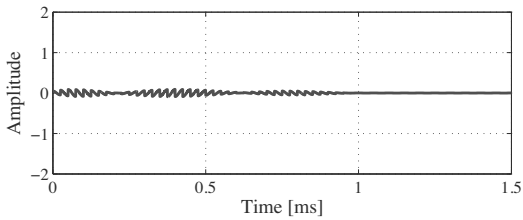

(a) f_{srs}: 20 kHz (the Nyquist frequency)

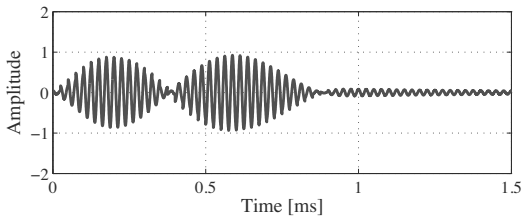

(b) f_{srs}: 40 kHz (the sampling frequency)

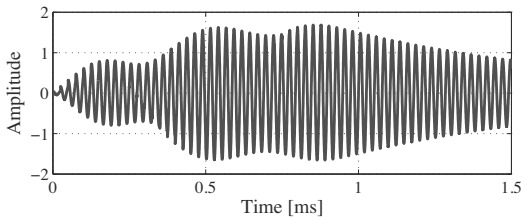

(c) f_{srs}: 38.7 kHz

FIGURE 4.36
Results of shock response $y_{srs}(t)$ using $\zeta_{srs} = 0.005$ with the polynomial wave shown by the solid line in Figure 4.33.

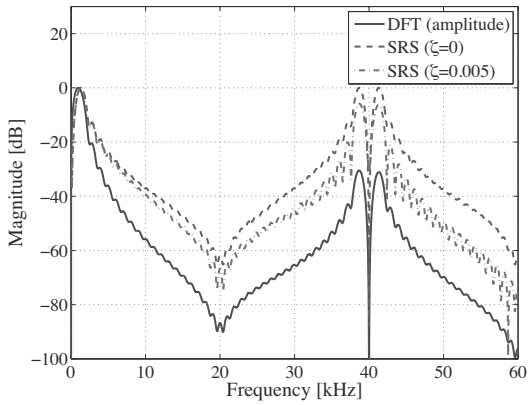

FIGURE 4.37
Comparison of SRS results with DFT of polynomial wave whose width is 40 samples. Solid: DFT (amplitude spectrum). Dashed : SRS ($\zeta_{srs} = 0$). Dashed-dot: SRS ($\zeta_{srs} = 0.005$).

4.5 Hard Disk Drive Example

In this section, the head-positioning control system in an HDD is used as a classical mechatronic product for design purposes. The head-positioning control system is one of the most widely used feedback control systems in the world, and is essential to the infrastructure of our advanced information society.

4.5.1 Head-Positioning Control System

An HDD is comprised of a Voice Coil Motor (VCM), several magnetic heads, several disks, and a spindle motor, as shown in Figure 4.38. The head-positioning control system in an HDD is illustrated in Figure 4.39. In the

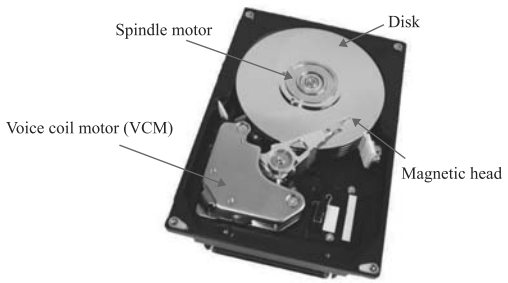

FIGURE 4.38
Primary components of an HDD.

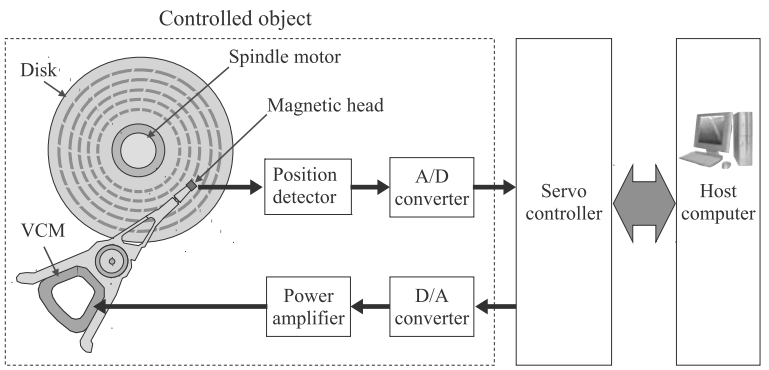

FIGURE 4.39
Illustration of the head-positioning system, which can be modeled as a sampled-data control system with a sampler and a hold.

head-positioning control system, the various sources of disturbances include periodic disturbances caused by disk rotation known as repeatable runout, effects of torque noise, and mechanical vibrations excited by the airflow induced by the spinning disks, etc. The controlled variable is the head-position signal, which is generated from embedded information on the disks and read at a fixed time interval. This means that the head-position signal is only available as a discrete-time signal. The control input is an input command value to a VCM driver amplifier, which is calculated by a digital signal processor at certain intervals. As such, the head-positioning control system can be thought of as a sampled-data control system that has a sampler and a hold.

4.5.1.1 Controlled Object

In this section, it is assumed that gain of the controlled object $P_c(j\omega)$ in the continuous-time system is negligible when $\omega > 2\omega_s$. In order to reduce the calculation load, the frequency response of $P_c(j\omega)$ is defined as

$$P_c(j\omega_0) = \begin{cases} P_{c0}(j\omega_0), & |\omega_0| \leq 2\omega_s, \\ 0, & |\omega_0| > 2\omega_s. \end{cases} \tag{4.62}$$

P_{c0} is assumed to be given by the product of the mechanical model P_s and the equivalent delay-time model P_{dl} as

$$P_{c0}(s) = P_s(s)P_{dl}(s). \tag{4.63}$$

The mechanical model P_s is given by

$$P_s(s) = K_p \sum_{l=1}^{\psi} \frac{\alpha_k(l)}{s^2 + 2\zeta_k(l)\omega_{nk}(l)s + \omega_{nk}(l)^2}, \tag{4.64}$$

where ψ is the number of modes, α_k is the residue of each mode, ω_{nk} and ζ_k are the natural frequency in rad/s and damping ratio of the resonance, respectively, and K_p is the plant gain. These parameters are chosen so that the frequency response of the model coincides with the measured result indicated by the solid line in Figure 4.40. To be more precise, $\psi = 7$ as the order of the model is 14, $K_p = 4.3 \times 10^7$, and the values of the other parameters are listed in Table 4.1. The dashed line in Figure 4.40 represents the frequency response of this mathematical model.

The equivalent time delay model P_{dl} includes the characteristics of the delay-time element, and is given by

$$P_{dl}(s) = e^{-\tau s}, \tag{4.65}$$

where τ is the equivalent time delay of 10 μs in this study.

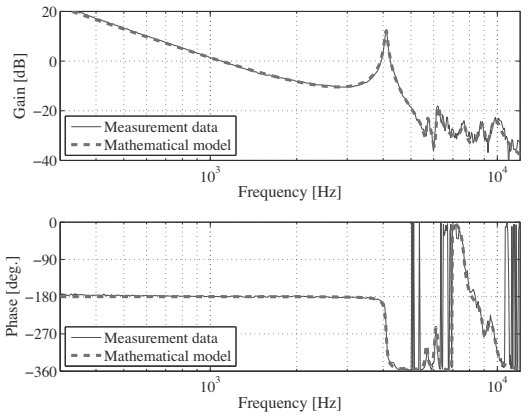

FIGURE 4.40
Frequency response of the mechanical system.

TABLE 4.1
Parameters of $P_s(s)$

l	$\omega_{nk}(l)$	$\alpha_k(l)$	$\zeta_k(l)$
1	0	1.00	0
2	$2\pi 4100$	−1.30	0.01
3	$2\pi 5700$	−0.03	0.01
4	$2\pi 6200$	−0.08	0.01
5	$2\pi 7650$	0.12	0.02
6	$2\pi 8900$	−0.13	0.02
7	$2\pi 9800$	−0.35	0.03

4.5.2 Sensitivity and Complementary Sensitivity Transfer Functions

In this example, the head-positioning control system uses a multi-rate filter, and its block diagram is shown in Figure 4.2. The sampling time T_s is set as 153.5 μs, resulting in $\omega_s = 2\pi 6516$ rad/s, and the multi-rate number m is set as 4. The multi-rate hold $\mathcal{H}_m$ is the ZOH, and its transfer characteristic is given by

$$\mathcal{H}_m(s) = \frac{1 - e^{-\frac{sT_s}{4}}}{s}. \tag{4.66}$$

The interpolator I_p consists of an up-sampler and an interpolation filter. The transfer function of the interpolation filter can be given by

$$I_p(z) = 1 + z^{-1} + z^{-2} + z^{-3}. \tag{4.67}$$

4.5.2.1 Design of Control System

In this example, it is desired to make $|S_{sd}| < 1$ for frequencies below 500 Hz which is the frequency range where $|d_c|$ is considered to be large. To check the characteristics above the Nyquist frequency, the other aim is to decrease $|S_{sd}|$ at 3600 Hz by using a multi-rate filter.

First, the multi-rate filter which creates the stable resonant characteristic is designed. To suppress the disturbance at 3.6 kHz, F_m needs to create the resonant characteristic which is an in-phase condition for the mechanical resonant mode of P_{dm} at 4.1 kHz such that the controller can stabilize both resonances simultaneously. In this case, a continuous-time filter F_{mc} is set as

$$F_{mc}(s) = 1 - \frac{0.1s^2}{s^2 + 2(0.003)(2\pi 3600)s + (2\pi 3600)^2}, \tag{4.68}$$

and F_m is the discretization of F_{mc} using Tustin transformation with frequency prewarping. The frequency response of F_m is shown in Figure 4.41, and the frequency response of WP_c is shown in Figure 4.42.

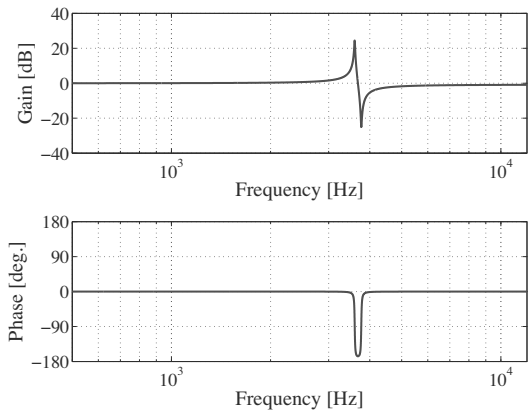

FIGURE 4.41
Frequency response of the multi-rate filter F_m which realizes the resonant characteristic at 3.6 kHz.

The frequency response of the controlled object P_{dm} in the discrete-time system is shown in Figure 4.43. These figures indicate that the multi-rate filter realizes the resonant characteristic at 3.6 kHz, which is an in-phase condition for the mechanical resonance at 4.1 kHz.

The Proportional-and-Integral (PI) lead filter structure is used in C for P_{dm}. To make the phase margin more than 30°, the gain margin greater than 4.5 dB, $|S_d| < 1$ for frequencies below 500 Hz, and to phase-stabilize the two resonant modes, C is chosen to be

$$C(z) = \frac{0.872(z - 0.490)(z - 0.865)(z - 0.908)}{(z - 0.0182)(z - 0.409)(z - 1)}. \tag{4.69}$$

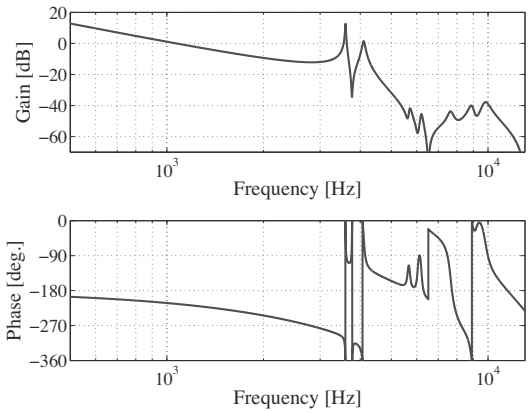

FIGURE 4.42
Frequency response of WP_c.

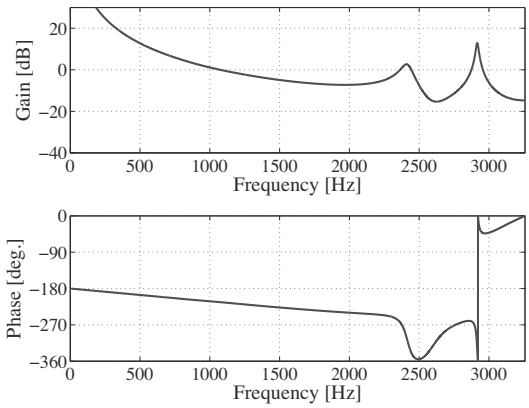

FIGURE 4.43
Frequency response of controlled object P_{dm} in discrete-time system.

The frequency response of C is shown in Figure 4.44, and the frequency response of the open-loop characteristics $P_{dm}C$ of the discrete-time system is shown in Figure 4.45.

The magnitude response of $\sum_{l=-\infty,\neq 0}^{\infty} |\Gamma_m(\omega_0, l)|$ is shown in Figure 4.46. This figure indicates that the control system makes $\sum_{l=-\infty,\neq 0}^{\infty} |\Gamma_m(\omega_0, l)|$ small at frequencies below 500 Hz and at 3.6 kHz.

The frequency responses of $|S_d|$ and $|T_d|$ are shown in Figure 4.47. The frequency responses of $|S_{sd}|$ and $|T_{sd}|$ are shown in Figure 4.48, and the frequency responses of $|S_\Delta|$ and $|T_\Delta|$ are shown in Figure 4.49.

It is clear that the characteristics of the sensitivity and complementary sen-

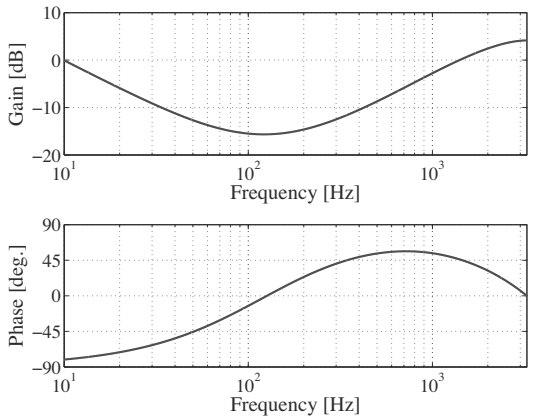

FIGURE 4.44
Frequency response of controller C designed for P_{dm}.

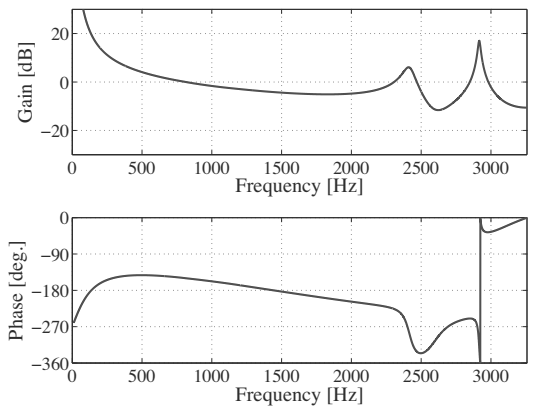

FIGURE 4.45
Frequency response of open-loop characteristics $P_{dm}C$ of discrete-time system.

sitivity transfer functions in the sampled-data control system are very different from that in the discrete-time control system for frequencies above 2 kHz. This means that the difference between the discrete-time control system and the sampled-data control system should be known even for frequencies below the Nyquist frequency.

4.5.2.2 Simulation and Experiment

Two time-domain simulations are performed for the control system. One uses a disturbance signal d_c at 3.6 kHz, and the other uses a disturbance signal d_c

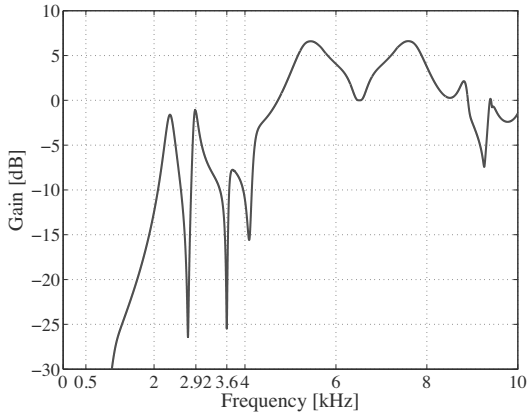

FIGURE 4.46
Frequency response of $\sum_{l=-\infty,\neq 0}^{\infty} |\Gamma_m(\omega_0, l)|$.

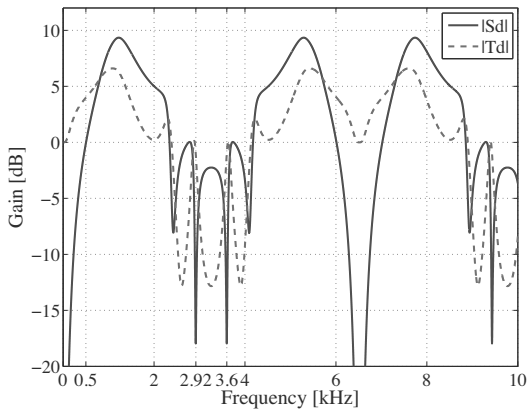

FIGURE 4.47
Magnitude responses of sensitivity and complementary sensitivity transfer functions of the discrete-time system. Solid:$|S_d|$. Dashed: $|T_d|$.

at 2.916 kHz which is an aliasing frequency of 3.6 kHz. In both simulations, the amplitude of $d_c = 0.1$ track pitch and reference r is set to 0.

The simulation results with $d_c = 3.6$ kHz are shown in Figure 4.50, and the simulation results with $d_c = 2.916$ kHz are shown in Figure 4.51. In both figures, y_d is indicated by the solid line in (a), y_{d0} is indicated by the dashed line in (a), y_c is indicated by the solid line in (b), and y_{c0} is indicated by the dashed line in (b).

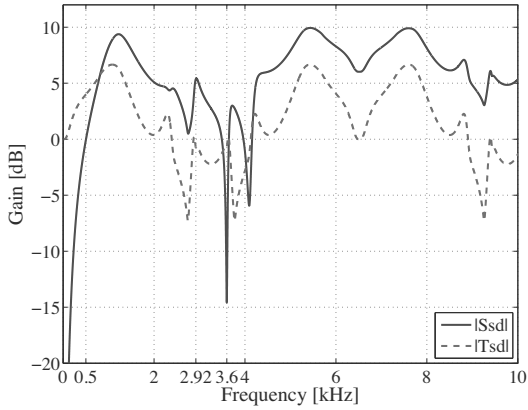

FIGURE 4.48
Magnitude responses of sensitivity and complementary sensitivity transfer functions of the sampled-data control system. Solid: $|S_{sd}|$. Dashed: $|T_{sd}|$.

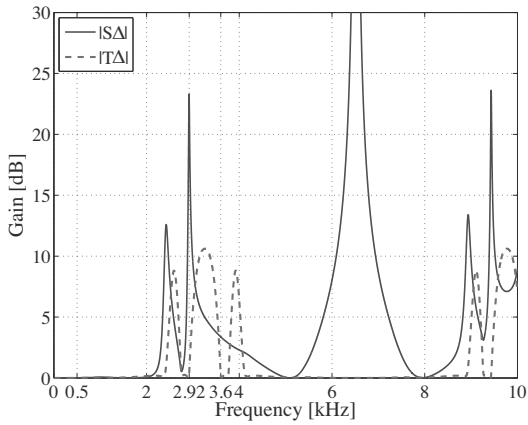

FIGURE 4.49
Magnitude responses of $|S_\Delta|$ and $|T_\Delta|$ which illustrate the difference between $|S_{sd}|$ and $|S_d|$, and the difference between $|T_{sd}|$ and $|T_d|$, respectively. Solid: $|S_\Delta|$. Dashed: $|T_\Delta|$.

The simulation results with $d_c = 3.6$ kHz show that

$$\frac{||y_c(t)||_\infty}{||d_c(t)||_\infty} = 0.18, \quad \frac{||y_{c0}(t)||_\infty}{||d_c(t)||_\infty} = 0.92,$$
$$\frac{||y_d(t)||_\infty}{||d_c(t)||_\infty} = 0.13, \quad \frac{||y_{d0}(t)||_\infty}{||d_c(t)||_\infty} = 0.90, \tag{4.70}$$

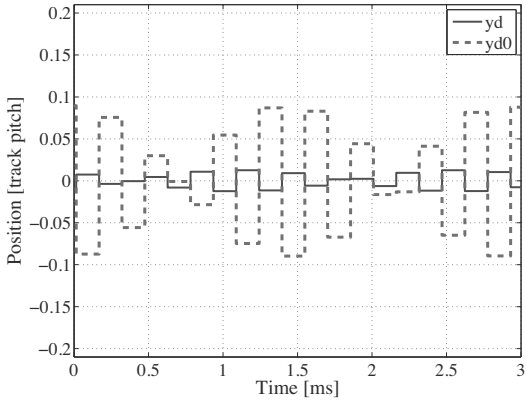

(a) y_d and y_{d0}

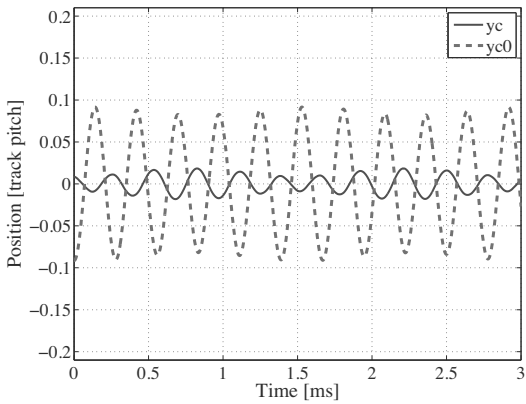

(b) y_c and y_{c0}

FIGURE 4.50
Simulated head-position with disturbance at 3.6 kHz.

and the simulation results with $d_c = 2.916$ kHz show that

$$\frac{||y_c(t)||_\infty}{||d_c(t)||_\infty} = 1.85, \quad \frac{||y_{c0}(t)||_\infty}{||d_c(t)||_\infty} = 0.92,$$
$$\frac{||y_d(t)||_\infty}{||d_c(t)||_\infty} = 0.13, \quad \frac{||y_{d0}(t)||_\infty}{||d_c(t)||_\infty} = 0.90. \tag{4.71}$$

These results indicate that the simulation results are almost identical to the results in Figures 4.47 and 4.48.

To validate the effects of the proposed method, experiments are conducted using conditions which are similar to those of the simulations. In these experiments, y_{c0} and y_c are discrete-time signals with a sampling time of 38.4 μs

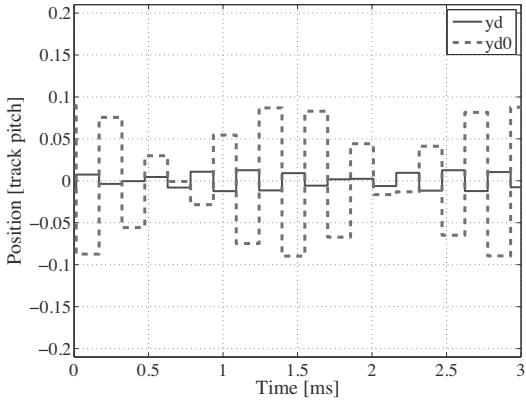

(a) y_d and y_{d0}

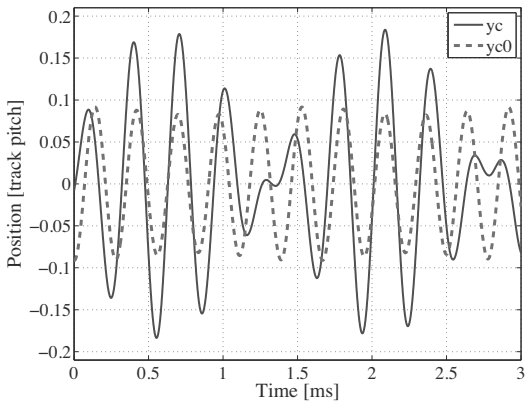

(b) y_c and y_{c0}

FIGURE 4.51
Simulated head-position with disturbance at 2.916 kHz.

which is $\frac{T_s}{4}$. This is because the continuous-time signal cannot be measured in actual head-positioning systems. The experimental results with $d_c = 3.6$ kHz are shown in Figure 4.52, and the results with $d_c = 2.916$ kHz are shown in Figure 4.53. In both figures, y_d is indicated by the solid line in (a), y_{d0} is indicated by the dashed line in (a), y_c is indicated by the solid line in (b), y_{c0} is indicated by the dashed line in (b). These experimental results show that they are also almost the same as the simulation results.

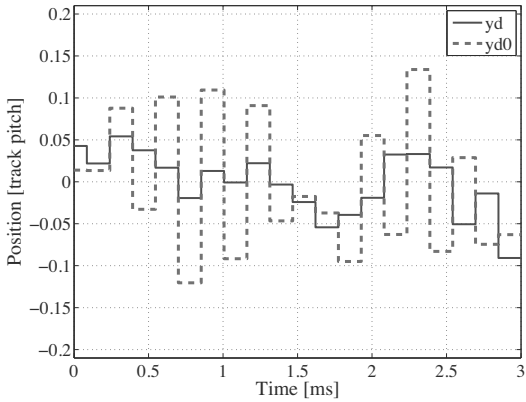

(a) y_d and y_{d0}

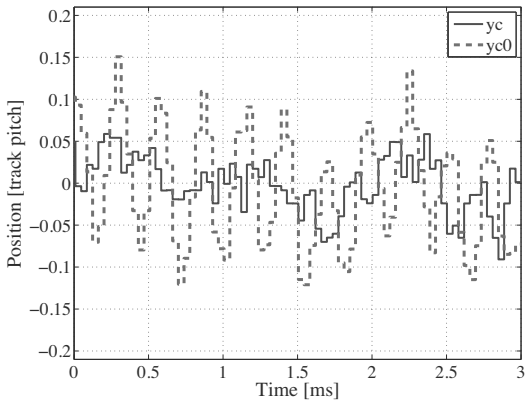

(b) y_c and y_{c0}

FIGURE 4.52
Experimental results illustrating head-position with disturbance at 3.6 kHz.

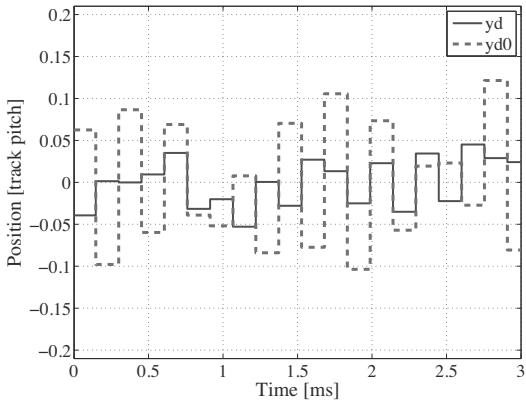

(a) y_d and y_{d0}

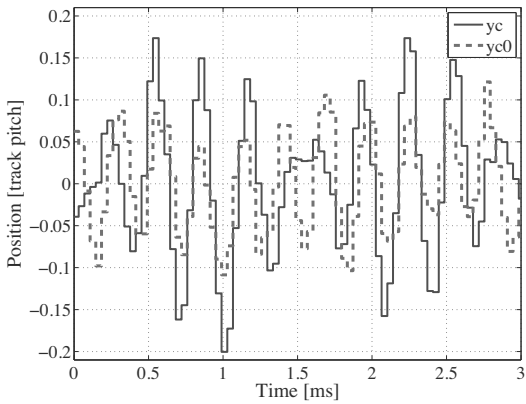

(b) y_c and y_{c0}

FIGURE 4.53
Experimental results illustrating head-positions with disturbance at 2.916 kHz.

4.5.3 Unobservable Oscillations

In this example, the unobservable magnitudes for oscillations in the head-positioning control system are analyzed. The controlled object has a primary mechanical resonance at 4.1 kHz and other mechanical resonances are much smaller than the primary resonance as shown by Figure 4.40 and Table. 4.1. As such, the focus in this example is on the unobservable oscillation of the primary resonant mode. The damped natural frequency $\omega_d = 2\pi 4100$ rad/s and the damping ratio $\zeta = 0.01$ as indicated by Table. 4.1, and y_{ui} are calculated.

The dependence of y_{ui} on the sampling frequency is shown in Figure 4.54. In the head-positioning control system, the number of servo sectors on the disks must be decided so that the sampling frequency does not coincide with the unacceptable sampling frequencies shown in Figure 4.54. For example, the solid line shows that most of the frequencies from 1 kHz to 10 kHz are unacceptable sampling frequencies when $N_s = 5$, and the acceptable level of unobservable magnitude is 0.1. The dashed line shows that the sampling frequency cannot be chosen to be around 1.02 kHz, 1.37 kHz, 2.05 kHz, 2.73 kHz, 4.10 kHz, 82.0 kHz, and 123 kHz when $N_s = 10$, and the acceptable level of unobservable magnitude is 0.1. The dot-dashed line shows that the sampling frequency cannot be chosen to be around 2.05 kHz, 4.10 kHz, and 8.20 kHz when N_s is 20, and the acceptable level of unobservable magnitude is 0.1.

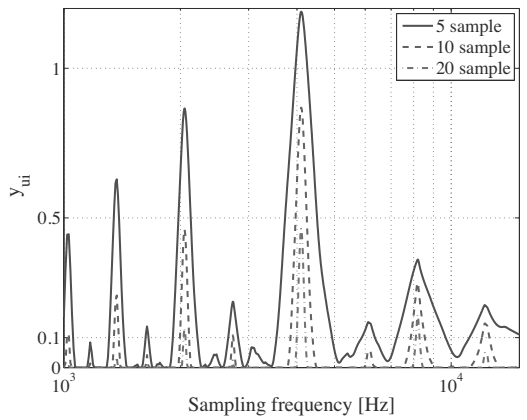

FIGURE 4.54
Relationship between y_{ui} and sampling frequency considering the primary mechanical resonance, with $\omega_d = 2\pi \cdot 4100$ and $\zeta = 0.01$. Solid: $N_s = 5$. Dashed: $N_s = 10$. Dashed-dot: $N_s = 20$.

The dependence of y_{ui} on the measurement time $\tau \times N_s$ for the judgment of maximum displacement is shown in Figure 4.55. In this figure, the solid line represents the result with $\tau = 244$ μs (4.1 kHz), the dashed line represents the

result with $\tau = 233$ μs (4.3 kHz), and the dot-dashed line represents the result with $\tau = 222$ μs (4.5 kHz). In the head-positioning control system, the sample number for the judgment of the maximum displacement N_s must be decided so that y_{ui} is smaller than the acceptable level of unobservable magnitude caused by the mechanical resonance at 4.1 kHz. For example, the dashed line shows that $\tau \times N_s$ should be more than 3 ms when the acceptable level of $y_{ui} = 0.1$ and $\tau = 233$ μs (4.3 kHz).

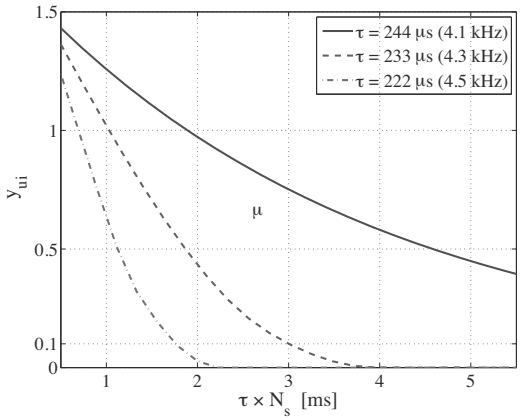

FIGURE 4.55
Relationship between y_{ui} and $\tau \times N_s$ considering the primary mechanical resonance. Solid: $\tau = 244$ μs (4.1 kHz). Dashed: $\tau = 233$ μs (4.3 kHz). Dot-dashed: $\tau = 222$ μs (4.5 kHz).

4.5.4 Residual Vibrations

In this example, the residual vibrations of the head-positioning control system that uses a Two-Degrees-of-Freedom (TDOF) control system are analyzed. The block diagram of a sampled-data control system based on TDOF control is shown in Figure 4.56.

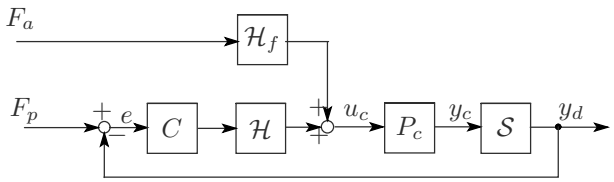

FIGURE 4.56
Block diagram of TDOF control system.

In this example, the results of residual vibrations in track-seeking con-

trol are presented. The head-positioning system uses a TDOF control system shown in Figure 4.57. In this figure, $\mathcal{S}$ is a sampler, C is a feedback controller, $\mathcal{H}$ is a hold for the feedback control input, $\mathcal{H}_f$ is a hold for the acceleration feedforward control input, and P_c is a controlled object in continuous time. F_a is an acceleration feedforward input signal in discrete time, F_p is a position feedforward input signal in discrete time, and I_p is an interpolator that consists of a ZOH and an up-sampler. M_f is a discrete-time model that generates the position feedforward input F_p from the acceleration feedforward input F_a, u_c is the control input in continuous time, y_c is a controlled variable in continuous time, y_d is a controlled variable in discrete time, and e is a tracking error signal in discrete time.

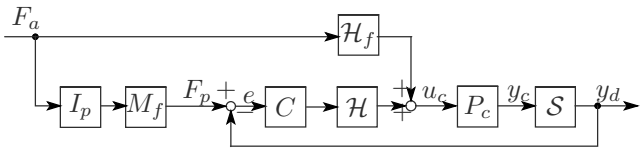

FIGURE 4.57
Block diagram of TDOF control system for experiments.

In this system, the sampling times of $\mathcal{S}$ and $\mathcal{H}$ are denoted as τ_{fb}, and the sampling times of F_a and $\mathcal{H}_f$ are denoted as τ_{ff}. To analyze the relationship between the mechanical resonant frequency and the sampling time of the ZOH, three different values of τ_{ff} are used since the mechanical resonant frequencies are fixed and only the sampling time of the ZOH can be changed. The sampling time of the position feedforward input signal F_p, M_f, and I_p is set as τ_{fb} so that the feedback control has the same performance when the sampling time of the acceleration feedforward input is changed.

4.5.4.1 Feedback Control System

In this control system, the major mechanical modes are Mode 1 which is the rigid-body mode and Mode 2 which is the primary mechanical resonant mode as listed in Table 4.1. The feedback controller $C(z)$ is given by the product of the PI-lead filter $C_p(z)$ and the notch filter $C_n(z)$. $C_p(z)$ provides integral action, and its phase stabilizes the rigid-body mode. $C_n(z)$ stabilizes the primary mechanical resonance by decreasing the gain of the resonance. $C_p(z)$ is the discretization of $C_{pc}(s)$ using bilinear transformation, and $C_n(z)$ is the discretization of $C_{nc}(s)$ using the pole-zero matching method. $C_{pc}(s)$ and $C_{nc}(s)$ provide more than 40° phase margin at 1 kHz and a gain margin of more than 5 dB. $C_{pc}(s)$ and $C_{nc}(s)$ are given by

$$C_{pc}(s) = \frac{1318(s + 628.3)(s + 1257)}{s(s + 25130)} \tag{4.72}$$

and

$$C_{nc}(s) = \frac{s^2 + 515.2s + 663.6 \times 10^6}{s^2 + 7728s + 663.6 \times 10^6}, \tag{4.73}$$

respectively.

The frequency response of $C(z)$ is shown in Figure 4.58. The frequency responses of the sensitivity and complementary sensitivity transfer functions are shown by the solid and dashed lines in Figure 4.59, respectively.

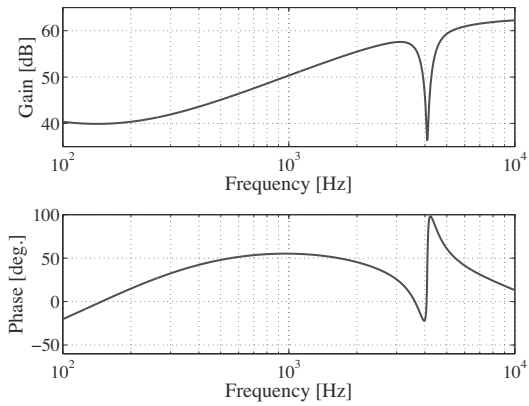

FIGURE 4.58
Frequency response of feedback controller.

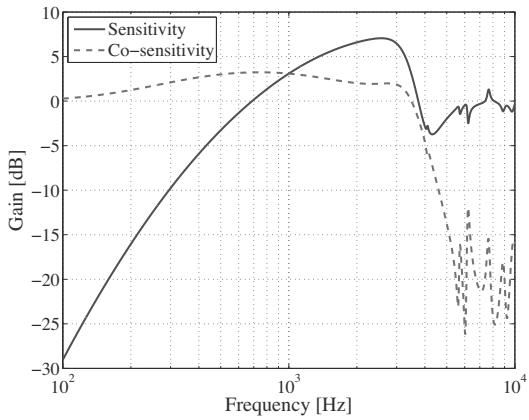

FIGURE 4.59
Magnitude responses of sensitivity and complementary sensitivity transfer functions.

4.5.4.2 Feedforward Control System

The acceleration input $F_a(n)$ is generated with the sampled-data polynomial shown in (4.60). To evaluate the relationship between the mechanical resonant frequency and the sampling frequency of the ZOH, three acceleration inputs whose target seek spans P_t of 500 tracks are used. For the first input, τ_{ff} which is the sampling time of the ZOH $\mathcal{H}_f$ is 115 μs, and target seek time $N = 40$. For the second input, $\tau_{ff} = 230$ μs and $N = 20$. For the third input, $\tau_{ff} = 307$ μs and $N = 15$. The time responses of $F_a(n)$ for the three cases where $\tau_{ff} = 115$ μs, $\tau_{ff} = 230$ μs, and $\tau_{ff} = 307$ μs are shown in Figure 4.60(a) using solid, dashed, and dashed-dot lines, respectively.

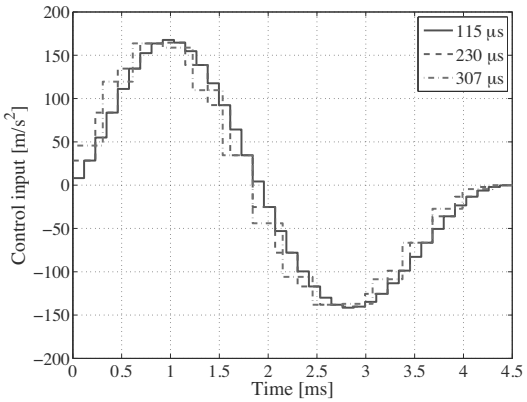

(a) Acceleration feedforward inputs

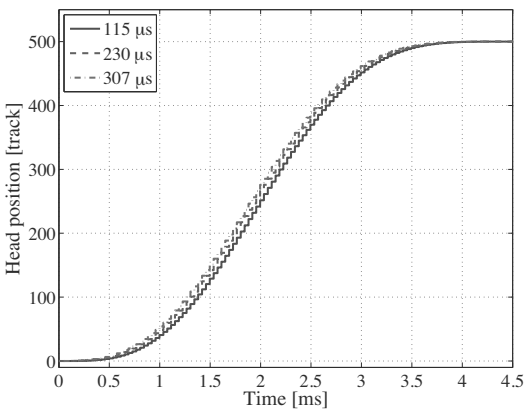

(b) Position feedforward inputs

FIGURE 4.60
Time responses of feedforward inputs. Solid: $\tau_{ff} = 115$ μs. Dashed: $\tau_{ff} = 230$ μs. Dashed-dot: $\tau_{ff} = 307$ μs.

The position feedforward input $F_p(n)$ is generated by the reference model $M_f(z)$ because the computational burden is lower than that of computing the polynomial for the position feedforward input. $F_a(n)$ is the input to $M_f(z)$ via $I_p(z)$, and the output signal from $M_f(z)$ becomes $F_p(n)$.

$M_f(z)$ can be calculated from the continuous-time transfer function $P_f(s)$ by including the delay time and performing discretization with ZOH. $P_f(s)$ is given by

$$P_f(s) = K_p \left(\frac{1}{s^2} + \frac{\alpha_f}{s^2 + 2\zeta_f \omega_f s + \omega_f^2} \right), \tag{4.74}$$

where α_f is the residue of the resonant mode, and ω_f and ζ_f are the natural frequency and damping ratio of the resonant mode, respectively.

ζ_f should be much larger than the damping ratio of the primary mechanical resonance to prevent oscillation in the reference model. To calculate the position feedforward input, α_f, ζ_f, and ω_f are determined so that the frequency response of $P_f(s)$ coincides with the measured frequency response of the mechanical system for frequencies below 2 kHz. As such, $\alpha_f = -1.3$, $\omega_f = 2\pi 3950$ rad/s, and $\zeta_f = 0.3$. By including the delay time T_{dl} and discretizing $P_f(s)$ using a ZOH, $M_f(z)$ is given by

$$M_f(z) = -3.157 \times 10^{-6} \frac{(z - 14.34)(z - 0.3574)(z + 0.1314)(z + 2.408)}{z(z-1)^2(z^2 - 0.9245z + 0.5648)}. \tag{4.75}$$

The position feedforward inputs $F_p(n)$ for the cases where $\tau_{ff} = 115$ μs, $\tau_{ff} = 230$ μs, and $\tau_{ff} = 307$ μs are shown in Figure 4.60(b) using solid, dashed, and dashed-dot lines, respectively.

4.5.4.3 SRS Analysis

The SRS results of the acceleration input in Figure 4.60(a) for the cases of $\tau_{ff} = 115$ μs, $\tau_{ff} = 230$ μs, and $\tau_{ff} = 307$ μs are shown in Figure 4.61 using solid, dashed, and dashed-dot lines, respectively. $\zeta_{srs} = 0.01$ because it should be approximately the same as that of the primary mechanical resonance at 4.1 kHz shown in Table 4.1. It should be noted that the damping ratio of this mechanical resonance in the head-positioning system of HDDs is relatively large.

The controlled object has a primary mechanical resonance at 4.1 kHz as shown by Figure 4.40 and Table 4.1. The SRS results show that the magnitude of the SRS at 4.1 kHz is smallest in the first case where $\tau_{ff} = 115$ μs, because the Nyquist frequency of the ZOH is about 4.3 kHz. The magnitude of the SRS at 4.1 kHz is largest in the second case where $\tau_{ff} = 230$ μs since the sampling frequency of the ZOH is about 4.3 kHz. In the third case where $\tau_{ff} = 307$ μs, the magnitude of the SRS at 4.1 kHz is smaller than that of the second case even though the sampling time is longer than that of the second case.

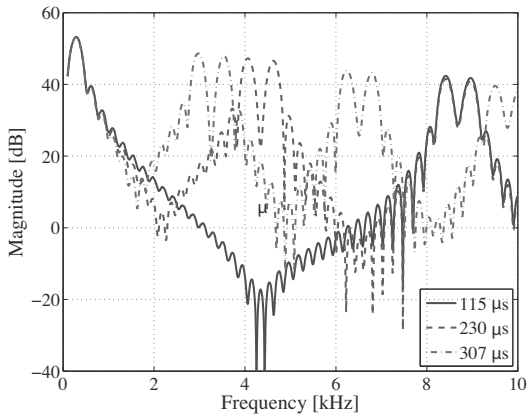

FIGURE 4.61
Results of SRS. Solid: $\tau_{ff} = 115$ μs. Dashed: $\tau_{ff} = 230$ μs. Dashed-dot: $\tau_{ff} = 307$ μs.

4.5.4.4 Simulation and Experimental Results

To verify the results of the SRS analysis, simulations and experiments are conducted for track-seeking control. The simulation results for the head-positions are shown in Figure 4.62, and those of the tracking error signals are shown in Figure 4.63. The experimental results for the head-positions are shown in Figure 4.64, and those of the tracking error signals are shown in Figure 4.65.

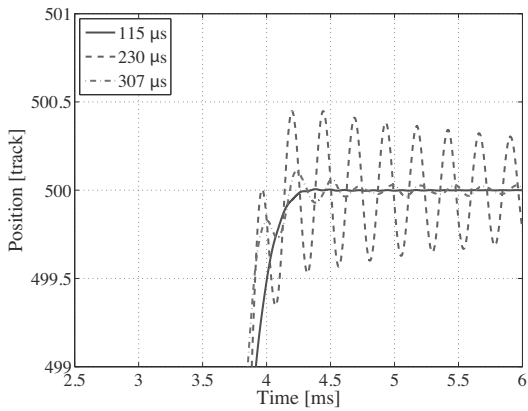

FIGURE 4.62
Simulation results for head positions. Solid: $\tau_{ff} = 115$ μs. Dashed: $\tau_{ff} = 230$ μs. Dashed-dot: $\tau_{ff} = 307$ μs.

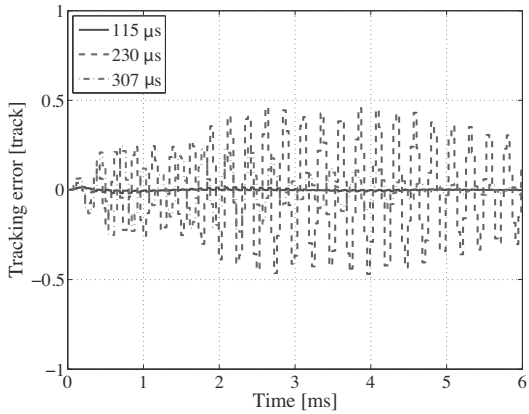

FIGURE 4.63
Simulation results for tracking errors. Solid: $\tau_{ff} = 115$ μs. Dashed: $\tau_{ff} = 230$ μs. Dashed-dot: $\tau_{ff} = 307$ μs.

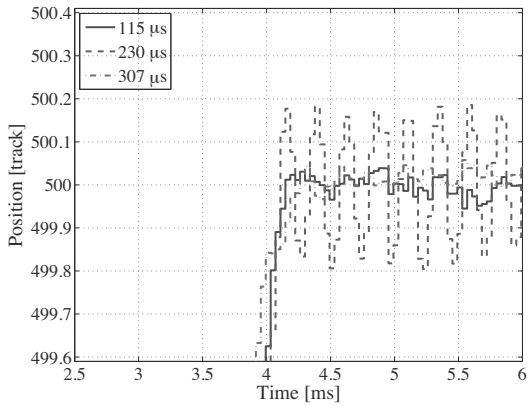

FIGURE 4.64
Experimental results for head positions. Solid: $\tau_{ff} = 115$ μs. Dashed: $\tau_{ff} = 230$ μs. Dashed-dot: $\tau_{ff} = 307$ μs.

These results show that the settling characteristics in simulations and experiments are similar to the SRS results. In other words, the acceleration input with ZOH excites the mechanical resonance near the sampling frequency during settling, but does not excite the mechanical resonances near the Nyquist frequency very much.

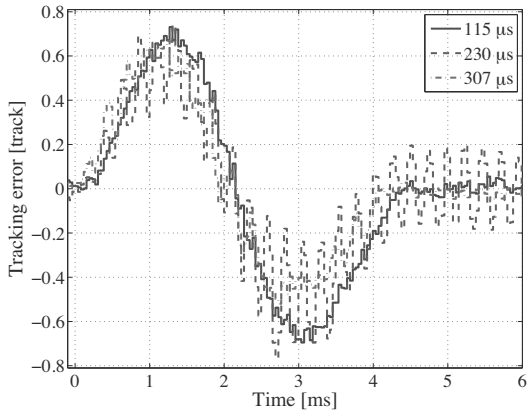

FIGURE 4.65
Experimental results for tracking errors. Solid: $\tau_{ff} = 115$ μs. Dashed: $\tau_{ff} = 230$ μs. Dashed-dot: $\tau_{ff} = 307$ μs.

Bibliography

[1] T. Atsumi and W. C. Messner, "Mixed Sensitivity Problem in Sampled-Data Positioning Control Systems," *Journal of System Design and Dynamics*, Vol. 5, No. 6, pp. 1294–1309, September 2011.

[2] T. Atsumi and W. C. Messner, "Analysis of Unobservable Oscillations in Sampled-Data Positioning Systems," *IEEE Transactions on Industrial Electronics*, Vol. 59, No. 10, pp. 3951–3960, October 2012.

[3] T. Atsumi and W. C. Messner, "Analysis of Residual Vibrations beyond the Nyquist Frequency in Sampled-Data Positioning Control System," *Journal of System Design and Dynamics*, Vol. 5, No. 7, pp. 1444–1459, November 2011.

[4] T. Atsumi, "Feedforward Control Using Sampled-Data Polynomial for Track Seeking in Hard Disk Drives," *IEEE Transactions on Industrial Electronics*, Vol. 56, No. 5, pp. 1338–1346, May 2009.

[5] R. Ehrlich, C. Taussig, and D. Abramovitch, "Identification of Sampled Data Systems at Frequencies beyond the Nyquist Rate," in *Proceedings of the* 28^{th} *IEEE Conference on Decision and Control*, pp. 646–652, Tampa, FL, USA, December 13–15, 1989.

[6] P. P. Vaidyanathan, *Multirate Systems and Filter Banks*, Prentice-Hall, Upper Saddle River, NJ, USA, 1993.

[7] G. F. Franklin, J. D. Powell, and M. Workman, *Digital Control of Dynamic Systems*, Addison Wesley Longman, Menlo Park, CA, USA, 1998.

[8] A. Okuyama, T. Hamaguchi, K. Watanabe, T. Horiguchi, K. Shishida, and Y. Nishimura, "A Design Method Based on a Shock-Response-Spectrum Analysis for Reducing Acoustic Noise of a Seeking Control System in a Hard Disk Drive," *Microsystem Technologies*, Vol. 9, No. 8, pp. 573–580, October 2003.

[9] C. Lalanne, *Mechanical Shock*, CRC Press, Taylor and Francis Group, Boca Raton, FL, USA, 2002.

[10] A. A. Mamun, G. Guo, and C. Bi, *Hard Disk Drive Mechatronics and Control*, CRC Press, Taylor and Francis Group, Boca Raton, FL, USA, 2006.

[11] T. Atsumi, A. Okuyama, and S. Nakagawa, "Vibration Control above the Nyquist Frequency in Hard Disk Drives," *IEEE Transactions on Industrial Electronics*, Vol. 55, No. 10, pp. 3751–3757, October 2008.

[12] T. Atsumi, "Disturbance Suppression beyond Nyquist Frequency in Hard Disk Drives," *Mechatronics*, Vol. 20, No. 1, pp. 67–73, February 2010.

[13] T. Atsumi and W. C. Messner, "Unobservable Settling Vibration on Head-Positioning Control in Hard Disk Drives," in *Proceedings of the* 18^{th} *IFAC World Congress*, pp. 4052–4060, Milano, Italy, August 28–September 2, 2011.

[14] T. Yamaguchi, M. Hirata, and C. K. Pang (eds.), *High-Speed Precision Motion Control*, CRC Press, Taylor and Francis Group, Boca Raton, FL, USA, 2011.

5

Dual-Stage Systems and Control

C. K. Pang

National University of Singapore

F. Hong

*A*STAR Data Storage Institute*

M. Nagashima

Naval Postgraduate School

CONTENTS

5.1 Introduction

To improve tracking and positioning accuracies in high-performance engineering systems, dual-stage actuation has been introduced to various industrial applications, e.g., optical disk drives [1, 2, 3], robot manipulators [4, 5, 6], fast tool servos [7, 8], stepper and scanners [9], nanopositioners [10, 11], and parallel kinematic machines [12, 13], etc., in order of volumetric magnitudes. A typical dual-stage actuator consists of a primary actuator (usually of higher mass, inertia, and stroke) used for coarse positioning in the low frequency range, and a secondary actuator (usually of lower mass, inertia, and stroke) for fine positioning in the high frequency range. While the application in various engineering fields might differ, the underlying system and control mechanisms are similar in general. In this chapter, dual-stage systems and control will be discussed using a commercial Hard Disk Drive (HDD) as a classical example of high-performance mechatronic system without loss of generality.

Dual-stage actuation has already been implemented in HDDs, and vast improvements have been achieved after its initial successful implementations. In such HDDs, dual-stage actuation is enabled via appending a small secondary actuator onto the Voice Coil Motor (VCM) which serves as the primary actuator. In recent years, MicroElectricalMechanicalSystems (MEMS) and even thermal actuators (which are still in experimental and prototyping stages) have attracted much attention and they are envisaged by many researchers as solutions for future data storage servo systems. Currently, three types of secondary actuators proposed for HDDs include the (i) suspension-based piezoelectric active suspension appended onto the VCM [14], (ii) slider-based MEMS-driven [15], and (iii) head-based [16] secondary actuators. Alternatively, they can also be categorized according to the actuation mechanism, e.g., (i) piezoelectric [17], (ii) electrostatic [18], (iii) electromagnetic [19], and (iv) thermal [20] driven actuators.

In this chapter, the dual-stage system employing the VCM as primary (coarse) actuator and the suspension-based Pb-Zr-Ti (PZT) active suspension as secondary (fine) actuator in an HDD is described. In Section 5.2, the mathematical models of the VCM and PZT active suspension are identi-

fied using continuous- and discrete-time measurements. The various methods of mechanical resonant modes compensation using gain-stabilization, inverse compensation, and phase-stabilization are described in Section 5.3. Section 5.4 presents the notion of multi-sensing servo systems where additional sensors and advanced control methodologies are used for active vibration control in dual-stage systems. Section 5.5 details the various dual-stage control configurations, and an example of dual-stage control is shown in Section 5.5.2. Our conclusion and future work are summarized in Section 5.6.

5.2 System Identification of Dual-Stage Actuators in HDDs

In this section, system identification of the primary actuator, i.e., the VCM, and the secondary actuator, i.e., the PZT active suspension, in dual-stage HDDs are carried out and detailed. A picture of a typical 3.5" dual-stage HDD depicting the VCM and the PZT active suspension is shown in Figure 5.1.

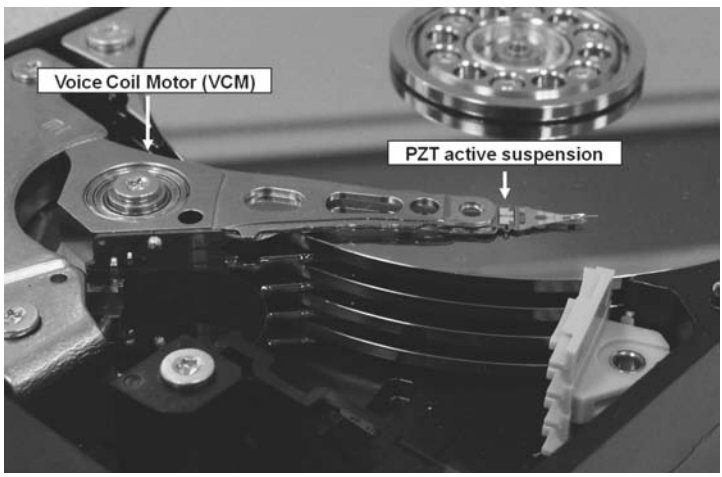

FIGURE 5.1
A picture of a typical 3.5" dual-stage HDD.

When performing parametric identification, an input-output relationship-based method is used and the physical quantities such as length, mass, force, etc., are coupled into the coefficients of identified transfer functions. The transfer function approach is practical and preferred over physical modeling for control systems design purposes even when the coefficients give no direct insight into the underlying physics of the mechanical actuators [21].

5.2.1 Primary Actuator: VCM

The VCM is harnessed between two very strong permanent magnets commonly called the yoke. Other components include a pivot (for rotary actuation), ball bearings, arms commonly known as the "E" block, flex cable, and suspensions at the tip to carry the sliders. When current passes through the coil of the VCM, force and hence displacement are transduced to translate the Read/Write (R/W) heads which are mounted onto the sliders.

5.2.1.1 Continuous-Time Measurement

For system identification of the VCM using continuous-time signals, a swept sine voltage excitation is generated from a Dynamic Signal Analyzer (DSA) and is injected into the VCM via a current amplifier. By exciting the VCM at frequencies of interests using an input current, the displacement of the VCM can be measured non-intrusively using a Laser Doppler Vibrometer (LDV). The frequency response measurements are then captured for offline system identification, and the experimental frequency response of the VCM is shown in Figure 5.2.

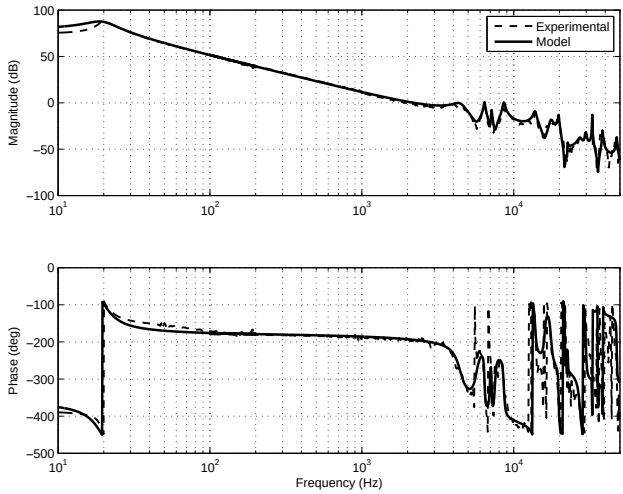

FIGURE 5.2
Frequency response of a VCM. Dashed: experimental. Solid: model.

With knowledge from physical modeling, e.g., the first principle approach in [22], the VCM can be represented by a double integrator with several flexible mechanical resonant modes (or poles) of interest. The overall transfer function

of a VCM in s-domain can be expressed as

$$P_V(s) = K_V \sum_{i=1}^{N_V} \frac{R_{V,i}}{s^2 + 2\zeta_{V,i}\omega_{V,i}s + \omega_{V,i}^2}, \tag{5.1}$$

where K_V is the loop gain and N_V is the number of mechanical resonant modes. $R_{V,i}$, $\zeta_{V,i}$, and $\omega_{V,i}$ are the residue, damping ratio, and natural frequency of the i^{th} mechanical resonant mode of the VCM, respectively. For the VCM shown in Figure 5.1, the identified parameters of $P_V(s)$ from 10 Hz to 50 kHz are given in Table 5.1. The identified frequency response of the VCM using these parameters with $K_V = 1.9 \times 10^4$ is shown in Figure 5.2.

TABLE 5.1
Modal Parameters of $P_V(s)$

i	$\omega_{V,i}$ (rad/s)	$R_{V,i}$	$\zeta_{V,i}$
1	2π19.5	7500	0.2
2	2π4449	–6500	0.09
3	2π6412	–1800	0.01
4	2π7141	–400	0.005
5	2π8599	–4800	0.015
6	2π13800	5500	0.02
7	2π17560	3800	0.025
8	2π19750	–2400	0.0065
9	2π22620	50	0.004
10	2π27270	–1300	0.003
11	2π29780	1000	0.01
12	2π32830	–1000	0.001
13	2π38410	–800	0.004
14	2π47610	650	0.005

5.2.1.2 Discrete-Time Measurement

In HDD head-positioning control systems, the output can be observed only at fixed time intervals as measurements can only be taken where the servo signals are available. Position Error Signal (PES) is the position offset between the R/W head and track center, and one of the factors which determines the sampling rate of PES is the number of embedded servo signals in a track. However, the area occupied by the servo signals needs to be minimized in order to maximize the areal density of HDDs. As a result, the plant often has critical dynamics above the Nyquist frequency, i.e., half of the PES sampling frequency. Conventional identification techniques are therefore not directly applicable due to the aliasing effect caused by the sampling operation for frequencies above the Nyquist frequency.

Although the LDV can also be used to measure the plant dynamics beyond the Nyquist frequency using a similar methodology to that described in the previous section, the displacement of the plant cannot be directly measured after full assembly of the HDD. As such, it is imperative to develop a method which can be carried out without external equipment for plant measurement and calibration of controller parameters in individual HDD units during mass production. It is worth noting that the measurement and identification methodology described in the previous section can be employed without distinguishing between continuous-time and discrete-time signals as well, if there are no significant dynamics beyond the Nyquist frequency.

In current literature, two kinds of non-parametric methods exist for identification of HDD plant above the Nyquist frequency of the PES sampling rate. One method is to interpolate or interlace the measured plant response with another measurement where the applied input excitation is shifted in time. Assuming the Linear Time-Invariant (LTI) property of the plant, the steady-state response of the plant for the time-shifted input excitation represents the plant response at sampling points equally shifted in time, if the sampling time of the observation is not changed. By interpolating the frequency responses, the frequency response that is equivalent to the one measured at increased sampling points can be reconstructed. The sampling rate of the measurements can be increased to arbitrarily high frequencies by reducing the size of the time shift and collecting as many measurements as necessary. The authors in [23] applied this principle to an HDD system using a discrete-time excitation signal. This approach can be used if the Digital-to-Analog (D/A) converter in the HDD is equipped with the functionality to shift its timing with respect to the PES sampling operation.

The other method is to excite the plant by a single continuous-time sinusoid. The method was developed by the authors in [24] to obtain the dynamics of a continuous plant embedded in a closed-loop sampled-data system, and the HDD is mentioned as a possible application. Theoretically, one can obtain the plant dynamics up to arbitrarily high frequencies far beyond the Nyquist frequency of the PES. In practice, the continuous-time sinusoid can be replaced by a discrete-time sinusoid signal sampled at a frequency sufficiently higher than the bandwidth of the plant as shown in [25]. Because of this approximation, the frequency range for satisfactory measurement accuracy is limited by the sampling rate of the discrete-time excitation signal.

In the following, a non-parametric method of identifying the plant dynamics above the Nyquist frequency based on [24] is presented. In the method, the approximation required in [24] due to the infinite summation in computing the transfer function is removed by directly measuring the sensitivity transfer function of the feedback system in the discrete-time domain, using a discrete-time excitation signal instead of a continuous-time signal [25].

To investigate the effect of the sampling operation, the mathematical expressions presented in [26] are briefly reviewed here. Sampling of a signal $f(t)$

can be expressed in time domain as

$$f^*(t) = \sum_{k=0}^{\infty} f(t)\delta(t - kT), \tag{5.2}$$

and in s-domain as

$$\begin{aligned} F^*(s) &= \int_{-\infty}^{\infty} f^*(t)e^{-st}dt \\ &= \frac{1}{T}\sum_{n=-\infty}^{\infty} F\left(s - jn\frac{2\pi}{T}\right), \end{aligned} \tag{5.3}$$

where the superscript "*" indicates the sampling operation and sampled signal, and T is the sampling period. The summation on the right-hand side of (5.3) causes the well-known *aliasing* effect, as illustrated in Figure 5.3 in time domain and Figure 5.4 in frequency domain, respectively, for a case where a 175 Hz sinusoid is sampled at 200 Hz.

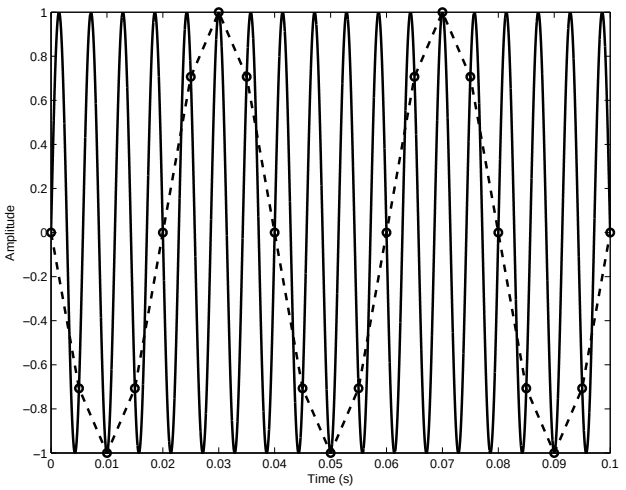

FIGURE 5.3
Example of aliasing by sampling operation in time domain.

The signal $F^*(s)$ represents a fictitious pulse train in frequency domain and the output of a system $G(s)$ with input $F^*(s)$ is written as $G(s)F^*(s)$.

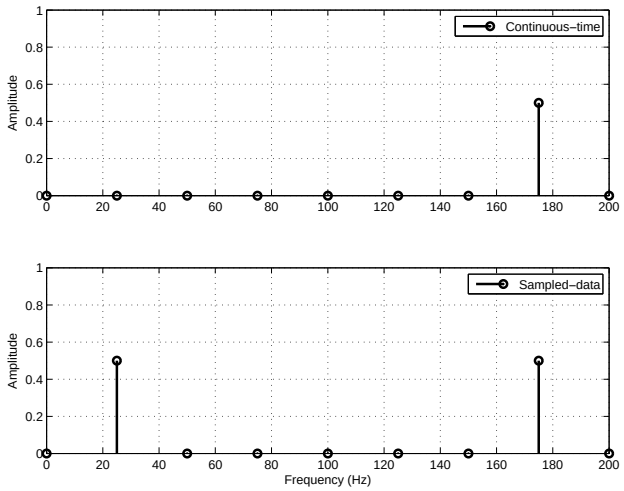

FIGURE 5.4
Example of aliasing by sampling operation in frequency domain.

As the sampled signal $F^*(s)$ is periodic, sampling of this signal is expressed as

$$\begin{aligned} Y^*(s) &= [G(s)F^*(s)]^* \\ &= G^*(s)F^*(s), \end{aligned} \tag{5.4}$$

since

$$\begin{aligned} [G(s)F^*(s)]^* &= \frac{1}{T}\sum_{n=-\infty}^{\infty} G\left(s - jn\frac{2\pi}{T}\right) F^*\left(s - jn\frac{2\pi}{T}\right) \\ &= \left[\frac{1}{T}\sum_{n=-\infty}^{\infty} G\left(s - jn\frac{2\pi}{T}\right)\right] F^*(s) \\ &= G^*(s)F^*(s), \end{aligned} \tag{5.5}$$

provided that all sampling operations are synchronized.

Using this property, the so-called *pulse transfer function* can be defined as

$$\begin{aligned} G^*(s) &= \frac{Y^*(s)}{F^*(s)} \\ &= \frac{1}{T}\sum_{k=-\infty}^{\infty} G\left(s - jk\frac{2\pi}{T}\right). \end{aligned} \tag{5.6}$$

The pulse transfer function represents the relationship from the input pulse train to the output of the plant observed in continuous time. Although this

transfer function is purely theoretical, it is useful to treat the discrete-time path of a sampled-data control system in the continuous-time domain.

Figure 5.5 shows the block diagram of a VCM plant measurement. The VCM, Zero-Order Hold (ZOH), and discrete-time controller are denoted by $P_1(s)$, $H(s)$, and $C(z)$, respectively. The identification of the VCM in an HDD head-positioning system is carried out in the closed-loop track-following mode to ensure that the PES is accurate within a certain range of the magnetic head offset from the track center.

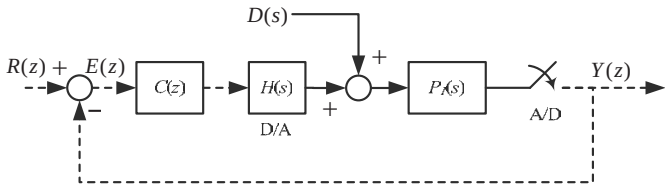

FIGURE 5.5
Block diagram of VCM measurement.

Since the sampling operation is linear (although it is not time-invariant), Figure 5.5 can be converted to an equivalent block diagram as shown in Figure 5.6, where $P_m(s) = P_1(s)$ is the VCM for the VCM measurement case.

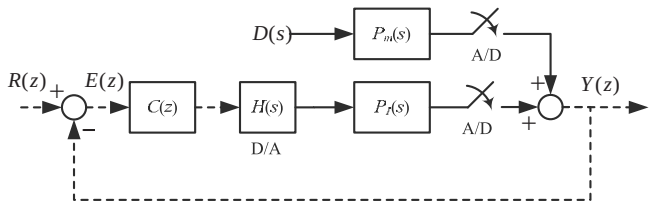

FIGURE 5.6
Equivalent block diagram of plant measurement.

The system is now represented as a discrete-time system with a continuous plant enclosed in the typical ZOH and sampling framework. The conversion of the continuous-time dynamics $P_m(s)H(s)$ to a discrete-time plant can be written in the pulse transfer function form as

$$G^*(s) = \frac{1}{T} \sum_{n=-\infty}^{\infty} P_m(s - jn\omega_T)H(s - jn\omega_T). \tag{5.7}$$

For system identification, the reference $R(z)$ is set to zero. The system

output $Y^*(s)$ is the product of the discrete-time input, which is the sampled response of the plant $P_m(s)$ subjected to a continuous-time excitation signal $D(s)$, and the sensitivity transfer function of the discrete-time system written as

$$Y^*(s) = S^*(s)[P_m(s)D(s)]^*. \tag{5.8}$$

In (5.8), $S^*(s)$ the sensitivity transfer function of the discrete-time feedback system represented in a pulse transfer function form

$$S^*(s) = \frac{G^*(s)C^*(s)}{1 + G^*(s)C^*(s)}. \tag{5.9}$$

The frequency response of $S^*(s)$ is periodic and can simply be obtained by evaluating $S_d(e^{j\omega T})$ at ω, where $S_d(z)$ is the discrete-time sensitivity transfer function with $z = e^{jwT}$. For measurement of the VCM, this includes the plant to be identified and therefore needs to be obtained experimentally by applying a discrete-time excitation signal to the feedback system and measuring the response of the sampled system. With $S_d(e^{j\omega T})$, the sampled frequency response of the plant subjected to an excitation signal $D(j\omega)$ can be obtained as

$$[P_m(j\omega)D(j\omega)]^* = \frac{Y^*(j\omega)}{S_d(e^{j\omega T})}. \tag{5.10}$$

Since (5.10) is periodic with period $\frac{2\pi}{T}$, the plant response to a sinusoidal excitation signal of frequency ω_d can be obtained by (5.10) at frequency

$$\omega_d' = \omega_d - n\frac{2\pi}{T}, \tag{5.11}$$

where $n \in \mathbb{Z}^+$ is chosen such that $0 < \omega_d' < \frac{2\pi}{T}$.

The frequency ω_d of the excitation signal is not restricted by the sampling rate of the measurement, and the frequency response of the plant above the Nyquist frequency of the sampling can be measured, except for frequencies that are integer multiples of $\frac{2\pi}{T}$.

Figure 5.7 shows the results of VCM plant identification obtained through numerical simulations conducted with the models shown in Figure 5.5. The sampling frequency of the PES measurement is 30 kHz, and the continuous-time VCM is simulated by a variable step solver with a maximum step size of 2.77 μs. In the simulation, the frequency response was measured for each fixed continuous-time sinusoidal excitation signal varying from 50 Hz to 60 kHz at an interval of 50 Hz. The VCM model used is the 28^{th} order model $P_V(s)$ identified previously in (5.1) with modal parameters in Table 5.1. It should be noted that the frequency responses at integer multiples of $\frac{2\pi}{T}$ are not plotted in Figure 5.7.

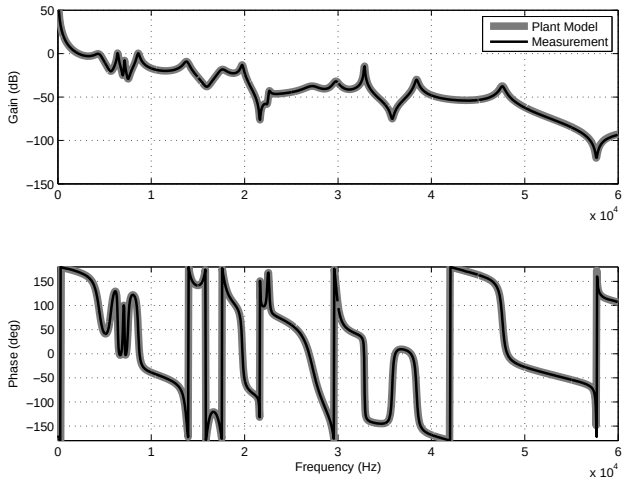

FIGURE 5.7
Frequency response measurement of VCM using PES sampled at 30 kHz.

In this example, the gain of the VCM controller $C(z)$ is 0.1365. The locations of the poles and zeros in discrete-time domain are shown in Table 5.2.

TABLE 5.2
Parameters of VCM Controller $C(z)$

Order	Zeros	Poles
1	$-0.2199 + 0.9392i$	0.0019
2	$-0.2199 - 0.9392i$	0.009
3	$0.0741 + 0.9824i$	0.5026
4	$0.0741 - 0.9824i$	1
5	$0.2163 + 0.9292i$	$0.0711 + 0.8581i$
6	$0.2163 - 0.9292i$	$0.0711 - 0.8581i$
7	$0.5777 + 0.7766i$	$0.2032 + 0.8504i$
8	$0.5777 - 0.7766i$	$0.2032 - 0.8504i$
9	$0.9896 + 0.0000i$	$0.5467 + 0.7287i$
10	$0.9896 - 0.0000i$	$0.5467 - 0.7287i$

In order to determine the frequency response of the continuous plant, the sensitivity transfer function $S_d(e^{j\omega T})$ is measured by applying a discrete-time sinusoid from 50 Hz to 60 kHz sampled at 30 kHz as the continuous-time excitation signal through the ZOH. This is equivalent to $S_d(e^{j\omega T})$ measured up to 30 kHz and periodically extended up to 60 kHz.

5.2.2 Secondary Actuator: PZT Active Suspension

To improve servo performance, the secondary actuator in a dual-stage system should be rigid (for higher damping and less number of mechanical resonant modes) yet light (for achieving higher servo bandwidth) simultaneously. Secondary actuators which possess these ideal characteristics can be used to reject disturbances in the control system for enhanced error correction in the high frequency range.

In this section, system identification of a piezoelectric secondary actuator or the PZT active suspension in a commercial dual-stage HDD is carried out. Two small parallel strips of PZT elements can be found at the base of the suspension, and the piezoelectric ceramic PZT element has a high stiffness which generates a large force by contraction and expansion. When a voltage is applied to these elements, one PZT strip expands while the other contracts to deflect the entire suspension and yields displacement of the R/W heads. PZT active suspensions often employ the push-pull or shear design according to the direction of polarization of the piezoelectric materials. Usually, the PZT active suspension is designed to achieve a stroke of about 1 μm with the first resonant mode in the range of 5–15 kHz. A picture of a two strip push-pull PZT active suspension is shown earlier in Figure 5.1.

5.2.2.1 Continuous-Time Measurement

Using the same methodology as the VCM case, the displacement of the PZT active suspension is measured using the LDV. A swept sine voltage excitation is generated from a DSA at frequencies of interests, and is injected into the PZT elements via a charge amplifier to reduce the effects of hysteresis. The frequency response measurements of the PZT active suspension are then captured for offline system identification as shown in Figure 5.8.

Figure 5.8 shows that the PZT active suspension can be modeled as a pure gain in a large range of frequencies coupled with several high frequency mechanical resonant modes. The transfer function of the PZT active suspension $P_M(s)$ can be expressed in s-domain as

$$P_M(s) = K_M \sum_{i=1}^{N_M} \frac{R_{M,i}}{s^2 + 2\zeta_{M,i}\omega_{M,i}s + \omega_{M,i}^2}, \tag{5.12}$$

where K_M is the DC gain and N_M is the number of mechanical resonant modes of the PZT active suspension. $R_{M,i}$, $\zeta_{M,i}$, and $\omega_{M,i}$ are the residue, damping ratio, and natural frequency of the i^{th} mechanical resonant mode of the PZT active suspension, respectively. For the PZT active suspension shown in Figure 5.1, the identified parameters of $P_M(s)$ from 10 Hz to 50 kHz are shown in Table 5.3. The identified frequency response of the PZT active suspension using these parameters and $K_M = 0.3616$ is shown in Figure 5.8.

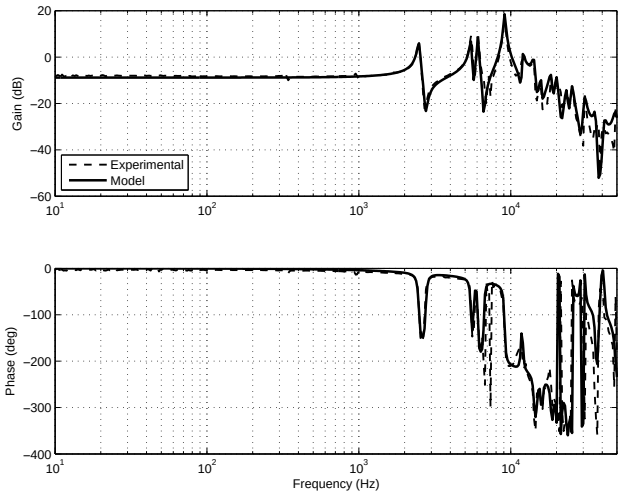

FIGURE 5.8
Frequency response of PZT active suspension. Dashed: experimental. Solid: model.

TABLE 5.3
Modal Parameters of $P_M(s)$

i	$\omega_{M,i}$ (rad/s)	$R_{M,i}(\times 10^8)$	$\zeta_{M,i}$
1	$2\pi 2484$	0.521	0.02
2	$2\pi 5461$	2.005	0.015
3	$2\pi 6074$	2.206	0.01
4	$2\pi 9103$	20.050	0.012
5	$2\pi 12000$	4.812	0.015
6	$2\pi 14240$	–7.218	0.015
7	$2\pi 15830$	–2.005	0.015
8	$2\pi 18380$	–5.213	0.015
9	$2\pi 20000$	–6.015	0.02
10	$2\pi 23230$	–4.010	0.02
11	$2\pi 25300$	–6.175	0.02
12	$2\pi 30640$	–5.213	0.02
13	$2\pi 36000$	2.566	0.015
14	$2\pi 41280$	–3.008	0.02
15	$2\pi 48950$	10.426	0.03

5.2.2.2 Discrete-Time Measurement

Similarly, the block diagram for obtaining the frequency response of the PZT active suspension using discrete-time measurements is shown in Figure 5.9. In Figure 5.9, $P_2(s)$ is the PZT active suspension and can be obtained from (5.10) by replacing $P_m(s)$ with $P_2(s)$, provided that the discrete-time sensitivity transfer function $S_d(z)$ is known *a priori*, which can be measured using the method described in Section 5.2.1.2.

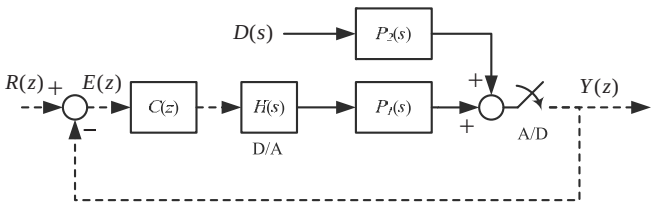

FIGURE 5.9
Block diagram of secondary actuator plant measurement.

Figure 5.10 shows the identification results of the PZT active suspension obtained through numerical simulations conducted with the models shown in Figure 5.9. The sampling frequency of the PES is 30 kHz, and the continuous-time PZT active suspension is simulated by a variable step solver with a maximum step size of 2.77 μs. In the simulation, the frequency response was measured for each fixed sinusoidal excitation signal applied from 50 Hz to 60 kHz at an interval of 50 Hz. The PZT active suspension model used is the 30^{th} order model $P_M(s)$ identified previously in (5.12) with modal parameters in Table 5.3.

Our results show successful identification of the VCM and PZT active suspension for more than three times the Nyquist frequency of 15 kHz of PES signal. As is in the VCM case, the values at integer multiples of the Nyquist frequency of the PES are removed due to the signal singularity. The error at higher frequency is due to the numerical error from continuous-time simulation of the plant. In theory, the frequency response of the continuous-time plant can be measured to arbitrarily high frequencies using the presented method.

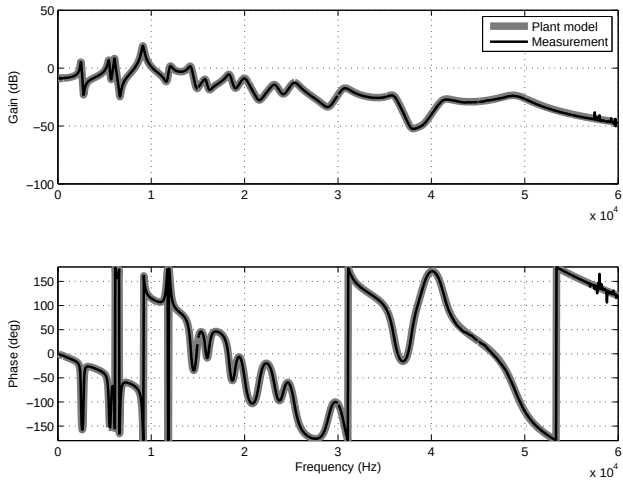

FIGURE 5.10
Frequency response measurements of PZT active suspension using PES sampled at 30 kHz.

5.3 Resonance Compensation Without Extraneous Sensors

To improve the servo performance for next generation of high-performance mechatronic systems, the servo bandwidth needs to be further increased for enhanced positioning accuracy and speed. To achieve this, the servo loop needs to be carefully designed to take care of the disturbances (especially those at the frequencies higher than the servo bandwidth) and should have enough robustness against gain and phase uncertainties. In particular, the open loop servo bandwidth should be designed at around one-third to one-quarter the frequency of the first critical mechanical resonant mode as a rule of thumb [27].

In dual-stage HDDs, the existence of mechanical resonant modes in both the VCM and PZT active suspension limits the increase of the gain crossover frequency as the gains of the actuators are usually very high at the resonant frequencies and will degrade the closed-loop stability. As a result, the mechanical resonant modes excited by the air-flow would be mainly in the frequency range higher than the servo bandwidth, and the vibrations are amplified by the mechanical resonant modes rather than being attenuated [28]. The large gains at the lightly damped poles not only cause oscillations in the step response, but even instability in the closed-loop servo system due to poor gain and phase margins. As such, several resonance compensation methods have been proposed to tackle these flexible resonant modes, and the commonly used control practices are presented in this section.

5.3.1 Gain Stabilization

Gain stabilization is a technique used to suppress the energy (hence gain) of the mechanical resonant modes at the resonant frequencies by attenuating the signal power to avoid excitation of the corresponding resonant modes. As such, notch filters are commonly used to suppress the gain of the mechanical resonant modes in the open loop transfer function [29]. Moreover, notch filters are easy to design and implement in both continuous- and discrete-time, and are preferred over Low Pass Filters (LPFs) for their narrower band reduction in magnitude of gain at the resonant frequencies.

Suppose the i^{th} mechanical resonant mode of a dual-stage actuator $R_i(s)$ can be represented by

$$R_i(s) = \frac{(2\pi f_{R,i})^2}{s^2 + 2\zeta_{R,i}(2\pi f_{R,i})s + (2\pi f_{R,i})^2}, \tag{5.13}$$

where $f_{R,i}$ and $\zeta_{R,i}$ are the natural frequency and damping ratio of the mechanical resonant mode with $(0 < \zeta_{R,i} < 1)$. To cancel the gain of the mechanical resonant mode, a straightforward notch filter design $N_i(s)$ for each i^{th} resonant mode $R_i(s)$ is

$$N_i(s) = \frac{(2\pi f_{D,i})^2}{(2\pi f_{R,i})^2} \frac{s^2 + 2\zeta_{R,i}(2\pi f_{R,i})s + (2\pi f_{R,i})^2}{s^2 + 2\zeta_{D,i}(2\pi f_{D,i})s + (2\pi f_{D,i})^2}. \tag{5.14}$$

The damping ratio of the notch filter $\zeta_{D,i}$ is usually chosen to be $\sqrt{2} < \zeta_{D,i} \leq 1$ to replace the lightly damped mechanical resonant modes with better damped filter poles. When $f_{R,i} = f_{D,i}$, some degradation in phase response is still apparent at the resonant frequency $f_{R,i}$. In this case, a high pass notch filter using $f_{D,i} > f_{R,i}$ can be constructed to reduce and even remove the phase loss.

A setback of using notch filters is that they are not robust to parametric variations, i.e., a shift in resonant frequencies might cause instability of the closed-loop system. Moreover, notch filters cannot completely reduce the residual vibrations arising from the end of the track-seeking mode during mode switching [30]. When the mechanical structural modes are excited by external disturbances, notch filters will also annihilate any control effort which is used for vibration damping [31].

5.3.2 Inverse Compensation

If the mechanical actuator contains minimum phase pole-zero pairs, a controller constructed by the approximated plant inverse can be used to make the system behave as a rigid body up to high frequencies. This technique not only compensates for the large gain at the resonant modes, but also increases the gain of the anti-resonant zeros to reduce the signal blocking effects of the anti-resonant zeros. This allows the actuator to be approximated by

the rigid-body mode for better error correction, especially at the frequencies of the anti-resonant zeros [32]. Moveover, inverse compensation reduces the relative degree hence phase lag of the system up to high frequencies resulting in a higher servo bandwidth, which achieves a low positive gain of the sensitivity transfer function at high frequencies after the gain crossover frequency [33]. This resonance compensation phenomenon is also commonly encountered when synthesizing $\mathcal{H}_2$ and $\mathcal{H}_\infty$ optimal controllers.

However, a perfect plant inverse is not realizable in presence of unstable zeros. As such, the effectiveness of the controller synthesized using the approximated plant inverse will have to be carefully evaluated and substantiated. In particular, the Zero Phase Error Tracking (ZPET) controller [34] is a good candidate to achieve inverse compensation characteristics up to high frequencies. Although the inverse compensation methodology does not appear to be robust against parametric perturbations and other uncertainties in the mechanical actuator, the disturbance rejection capabilities and closed-loop stability are retained even when there is a $\pm 5\%$ shift in resonant frequencies of the mechanical resonant modes [33].

5.3.3 Phase Stabilization

Contrary to gain stabilization or inverse compensation designs, the phase-stabilization design *retains* the high gain of the mechanical resonant mode but shapes the phase of the open loop transfer function to achieve closed-loop stability. The phase-stabilization method involves designing lead compensators to lift the phase response of the open loop transfer function away from -180° to maintain stability. As such, the high loop gain at the resonant frequencies can be maintained so that the sensitivity transfer function will have extra gain attenuation at the resonant frequencies, resulting in enhanced disturbance rejection capabilities [22]. As the phase-stabilization methodology is achieved via phase shaping, the technique is generally very robust if there are little phase uncertainties in the mechanical actuator.

In the absence of mechanical resonant modes, LTI and Linear Time-Varying (LTV) *peak filters* can also be designed and included into the control loop to emulate these desirable effects.

5.3.3.1 Using Mechanical Resonant Modes

The phase characteristics of the flexible resonant modes with respect to the rigid body mode determines if the mechanical resonant modes are *in-phase* or *out-of-phase*. Besides performing modal analysis, this phase characteristic can also be observed from the frequency response; a mechanical resonant mode which is in-phase with the rigid body mode will exhibit a stable zero between them, while a mechanical resonant mode which is out-of-phase with the rigid body mode will exhibit an unstable zero between them.

The existence of in-phase mechanical resonant modes in actuators allows

the phase-stabilization design to be achieved via low order controllers. In this design methodology, the notion of phase margins can be extended to second phase margin [35] or even tertiary phase margins [31] when multiple in-phase mechanical resonant modes exist. Interested readers are kindly referred to [22, 31, 35] for more details which are omitted here for brevity.

5.3.3.2 Using LTI Peak Filters

Peak filters with a high loop gain at its center frequency can also be used to create notches in the sensitivity transfer function to reject narrow frequency band disturbances, similar to the advantages achieved via phase-stabilized mechanical resonant modes. In general, it is preferable to augment the filters into the existing servo loop in an "add-on" fashion so that the design of each loop can be decoupled [36]. In [37, 38], the add-on filters were placed at the disturbance frequencies where there were no significant plant dynamics, i.e., lightly damped plant poles. The phase stabilizability can be guaranteed by appropriately placing a zero so that the closed-loop is robust against phase uncertainties around the disturbance frequency [39, 40]. In other cases, the poles of the peak filter should be placed near some lightly damped plant poles. In this case, setting the damping of the peak filter as that of the plant poles which are within the bandwidth of the filter could be a compromise made between performance and stability as shown in [39, 41].

In this section, novel solutions are provided for designing the disturbance filter when significant plant dynamics are within the bandwidth of the peak filter. The filter zero is designed appropriately so that the root loci originating from both the filter poles and lightly damped plant poles enter the left-half plane under certain low gain conditions. As such, the departure angles from the filter poles are no longer 180° but ±90°, i.e., compromised departure angles from both the filter poles and plant poles. By doing so, the stability margin especially the gain margin is dramatically increased [42]. The resulting closed-loop systems can provide large gain attenuation, i.e., disturbance rejection capability at the disturbance frequency.

A peak filter is augmented into the existing servo loop in an add-on fashion as shown in Figure 5.11, where $P(s)$, $C(s)$, and $F(s)$ are the plant, baseline controller, and disturbance filter, respectively. d, y, and r denote the output disturbance, plant output, and reference signal, respectively.

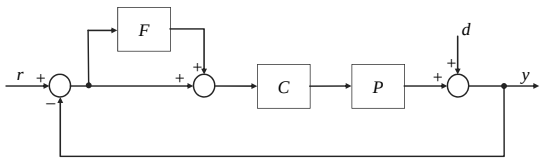

FIGURE 5.11
Block diagram of control system with an add-on peak filter.

The overall sensitivity transfer function $S(s)$ can be given by

$$S(s) = S_0(s)S_F(s), \tag{5.15}$$

where $S_0(s)=\frac{1}{1+P(s)C(s)}$ is the baseline sensitivity transfer function, i.e., $S(s) = S_0(s)$ when $F(s) = 0$, and $S_F(s)$ can be expressed as

$$S_F(s) = \frac{1}{1 + S_h(s)F(s)}, \tag{5.16}$$

where $S_h(s)=\frac{P(s)C(s)}{1+P(s)C(s)}$ is the baseline complimentary sensitivity transfer function. From (5.15), it can be seen that the design of baseline servo loop and the peak filter can be decoupled [36]. The baseline controller $C(s)$ takes care of the plant $P(s)$ to guarantee the basic stability margin, while the peak filter $F(s)$ takes care of the pseudo "plant" $S_h(s)$ so that the resulting $S_F(s)$ has desired attenuation at those disturbance frequencies.

Two kinds of plant models will be considered; namely, one without significant plant dynamics within the bandwidth of the peak filter followed by the other with them. The peak filter $F(s)$ is given in the form of

$$F(s) = K\frac{s(s\cos\varphi + \omega_1 \sin\varphi)}{s^2 + 2\zeta_1\omega_1 s + \omega_1^2}, \tag{5.17}$$

where $K>0$ is the gain of the filter and can be chosen by means of root locus analysis to guarantee closed-loop stability. In particular, one zero of $F(s)$ is placed at the origin to maintain a low gain in the frequency range lower than the disturbance frequency so that the effect of the peak filter $F(s)$ to the baseline servo loop can be minimized at the frequencies other than the disturbance frequency. The other zero will be placed optimally so that the root loci of $S_h(s)F(s)$ originating from the poles associated with $F(s)$ will move in the most stable direction [40]

$$\varphi = \arg[S_h(j\omega_1)] + \frac{\pi}{2}, \quad \varphi \in [-\frac{\pi}{2}, \frac{\pi}{2}]. \tag{5.18}$$

An illustration example is shown in Figures 5.12 and 5.13. Figure 5.12 plots the root loci of $S_h(s)F(s)$, where the solid and dashed line are the root loci associated with the filter and pseudo plant, respectively. It can be seen that the angles of departure from the complex conjugate poles of $F(s)$ are 180° as depicted by the solid line in Figure 5.12, which gives a most stable phase margin of ±90°.

Define the pseudo open loop transfer function $G(s)$ as

$$G(s) = S_h(s)F(s), \tag{5.19}$$

the phase at the disturbance frequency can be calculated by

$$\arg[G(j\omega_1)] = \arg[S_h(j\omega_1)] + \arg[F(j\omega_1)]. \tag{5.20}$$

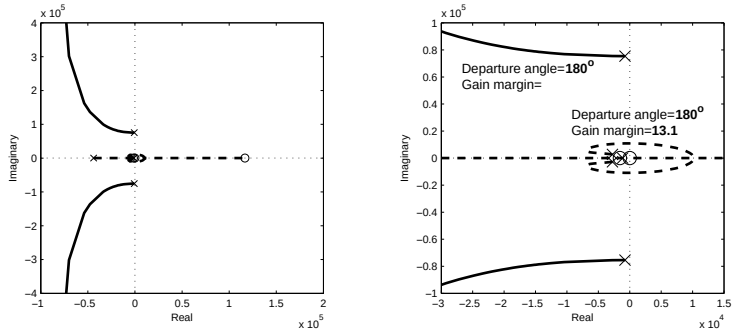

FIGURE 5.12
Root loci of $S_h(s)F(s)$. Solid: filter pole. Dashed: plant pole.

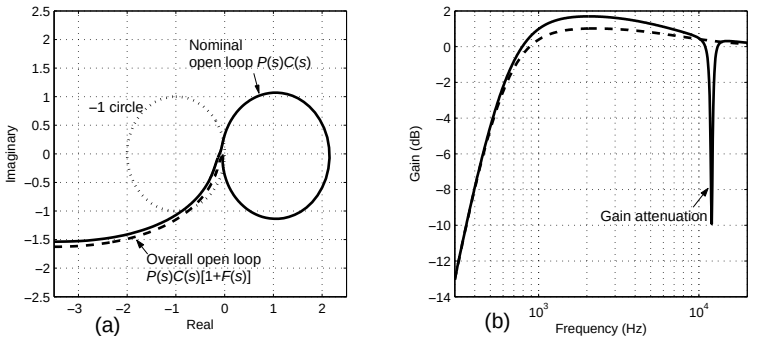

FIGURE 5.13
(a) Nyquist plot of the open loop system; (b) Magnitude of sensitivity transfer function of the closed-loop system. Solid: without $F(s)$. Dashed: with $F(s)$.

Noting $\arg[F(j\omega_1)] = \arctan(\frac{\cos\varphi}{\sin\varphi})$ and from (5.18), it follows that

$$\arg[G(j\omega_1)] = \arg[S_h(j\omega_1)] + \arctan\left\{-\tan\left[\arg[S_h(j\omega_1)]\right]\right\} = 0. \quad (5.21)$$

In addition, the relationship among the transfer functions of the overall resulting open loop, baseline open loop, and pseudo open loop is

$$P(s)C(s)[1 + F(s)] = [1 + P(s)C(s)][1 + S_h(s)F(s)] - 1. \quad (5.22)$$

If there are no significant plant dynamics near the disturbance frequency and the disturbance frequency is much higher than the servo bandwidth, i.e., the contribution of gain and phase of the nominal open loop $P(s)C(s)$ to

$[1+P(s)C(s)]$ at the disturbance frequency is trivial, the following property holds

$$\arg[1 + P(j\omega_1)C(j\omega_1)] \approx 0. \tag{5.23}$$

Since $\arg[S_h(j\omega_1)F(j\omega_1)] = 0$ as shown in (5.21), it follows that

$$\arg[1 + S_h(j\omega_1)F(j\omega_1)] = 0. \tag{5.24}$$

From (5.23) and (5.24), it can be proven that

$$\arg\{[1 + P(j\omega_1)C(j\omega_1)][1 + S_h(j\omega_1)F(j\omega_1)]\} \approx 0,$$

such that the phase property of the right side of (5.22) is

$$\arg\{[1 + P(j\omega_1)C(j\omega_1)][1 + S_h(j\omega_1)F(j\omega_1)] - 1\} \approx 0.$$

As such, it can be concluded that the phase of the overall open loop transfer function at disturbance frequency is

$$\arg\left\{P(j\omega_1)C(j\omega_1)[1 + F(j\omega_1)]\right\} \approx 0, \tag{5.25}$$

i.e., the overall open loop has zero phase at the disturbance frequency. The gain of the open loop transfer function at the disturbance frequency is high, which guarantees maximum gain attenuation in magnitude of the sensitivity transfer function. This property is also illustrated in the Nyquist plot given in Fig. 5.13(a), which compares the baseline open loop transfer function and the open loop transfer function with presented peak filter. Compared with the baseline servo, the augmentation of the peak filter resulted in more attenuation in sensitivity magnitude at the disturbance frequency as can be seen in Figure 5.13(b).

When there are significant plant dynamics within the bandwidth of the peak filter, i.e., there are lightly damped plant poles as well as lightly damped filter poles, the stability of these plant poles are as critical as that of the filter poles. As such, it should be guaranteed that the root loci originating from both the filter poles and lightly damped plant poles will enter into the left-half plane with sufficient margin.

To determine the angle of departure from the lightly damped plant poles, we can choose a test point s_0 and move it in the very vicinity of the pole at $p_{h_1}=-\zeta_{h_1}\omega_{h_1}+j\omega_{h_1}\sqrt{1-\zeta_{h_1}^2}$, as shown in Figure 5.14.

For the test point s_0 to be on the root locus, the sum of angles from all the open loop poles and zeros to the test point s_0 should satisfy the *angle condition*, i.e.,

$$\angle S_h(s_0) + \angle F(s_0) = \pm 180^\circ(2k+1), \quad k = 0, 1, 2, \cdots, \tag{5.26}$$

where

$$\angle S_h(s_0) = -\angle(s_0 - p_{h_1}) + \sum_i \angle(s_0 - z_{h_i}) - \sum_{i\neq 1} \angle(s_0 - p_{h_i}), \tag{5.27}$$

$$\angle F(s_0) = -\angle(s_0 - p_1) - \angle(s_0 - p_2) + \angle(s_0 - z_1) + \angle(s_0 - z_2), \tag{5.28}$$

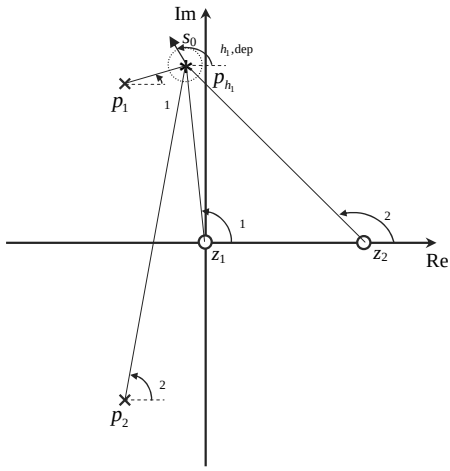

FIGURE 5.14
Determination of angle of departure from a plant pole. "o": zeros z_1 and z_2 of $F(s)$. "x": poles p_1 and p_2 of $F(s)$. "*": pole of the plant.

with z_{h_i} and p_{h_i} being the zeros and poles of the plant, respectively. z_1=0, z_2=$-\omega_1 \tan\varphi$, and $p_{1,2} = -\zeta_1\omega_1 \pm j\omega_1\sqrt{1-\zeta_1^2}$ are the zeros and poles of the peak filter, respectively.

The angle of departure from the plant pole at p_{h_1} is defined as the angle from p_{h_1} to the test point s_0, i.e.,

$$\phi_{h_1,\text{dep}} = \angle(s_0 - p_{h_1}). \tag{5.29}$$

As p_{h_1}, p_1, and p_2 are lightly damped poles, i.e., they are very close to the imaginary axis and s_0 is in the very vicinity of p_{h_1}, the following approximations hold

$$\angle(s_0 - p_2) \approx \angle(p_{h_1} - p_2) \approx \angle(p_1 - p_2) = 90^\circ, \tag{5.30}$$
$$\angle(s_0 - z_1) \approx \angle(p_{h_1} - z_1) \approx 90^\circ, \tag{5.31}$$
$$\angle(s_0 - z_2) \approx \angle(p_{h_1} - z_2) \approx \angle(p_1 - z_2) = 90^\circ - \varphi. \tag{5.32}$$

If φ is given by (5.18), i.e.,

$$\varphi = \sum_i \angle(j\omega_1 - z_{h_i}) - \sum_i \angle(j\omega_1 - p_{h_i}) + 90^\circ, \tag{5.33}$$

the following approximation can be obtained by noting that the point $j\omega_1$ is very close to p_1, p_{h_1}, and s_0 with

$$\sum_i \angle(j\omega_1 - z_{h_i}) \approx \sum_i \angle(s_0 - z_{h_i}). \tag{5.34}$$

In addition, the sum of the angle from $j\omega_1$ to all the plant poles except the pole at p_{h_1} can also be approximated by

$$\sum_{i\neq 1} \angle(j\omega_1 - p_{h_i}) \approx \sum_{i\neq 1} \angle(s_0 - p_{h_i}). \tag{5.35}$$

As such, it can be concluded from (5.26)–(5.35) that

$$-\phi_{h1,\text{dep}} - \angle(s_0 - p_1) + \angle(j\omega_1 - p_{h_1}) = \pm 180^\circ(2k+1). \tag{5.36}$$

In Figure 5.15, we define $\phi_1 = \angle(s_0 - p_1)$ and $\theta_0 = \angle(j\omega_1 - p_{h_1})$. The resonant frequency in the closed-loop (i.e., the pseudo-plant) will be slightly pushed down and the damping ratio will be smaller when there is no loop-shaping for the resonant mode. This makes the pole of the pseudo-plant at p_{h_1} lower than the resonant frequency in the complex s-plane. On the other hand, the imaginary part of the pole at p_1 will be almost equivalent to that of $j\omega_1$ if the damping ratio ζ_1 is very small. The resulting layout of p_1, p_{h_1}, and $j\omega_1$ is depicted in Figure 5.15(a).

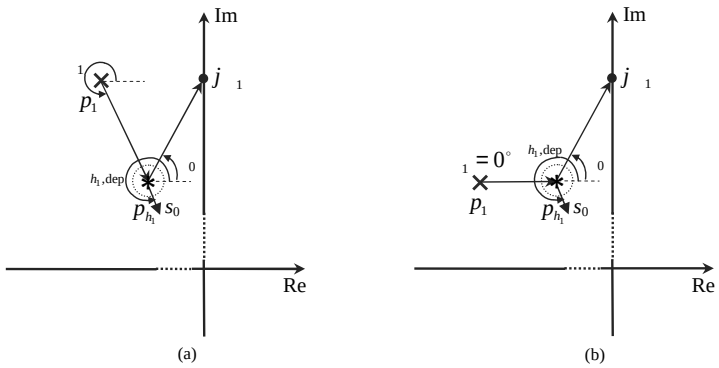

FIGURE 5.15
Relationship of angles: (a) phase-shift method; (b) frequency-shift method.

Under this framework and for the resonance located at a very high frequency range especially those above 10 kHz, $\phi_1 \approx \angle(p_{h_1} - p_1) \approx (-75^\circ, -90^\circ)$ and $\theta_0 \approx (75^\circ, 90^\circ)$. From (5.36) it can be concluded that the angle of departure from the plant pole at p_{h_1} is

$$\phi_{h1,\text{dep}} = 360^\circ k, \quad k = 0, 1, 2, \cdots, \tag{5.37}$$

which means that the plant poles will enter into the right-half plane under a very small gain margin. The closed-loop system will then be considered as unstable.

An example which has a resonant mode at 12 kHz and a damping ratio

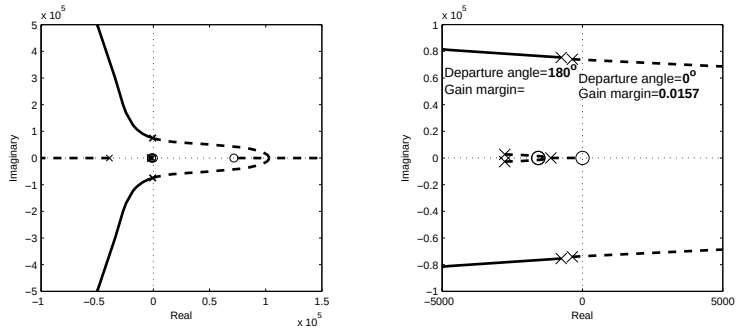

FIGURE 5.16
Root loci of $S_h(s)F(s)$. Solid: filter pole. Dashed: plant pole.

of 0.015 is simulated. The peak filter $F(s)$ is designed to center at 12 kHz with a damping ratio of 0.01. Figure 5.16 plots the root loci of the pseudo open loop transfer function $S_h(s)F(s)$. It can be clearly seen that the departure angle from the plant pole is 0° so that the plant pole will enter into the most unstable region with the gain margin as small as 0.0157, though the filter pole will still enjoy the 180° departure angle and enter into the left-half plane.

Two methods, i.e., the *phase-shift* and *frequency-shift* methods, are presented to design the stable peak filter $F(s)$ when there are significant plant dynamics within the bandwidth of $F(s)$. When there is a very small phase variation within the bandwidth of $F(s)$, the phase-shift method is preferable. On the other hand, the frequency-shift method will be used if the phase change is big and frequency variations are small.

Firstly, the phase-shift method is presented for the peak filter in (5.17). However, the design of the filter zero is chosen as

$$\varphi = \arg[S_h(j\omega_1)], \quad \varphi \in [-\frac{\pi}{2}, \frac{\pi}{2}]. \tag{5.38}$$

The angle of departure from the plant pole at p_{h_1} can be determined similarly by following the same analysis. It is known that (5.26)–(5.32) still hold while (5.33) changes to

$$\varphi = \sum_i \angle(j\omega_1 - z_{h_i}) - \sum_i \angle(j\omega_1 - p_{h_i}). \tag{5.39}$$

The approximations given in (5.34) and (5.35) are still valid. As such, it can be concluded that

$$\phi_{h1,\text{dep}} \approx -90°. \tag{5.40}$$

Similarly, it can also be concluded that the angle of departure from the filter pole at p_1 is

$$\phi_{1,\text{dep}} \approx 90°. \tag{5.41}$$

The same example with a resonant mode at 12 kHz and damping ratio of 0.015 is simulated. The peak filter is also designed to center at 12 kHz with damping ratio of 0.01. The root loci of the pseudo open loop transfer function $S_h(s)F(s)$ are plotted in Figure 5.17, which show that the departure angle from the plant pole is $-90°$ and that from the filter pole is $90°$. Under the compromised departure angles from both filter poles and plant poles, the achieved gain margin is increased dramatically to 11.7 so that the closed-loop system is stable. The Nyquist plot given in Figure 5.18(a) shows the higher gain at disturbance frequency of the overall open loop as compared to that of the nominal open loop. The resulting magnitude of the sensitivity transfer function given in Figure 5.18(b) verifies the effective gain attenuation at disturbance frequency at extra 10 dB by augmenting the baseline controller with the presented peak filter, and at the same time the magnitude of the sensitivity transfer function has lower peak positive sensitivity as compared to that of the baseline control.

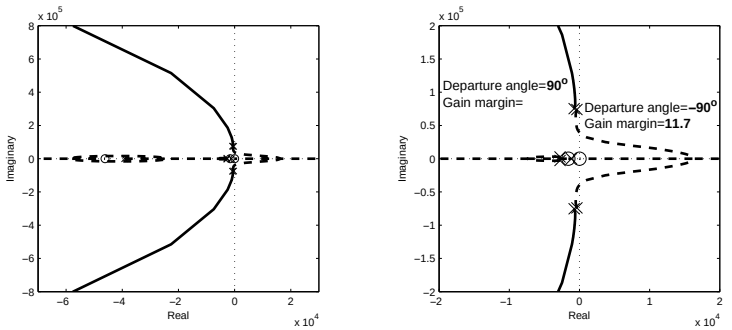

FIGURE 5.17
Root loci of $S_h(s)F(s)$. Solid: filter pole. Dashed: plant pole.

Next, the other method is known as the frequency-shift method, i.e., shifting the frequency of the peak filter rather than its phase. In this method, the natural frequency of the peak filter is placed at the resonant frequency of the pseudo-plant, i.e., slightly lower than the resonant frequency of the original plant. The filter zero is placed according to (5.18), i.e.,

$$\varphi = \arg[S_h(j\omega_1)] + \frac{\pi}{2}, \quad \varphi \in [-\frac{\pi}{2}, \frac{\pi}{2}]. \tag{5.42}$$

Under this setting, (5.26)–(5.36) still hold, i.e.,

$$-\phi_{h1,\text{dep}} - \angle(s_0 - p_1) + \angle(j\omega_1 - p_{h_1}) = \pm 180°(2k+1). \tag{5.43}$$

Since the imaginary parts of the pole at p_1 and the pole at p_{h_1} are identical as can be seen from Figure 5.15(b), it is known that

$$\angle(s_0 - p_1) \approx \angle(p_{h_1} - p_1) \approx 0°. \tag{5.44}$$

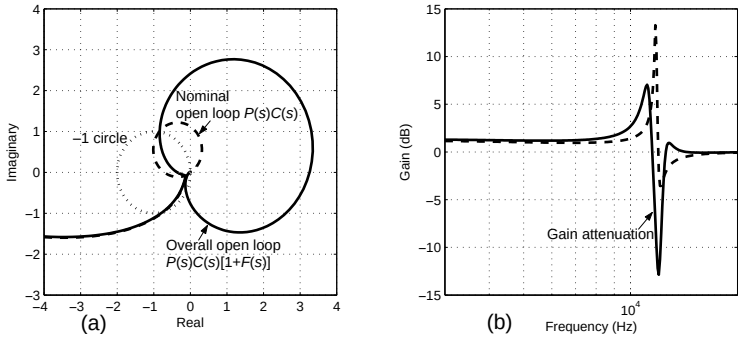

FIGURE 5.18
(a) Nyquist plot of the open loop system; (b) Magnitude of the sensitivity transfer function of the closed-loop system. Solid: with $F(s)$. Dashed: without $F(s)$.

As such, the angle of departure from the pole at p_{h_1} is

$$\phi_{h1,\text{dep}} \approx \pm 90^\circ. \tag{5.45}$$

The angle of departure from the filter pole at p_1 can also be similarly approximated by

$$\phi_{1,\text{dep}} \approx \pm 90^\circ. \tag{5.46}$$

The same example with a resonant mode at 12 kHz and damping ratio being 0.015 is simulated. The peak filter is designed to center slightly lower at 11.8 kHz with a damping ratio 0.01. The root loci of the pseudo open loop $S_h(s)F(s)$ are plotted in Figure 5.19, which shows that the departure angle from the plant pole is -90° and that from the filter pole is 90°. Under these compromised departure angles from both filter poles and plant poles, the achieved gain margin is increased dramatically to 8.22 so that the closed-loop system is stable. The Nyquist plot given in Figure 5.20(a) shows the higher gain at disturbance frequency of the overall open loop transfer function as compared to that of the nominal open loop transfer function. The resulting magnitude of the sensitivity transfer function given in Figure 5.20(b) verifies the effective gain attenuation at disturbance frequency with an extra 8 dB by augmenting the baseline controller with the presented peak filter, and at the same time the magnitude of sensitivity transfer function has a lower peak positive sensitivity as compared to the baseline control.

5.3.3.3 Using LTV Peak Filters

In addition to the amount of gain attenuation, the duration of the transient response is the other critical design factor when designing peak filters.

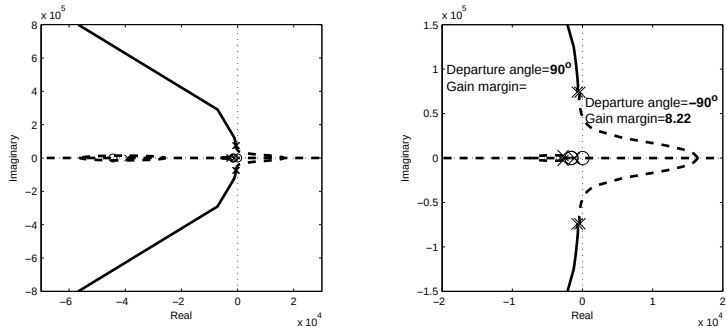

FIGURE 5.19
Root loci of $S_h(s)F(s)$. Solid: filter pole. Dashed: plant pole.

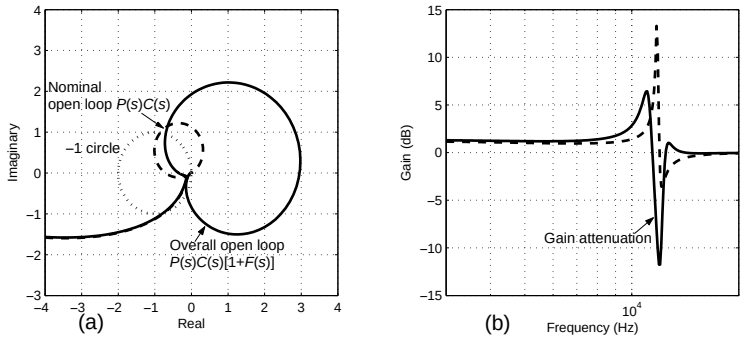

FIGURE 5.20
(a) Nyquist plot of the open loop system; (b) Magnitude of the sensitivity transfer function of the closed-loop system. Solid: with $F(s)$. Dashed: without $F(s)$.

However, these two design factors are contradictory to each other. Usually, a trade-off exists between the transient response and the bandwidth of the gain notch [43, 44, 45]. The simultaneous improvement for transient response in time-domain and gain attenuation in frequency-domain could be very hard to achieve for conventional LTI filters. As such, Linear Time-Varying (LTV) filters have been proposed in [46] and [47] with varying filter gain and damping ratio (or quality factor Q in communications and filter engineering).

In this section, a peak filtering scheme with improved transient response is presented using the same peak filter structure in (5.17). The properties of the LTV peak filters are (i) the gain and the damping ratio of the filter are

adjusted along the time to ensure faster attenuation in time-domain and wider bandwidth in the frequency-domain, (ii) the stability during the transient period is guaranteed by taking into account the poles of the lightly damped plant as critical poles, and ensuring the root loci originating from these poles enter into the left-half plane through placing the filter zero properly, and (iii) during steady-state, both filter poles and plant poles should be taken into account so that compromised departure angles from both filter poles and plant poles are adopted to ensure closed-loop stability [48].

In the transient stage, the width of the disturbance rejection band shall be large to ensure faster attenuation. As such, the gain and damping ratio of the peak filter should be large and their values should be scheduled to reduce along the time as

$$\theta(t) = \bar{\theta}[d - (d-1)h(t)], \tag{5.47}$$

where $\theta{=}K$ or ζ_1, $d{=}\theta(0)/\bar{\theta}$ defines the variation range of $\theta(t)$, and $h(t)$ describes the step response of a supportive system $H(s)$, i.e., $h(t){=}\mathcal{L}^{-1}\{s^{-1}H(s)\}$ where $\mathcal{L}^{-1}$ is the inverse Laplace transform operator. For our design, $H(s)$ is chosen as a first-order system as

$$H(s) = \frac{\gamma}{s+\gamma}, \quad \gamma > 0. \tag{5.48}$$

In this case, $0 < \bar{\theta} < \theta(0)$ is the lower bound of $\theta(t)$ so that $\theta(t)$ decreases in the variation interval for $d > 1$. As such, (5.47) can be rewritten as

$$\theta(t) = \bar{\theta}\left[1 + \left(\frac{\theta(0)}{\bar{\theta}} - 1\right)e^{-\gamma t}\right], \tag{5.49}$$

or in discrete-time as

$$\theta(kT_s) = \bar{\theta}\left[1 + \left(\frac{\theta(0)}{\bar{\theta}} - 1\right)e^{-\gamma kT_s}\right], \tag{5.50}$$

with T_s being the step size for parametric updates.

The initial value of the damping ratio can be chosen such that the poles of the resulting filter are well-damped to ensure stability of the lightly damped plant poles which are comparatively more critical. The lower bound of the damping ratio is chosen to achieve the desired width of attenuation. To guarantee the closed-loop stability for the transient stage, the root loci originating from the lightly damped plant poles should enter into the left-half plane. The filter zero is placed according to

$$\varphi = \arg[S_h(j\omega_1)] + \pi, \quad \varphi \in [-\frac{\pi}{2}, \frac{\pi}{2}]. \tag{5.51}$$

Similarly, the angle of departure from the plant poles is

$$\phi_{p,\text{dep}} \approx -180^\circ, \tag{5.52}$$

and the angle of departure from the filter poles is

$$\phi_{f,\text{dep}} \approx 0^\circ. \tag{5.53}$$

In the steady-state stage, the lower bound for the parameter tuning $\bar{\theta}$ will be adopted and fixed for the peak filter.

Due to the small damping ratio, stability of the resulting lightly damped filter poles is as critical as that of the plant poles. As such, the root loci originating from both the filter poles and the plant poles should enter into the left-half plane. The scheme of compromised departure angles similar to the LTI peak filter case in the previous section will be adopted here such that the angles of departure from the filter poles and the plant poles are

$$\phi_{p,\text{dep}} \approx \pm 90^\circ, \tag{5.54}$$

and

$$\phi_{f,\text{dep}} \approx \mp 90^\circ. \tag{5.55}$$

A simple example is given here to illustrate and showcase the effectiveness of the presented method. A second-order system with a low frequency mode at 50 Hz and damping ratio of 0.4 plus a resonant mode at 12 kHz and damping ratio of 0.015 is used. The peak filter is designed to center at 12 kHz. The initial values of the parameter tuning in transient stage are chosen as $K(0) = 1$, $\zeta_1(0) = 0.1$, and the lower bounds are $\bar{K} = 0.2$, $\bar{\zeta}_1 = 0.02$, and $\gamma = 3000$.

The root loci of the open loop at the initial stage are plotted in Figure 5.21, where it can be seen that the departure angle from a plant pole is -180° and that from a filter pole is 0°. The gain margin of the plant pole is 108 while the gain margin of the filter pole is infinity. Figure 5.22 plots the root loci of the open loop at steady-state. By providing the compromised departure angles for both filter poles and plant poles, which are 90° and -90°, respectively, the achieved gain margin is sufficiently large as infinity and 16, respectively.

The stability margins of the closed-loop systems during both transient and steady-state stages are improved using the presented add-on LTI and LTV peak filters with improved transient responses.

5.3.4 Experimental Verifications

In this section, the phase-stabilization method of resonance compensation using mechanical resonant modes, LTI peak filters, and LTV peak filters are verified with simulations and experiments on a VCM-actuated arm in a typical mechatronic system. In the experiments, the LDV is used to measure the lateral displacement of the VCM-actuated arm, and our presented control algorithms are implemented on dSPACE at a sampling frequency of 30 kHz. The frequency responses of the open loop and sensitivity transfer functions are shown in Figures 5.23 and 5.24, respectively.

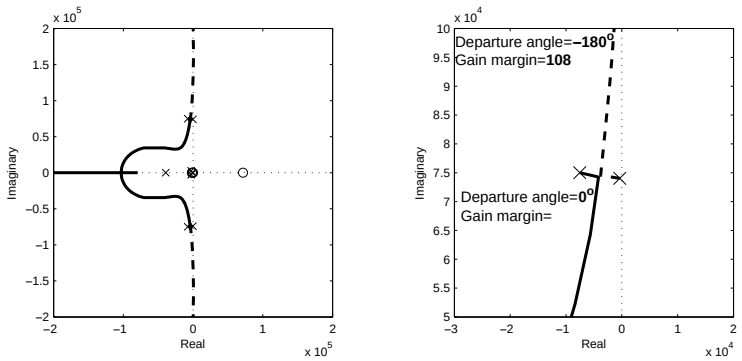

FIGURE 5.21
Root loci and angles of departure. Solid: filter pole. Dashed: plant pole.

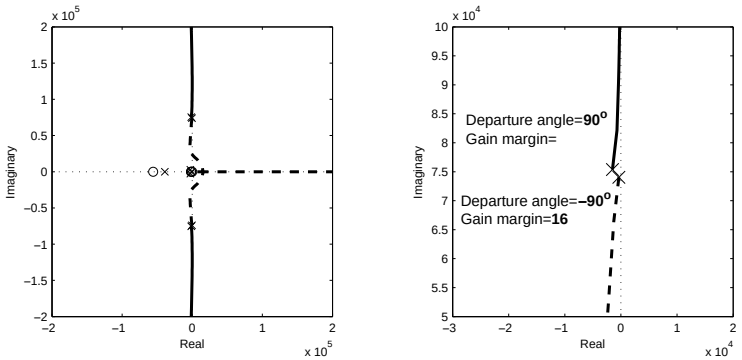

FIGURE 5.22
Root loci and angles of departure. Solid: filter pole. Dashed: plant pole.

From Figure 5.23, it can be seen that the in-phase mechanical resonant mode at 5161 Hz has been phase-stabilized, while the out-of-phase resonant mode at 7913 Hz has been *reshaped* to be in-phase with the rigid body mode using the presented resonance compensation methods with peak filters. As a result, an attenuation gain of more than 12 dB can be observed at 5161 Hz and 7913 Hz in the magnitudes of the sensitivity transfer functions as shown in Figure 5.24, which greatly improve the disturbance rejection capabilities at both resonant frequencies.

The transient performance is evaluated and compared between peak filters with time-varying parameters using a look-up table and time-invariant parameters via simulations. Firstly, a set of gain and damping ratio values is obtained to reshape the critical mechanical resonant mode at 7913 Hz to

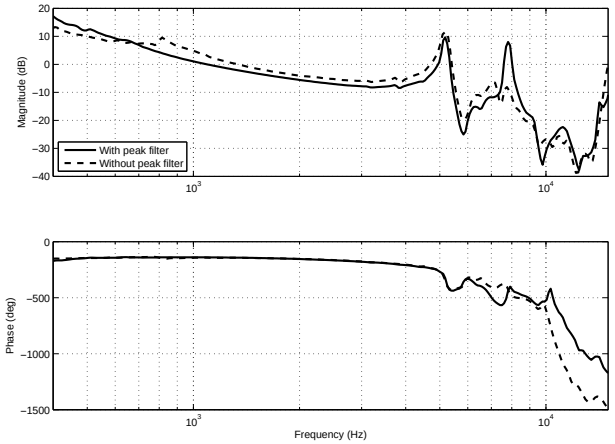

FIGURE 5.23
Frequency responses of open loop transfer functions.

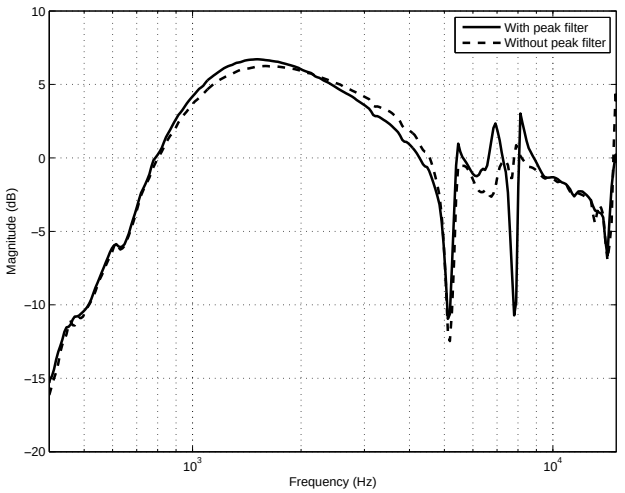

FIGURE 5.24
Frequency responses of sensitivity transfer functions.

be in-phase, and are chosen as their steady-state values. Secondly, the initial values of the gain and damping ratio are chosen to be relatively larger than their steady-state values. Thirdly, the gain K_f and damping ratio ζ of the

peak filter are updated using

$$\theta(t)=\theta_s\left[1+\left(\frac{\theta_i}{\theta_s}\right)e^{-\gamma t}\right], \tag{5.56}$$

where $\gamma>0$ is the decaying rate of the parameters. θ_i and θ_s are the initial and steady-state values of the gain or damping ratio, respectively. A sinusoidal signal of 7913 Hz with unity amplitude is used as the output disturbance to evaluate the transient performances of the two schemes with no measurement noise included. The LTV peak filter with initial and steady-state values of $(K_f, \zeta)=(2, 0.1) \rightarrow (0.5, 0.01)$ shows improved transient performance over the LTI peak filter as shown in Figure 5.25.

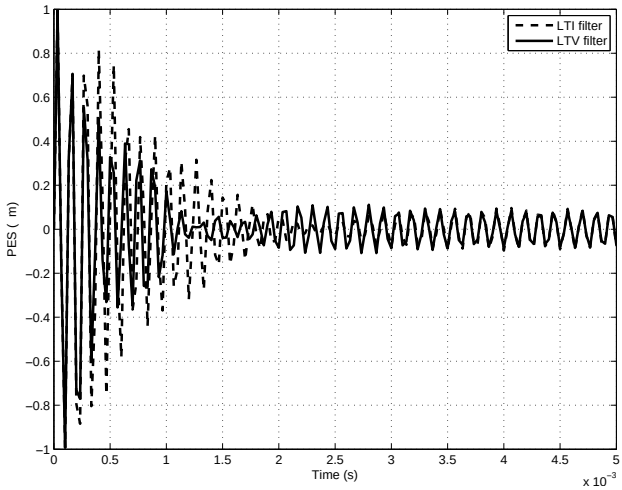

FIGURE 5.25
Transient performances of presented LTV and LTI peak filters.

5.4 Resonance Compensation With Extraneous Sensors

In dual-stage servo systems, it is common that the combined output remains as the only available feedback signal even when there are two mechanical actuators to be precisely controlled. With the improvements in disturbance rejection performance by incorporation of extraneous sensors and active-sensing methodologies, the feasibility of employing *multi-sensing* servo systems [49] through enhanced sensor fusion in mechatronic systems have been studied. Recently, advances in piezoelectric materials also allow self-sensing servo systems

to be realized, where the mechanical actuators are used as sensors and actuators *simultaneously*. In this section, the model-based and non-model-based active control schemes using Self-Sensing Actuation (SSA) are presented with experimental verifications.

5.4.1 Active Damping

It is well known from control theory that lowest positive area under the sensitivity transfer function is achievable if and only if a control system is stable and of zero relative degree. While this is not possible for most physical systems, placement of extra sensors ensure more states to be measured, which can reduce the order of the controllers as in state feedback. In high-performance mechatronic systems, adding sensors to pick up extra actuator's information, e.g., displacement/deformation, velocity, acceleration, strain, etc., is intuitive and is a common practice in current literature. For HDDs, several methods including employing (i) accelerometers [50] in a single-stage HDD, (ii) PZT compound actuator as a vibration sensor [51] and (iii) one of the two PZT strips as a vibration sensor and the other as an actuator [52] for dual-stage HDDs, etc., have been reported in current literature for active damping of mechanical resonant modes.

5.4.2 Self-Sensing Actuation (SSA)

Common piezoelectric materials currently employed as actuators/sensors include the PolyVinylDeneFlouride (PVDF) and the Lead-Zirconate-Titanate (Pb-Zr-Ti, or PZT) elements. The piezoelectric property is made possible by excessive exposure of the ceramic to strong electric fields during the manufacturing process, thereby inducing permanent dipoles in the material. When electrically polarized, the dipoles respond collectively to produce an expansion and hence mechanical strain within the material, leading to perpendicular displacement. Conversely when piezoelectric materials are subjected to strain, charges arise on the surface of the material and set up an electric field, analogous to back Electro-Motive Force (EMF) in magnetic systems. This *reversible* property allows the piezoelectric material to function as an actuator and/or a sensor.

In SSA, the piezoelectric elements are used as sensors and actuators simultaneously. Using a typical PZT-actuated arm commonly found in precision mechatronic systems as an example, the mechanical structure can be modeled as a flexible cantilever beam (one end fixed and the other end free) as shown in Figure 5.26 for simplicity but without loss of generality.

The linear electromechanical equations of the PZT elements are [53]

$$S = s^E T + d^T E, \tag{5.57}$$

$$D = dT + \varepsilon^T E, \tag{5.58}$$

where S, T, E, and D are the mechanical strain, mechanical stress, electri-

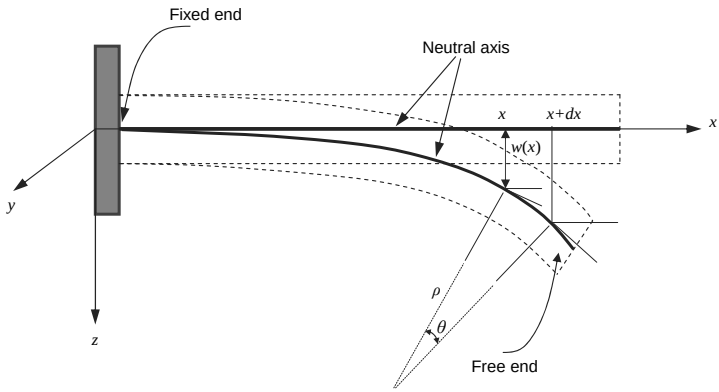

FIGURE 5.26
Schematic of typical PZT-actuated arm.

cal field, and electrical charge density of the PZT elements, respectively. s^E is the mechanical compliance at zero electric field, i.e., at $E = 0$, d is the matrix for the direct piezoelectric effect, and ε is the permittivity evaluated at constant mechanical strain. When the mechanical structure vibrates, the mechanical energy strains the piezoelectric material and generates electrical energy, i.e., voltage. As such, the mechanical information of the PZT elements such as strain can be measured by capturing the voltage created across the PZT elements.

SSA has already been applied to many practical engineering problems, e.g., control of robot manipulators and cantilever beams (see [54, 55] and the references therein). SSA is attractive in active control applications because the actuator and sensor arrangement are a collocated (or in many applications, near-collocated) pair. When applied in mechatronics, SSA usually requires only additional cheap electronic circuitry and does not reduce the effective actuation of the secondary actuator.

In SSA, the piezoelectric material can be modeled as a capacitance in series with a variable voltage source v_M where the capacitor represents the dipoles and the variable voltage source v_M represents the electric field setup by the dipoles during actuation. If the capacitance of the piezoelectric material is known, one can decouple the variable voltage (i.e, strain, displacement, or deformation information) from the input signal u_M using a *bridge circuit*. Two different types of SSA bridge circuits are described in the following sections, namely the Direct-Driven SSA (DDSSA) and Indirect-Driven SSA (IDSSA).

5.4.2.1 Direct-Driven SSA (DDSSA)

The PZT elements of a PZT-actuated arm can be modeled as a capacitor C_{PZT} in series with a dependent voltage source v_M as shown in Figure 5.27, where

a Direct-Driven SSA (DDSSA) scheme is employed as the input signal u_M is applied across the entire bridge circuit.

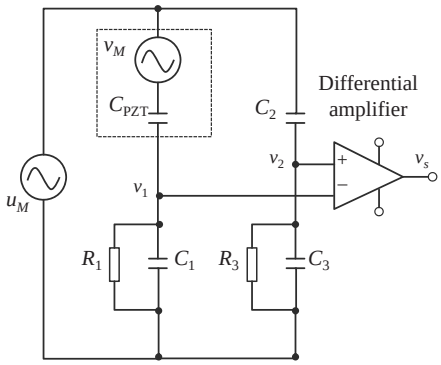

FIGURE 5.27
Direct-Driven SSA bridge circuit.

In Figure 5.27, resistors R_1 and R_3 are sometimes placed in parallel with capacitors C_1 and C_3 to prevent DC drifts, and the values of capacitors C_1, C_2, and C_3 are to be determined. When the bridge circuit is subjected to input voltage u_M, the PZT-actuated arm is transduced to give displacement y_M. The voltage v_M generated is hence proportional to y_M (arising from mechanical strain) of the PZT-actuated arm, and can be be decoupled from u_M using a differential amplifier. From Figure 5.27, the following equations hold

$$v_1 = \frac{C_{\text{PZT}}}{C_1 + C_{\text{PZT}}}(u_M - v_M), \tag{5.59}$$

$$v_2 = \frac{C_2}{C_2 + C_3}u_M, \tag{5.60}$$

$$\begin{aligned} v_s &= v_2 - v_1 \\ &= \left(\frac{C_{\text{PZT}}}{C_1 + C_{\text{PZT}}} - \frac{C_2}{C_2 + C_3}\right)u_M + \frac{C_{\text{PZT}}}{C_1 + C_{\text{PZT}}}v_M. \end{aligned} \tag{5.61}$$

By measuring C_{PZT} *a priori* and ensuring that capacitors $C_1 = C_2 = C_3 = C_{\text{PZT}}$, the bridge circuit is *balanced*. A PZT-actuated arm displacement estimator is established as

$$\begin{aligned} v_s &= \frac{C_{\text{PZT}}}{C_1 + C_{\text{PZT}}}v_M \\ &= \frac{v_M}{2}. \end{aligned} \tag{5.62}$$

As such, v_M is decoupled from the input signal u_M and can be used for active control purposes. The only trade-off when driving the PZT-actuated arm and the bridge circuit directly using the input signal u_M is that a larger u_M

is needed for the same amount of required displacement y_M as compared to that without the bridge circuit [54]. This loads the input signal u_M, and can be alleviated by using the Indirect-Driven SSA (IDSSA) bridge circuit.

5.4.2.2 Indirect-Driven SSA (IDSSA)

In the Indirect-Driven SSA (IDSSA) circuit as shown in Figure 5.28, additional capacitors and resistors are required in the feedback loops of operational amplifiers so that the circuit acts as a high-pass filter after differential amplification. This results in better self-sensing performance for higher Signal-to-Noise Ratio (SNR) measurements and wider sensing bandwidth to detect high frequency mechanical resonant modes in the PZT-actuated arm.

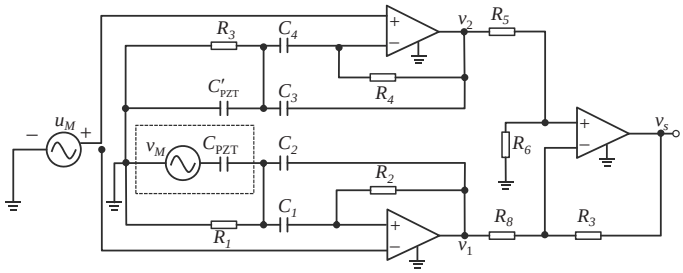

FIGURE 5.28
Indirect-Driven SSA bridge circuit.

The sensing voltage v_M generated from the strain of the PZT element can be decoupled from u_M as shown in the following derivations. The Laplace transform of $v_1(t)$ and $v_2(t)$ can be derived as

$$v_1(s) = \left[1 + \frac{C_1 C_{\mathrm{PZT}} R_1 R_2 s^2 + C_1 R_2 s}{C_1 C_2 R_1 R_2 s^2 + (C_{\mathrm{PZT}} + C_1 + C_2) R_1 s + 1}\right] u_M(s) - \frac{(C_{\mathrm{PZT}}/C_2) s^2}{s^2 + (C_{\mathrm{PZT}} + C_1 + C_2) s / C_1 C_2 R_2 + (1/C_1 C_2 R_1 R_2)} v_M(s),$$

$$v_2(s) = \left[1 + \frac{C_3 C'_{\mathrm{PZT}} R_3 R_4 s^2 + C_3 R_4 s}{C_3 C_4 R_3 R_4 s^2 + (C'_{\mathrm{PZT}} + C_3 + C_4) R_1 s + 1}\right] u_M(s), \quad (5.63)$$

and the output of the IDSSA bridge circuit $v_S(s)$ is given by

$$v_S(s) = \frac{R_6}{R_5 + R_6} \frac{R_7 + R_8}{R_8} v_2(s) - \frac{R_7}{R_8} v_1(s). \quad (5.64)$$

In this case, the components in Figure 5.28 are chosen to be

$$\begin{cases} C_1 = C_2 = C_3 = C_4 = C'_{\mathrm{PZT}} = C_{\mathrm{PZT}}, \\ R_1 = R_2 = R_3 = R_4, \\ R_5 = R_8, \\ R_6 = R_7 = k R_5, \end{cases} \quad (5.65)$$

the bridge circuit is balanced and $v_M(s)$ is similarly decoupled from $u_M(s)$ with

$$\frac{v_S(s)}{v_M(s)} = \frac{ks^2}{s^2 + 2\zeta(2\pi f_c)s + (2\pi f_c)^2}, \tag{5.66}$$

where $f_c = \frac{1}{2\pi\sqrt{C_1C_2R_1R_2}}$, $\zeta = \frac{\sqrt{C_1C_2R_1R_2}(C_1+C_2+C_{\mathrm{PZT}})}{2C_1C_2R_2}$, and k are the cut-off frequency, damping ratio, and gain of the high-pass filter, respectively. The components of resistors and capacitors in Figure 5.28 are chosen depending on the desired corner frequency of the high-pass filter and sensing bandwidth accordingly.

With the presented SSA bridge circuits, inner loop control methodologies can be developed to stiffen the PZT-actuated arm via active damping *before* the entire outer dual-stage control loop is closed. The model-based and non-model-based designs are described in the following sections for inner loop damping of the mechanical resonant modes in the PZT-actuated arm. For the rest of the chapter, a sampler is used in the place of the ZOH $H(s)$ in all control block diagrams for brevity but without loss of generality.

5.4.3 Model-Based Design

In this section, the model-based resonance compensation design using SSA is described in detail. The model-based SSA control topology with the Active Mode Damping (AMD) controller C_D is shown in Figure 5.29.

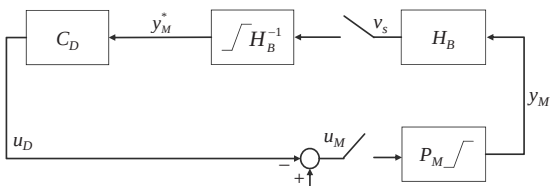

FIGURE 5.29
Model-based SSA control topology.

In Figure 5.29, the estimated displacement of the PZT-actuated arm y_M^* is obtained from SSA for feedback control. The digital inverse of displacement estimation circuit $H_B^{-1}(z)$ is designed from the dynamics of the displacement estimation circuit H_B. $H_B^{-1}(z)$ is required to obtain a real time estimated y_M^* for the AMD controller C_D to damp the PZT-actuated arm's sway modes using inner loop compensation, with possible attenuation of the torsion modes which was previously impossible if y_M^* using SSA was unavailable [54].

The PZT-actuated arm displacement estimation circuit H_B consists of the PZT-actuated arm/sensor and a differential amplifier. As v_M (hence v_s) in Figures 5.27 and 5.28 arises from y_M, H_B should be modeled by a transfer

function $H_B(s) = \frac{v_s(s)}{y_M(s)}$. A digital inverse of $H_B(s)$, $H_B^{-1}(z)$, is constructed to provide an estimate of the displacement of the PZT-actuated arm y_M^*. A saturation function is also included to take into account the saturation of the PZT-actuated arm as shown in Figure 5.29.

Using SSA, the collocation of the PZT-actuated arm and the PZT-actuated arm's displacement sensor is nearly achieved. As such, a robust AMD controller for damping the PZT-actuated arm's mechanical resonant modes can be designed, and the AMD controller $C_{D,i}(s)$ for each i^{th} mechanical resonant mode is given by

$$C_{D,i}(s) = K_{D,i} \frac{s + \frac{\omega_{n,i}}{\varepsilon_i}}{s + \frac{\kappa_i \omega_{n,i}}{\varepsilon_i}} \frac{s + \omega_{n,i}}{s + \frac{\varepsilon_i \omega_{n,i}}{\kappa_i}}, \tag{5.67}$$

to increase the damping ratios (hence reduced gains) of the PZT-actuated arm's torsion modes and sway modes. $K_{D,i}$ is set to ε_i in most cases. ε_i and κ_i are tuning parameters, and $1 < \varepsilon_i \leq P$ is chosen usually for robustness against natural frequency variations P % ($P < 3$ for most physical systems). $5 < \kappa_i < 15$ is then chosen to determine the amount of phase lift required to stabilize the resonant mode at the natural frequency $\omega_{n,i}$.

The overall AMD controller C_D can be obtained from the product $C_{D,i}(s)$ for the total number of torsion and sway modes to be damped. Phase lead compensators are sometimes added to reduce the phase loss introduced by the AMD controllers and to increase the gain of the PZT-actuated arm's displacement for high frequency mode detection. In essence, C_D is a general case of traditional Positive Position Feedback (PPF) vibration controllers [56] with additional zeros. The zeros prevent causality issues in PPF arrangements, and improve the stability margin of the closed-loop system. The presented AMD controller increases the gain of each resonant mode and stabilizes the control loop using a phase lead from the zeros at $\frac{\omega_{n,i}}{\varepsilon_i}$, which is a common result when using optimal control methods such as $\mathcal{H}_\infty$ loop shaping techniques.

Assuming the PZT-actuated arm P_M has resonant modes at natural frequencies $\omega_{n,i}$ and the AMD controller C_D in (5.67) is included in a negative feedback configuration as shown in Figure 5.29. The following closed-loop equation holds

$$\frac{y_M(s)}{u_M(s)} = \frac{P_M(s)}{1 + C_D(s) P_M(s)}, \tag{5.68}$$

if the closed-loop system is stable. As such, the gains of the mechanical resonant modes are suppressed by the AMD controller at the frequencies $\omega_{n,i}$ of

the modes effectively by a factor of $\frac{1}{|C_D(j\omega_{n,i})|}$ as

$$\begin{aligned}\left|\frac{y_M(j\omega_{n,i})}{u_M(j\omega_{n,i})}\right| &= \left|\frac{P_M(j\omega_{n,i})}{1+C_D(j\omega_{n,i})P_M(j\omega_{n,i})}\right| \\ &\approx \frac{|P_M(j\omega_{n,i})|}{|C_D(j\omega_{n,i})P_M(j\omega_{n,i})|} \\ &= \frac{1}{|C_D(j\omega_{n,i})|}, \end{aligned} \tag{5.69}$$

if $|C_D(j\omega_{n,i})P_M(j\omega_{n,i})| >> 1$.

To illustrate the effectiveness of the presented scheme on PZT-actuated arms in precision mechatronic systems, a PZT active suspension in a commercial dual-stage HDD is modeled as $P_M(s)$ and identified to have torsion modes at 4.31 kHz and 6.52 kHz, a bending mode at 11.04 kHz, and a sway mode at 21.08 kHz [54]. The simulated frequency responses of the presented AMD controller $C_D(s)$ and the open loop transfer function $C_D(s)P_M(s)$ are shown in Figure 5.30.

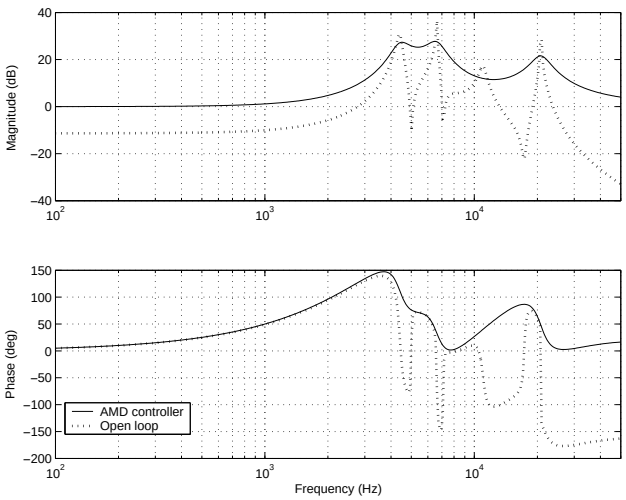

FIGURE 5.30
Simulated frequency responses. Solid: AMD controller $C_D(s)$. Dotted: open loop transfer function $C_D(s)P_M(s)$.

With $C_D(s)$ in the feedback path as shown in Figure 5.29 and (5.67), the loop is closed to damp the PZT active suspensions's torsion modes and sway mode. The experimental frequency responses of the PZT active suspension with and without the presented AMD controller C_D are shown in Figure 5.31. It can be seen from Figure 5.31 that the PZT active suspension's torsion modes

at 4.31 kHz and 6.52 kHz (about 5 dB) as well as sway mode at 21.08 kHz (about 30 dB) are all damped by the AMD controller C_D.

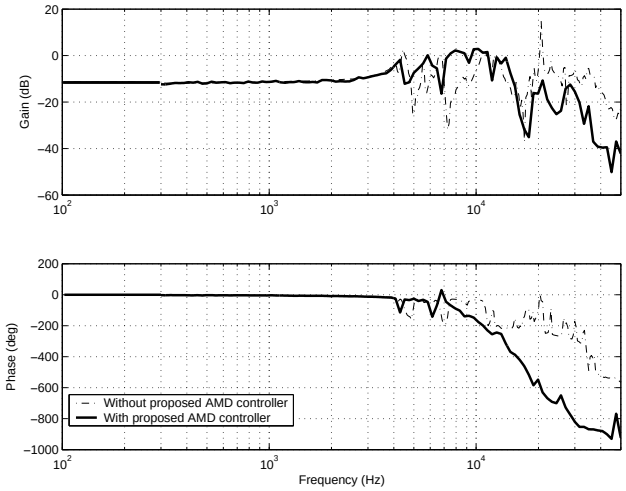

FIGURE 5.31
Experimental frequency responses of PZT active suspension. Solid: without AMD controller C_D. Dashed-dot: with AMD controller C_D.

The presented AMD controller C_D using the model-based design is more effective in suppressing the sway modes as compared to the torsion modes (and bending modes). This is obvious as the estimated PZT-actuated arm's displacement y_M^* from the displacement estimation circuit H_B is only effective in measuring in-plane components (making the in-plane sway modes observable and controllable) of the PZT-actuated arm and not the torsion modes (out-of-plane weakly controllable modes). This is unavoidable as the PZT-actuated arm's displacement estimation circuit H_B produces a scalar signal and the PZT-actuated arm has more degrees of freedom than control inputs, i.e., *under-actuation*.

5.4.4 Non-Model-Based Design

Rather than directly feeding back the strain signal from SSA, an adaptive *non-model-based control* scheme is used to enhance the performance of vibration suppression. In this section, the structure of the PZT-actuated arm is analyzed, followed by the adaptive algorithm and its stability proof [57].

Assume that the cross-section of the suspension is a symmetrical area (in $y-z$ plane) which is perpendicular to the neutral plane (in $x-z$ plane) as shown earlier in Figure 5.26. When deformed in the $x-z$ plane with the x-

axis being the neutral axis, the strain along the x-axis is given by

$$\varepsilon_x = -z\frac{d^2w}{dx^2}, \tag{5.70}$$

where w is the deformation of the beam along the z-axis at a point of interest x. z is the distance from the neutral axis to x, and $\rho = 1/\left(\frac{d^2w}{dx^2}\right)$ is the radius of curvature.

SSA circuits are used to extract the strain signal of the PZT-actuated arm. The strain signal can then be used for adaptive non-model-based controller design to compensate for the structural vibrations at the critical resonant modes.

Figure 5.32 shows the block diagram of the control system with the add-on adaptive control, where the baseline control C_M is comprised of a Proportional-Integral (PI) controller cascaded with several notch filters, and an adaptive non-model-based control is used in the add-on strain feedback loop to enhance the performance of vibration suppression at the critical resonant modes of the PZT-actuated arm.

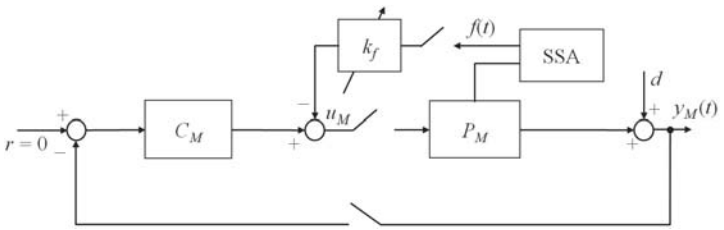

FIGURE 5.32
Adaptive non-model-based SSA control topology.

The adaptive non-model-based control is derived based on an *energy* function [58] as

$$[E_k(t) + E_p(t)] - [E_k(0) + E_p(0)] = \int_0^t u_M(\tau)\dot{y}_M(\tau)d\tau, \tag{5.71}$$

where $E_k(t)$ and $E_p(t)$ are the total *kinetic* and *potential* energy of the system at time t, respectively. $E_k(0)$ and $E_p(0)$ are the initial kinetic and potential energy of the system at $t = 0$, respectively. $u_M(\tau)$ and $\dot{y}_M(\tau)$ are the input and velocity of the PZT-actuated arm, respectively.

The time derivative of (5.71) is

$$\dot{E}_k(t)+\dot{E}_p(t) = u_M(t)\dot{y}_M(t), \tag{5.72}$$

where $\dot{E}_k(t)$ and $\dot{E}_p(t)$ are the time derivatives of the kinetic and potential energy, respectively.

The adaptive non-model-based control $u_M(t)$ is designed as the combination of a PI control and an adaptive strain feedback term, which is expressed as

$$u_M(t) = -k_p y_M(t) - k_i \int_0^t y_M(\tau)d\tau - k_f f(t) \int_0^t f(\tau)d\tau, \tag{5.73}$$

where k_p and $k_i > 0$ are proportional and integral gains, respectively. $f(t)$ is a signal reflecting the deformation of the controlled plant, e.g., the strain, which should be chosen such that it is zero when the controlled plant is static without deformation. The gain $k_f > 0$ is for the add-on strain feedback loop, where a larger k_f leads to faster transient performance but undesired high-gain control and more energy consumption, and vice versa.

An adaptive tuning for k_f can be achieved by setting $k_f = Y_s^2(t)$, and $Y_s(t)$ is updated by

$$\dot{Y}_s(t) = \alpha Y_s(t)\dot{y}_M(t)f(t) \int_0^t f(\tau)d\tau - \beta Y_s(t), \tag{5.74}$$

where $\alpha > 0$ sets the updating rate. $\beta > 0$ is introduced to avoid divergence of the integral gains in the presence of various disturbances and plant uncertainties. With β, $Y_s(t)$ acts as a first order filter of $\alpha Y_s(t)\dot{y}_M(t)f(t)\int_0^t f(\tau)d\tau$ thus guaranteeing convergence.

Note that PI control is used in (5.73) rather than PD control in [58]. The integral term is used to eliminate the steady-state error. To accommodate the extra term, the integral gain is chosen as $k_i = k_0^2(t)$, where $k_0(t)$ is adaptively tuned by

$$\dot{k}_0(t) = \gamma k_0(t)\dot{y}_M(t) \int_0^t y_M(\tau)d\tau, \tag{5.75}$$

where $\gamma > 0$ sets the updating rate of $k_0(t)$.

The stability of the closed-loop system with the add-on adaptive control is proven as follows. The Lyapunov function candidate is chosen as

$$V(t) = E_k(t) + E_p(t) + \frac{1}{2}k_p y_M^2(t) + \frac{1}{2}\alpha^{-1}Y_s^2(t) + \frac{1}{2}\gamma^{-1}k_0^2(t). \tag{5.76}$$

Using (5.72), the time derivative of $V(t)$ is

$$\dot{V}(t) = u_M(t)\dot{y}_M(t) + k_p y_M(t)\dot{y}_M(t) + \alpha^{-1}Y_s(t)\dot{Y}_s(t) + \gamma^{-1}k_0(t)\dot{k}_0(t). \tag{5.77}$$

Substituting (5.73)–(5.75) into (5.77) yields

$$\begin{aligned}
\dot{V}(t) &= \Big[- k_p y_M(t) - k_i \int_0^t y_M(\tau)d\tau - k_f f(t) \int_0^t f(\tau)d\tau \Big]\dot{y}_M(t) \\
&\quad + \alpha^{-1}Y_s(t)\Big[\alpha Y_s(t)\dot{y}_M(t)f(t) \int_0^t f(\tau)d\tau - \beta Y_s(t)\Big] \\
&\quad + k_p y_M(t)\dot{y}_M(t) + k_0^2(t)\dot{y}_M(t) \int_0^t y_M(\tau)d\tau \\
&= -\alpha^{-1}\beta Y_s^2(t) \le 0,
\end{aligned} \tag{5.78}$$

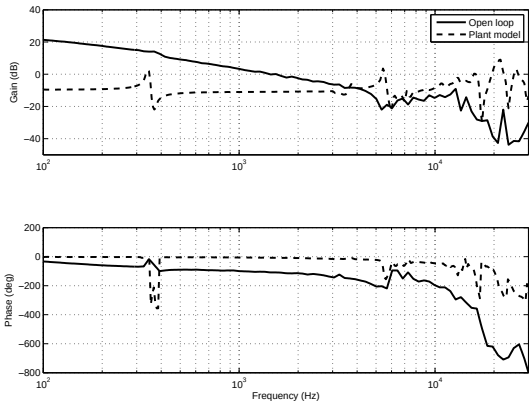

FIGURE 5.33
Frequency responses of open loop transfer functions. Dashed: plant model. Solid: open loop.

which is negative semi-definite, i.e., the closed-loop system is *energy dissipative* and stable. Since the stability condition in (5.78) is independent of system dynamics, the control system is robust against plant uncertainties.

The effectiveness of the presented scheme on PZT-actuated arms is evaluated with experiments on a PZT active suspension in a commercial dual-stage HDD. From Figure 5.33, it can be seen that the PZT active suspension has resonant modes at 5.4 kHz, 16 kHz, 20.9 kHz, and 25.6 kHz. A PI controller in series with four notch filters at these natural frequencies is used as the baseline controller C_M. The frequency response of the open loop transfer function is shown in Figure 5.33, and a gain crossover frequency of about 1.5 kHz with sufficient gain margin and phase margins are achieved.

To explore the effects of the adaptive non-model-based control in the frequency range of interests, the amplitudes of the sensitivity transfer functions with and without the presented adaptive non-model-based control are plotted in Figure 5.34. Note that the sensitivity transfer function with the adaptive non-model-based control is measured at steady-state, i.e., after the adaptation has converged at each frequency. Figure 5.34 shows a 50% and 75% improvements in vibration suppression capabilities at critical resonant modes at 5.4 kHz and 21 kHz when using the presented adaptive non-model-based control with SSA.

In the mass production of PZT-actuated arms for mechatronic systems, significant amount of parametric perturbations exist in the natural frequencies, damping ratios, and residues of the critical resonant modes. The presented adaptive non-model-based control with SSA is more robust against parametric perturbations as the strain signal is proportional to the mechanical de-

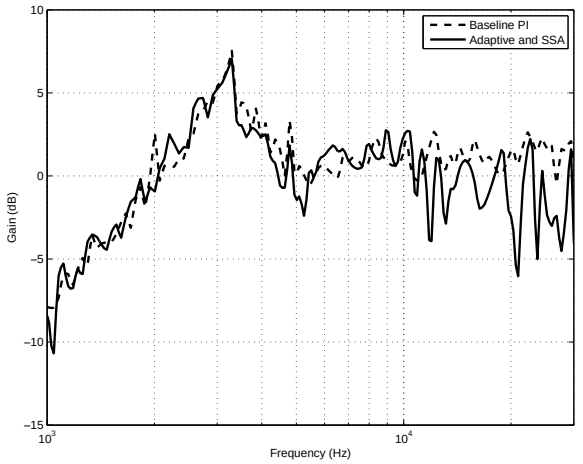

FIGURE 5.34
Frequency responses of sensitivity transfer functions. Dashed: baseline control. Solid: with non-model-based control and SSA.

formation, i.e., the sensing signal of the SSA circuit varies directly with the parametric perturbations of the critical resonant modes of the PZT-actuated arms. The presented energy-based adaptive control is also non-model-based thereby independent of plant dynamics.

It is worth noting that both model-based or non-model-based mode-stiffening methods employing SSA can be used in the inner secondary actuator loop before closing the outer dual-stage loop. The control topologies for closing the overall outer dual-stage loop after resonance compensation (with or without extraneous sensors) are detailed in the following section.

5.5 Dual-Stage Controller Design

In a dual-stage servo system, the secondary actuator is usually of much smaller dimension or form factor as compared to the primary actuator. Due to the small relative stroke achievable by the secondary actuator, it is usually not used for large-span seek operations but rather high frequency error correction during regulation. Care has to be taken to prevent saturation of the secondary actuator which will tend to destabilize the servo loop when linear controllers are used, and simple nonlinear controllers can be used for short-span seeks to tackle the effect of actuator saturation effectively [59].

5.5.1 Control Structure

Three common control structures, i.e., the parallel, Coupled Master-Slave (CMS), and Decoupled Master-Slave (DMS), will be described in this section. It is assumed that the resonance compensation methods described in the previous section are used for both the primary and secondary actuators, and are included in the corresponding controllers accordingly *a priori*.

Assuming the following nomenclature with P_V being the primary actuator and P_M as the secondary actuator, C_V being the primary actuator controller and C_M as the secondary actuator controller. Define L_D as the open loop transfer function and $T_D = \frac{L_D}{1+L_D}$ as the complementary sensitivity transfer function (or closed-loop transfer function) of the dual-stage control loop. Define $S_V = \frac{1}{1+C_V P_V}$, $S_M = \frac{1}{1+C_M P_M}$, and $S_D = \frac{1}{1+L_D}$ as the sensitivity transfer functions of the primary actuator loop, secondary actuator loop, and overall dual-stage control loop, respectively. Define e_V and e_M as the error signals, u_V and u_M as the control signals, y_V and y_M as the displacements, where the subscripts V and M indicate the primary and secondary loop, respectively. Define r as the reference and y as the output of the dual-stage servo system. Note that the effects of disturbances and noises are omitted in the following block diagrams.

5.5.1.1 Parallel

As there are two actuators to be controlled in a dual-stage servo system, the following Dual-Input-Single-Output (DISO) parallel control structure is intuitive. The functional block diagram of the parallel structure is shown in Figure 5.35, where the corresponding open loop, sensitivity, and complementary sensitivity transfer functions of the parallel configuration are

$$L_D = C_V P_V + C_M P_M, \tag{5.79}$$

$$S_D = \frac{1}{1 + C_V P_V + C_M P_M}, \tag{5.80}$$

$$T_D = \frac{C_V P_V + C_M P_M}{1 + C_V P_V + C_M P_M}. \tag{5.81}$$

From (5.79), it can be seen that the gain crossover frequency of the dual-stage control loop is higher than that when using single-stage actuation solely. This can be achieved when the phase of the $C_V P_V$ and $C_M P_M$ are approximately equal at the gain crossover frequency. In addition, the sensitivity function has an addition of $C_M P_M$ in the denominator as can be seen from (5.80), resulting in more effective disturbance suppression and rejection in the dual-stage control loop. Controller designs using the parallel structure usually result in $|C_V P_V| \gg |C_M P_M|$ in the low frequency range and $|C_V P_V| \ll |C_M P_M|$ in the high frequency range. This frequency allocation allows the secondary actuator to reject disturbances in the high frequency range, while the primary actuator functions in the low frequencies for error correction.

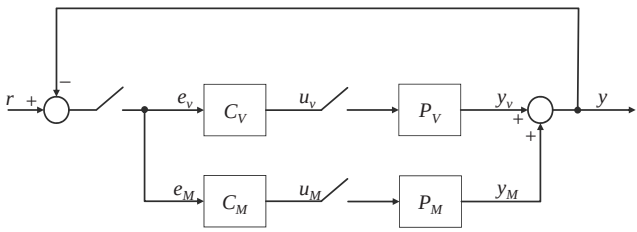

FIGURE 5.35
Parallel configuration.

Among the various works on HDD dual-stage servo control using the parallel configuration, the authors proposed the so-called PQ method in [60]. The PQ method is a systematic procedure that simplifies the DISO control system into a fictitious Single-Input-Single-Output (SISO) control system for successive loop closures design in the frequency domain, and interested readers are referred to [60] for more details.

5.5.1.2 Coupled Master-Slave (CMS)

The primary advantage of a master-slave configuration is to have priority onto one actuator over the other [61], making the secondary actuator respond faster to external disturbances by being the "master" and the bulkier primary actuator as the "slave" to compensate for slower variations in the relative displacement between the actuators.

The master-slave configuration comes in a slight variation, namely the Coupled Master-Slave (CMS) and the Decoupled Master-Slave (DMS) control structure. Both configurations require a secondary actuator model P_M^* to estimate the output of the secondary actuator y_M^* which is fed to the primary actuator controller C_V. The functional block diagram of the CMS configuration is shown in Figure 5.36.

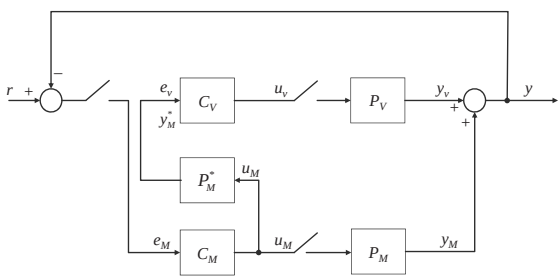

FIGURE 5.36
Coupled master-slave configuration.

The corresponding open loop, sensitivity, and complementary sensitivity transfer functions of the CMS configuration are

$$L_D = (1 + C_V P_V) C_M P_M, \tag{5.82}$$

$$S_D = \frac{1}{1 + C_M P_M + C_V P_V C_M P_M}, \tag{5.83}$$

$$T_D = \frac{(1 + C_V P_V) C_M P_M}{1 + C_M P_M + C_V P_V C_M P_M}, \tag{5.84}$$

if $P_M = P_M^*$.

5.5.1.3 Decoupled Master-Slave (DMS)

For the DMS topology, the sum of the total error signal (i.e., the difference between the reference r and output y) and the estimated output of the secondary actuator y_M^* (which in essence provides the error signal of the primary actuator path e_V) is channeled back into the input of the primary actuator controller C_V. This is desirable as the total error signal is split into the error signals e_V and e_M for decoupled control of the primary actuator loop and secondary actuator loop, respectively. The functional block diagram of the DMS configuration is shown in Figure 5.37, where the corresponding open loop, sensitivity, and complementary sensitivity transfer functions of the DMS configuration are

$$L_D = (1 + C_M P_M) C_V P_V + C_M P_M, \tag{5.85}$$

$$S_D = \frac{1}{(1 + C_M P_M)(1 + C_V P_V)} \tag{5.86}$$

$$= S_V S_M, \tag{5.87}$$

$$T_D = \frac{(1 + C_M P_M) C_V P_V + C_M P_M}{(1 + C_M P_M)(1 + C_V P_V)}, \tag{5.88}$$

if $P_M = P_M^*$.

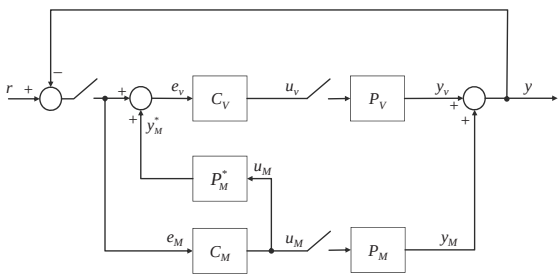

FIGURE 5.37
Decoupled master-slave configuration.

Note that the sensitivity transfer function of the DMS structure is the *product* of the sensitivity transfer functions of the primary actuator and the secondary actuator loop, hence decoupled. Obviously, the DMS design can be converted into the parallel design when the new primary actuator C_{VP} is designed as

$$C_{VP} = (1 + C_M P_M) C_V. \tag{5.89}$$

Using the DMS control structure, controller design and implementation will be eased as the loops can be designed independently and dual-stage closed-loop stability will be ensured if the primary and secondary actuator loops are stable. Moreover, enhanced disturbance rejection can be ensured via sensitivity transfer function loop shaping independently, since the overall dual-stage sensitivity transfer function S_D is the product of the sensitivity functions in the individual paths. The authors in [35] designed a phase-stable controller for the PZT active suspension using the proposed second phase margin index to retain the large gain of the resonant poles for notches in the sensitivity transfer function. In [33], the authors proposed a Near Perfect Modeling (NPM) method to construct a virtual PZT actuated active suspension digital model inverse to reduce the positive gain of the dual-stage sensitivity transfer function using Discrete Bode's Integral Theorem.

The performances of the CMS and DMS configuration depend highly on the effectiveness of the secondary actuator estimator P_M^*. If the estimator provides a fairly accurate estimation, i.e., $y_M \approx y_M^*$, the expected disturbance rejection capabilities and servo performance can be achieved as a good estimate of the error e_V in the primary actuator loop is available for decoupling control. These can be achieved in some cases, e.g., using SSA on piezoelectric-driven secondary actuators [54] as described in the previous section.

5.5.2 Design Example

In this section, the dual-stage controller design methodologies are illustrated on a commercial dual-stage HDD using a DMS configuration for simplicity but without loss of generality. In a dual-stage HDD using the PZT active suspension as the secondary actuator, only the relative displacement of the R/W head or PES is available. With the DMS configuration, controller design is usually carried out on the VCM and PZT active suspension loop *separately* and then combined into a complete dual-stage loop. This method gives actual insight into the working principles of the two actuators at different frequency ranges, and different control topologies will be discussed in this section.

Due to the limited displacement range of the PZT active suspension, the actuation effort between the two actuators should be distributed properly when designing the respective controllers. An effective dual-stage HDD loop should have the following characteristics so that the actuators will not compete with one another [62]

- The VCM should respond to correct the errors at low frequency while the secondary actuator will respond to the error signal at higher frequencies;
- Not more than 120° phase difference between the secondary actuator and VCM output at the so-called "hand-off" frequency. The typical hand-off frequency is about 400 Hz; and
- The VCM output should exceed secondary stage output by 20 dB below 60 Hz to prevent saturation of the secondary actuator.

5.5.2.1 Primary Actuator Controller: VCM Loop

Using (5.1) and the identified parameters in Table 5.1, the VCM can be approximated by a rigid body modeled as a double integrator at low frequencies, i.e.,

$$P_V(s) \approx \frac{1.425 \times 10^8}{s^2}. \tag{5.90}$$

To increase the low frequency disturbance rejection capabilities while maintaining sufficient phase margin at the gain crossover frequency, it is desired to have an open loop transfer function with about −20 dB/dec slope at the gain crossover frequency and less than −40 dB/dec gradient before and after the gain crossover frequency. As such, a lead-lag controller $C_{CV}(s)$ for the VCM is designed as

$$C_{CV}(s) = K_{CV}\frac{(s+100\pi)^2}{s(s+2\pi 30000)}, \tag{5.91}$$

where K_{CV} is the gain of $C_{CV}(s)$.

Using the gain stabilization technique, the VCM loop controller $C_V(s)$ consists of $C_{CV}(s)$ with $K_{CV} = 5$ and a series of notch filters of the form in (5.14) with natural frequencies $f_{R,i}$ at 4449 Hz, 6412 Hz, 7141 Hz, and 8600 Hz to ensure that the open loop transfer function is below 0 dB after the gain crossover frequency. Using the inverse compensation technique, the VCM loop controller $C_V(s)$ consists of $C_{CV}(s)$ with $K_{CV} = 3.3302$ and a series of second-order filters with zero-pole pairs at $(4449, 4775)$ Hz, $(6412, 5691)$ Hz, $(7141, 6973)$ Hz, and $(8599, 7515)$ Hz to compensate for the stable mechanical resonant mode and anti-resonant zero pairs.

Without considering the input delay of the plant, the mechanical resonant modes which are in-phase with the rigid body mode can generally be phase-stabilized simultaneously using a phase-lead or phase-lag compensator if the phase of the resonant modes are in the ranges of $[-180°, 0°)$ or $[0°, 180°)$. Using the phase stabilization technique, the VCM loop controller $C_V(s)$ consists of $C_{CV}(s)$ and two notch filters of the form in (5.14) with natural frequencies $f_{R,i}$ at 3800 Hz and 4449 Hz are used. The resonant mode at 4449 Hz is phase-stabilized using an additional peak filter of the form in (5.17) where $K = 0.1778$, $\phi = 2.5414$ rad, $\omega_1 = 2\pi 4449$ rad/s, and $\zeta_1 = 0.015$ for a larger

primary phase margin. ϕ is chosen to be equivalent to the phase of the baseline closed-loop transfer function at ω_1. The baseline controller consists of $C_{CV}(s)$ with $K_{CV} = 4.9175$ in series with the notch filters at 3800 Hz and 4449 Hz. ζ_1 is chosen based on the desired disturbance attenuation bandwidth, and K is chosen such that the spillover in the frequency response of the sensitivity transfer function of the VCM loop is evenly distributed between frequencies less than and greater than ω_1.

A complex lag compensator $C_{lag}(s)$ centered at 6900 Hz in the form as [63]

$$C_{lag}(s) = \frac{\omega_p}{\omega_z}\frac{s^2 + 2\zeta_{lg}\omega_z s + \omega_z^2}{s^2 + 2\zeta_{lg}\omega_p s + \omega_p^2}, \tag{5.92}$$

where $\zeta_{lg} = 0.1$, and

$$\omega_p = \omega_m(-\zeta_{lg}\tan\phi_m + \sqrt{\zeta_{lg}^2\tan^2\phi_m + 1}), \tag{5.93}$$

$$\omega_z = \omega_m(\zeta_{lg}\tan\phi_m + \sqrt{\zeta_{lg}^2\tan^2\phi_m + 1}), \tag{5.94}$$

where $\omega_m = 2\pi 6900$ rad/s and $\phi_m = 1.1519$ rad, is also cascaded in series to ensure that a phase lag of $2\phi_m$ is provided at ω_m. ζ_{lg}, ω_m, and ϕ_m are chosen such that sufficient phase lag is provided to phase-stabilize the resonant modes at 6412 Hz, 7141 Hz, and 8599 Hz. In addition, $C_{lag}(s)$ is designed to have its poles and zeros close to the pair of VCM zeros at 5691 Hz and the pair of VCM poles at 8599 Hz, respectively, considering the changes in magnitude from addition of $C_{lag}(s)$.

The mechanical resonant modes at frequencies ranging from 4449 Hz to 8599 Hz are in-phase with the rigid body mode while the resonant mode at 13800 Hz is out-of-phase with the rigid body mode. The resonant modes of the VCM at 4449 Hz, 6412 Hz, 7141 Hz, 8599 Hz, and 13800 Hz are phase-stabilized. It is worth noting that the out-of-phase resonant mode at 13800 Hz is phase-stabilized as well due to sufficient phase lead provided by $C_V(s)$.

The open loop frequency responses of the VCM loop, i.e., $C_V(s)P_V(s)$, are shown in Figure 5.38. It is worth noting that different values of K_{CV} are used to ensure that the gain crossover frequencies are identical for comparison and illustration purposes.

5.5.2.2 Secondary Actuator Controller: PZT Active Suspension Loop

Using (5.12) and the identified parameters in Table 5.3, the PZT active suspension can be approximated as a rigid body with pure gain at low frequencies as

$$P_M(s) \approx K_M = 0.3616. \tag{5.95}$$

The secondary actuator path can be easily stabilized by a Proportional-Integral (PI) compensator, and a first-order lag compensator $C_{CM}(s)$ of zero

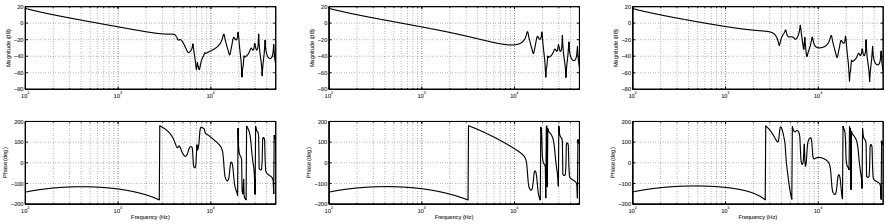

(a) Gain stabilization (b) Inverse compensation (c) Phase stabilization

FIGURE 5.38
Open loop frequency responses of the VCM loop.

relative degree is used for low positive sensitivity [33]

$$C_{CM}(s) = K_{CM}\frac{s + 2\pi 30000}{s + 2\pi 900}, \tag{5.96}$$

where K_{CM} is the gain of $C_{CM}(s)$.

Similar to the gain stabilization technique, the PZT active suspension loop controller $C_M(s)$ consists of $C_{CM}(s)$ with $K_{CM} = 0.18$ and a series of notch filters in the form of (5.14) with natural frequencies $f_{R,i}$ at 2484 Hz, 5461 Hz, 6074 Hz, 9103 Hz, and 12000 Hz to ensure that the open loop transfer function is below 0 dB after the gain crossover frequency. Using the inverse compensation technique, the PZT active suspension loop controller $C_M(s)$ consists of $C_{CM}(s)$ with $K_{CM} = 0.2473$ and a series of second-order filters with zero-pole pairs at $(2484, 2751)$ Hz, $(5461, 5686)$ Hz, $(6074, 6646)$ Hz, $(9103, 9549)$ Hz, and $(12000, 11672)$ Hz to compensate for the stable mechanical resonant mode and anti-resonant zero pairs.

Using the phase stabilization technique, the PZT active suspension loop controller $C_M(s)$ consists of $C_{CM}(s)$ and a second-order filter with a zero-pole pair at $(2484, 2751)$ Hz for inverse compensation. The resonant mode at 2484 Hz is phase-stabilized using an additional peak filter of the form in (5.17) where $K = 0.1585$, $\phi = 4.2603$ rad, $\omega_1 = 2\pi 2484$ rad/s, and $\zeta_1 = 0.02$, as using the complex zero-pole pair second-order filter to simultaneously phase-stabilize this resonant mode will result in large gain at high frequencies. In this case, ϕ is chosen to be equivalent to the phase of the baseline closed-loop transfer function at ω_1. The baseline controller consists of $C_{CM}(s)$ with $K_{CM} = 0.1737$ in series with the second-order filter with a zero-pole pair at $(2484, 2751)$ Hz for inverse compensation. Using a second-order filter for inverse compensation results in a larger phase margin as opposed to the notch filter for gain stabilization. Similarly, ζ_1 is chosen based on the desired disturbance attenuation bandwidth, and K is chosen such that the spillover in the frequency response of the sensitivity transfer function of the DMS dual-stage loop is evenly distributed between frequencies less than and greater than ω_1.

A complex zero-pole pair second-order filter is also cascaded and inserted at $(4600, 8000)$ Hz to provide phase lead which phase-stabilizes the resonant modes at 5461 Hz and 6074 Hz. The damping ratios of the complex zeros and complex poles are 0.03 and 0.7, respectively. The zeros are lightly damped to provide a sharp phase lead around 4600 Hz, and the poles are well damped to reduce the gain around 8000 Hz. Due to the presence of an input delay in the PZT active suspension, a partial inverse compensator is added to increase the amount of phase lead at 6074 Hz. In addition, a zero-pole pair is also cascaded and inserted at $(6074, 6646)$ Hz for partial inverse compensation, and a first-order lag compensator with zero-pole pair at $(15000, 6074)$ Hz is included along with notch filters in the form of (5.14) with natural frequencies $f_{R,i}$ at 9103 Hz and 13120 Hz. The first-order lag compensator is designed to reduce the high frequency gain amplification from the second-order filter with complex zero-pole pair at $(4600, 8000)$ Hz and to phase-stabilize the resonant mode at 14240 Hz.

The mechanical resonant modes at frequencies ranging from 2484 Hz to 12000 Hz are in-phase with the rigid-body mode, while the resonant mode at 14240 Hz is out-of-phase with the rigid-body mode. The resonant modes of the PZT active suspension at 2484 Hz, 5461 Hz, 6074 Hz, and 14240 Hz are phase-stabilized, and the resonant modes at 9103 Hz and 12000 Hz are gain-stabilized instead due to the amount of phase lag introduced by the input delay of the PZT active suspension. It is worth noting that the input delay makes it possible for the out-of-phase resonant mode at 14240 Hz to be phase-stabilized.

The open loop frequency responses of the PZT active suspension loop, i.e., $C_M(s)P_M(s)$, are shown in Figure 5.39.

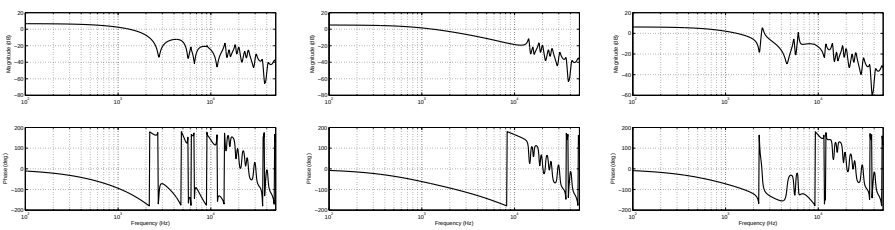

(a) Gain stabilization (b) Inverse compensation (c) Phase stabilization

FIGURE 5.39
Open loop frequency responses of PZT active suspension loop.

5.5.3 Simulation Results

In this section, simulation results of the above-mentioned dual-stage control design will be evaluated. For the combined dual-stage control, a DMS structure using the gain stabilization, inverse compensation, and phase stabilization

resonance compensation methodologies will be used in the simulations. The frequency responses of open loop transfer functions L_D using the DMS dual-stage control scheme are shown in Figure 5.40.

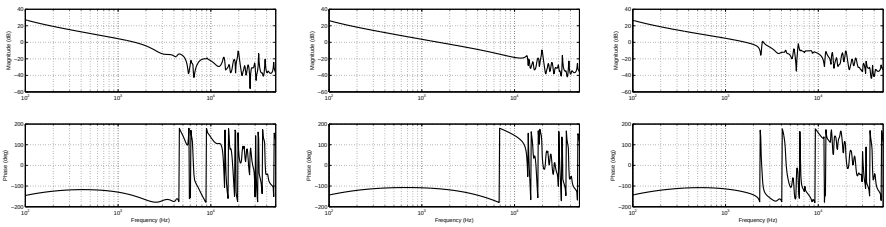

(a) Gain stabilization (b) Inverse compensation (c) Phase stabilization

FIGURE 5.40
Frequency responses of open loop transfer functions using the DMS dual-stage control scheme.

Using the gain-stabilization technique with notch filters in both the VCM and PZT active suspension loops, a dual-stage gain crossover frequency 1510 Hz is obtained, along with gain and phase margins of 14.1 dB and 31.8°, respectively. Using the inverse compensation technique for both the VCM and PZT active suspension loops, a dual-stage gain crossover frequency of 1520 Hz is obtained, along with gain and phase margins of 14.3 dB and 66.9°, respectively. Using the phase-stabilization technique for both the VCM and PZT active suspension loops, a dual-stage gain crossover frequency of 1640 Hz is obtained, along with gain and phase margins of 9.28 dB and 49.7°, respectively. The second phase margin is 223.8°.

The frequency responses of sensitivity transfer functions using the DMS dual-stage control scheme for the three different compensation methods are shown in Figure 5.41. It can be observed from these results that the VCM and

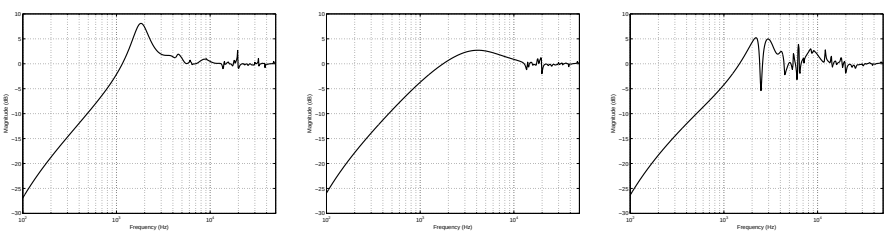

(a) Gain stabilization (b) Inverse compensation (c) Phase stabilization

FIGURE 5.41
Frequency responses of sensitivity transfer functions using the DMS dual-stage control scheme.

PZT active suspension do not compete with each other during actuation, and

therefore they do not cause destructive interferences. At the hand-off frequency where the magnitudes of the VCM and PZT active suspension intersect, the phase difference between the VCM output and PZT active suspension output is also much less than the suggested 120°.

Table 5.4 shows the design specifications achieved using the above-mentioned controller designs.

TABLE 5.4
Design Specifications Achieved with Dual-Stage Servo Controllers

	Gain Stabilization	Inverse Compensation	Phase Stabilization
Order of C_V	10	10	10
Order of C_M	11	11	14
Hand-off frequency	304 Hz	371 Hz	317 Hz
Phase difference	84.9°	88.0°	86.7°
Gain crossover frequency	1.51 kHz	1.52 kHz	1.64 kHz
Gain margin	14.1 dB	14.3 dB	9.3 dB
Phase margin	31.8°	66.9°	49.7°
$\|\|S\|\|_\infty$	8.1 dB	2.7 dB	5.2 dB

5.6 Conclusion

In this chapter, various aspects of dual-stage systems and control from system identification (using continuous- and discrete-time measurements) to dual-stage control topologies and controller design are detailed. In the absence of extraneous sensors, the gain-stabilization, inverse compensation, and phase-stabilization techniques for resonance compensation are described. The phase-stabilization design can be realized using the actuator's in-phase mechanical resonant modes, as well as additional add-on Linear Time-Invariant (LTI) or Linear Time-Varying (LTV) peak filters. With advanced sensor fusion, active damping of the mechanical resonant modes can be achieved via multi-sensing or Self-Sensing Actuation (SSA) using direct-driven and indirect driven topologies on piezoelectric actuators. The additional displacement or strain information allows the mechanical resonant modes to be stiffened in the inner loop by the developed model-based and non-model-based active control methodologies. Using the HDD as a classic example of high-performance mechatronic systems, the effectiveness of the presented methodologies is evaluated and verified on a commercial dual-stage 3.5" HDD with extensive simulations and experiments.

Bibliography

[1] W. -I. Cho, N. -C. Park, H. Yang, and Y. -P. Park, "Swing-Arm-Type PZT Dual Actuator with Fast Seeking for Optical Disk Drive," *Microsystem Technologies*, Vol. 8, Nos. 2–3, pp. 139–148, May 2002.

[2] K. H. Park, J. H. Lee, S. H. Kim, and Y. K. Kwak, "High Speed Micro Positioning System Based on Coarse/Fine Pair Control," *Mechatronics*, Vol. 5, No. 6, pp. 645–663, September 1995.

[3] K. H. Park, C. H. Choi, and J. Ryu, "Hybrid Actuator for High Speed and High Precision Optical Disk Drives," *Mechatronics*, Vol. 11, No. 5, pp. 527–543, August 2001.

[4] K. L. Hillsley and S. Yurkovich, "Vibration Control of a Two-Link Flexible Robot Arm," *Dynamics and Control*, Vol. 3, No. 3, pp. 261–280, July 1993.

[5] A. Sharon, N. Hogan, and D. E. Hardt, "The Macro/Micro Manipulator: An Improved Architecture for Robot Control," *Robotics and Computer-Integrated Manufacturing*, Vol. 10, No. 3, pp. 209–222, June 1993.

[6] D. Shin, I. Sardellitti, Y. L. Park, O. Khatib, and M. Cutkosky, "Design and Control of a Bio-Inspired Human-Friendly Robot," *International Journal of Robotics Research*, Vol. 29, No. 5, pp. 571–584, April 2010.

[7] B. S. Kim, J. Li, and T. C. Tsao, "Two Parameter Robust Repetitive Control with Application to a Novel Dual-Stage Actuator for Noncircular Machining," *IEEE/ASME Transactions on Mechatronics*, Vol. 9, No. 4, pp. 644–652, December 2004.

[8] A. T. Elfizy, G. M. Bone, and M. A. Elbestawi, "Design and Control of a Dual-Stage Feed Drive," *International Journal of Machine Tools and Manufacture*, Vol. 45, No. 2, pp. 153–165, February 2005.

[9] C. W. Lee and S. W. Kim, "An Ultraprecision Stage for Alignment of Wafers in Advanced Microlithography," *Precision Engineering*, Vol. 21. Nos. 2–3 pp. 113–122, September–December 1997.

[10] S. Woody and S. Smith, "Design and Performance of a Dual Drive System for Tip-Tilt Angular Control of a 300 mm Diameter Mirror," *Mechatronics*, Vol. 16 No. 7, pp. 389–397, September 2006.

[11] S. K. Hung, E. T. Hwu, M. Y. Chen, and L. C. Fu, "Dual-Stage Piezoelectric Nano-Positioner Utilizing a Range-Extended Optical Fiber Fabry-Perot Interferometer," *IEEE/ASME Transactions on Mechatronics*, Vol. 12, No. 3, pp. 291–298, June 2007.

[12] D. S. Kang, T. Seo, Y. H. Yoon, B. S. Shin, X. -J. Liu, and J. Kim, "A Micro-Positioning Parallel Mechanism Platform with 100-Degree Tilting Capability," *CIRP Annals-Manufacturing Technology*, Vol. 55, No. 1, pp. 377–380, 2006.

[13] T. W. Seo, D. S. Kang, H. S. Kim, and J. Kim, "Dual Servo Control of a High-Tilt 3-DOF Microparallel Positioning Platform," *IEEE/ASME Transactions on Mechatronics*, Vol. 14, No. 5, pp. 616–625, October 2009.

[14] R. Evans, J. Griesbach, and W. Messner, "Piezoelectric Micro-Actuator for Dual-Stage Control," *IEEE Transactions on Magnetics*, Vol. 35, No. 2, pp. 977–982, March 1999.

[15] T. Hirano, L. Fan, W. Lee, J. Hong, W. Imaino, S. Pattanaik, S. Chan, P. Webb, R. Horowitz, S. Aggarwal, and D. Horsley, "High Bandwidth High Accuracy Rotary Microactuator for Magnetic Hard Disk Drive Tracking Servos," *IEEE/ASME Transactions on Mechatronics*, Vol. 3, No. 3, pp. 156–165, September 1998.

[16] H. Toshiyoshi, M, Mita, and T. Fujita, "A MEMS Piggyback Actuator for Hard Disk Drives," *IEEE Journal of Microelectromechanical Systems*, Vol. 11, No. 6, pp. 648–654, December 2002.

[17] Y. Soeno, S. Ichikawa, T. Tsuna, Y. Sato, and I. Sato, "Piezoeletric Piggy-Back Microactuator for Hard Disk Drive," *IEEE Transactions on Magnetics*, Vol. 35, No. 2., pp. 983-987, March 1999.

[18] H. Fujita, K. Suzuki, M. Ataka, and S. Nakamura, "A Microactuator for Head Positioning System of Hard Disk Drives," *IEEE Transactions on Magnetics*, Vol. 35, No. 2, pp. 1006–1010, March 1999.

[19] S. Koganezawa, K. Takashi, Y. Uematsu, T. Yamada, S. Hasegawa, and T. Ueno, "A Flexural Piggyback Milli-Actuator for Over 5 GBit/in^2 Density Magnetic Recording," *IEEE Transactions on Magnetics*, Vol. 32, No. 5, pp. 3908–3910, September 1996.

[20] J. Liu, K. Ono, J. Xu, J. Li, and M. Furukawa, "Thermal Actuator for Accurate Positioning Read/Write Element in Hard Disk Drive," *Microsystem Technologies*, Vol. 18, Nos. 9–10, pp. 1583–1589, September 2012.

[21] L. Ljung, *System Identification: Theory for the User*, 2nd Edition, Prentice Hall, Englewood Cliffs, NJ, USA, 1999.

[22] T. Yamaguchi, M. Hirata, and C. K. Pang (eds.), *High-Speed Precision Motion Control*, CRC Press, Taylor and Francis Group, Boca Raton, FL, USA, 2011.

[23] M. Kawafuku, J. Eom, M. Iwasaki, and Hiromu Hirai "Identification Method for Plant Dynamics Over Nyquist Frequency," in *Proceedings of the* 33rd *Annual Conference of the IEEE IECON*, pp. 362–367, Taipei, Taiwan, November 5–8, 2007.

[24] R. Ehrlich, C. Taussig, and D. Abramovitvh, "Identification of Sampled Data Systems at Frequencies Beyond the Nyquist Rate," in *Proceedings of the IEEE CDC*, pp. 646–652, Tampa, FL, USA, December 1989.

[25] M. Nagashima and S. Nakagawa, "Identification of the Secondary Actuator Dynamics at Frequencies Beyond the Nyquist Rate in Dual-Stage Actuator Hard Disk Drive Systems," *Transactions of the Institute of Measurement and Control*, Vol. 32, No. 2, pp. 188–210, April 2010.

[26] G. F. Franklin, J. D. Powell, and M. Workman, *Digital Control of Dynamic Systems*, Addison-Weasley, 3rd Edition, 1997.

[27] C. Mohtadi, "Bode's Integral Theorem For Discrete-Time Systems," *IEE Proceedings D Control Theory and Applications*, Vol. 137, No. 2, pp. 57–66, March 1990.

[28] R. Horowitz, Y. Li, K. Oldham, S. Kon, and X. Huang, "Dual-Stage Servo Systems and Vibration Compensation in Computer Hard Disk Drives," *Control Engineering Practice*, Vol. 15, No. 3, pp. 291–305, March 2007.

[29] D. Abramovitch and G. Franklin, "A Brief History of Disk Drive Control," *IEEE Control Systems Magazine*, Vol. 22, No. 3, pp. 28–42, June 2002.

[30] H. Uchida and T. Semba, "A Study of the Residual Vibration During the Seek-Settling Period for Hard Disk Drives," in *Digests of the 2000 APMRC*, pp. MP19-1–MP19-2, Tokyo, Japan, November 6–8, 2000.

[31] C. K. Pang, F. Hong, and X. Wang, "Integrated Servo-Mechanical Control Systems Design Using Nyquist Plots for High-Performance Mechatronics," *Microsystem Technologies*, Vol. 18, Nos. 9–10, pp. 1719–1729, October 2012.

[32] C. K. Pang, S. C. Tam, G. Guo, B. M. Chen, F. L. Lewis, T. H. Lee, and C. Du, "Improved Disturbance Rejection with Online Adaptive Pole-Zero Compensation on a Φ-Shaped PZT Active Suspension," *Microsystem Technologies*, Vol. 15, Nos. 10–11, pp. 1499–1508, October 2009.

[33] C. K. Pang, D. Wu, G. Guo, T. C. Chong, and Y. Wang, "Suppressing Sensitivity Hump in HDD Dual Stage Servo Systems," *Microsystem Technologies*, Vol. 11, Nos. 8–10, pp. 653–662, August 2005.

[34] M. Tomizuka, "Zero Phase Error Tracking Algorithm for Digital Control," *Journal of Dynamic Systems, Measurement, and Control*, Vol. 109, No. 1, pp. 65–68, March 1987.

[35] M. Kobayashi, S. Nakagawa, and S. Nakamura, "A Phase-Stabilized Servo Controller for Dual-Stage Actuators in Hard-Disk Drives," *IEEE Transactions on Magnetics*, Vol. 39, No. 2, pp. 844–850, March 2003.

[36] L. Guo, "Reducing the Manufacturing Costs Associated with Hard Disk Drives—A New Disturbance Rejection Control Scheme," *IEEE/ASME Transactions on Mechatronics*, Vol. 2, No. 2, pp. 77–85, June 1997.

[37] Y. -H. Kim, C. -I. Kang, and M. Tomizuka, "Adaptive and Optimal Rejection of Non-Repeatable Disturbance in Hard Disk Drives," in *Proceedings of the 2005 IEEE/ASME International Conference on Advanced Intelligent Mechatronics*, pp. 1–6, Monterey, CA, USA, July 24–28, 2005.

[38] J. Zheng, G. Guo, Y. Wang, and W. E. Wong, "Optimal Narrow-Band Disturbance Filter For PZT-Actuated Head Positioning Control on a Spinstand," *IEEE Transactions on Magnetics*, Vol. 42, No. 11, pp. 3745–3751, November 2006.

[39] L. Sievers and A. Flotow, "Comparison and Extensions of Control Methods For Narrow-Band Disturbance Rejection," *IEEE Transactions on Signal Processing*, Vol. 40, No. 10, pp. 2377–2391, October 1992.

[40] W. Messner and M. Bodson, "Design of Adaptive Feedforward Controllers Using Internal Model Equivalence," in *Proceedings of the 1994 American Control Conference*, pp. 1619–1623, Baltimore, MD, USA, June 29—July 1, 1994.

[41] K. B. Scribner, L. A. Sievers, and A. H. von Flotow, "Active Narrow-Band Vibration Isolation of Machinery Noise from Resonance Substructure," *Journal of Sound and Vibration*, Vol. 167, No. 1, pp. 17–40, October 1993.

[42] F. Hong and C. Du, "Stable Peak Filtering Method to Reject High Frequency Disturbance in Hard Disk Drives," *Journal of Advanced Mechanical Design, Systems, and Manufacturing*, Vol. 4, No. 1, pp. 119–129, February 2010.

[43] S. -C. Pei and C. -C. Tseng, "Elimination of AC Interference in Electrocardiogram Using IIR Notch Filter With Transient Suppression," *IEEE Transactions on Biomedical Engineering*, Vol. 42, No. 11, pp. 1128–1132, November 1995.

[44] R. Agarwal, E. I. Plotkin, and M. N. S. Swamy, "LMS-Optimal Notch Filters With Improved Transient Performance," in *Proceedings of the* 37$^{\text{th}}$ *Midwest Symposium on Circuits and Systems*, pp. 1019–1022, Lafayette, LA, USA, August 3–5, 1994.

[45] P. Sadovsky and K. Bartusek, "Optimisation of the Transient Response of a Digital Filter," *Radioengineering*, Vol. 9, No. 2, pp. 14–17, June 2000.

[46] C. K. Thum, C. Du, B. M. Chen, E. H. Ong, and K. P. Tan, "Midfrequency Runout Compensation in Hard Disk Drives via a Time-Varying Group Filtering Scheme," *IEEE Transactions on Magnetics*, Vol. 44, No. 12, pp. 4769–4779, December 2008.

[47] J. Piskorowski, "Digital Q-Varying Notch IIR Filter With Transient Suppression," *IEEE Transactions on Instrumentation and Measurement*, Vol. 59, No. 4, pp. 866–872, April 2010.

[48] F. Hong and C. K. Pang, "A Peak Filtering Method with Improved Transient Response for Narrow-Band Disturbance Rejection in Hard Disk Drives," *International Journal of Systems Science*, in press.

[49] M. Kobayashi, T. Yamaguchi, T. Yoshida, and H. Hirai, "Multi-Sensing Servo with Carriage-Acceleration Feedback for Magnetic Disk Drives," in *Proceedings of the 1998 American Control Conference*, Vol. 5, pp. 3038–3042, Philadelphia, PA, USA, June 24–26, 1998.

[50] F. Y. Huang, W. Imaino, F. Lee, and T. Semba, "Active Damping in HDD actuator," *IEEE Transactions on Magnetics*, Vol. 37, No. 2, pp. 847–849, March 2001.

[51] S. -H. Lee, C. C. Chung, and C. W. Lee, "Active High-Frequency Vibration Rejection in Hard Disk Drives," *IEEE/ASME Transactions on Mechatronics*, Vol. 11, No. 3, pp. 339–345, June 2006.

[52] Y. Li, R. Horowitz, and R. Evans, "Vibration Control of a PZT Actuated Suspension Dual-Stage Servo System Using a PZT Sensor," *IEEE Transactions on Magnetics*, Vol. 39, No. 2, pp. 932–937, March 2003.

[53] J. J. Dosch, D. J. Inman, and E. Garcia, "A Self-Sensing Piezoelectric Actuator For Collocated Control, *Journal of Intelligent Material Systems and Structures*, Vol. 3, No. 1, pp. 166–183, 1992.

[54] C. K. Pang, G. Guo, Ben M. Chen, and T. H. Lee, "Self-Sensing Actuation for Nanopositioning and Active-Mode Damping in Dual-Stage HDDs," *IEEE/ASME Transactions on Mechatronics*, Vol. 11, No. 3, pp. 328–338, June 2006.

[55] H. Yamada, M. Sasaki, and Y. Nam, "Control of a Micro-Actuator for Hard Disk Drives Using Self-Sensing Actuator, *International Journal of Applied Electromagnetics and Mechanics*, Vol. 25, No. 1, pp. 247–259, 2007.

[56] M. I. Friswell and D. J. Inman, "The Relationship Between Positive Position Feedback and Output Feedback Controllers," *Smart Materials and Structures*, Vol. 8, pp. 285-291, June 1999.

[57] F. Hong and C. K. Pang, "Robust Vibration Control at Critical Resonant Modes Using Indirect-Driven Self-Sensing Actuation in Mechatronic Systems," *ISA Transactions*, Vol. 51, No. 6, pp. 834–840, November 2012.

[58] N. Jalili, M. Dadfarnia, F. Hong, and S. S. Ge, "Adaptive Non Model-Based Piezoelectric Control of Flexible Beams with Translational Base," in *Proceedings of the 2002 American Control Conference*, pp. 3802–3807, Anchorage, AK, USA, May 8–10, 2002.

[59] G. Guo, D. Wu, and T. C. Chong, "Modified Dual-Stage Controller for Dealing With Secondary-Stage Actuator Saturation," *IEEE Transactions on Magnetics*, Vol. 39, No. 6, pp. 3587–3592, November 2003.

[60] S. J. Schroeck, W. C. Messner, and R. J. McNab, "On Compensator Design for Linear Time Invariant Dual-Input Single-Output Systems," *IEEE/ASME Transactions on Mechatronics*, Vol. 6, No. 1, pp. 50-57, March 2001.

[61] L. Guo, D. Martin, and D. Brunnett, "Dual-Stage Actuator Servo Control for High Density Disk Drives," in *Proceedings of the 1999 IEEE/ASME International Conference on Advanced Intelligent Mechatronics*, pp. 132–137, Atlanta, GA, USA, September 19–23, 1999.

[62] M. Karaman and W. C. Messner, "Robust Dual-Stage HDD Track Follow Control Systems Design for Hand Off Shaping," in *Digests of the 2002 APMRC*, pp. BA5-01–BA5-02, Singapore, August 27–29, 2002.

[63] W. C. Messner, M. D. Bedillion, L. Xia, and D. C. Karns, "Lead and Lag Compensators with Complex Poles and Zeros: Design Formulas for Modeling and Loop Shaping," *IEEE Control Systems Magazine*, Vol. 27, No. 1, pp. 44–54, February 2007.

6

Concluding Remarks from Editors

T. Yamaguchi

Ricoh Company Ltd.

M. Hirata

Utsunomiya University

C. K. Pang

National University of Singapore

CONTENTS

6.1 Transferring Technologies to Other Industries (T. Yamaguchi)

In this book, the control technologies developed and applied onto Hard Disk Drive (HDD) head-positioning servo systems are described, along with several realistic applications in other products and industries. In general, technologies which have been developed based on specific desired features of the products tend to achieve vast improvements in terms of product specifications. Such cases are commonly encountered in industries, and it is always assumed that such technologies are specific domain knowledge while other engineers tend to think that these technologies cannot be applied to their own products. However, it has been shown in this book that there are many cases where these technologies could be successfully transferred onto other products. This means that new effective technologies can be developed not only from science or theory, but also from technologies developed in different industries.

In this section, I will describe several "insights" for understanding technologies in different industries so that engineers can find ways to apply these technologies to their own products, since I am one of the engineers who has been working in industries for many years. Although the mentioned technologies are limited to servo and motion control, this general approach is applicable to other technologies as well.

6.1.1 What is High-Speed Precision Motion Control?

In control technologies, which handle dynamics of physical systems like servo control, the main specification may not be just the *absolute* positioning accuracy but rather a *relative* measure such as the ratio of actuator stroke to positioning accuracy. For example, an actuator with a stroke of 10 nm requiring a 1 nm positioning accuracy can be considered nearly as a static problem and the problem of dynamics may not be a major issue. However if its stroke is 10 mm, the access time to reach the target position and settle the actuator into its required positioning accuracy will be another important specification for this product. As such, the ratio of stroke to positioning accuracy may be an appropriate specification for high-speed precision mechatronics.

Figure 6.1 shows the ratio of stroke to positioning accuracy or resolution for various precise positioning products, which is called the *dynamic range* in this case. In Figure 6.1, the dynamic range of the Scanning Probe Microscopy (SPM) whose positioning accuracy is in the order of 0.1 nm and that of a table of machining center whose stroke is in the order of several meters can

be plotted on the same line. However, the dynamic range of recent HDD approaches to 10^{-7}. While the actuator stroke in 2.5″ and 3.5″ HDDs has not changed much due to the de facto form factor of HDDs, their track densities have been greatly increased which resulted in the requirement of smaller and smaller positioning accuracies. It can be seen that the dynamic range is a good metric or index to estimate the difficulty of specifications in high-speed precision positioning devices.

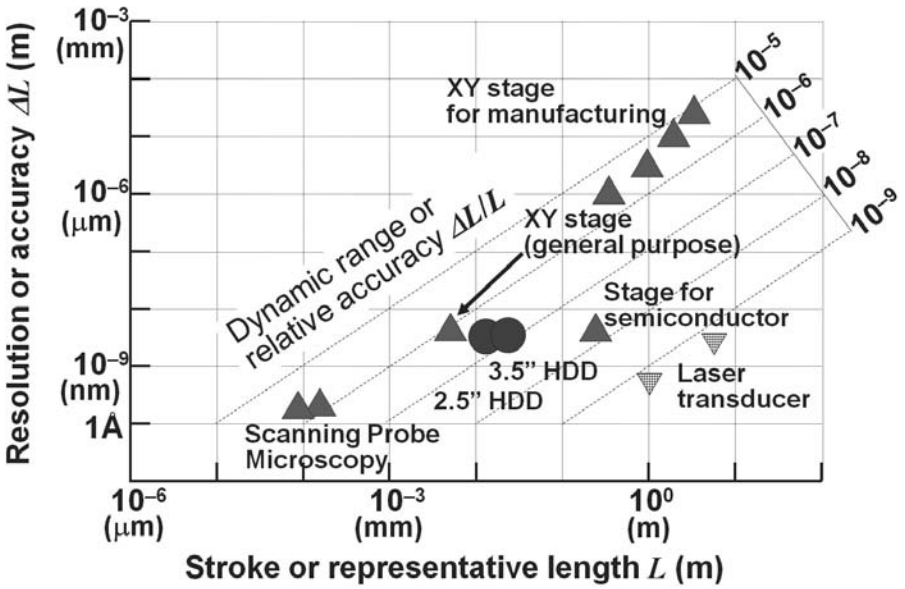

FIGURE 6.1
Dynamic ranges of various ultra-high precision devices.

6.1.2 Sensing and Closing the Loop: Shifting Resource Power to a Right Field

In a feedback control system, it is important to determine where the sensors should be placed in the control system and which state variables can be detected. This translates to designing a basic structure of the system such that necessary states can be detected by sensors, and also making decisions on which areas of technologies should be focused on for future development. In HDDs, the magnetic read/write head can detect the relative position error between the head and the track center, and is a control variable. As such, this is a closed-loop control or full closed-loop control, though the distance between the read and write heads in recent HDDs has to be measured *a priori* to be more precise. On the other hand, the control variable is the object's position

and the sensor can often detect the position of the actuator, e.g., a wafer on the XY stage for semiconductor. In this case, the relative position error between the object and the table may fluctuate due to temperature changes and cannot be detected, resulting in a semi closed-loop control.

During closed-loop control, the object is exactly on the right position when its position error in a feedback loop is zero, but the plant dynamics and disturbances are in the control loop. As such, the design of the feedback controller tends to be rather difficult in order to meet required performances while guaranteeing robust stability. In the semi-closed loop control, the control of such dynamics and disturbances is of utmost importance since some of the plant dynamics and disturbances are *out* of the feedback loop. Controlling the ambient conditions such as temperature and active damping systems are commonly used to stabilize or remove these effects since disturbances are the main issue in the design of the system.

When investigating the control systems of products in various industries, it can be seen what technologies have been mainly developed for the products by realizing how the control loop is closed. Sensor fusion and closing the control loop are important issues at the basic structural design phase in the product development process.

6.1.3 Control Structure: Generating New Design Parameters

In the case of a simple control structure such as a single feedback loop using a compensator like the Proportional-Integral-Derivative (PID) controller, the control design and its implementation are easier but the expected performance may be restricted due to less design parameters. On the other hand, a complicated control structure may have more design parameters which may improve various performances, though it should be noted that complicated implementations may result in increased costs and longer execution time. A complicated control structure allows advanced control theories such as adaptive control to be realized. Another possible advantage is to create new design parameters and find a way to improve targeted performances without deteriorating or changing other performances. This is one of the greatest pleasures of being an engineer in industries.

Examples of creating new design parameters by modifying the control structure are the Initial Value Compensation (IVC) using Mode Switching Control (MSC) as shown in Chapter 3, and a digital controller with variable multi-rate sampling [1]. These examples are not just applications of advanced control theories but rather modifying the control structure to create new design parameters, and then improving the performances such as settling time and acoustic noise.

After deciding on the basic structure of the control system, one of the important insights in designing a control structure is whether it is necessary to add new design parameters to overcome any trade-offs of the control de-

sign indices. In this case, additional components are required in the control structure to create such new design parameters.

6.1.4 Modeling: Necessity of Precise Disturbance Modeling

Recently, the importance of modeling has been well-recognized, such as the model-based development approach, but modeling is mainly carried out on the plant or controlled object. In a typical feedback control system, the essence of the control design is to design an optimal sensitivity transfer function for disturbance and plant perturbation suppression, as well as an optimal complementary sensitivity transfer function for robust stability. In other words, the control design is a problem on how to find a compromise between them. However, more sophisticated designs to improve positioning accuracy are required in HDD industries due to continuous requirements of storage capacity growth. As such, disturbance estimation and reduction using disturbance observers and learning or repetitive control to suppress specific periodic disturbances have been widely studied. Recently, precise loop-shaping based on detailed disturbance modeling has also been studied.

A peak filter is designed to have high gain just at around 6.7 kHz where a big windage or disturbance caused by airflow is seen. The frequency response of the controllers with and without windage compensation are shown in Figure 6.2. The shaded region is the frequency range of windage, and the open loop characteristics of the system are shown in Figure 6.3. It can be seen that the proposed peak filter is phase-stable.

Since the peak filter reduces the amplitude of the sensitivity transfer function at around 6.7 kHz very much as shown in Figure 6.4, the influence of windage is greatly reduced and the positioning accuracy is improved as shown by the PES spectra in Figure 6.5.

It is worth noting that 6.7 kHz is of much higher frequency as compared to the bandwidth of feedback control. This implies that it is difficult to achieve a high gain at such a high frequency range, but it is possible to find a way of improving positioning accuracy by modifying the controller accordingly once the characteristics of disturbances and plant (i.e., phase characteristics in this case) are precisely known. After fixing the control structure, we can design individual controllers based on not only plant modeling *but also* disturbance modeling as well.

6.1.5 Summary

In all, it is worthy to understand excellent servo control and motion control developed for various industries and to try to apply them to your products. In order to do so, it is necessary to understand the basic features of the control system. In this section, several insights on how to understand the features of the high-speed precision servo control system are shown along with the control system development phases, i.e.,

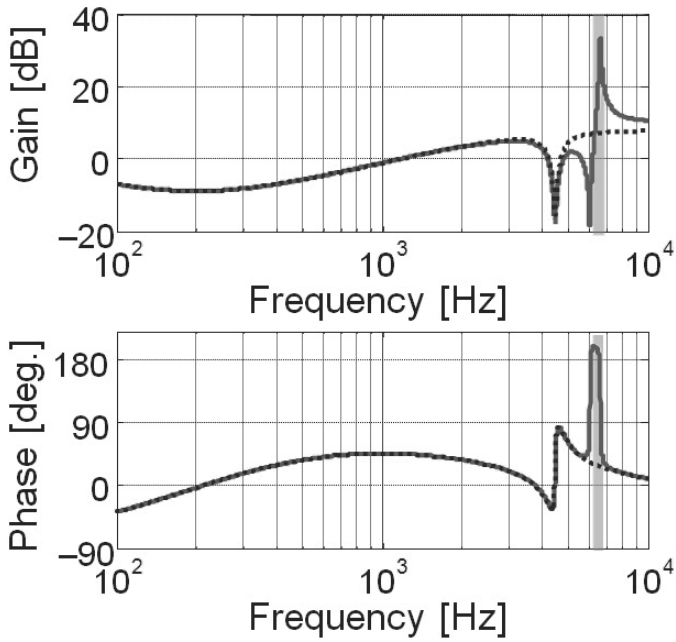

FIGURE 6.2
Frequency responses of controllers. Dashed: without windage compensation. Solid: with windage compensation.

1. Decision on target specifications;
2. Design of basic structure of the system;
3. Design of basic control structure; and
4. Design of each control algorithm.

As mentioned in previous sections, it would be useful for engineers to check the dynamic range in Phase 1, sensor locations and loop closure methods in Phase 2, new design parameters by additional control structures in Phase 3, and control design based on disturbance modeling in Phase 4. Of course, there are many other important factors to understand the features of the control system. I hope these insights will bring readers new and useful ideas when designing their control systems.

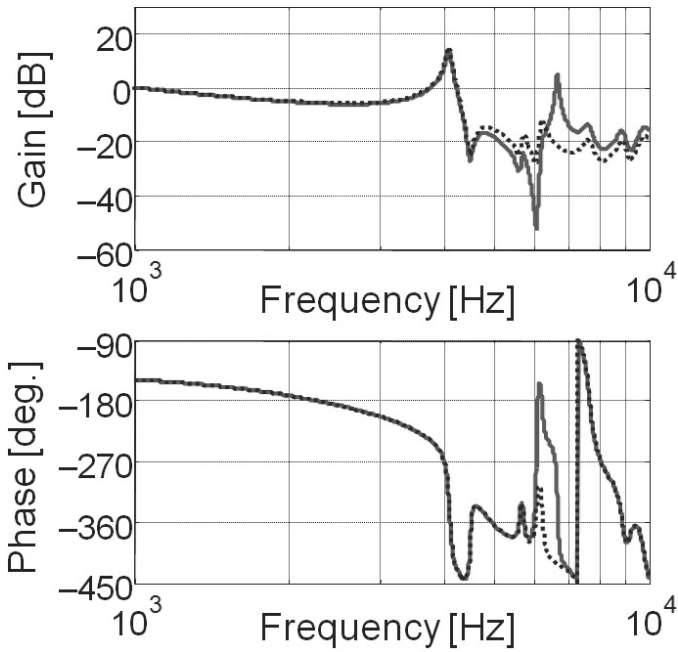

(a) Bode diagram.

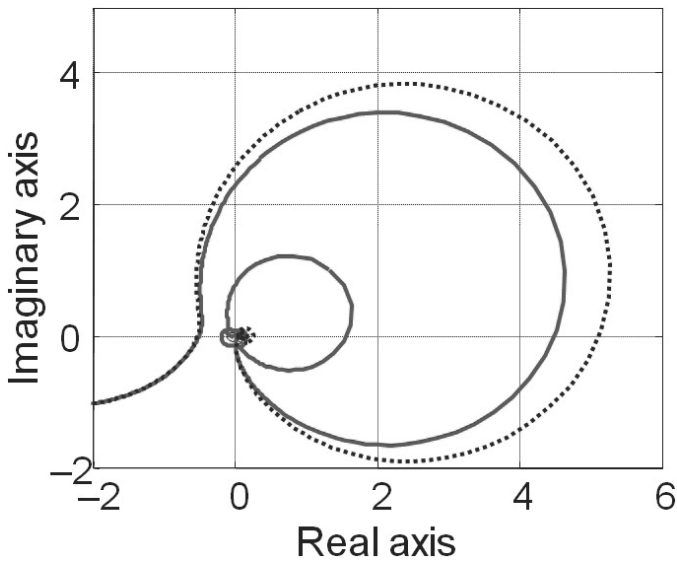

(b) Nyquist plot.

FIGURE 6.3
Open loop characteristics of the system. Dashed: without windage compensation. Solid: with windage compensation.

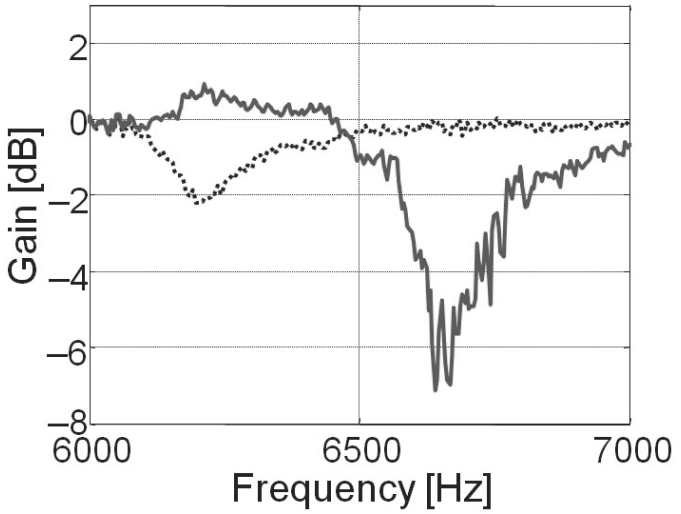

FIGURE 6.4
Frequency responses of sensitivity transfer functions of the system. Dashed: without windage compensation. Solid: with windage compensation.

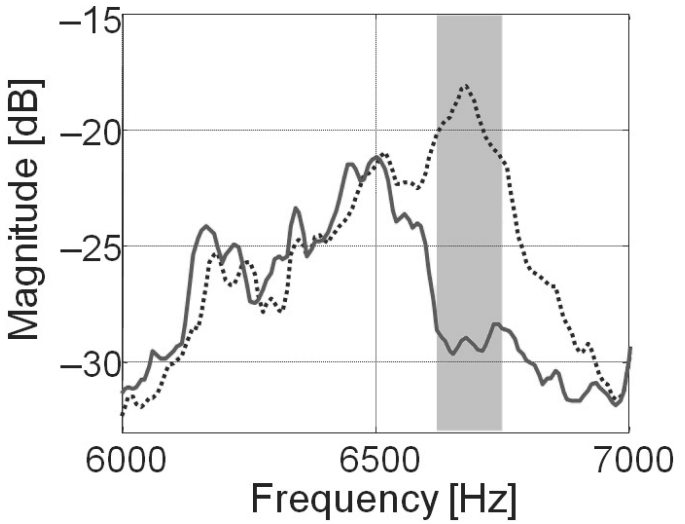

FIGURE 6.5
PES spectra. Dashed: without windage compensation. Solid: with windage compensation.

6.2 What Can We Do when the Positioning Accuracy Reaches a Limit? (M. Hirata)

6.2.1 Motivation

To improve the positioning accuracies, much effort has been devoted to applying various control theories in high-performance mechatronic systems. However, what can we do when further improvements of the control accuracies are impossible?

In many positioning control systems, the completion of the positioning phase must be determined correctly in order to initiate the start of the next task. For example in HDDs, the data read or write process cannot be started until the R/W head (arriving from adjacent tracks) is settled at the center of the target track with an allowable positioning-error bound. As such, a fast and accurate method of determining the completion of the positioning phase could enhance the control performances further even when improvements in control accuracies are impossible. In particular, the determination will be difficult as the required control accuracy is higher than that of the current control accuracy and the output may exceed the tracking error bound again.

A simple way of determining the end of the positioning phase is to wait for several sampling periods in order to confirm that the output does not exceed the error bound. This makes the unnecessary wait inevitable.

In this section, a method using Support Vector Machines (SVMs) is introduced [3]. The SVM is a well-known approach for classification, and uses a discriminant function to separate the data space into two regions. As such, the SVM has the ability to determine if the positioning phase has been fully completed.

6.2.2 Support Vector Machine

For given training data points $(\boldsymbol{x}_i, y_i)$ comprising of input data $\boldsymbol{x}_i \in \mathcal{R}^n$ and class label $y_i \in \{-1, 1\}$, the SVM is formulated as a problem to find a linear discriminant function f that separates the data points $\boldsymbol{x}_i$ into two classes as [4]

$$f(\boldsymbol{x}_i) = \langle \boldsymbol{w}, \boldsymbol{x}_i \rangle + b, \tag{6.1}$$

where $\langle \cdot, \cdot \rangle$ is an inner-product, $\boldsymbol{w}$ is a normal vector of the hyperplane, and b is a bias term. As shown in Figure 6.6, the SVM separates the data points using the hyperplane such that the distance from the hyperplane to the nearest data point is maximized. The data points nearest to the hyperplane are called *support vectors*.

The problem that maximizes the margin between the hyperplane and the

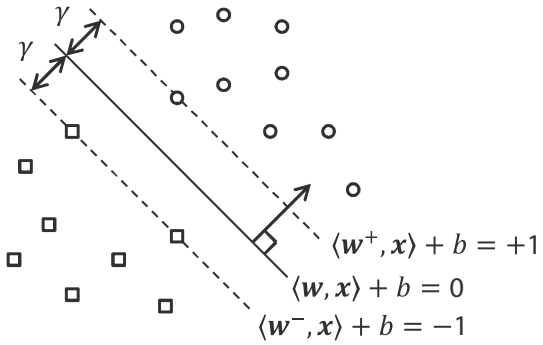

FIGURE 6.6
Training data and hyperplane.

nearest data point can be formulated as a quadratic programming problem as

$$\min_{\boldsymbol{w},b} \mathcal{J}(\boldsymbol{w}) \quad = \quad \min_{\boldsymbol{w},b} \frac{1}{2}\langle \boldsymbol{w}, \boldsymbol{w}\rangle, \tag{6.2}$$

$$\text{subjected to} \qquad (\langle \boldsymbol{w}, \boldsymbol{x}_i\rangle + b)y_i \geq 1, \quad i = 1, \cdots, N, \tag{6.3}$$

where the maximum margin is $\gamma = 1/\|\boldsymbol{w}\|$. This formulation is also referred to as a *primal problem*. A Lagrange function is given by

$$\mathcal{L}(\boldsymbol{w}, b, \boldsymbol{\alpha}) = \langle \boldsymbol{w}, \boldsymbol{w}\rangle - \sum_{i=1}^{N} \alpha_i \{(\langle \boldsymbol{w}, \boldsymbol{x}_i\rangle + b)y_i - 1\}. \tag{6.4}$$

The dual problem

$$\max_{\alpha} \mathcal{Q}(\alpha) \quad = \quad \max_{\alpha} \left(\sum_{i=1}^{N} \alpha_i - \frac{1}{2} \sum_{i,j=1}^{N} y_i y_j \alpha_i \alpha_j \langle \boldsymbol{x}_i, \boldsymbol{x}_j\rangle \right),$$

$$\text{subjected to} \qquad \sum_{i=1}^{N} y_i \alpha_i = 0, \quad \alpha_i \geq 0, \ i = 1, \cdots, N, \tag{6.5}$$

is obtained by differentiating (6.4) with respect to $\boldsymbol{w}, b$ and replacing them with zeros.

When the data points are not linearly separable, they are mapped onto a higher dimensional space using a nonlinear function $\phi(\cdot)$ to make them separable as shown in Figure 6.7. This is equivalent to using a nonlinear discriminant function

$$f(\boldsymbol{x}_i) = \langle \boldsymbol{w}, \boldsymbol{\phi}(\boldsymbol{x}_i)\rangle + b \tag{6.6}$$

instead of (6.1).

In general, the dimension of $\phi(\boldsymbol{x}_i)$ tends to be very high and optimization

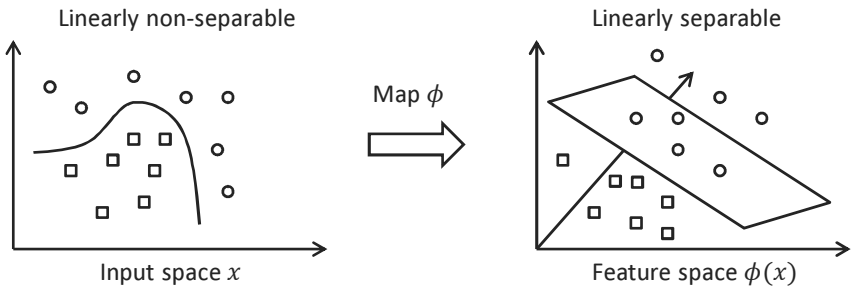

FIGURE 6.7
Mapping to a higher dimensional feature space.

might be difficult. However, this can be avoided by using the dual problem in (6.5) since the higher dimensional space does not appear explicitly in

$$\max_{\alpha} \mathcal{Q}(\alpha) = \max_{\alpha} \left(\sum_{i=1}^{N} \alpha_i - \frac{1}{2} \sum_{i,j=1}^{N} y_i y_j \alpha_i \alpha_j \langle \phi(\boldsymbol{x}_i), \phi(\boldsymbol{x}_j) \rangle \right).$$

This formulation requires the calculation of the inner product of $\phi(\cdot)$, and $K(\boldsymbol{x}_i, \boldsymbol{x}_j) = \langle \phi(\boldsymbol{x}_i), \phi(\boldsymbol{x}_j) \rangle$ is referred to as the *kernel function* [4]. This technique is well-known as the *kernel trick*. A polynomial kernel, Gaussian kernel, or Sigmoid kernel is commonly used.

6.2.3 Application to the Head-Positioning Control Problem in HDDs

6.2.3.1 Approach

In head-positioning control of HDDs, the completion of the track-seeking phase must be determined correctly to switch from the track-seeking mode to the track-following mode for data read and write. The proposed approach using SVMs is shown in Figure 6.8. As shown in Figure 6.8, it is assumed that the state variables of the plant can be obtained, and the completion of the track-seeking phase is determined if the plant state belongs to Classes 1 or 2.

6.2.3.2 Plant Model

A plant model $P(s)$ including a rigid-body mode and two vibration modes is given by

$$P(s) = \frac{k_f}{mT_p} \left(\frac{1}{s^2} + \sum_{i=1}^{2} \frac{k_i}{s^2 + 2\zeta_i \omega_i s + \omega_i^2} \right), \tag{6.7}$$

where the plant parameters are determined based on the HDD Benchmark Problem as $k_f = 1.0$ N/A, $m = 1.0 \times 10^{-3}$ kg, $T_p = 2.54 \times 10^{-7}$ m, $\zeta_1 = 0.03$,

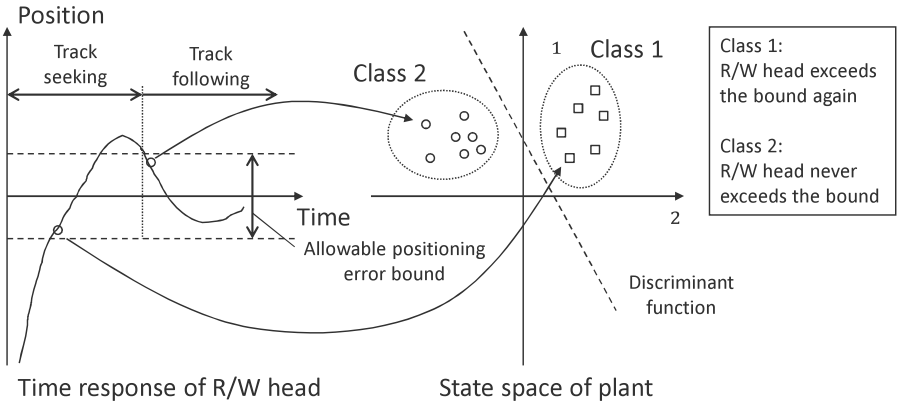

FIGURE 6.8
End of track-seeking phase determined using the SVM.

$\zeta_2 = 0.01$, $\omega_1 = 2\pi 4100$ rad/s, $\omega_2 = 2\pi 7000$ rad/s, $k_1 = -1.0$, and $k_2 = -1.0$. The state-space representation of (6.7) is omitted here due to limited space. It should be noted that the dimension of the state space is six.

6.2.3.3 Training the Discriminant Function

To extract training data from track-seeking responses, Final-State Control (FSC) inputs were obtained for a rigid-body mode model $P_n = k_f/(mT_p s^2)$. P_n was discretized using the Zero-Order Hold (ZOH) method at a sampling period of $T_s = 37.879$ μs, and the FSC inputs were obtained for various combination of seek distances from 10 to 900 tracks and seek times from 24 to 130 sampling steps.

The obtained FSC inputs were applied to the plant having two vibration modes defined in (6.7), and the output responses were obtained. The magnified plot around the target track is shown in Figure 6.9 when the seek distance is fifty tracks. It should be noted that the initial positions were adjusted so that the target track is at Track 0. The allowable tracking-error bound is assumed to be ± 0.03 of a track, which is shown by the dotted lines in Figure 6.9.

To construct a set of training data, the plant states where the corresponding outputs were located in the allowable tracking-error bound were collected. Next, the collected states were classified into two classes. Class 1 is a set of the plant states where the corresponding output exceeds the allowable tracking-error bound again after the current output, and Class 2 is a set of the plant states where the corresponding output never exceeds the bound. Finally, the nonlinear discriminant function that separates Classes 1 and 2 was obtained by the SVM using a 4^{th} order polynomial kernel [4].

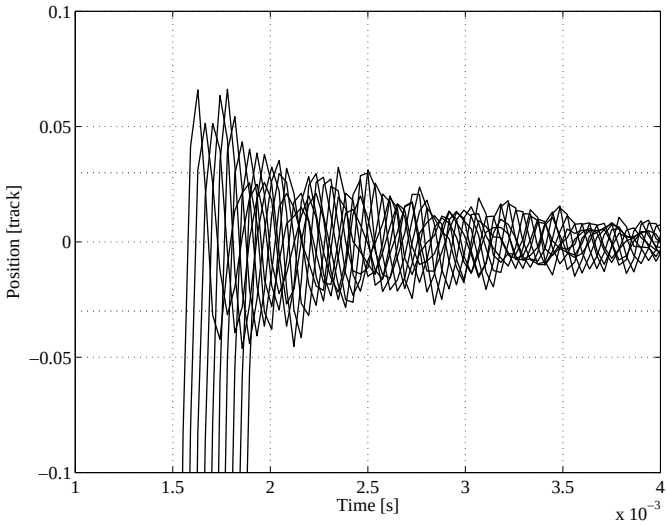

FIGURE 6.9
Magnified track-seeking responses.

6.2.3.4 Validation

The obtained discriminant function was evaluated by simulations. For one hundred combinations of seek distances from 5 to 1000 tracks and seek times from 20 to 135 sampling steps, the FSC inputs were designed for validation purposes. The completion of the track-seeking phase was determined by the obtained discriminant function for each track-seeking response, and the results are shown in Figure 6.10. The horizontal axis shows the judgment point $N_{SVM} - N_0$ where N_{SVM} and N_0 are the determined time using the SVM and the actual time of completion of the track-seeking phase, respectively. The vertical axis shows the number of track-seeking responses for each judgment point. For example, the judgment point "1" shows the number of track-seeking responses where the completion of the track-seeking phase was determined one sample after the actual completion of the track-seeking phase. When $N_{SVM} - N_0$ is negative, the corresponding track-seeking response was classified into "failure" in the horizontal axis.

For comparison purposes, the completion of the track-seeking phase was determined when the output was settled within the allowable tracking-error bound five times in a row, and the result is shown in Figure 6.11. This method is referred to as the conventional method. It is clear from Figure 6.11 that more time is required to determine the completion of the track-seeking phase and the number of failures is also increased.

In order to decrease the number of failures using the proposed method, a margin of the SVM can be introduced to determine the completion of the

track-seeking phase on the safe side. This can be done by using the discriminant function $\langle \boldsymbol{w}, \boldsymbol{x} \rangle + b = -0.8$ instead of $\langle \boldsymbol{w}, \boldsymbol{x} \rangle + b = 0$ in Figure 6.6. The result is shown in Figure 6.12, and it is confirmed that the number of failures is drastically reduced. However, more time might be required to determine the completion of the track-seeking phase in some cases.

6.2.4 Summary

In this example, the discriminant function was obtained by learning from the data via simulations, though the training data from experiments can also be used. In this case, the plant model is not required, and nonlinearity of the plant will be incorporated in the discriminant function automatically.

In order to enhance the control performances of mechatronic systems, various approaches other than merely increasing the positioning speeds and accuracies are also important. For this purpose, powerful tools such as the SVM developed in other fields of research may provide significant improvements. I hope this stimulates potential readers to find new and innovative approaches developed in other areas of research.

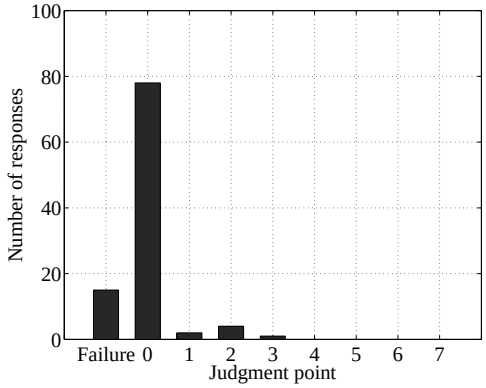

FIGURE 6.10
Simulation results of the proposed method using SVM.

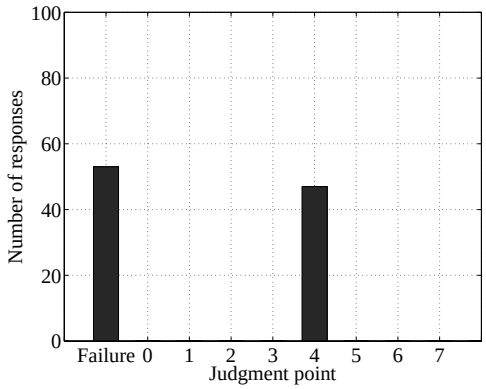

FIGURE 6.11
Simulation results of the conventional method.

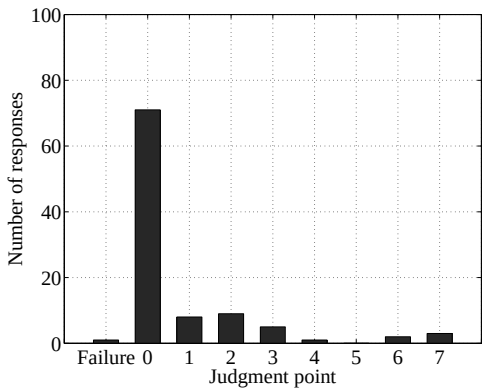

FIGURE 6.12
Simulation results of the proposed method using SVM when a margin is considered.

6.3 Control Constraints and Specifications (C. K. Pang)

In this section, the constraints and specifications of future high-performance mechatronic systems are detailed from a control theory perspective.

6.3.1 Constraints and Limitations

The block diagram of a typical sampled-data mechatronic system is shown in Figure 6.13. In Figure 6.13, a sampler is used in the place of the ZOH $H(s)$ for brevity but without loss of generality.

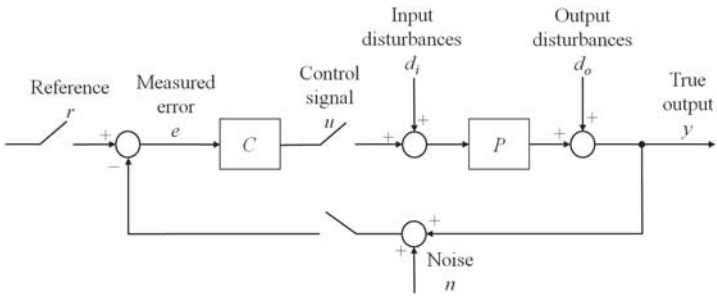

FIGURE 6.13
Block diagram of a typical sampled-data mechatronic system.

In this section, sampled-data systems will be handled using an approximated continuous time system as shown in Figure 6.14.

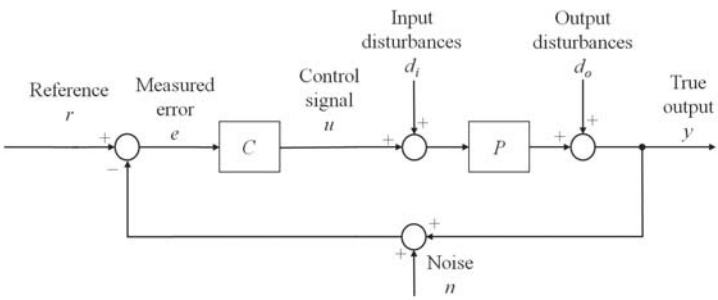

FIGURE 6.14
Block diagram of a continuous control system.

For simplicity but without loss of generality, consider the plant $P = \frac{N_P}{D_P}$ to be of Single Input Single Output (SISO) in series with controller $C =$

$\frac{N_C}{D_C}$ in a negative feedback configuration. In Figure 6.14, the plant P is the mechanical actuator to be precisely controlled, and the controller C is the controller to be designed and synthesized. N_C and N_P are the *zero* polynomials of C and P, respectively, while D_C and D_P are the *pole* polynomials of C and P, respectively.

The open loop transfer function L is given by $L = CP$. The true output y with input disturbances d_i, output disturbances d_o, and noise n in the servo loop can be obtained by

$$y = SPd_i + Sd_o - Tn, \tag{6.8}$$

where S and T are the sensitivity transfer function and complementary sensitivity transfer function, respectively, defined by

$$\begin{aligned} S &= \frac{1}{1+L} = \frac{1}{1+\frac{N_C N_P}{D_C D_P}} \\ &= \frac{D_C D_P}{D_C D_P + N_C N_P}, \end{aligned} \tag{6.9}$$

$$\begin{aligned} T &= \frac{L}{1+L} = \frac{\frac{N_C N_P}{D_C D_P}}{1+\frac{N_C N_P}{D_C D_P}} \\ &= \frac{N_C N_P}{D_C D_P + N_C N_P}. \end{aligned} \tag{6.10}$$

The above relationships hold in both continuous and discrete time.

In the standard unity negative feedback configuration shown in Figure 6.14, there exist control conflicts and unavoidable trade-offs between attenuating disturbances as well as filtering measurement error and noise. For good tracking performance and rejection of disturbances at low frequencies, effective control loop-shaping techniques are essential to avoid large control signals which saturate the mechatronic system.

From (6.8), it can be seen that a small S is ideal for disturbance rejection, while a small T is good for robustness against measurement noise and high frequency uncertainties. Due to the immediate definitions of S and T in (6.9) and (6.10), respectively, the following identity always holds

$$S + T \equiv 1, \tag{6.11}$$

i.e., S and T cannot be small simultaneously and in particular, $|S|$ and $|T|$ cannot be less than one-half at the same time. Fortunately, this conflict can be resolved by making one transfer function small at one frequency band and the other small at another. This is possible as the power spectra of references and disturbances are usually concentrated at low frequencies, while the power spectra of measurement errors and noises are concentrated at high frequencies.

Knowing that $T = SL$ as well as design specifications on S and T, an intuitive approach to find the stabilizing controller C is via closed-loop synthesis,

i.e.,

$$\begin{aligned} C &= P^{-1}L \\ &= P^{-1}S^{-1}T. \end{aligned} \tag{6.12}$$

A problem now obviously arises as one has to choose among the many possible arbitrary combinations of S and T although their solution "shapes" are known. The properness and characteristics of plant P are ignored and the controller C derived via such a method might be non-causal, or even unstable if P is non-minimum phase.

As such, a more common and easier solution is to use the open loop approach with $L = CP$. A good rule of thumb is to use high gain over low frequencies and decrease the gain as rapidly as possible after the gain crossover frequency. Cascading a large number of Low Pass Filters (LPFs) is not admissible due to the amount of phase lag introduced. Using Bode's Stability Criterion, the typical magnitude shape of a compensated open loop transfer function of a negative feedback control system should have [5]

- Low frequency band: A large gain $\gg 0$ dB and descending with a slope of $-20N$ dB/dec;
- Mid frequency or crossover frequency band: Pass through 0 dB with ≈ -20 dB/dec for stability; and
- High frequency band: A low gain < 0 dB and descending with a slope of $-20N$ dB/dec;

where $N \in \mathbb{Z}^+ \backslash \{1\}$.

The following results are presented.

6.3.1.1 Anti-Resonant Zeros

The presence of *anti-resonant* zeros implies blocking of certain signal frequencies by mechanical plant P. From (6.10), it can be seen that the zero polynomial of the open loop transfer function L is the same as that of the closed-loop transfer function T, i.e., the locations of the zeros are unaffected by feedback control. As such, it is obvious that these zeros will inhibit input disturbance d_i rejection capabilities (by plant P) as well as noise rejection and tracking capabilities (by T) at the frequencies of the anti-resonant zeros as can be seen from (6.8). To address the effects of stable anti-resonant zeros in P and T, corresponding stable poles are placed by feedback controller C in the series compensation topology [6, 7].

In the presence of non-minimum phase (unstable) zeros, an undershoot will be observed in the time responses with prolonged settling time. In addition, the closed-loop bandwidth has to be lowered as the extra phase lag introduced by these zeros reduces the phase margin. The magnitude and overall positive area under the sensitivity transfer function also increase significantly

at frequencies beyond the open loop bandwidth as depicted in the Discrete Bode's Integral Theorem [8, 9]. To handle the effects of unstable zeros in P and T, the Generalized Kalman-Yakubovic-Popov (GKYP) Lemma for integrated servo-mechanical design of the mechanical plant P is used to ensure that T is positive real within a finite frequency range [10], by considering that a discrete-time system (with an equal number of inputs and outputs) is minimum phase if it is positive real [11].

6.3.1.2 Resonant Poles

Feedback control effectively shifts the location of closed-loop poles which can be arbitrarily placed by designing C, if the mechanical plant P is *controllable*. From (6.9), it can be seen that the zeros of S are essentially the union set of poles of C and P. In order to create gain notches in S for enhanced disturbance rejection and error correction, the gain of the resonant poles in P should not be fully compensated by using the phase-stabilization technique, e.g. [1, 12], or created by C using add-on peak filters, e.g. [13].

If C is chosen to be of low-order and the frequencies of mechanical resonant modes in P are fixed, the disturbance attenuation capabilities can only be achieved at high frequencies by decreasing the damping ratios of the poles in C and P. Similarly, the GKYP Lemma for integrated servo-mechanical design of the mechanical plant P is used to ensure the mechanical resonant modes (poles) of P are shaped to be in-phase based on finite frequency constraints imposed on S [10].

6.3.1.3 Sensitivity Transfer Function

The sensitivity transfer function S is the transfer function from output disturbances d_o to the true output y or reference r to measured error e. As such, many existing loop-shaping methods in current literature put much emphasis on improvements on tracking performances at low frequencies and disturbance rejection. One commonly used graphical tool for loop-shaping and control system design evaluation is the Nyquist plot. Two typical Nyquist curves $L_1(j\omega)$ and $L_2(j\omega)$ are shown in Figure 6.15, and the relationships between the open loop transfer function $L(j\omega)$ and sensitivity transfer function $S(j\omega)$ using the Nyquist diagram are discussed in the continuous domain for brevity but without loss of generality.

Since $S(j\omega) = \frac{1}{1+L(j\omega)}$ with $1 + L(j\omega)$ as the output return difference equation, the locus of $|S(j\omega)| = 1$ can be plotted as a unit disc with center at the critical point $(-1 + j0)$. Define this disc as the *Sensitivity Disc* (SD) [6, 14]. For some frequencies ω_- and ω_+, an $L(j\omega_-)$ outside the SD results in $|S(j\omega_-)| < 1$ while an $L(j\omega_+)$ inside SD yields $|S(j\omega_+)| > 1$ since $|S(j\omega)|$ is the reciprocal of the distance of $L(j\omega)$ to $(-1 + j0)$. An $L(j\omega)$ intersecting the SD corresponds to unity gain or 0 dB on the Bode Diagram of $|S(j\omega)|$.

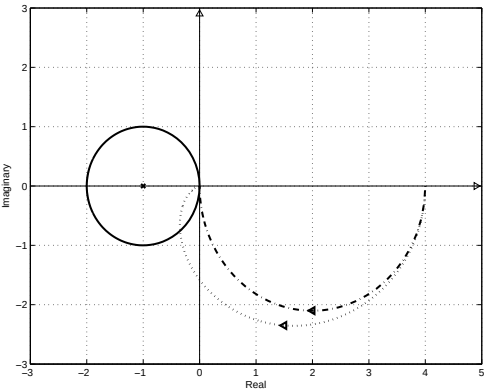

FIGURE 6.15
Nyquist plots. Solid: Sensitivity Disc (SD) with $|S(j\omega)| = 1$. Dashed: $L_1(j\omega)$. Dashed-dot: $L_2(j\omega)$.

As such, it can be seen from Figure 6.15 that $L_2(j\omega)$ will not have a positive area (or *hump*) in the sensitivity transfer function S. On the other hand, $L_1(j\omega)$ enters the SD when $\omega \geq \omega_+$ and approaches the origin with a phase angle less than $-\frac{\pi}{2}$. It is interesting to note that feedback is actually decreasing the performance of the control system when $\omega \geq \omega_+$ and the hump is increased.

With these constraints and limitations in mind, the controller C is designed to ensure that [6]

1. $L(j\omega)$ is far from and does intersect with SD. If this is not possible, make $L(j\omega)$ avoid SD where the frequency spectra of the disturbances are concentrated;

2. $L(j\omega)$ approach the origin at $-\frac{\pi}{2} \leq \angle L(j\omega) \leq \frac{\pi}{2}$ as $\omega \to \infty$ so that the SD is avoided. If this is not possible, make $|L(j\omega)| \approx 0$ at these frequencies; and

3. $L(j\omega)$ do not encircle $(-1 + j0)$ clockwise for stability.

These considerations are valid for discrete time systems below the Nyquist frequency as well.

6.3.1.4 Limitations on Positioning Accuracy

Assume that the input disturbances and noise are converted to an overall disturbance model D at the output with Gaussian white noise input. The

variance of true output y can be given by [15]

$$\text{var}(y) = \frac{1}{\pi}\int_0^\infty |S(j\omega)D(j\omega)|^2\, d\omega. \tag{6.13}$$

Assume that the open loop transfer function $L = CP$ is strictly proper and the gain of L satisfies the following inequality for bandwidth requirement [16] as

$$|L(j\omega)| \leq \delta\left(\frac{\Omega}{\omega}\right)^{k+1}, \tag{6.14}$$

where $\delta > 0$ and $k \geq 1$ are pre-specified scalars and $\delta < 0.5$ is usually selected [17]. It is obvious that the gain of L is smaller than δ for all $\omega > \Omega$ where Ω is the closed-loop bandwidth, and the roll-off is at least $-20N$ dB/dec where $N \in \mathbb{Z}^+\backslash\{1\}$.

Using the definition of S, the following inequality is obtained

$$\frac{1}{1+\delta\left(\frac{\Omega}{\omega}\right)^{k+1}} \leq |S(j\omega)| \leq \frac{1}{1-\delta\left(\frac{\Omega}{\omega}\right)^{k+1}}. \tag{6.15}$$

The variance of true output y is bounded by [16]

$$\text{var}(y) \geq \frac{\Omega}{\pi}e^{\beta} + \frac{1}{\pi}\int_\Omega^\infty \frac{|D(j\omega)|^2}{\left[1+\delta\left(\frac{\Omega}{\omega}\right)^{k_e}\right]^2}\, d\omega, \tag{6.16}$$

where $k_e = k+1$ when k is odd, $k_e = k$ when k is even, and $\beta = \frac{\int_0^\Omega \ln|D(j\omega)|^2\, d\omega}{\Omega}$.

From (6.16), it can be seen that the positioning accuracy given by $\text{var}(y)$ is a decreasing function of Ω. This supports the notion of improving positioning accuracy via increasing the open loop bandwidth or gain crossover frequency, and illustrates the importance of an accurate disturbance model as depicted in the previous section. The shape of the sensitivity transfer function S is also important in improving the disturbance rejection capabilities, and is bounded by the Bode's Integral Theorem.

6.3.2 Bode's Integral Theorem

The Bode's Integral Theorem was initially used to study the limitations of linear control systems with non-minimum phase zeros or unstable poles. In this section, the Continuous and Discrete Bode's Integral Theorems are discussed along with their implications on servo control of high-performance mechatronic systems.

6.3.2.1 Continuous Bode's Integral Theorem

Theorem 1 *Continuous Bode's Integral Theorem [9]*
A continuous SISO and minimum phase Linear Time-Invariant (LTI) system has a stable open loop transfer function $L(j\omega)$. The sensitivity transfer

function of the unity negative feedback system is $S(j\omega) = \frac{1}{1+L(j\omega)}$. *If the closed-loop system is stable, then*

$$\int_0^\infty \ln |S(j\omega)|\, d\omega = -\frac{\pi}{2} K_s, \tag{6.17}$$

where $K_s = \lim_{s\to\infty} sL(s)$.

Corollary 1 *When the relative degree of the open loop transfer function* $L(j\omega)$ *is greater than or equal to two, both* K_s *and the total area under the sensitivity transfer function* S *is zero. For* $|S(j\omega)| < 1$ *over some frequency, it is necessary that* $|S(j\omega)| > 1$ *over another frequency range, thereby causing a degradation of disturbance rejection capabilities at frequencies whereby* $|S(j\omega)| > 1$. *This phenomenon is termed as the "waterbed" effect, and the relative degree of the open loop transfer function* $L(j\omega)$ *has to be one for unity gain of the sensitivity transfer function* $|S(j\omega)|$ *at high frequencies.*

For discrete time systems, the Discrete Bode's Integral Theorem is more stringent and their conclusions differ.

6.3.2.2 Discrete Bode's Integral Theorem

Theorem 2 *Discrete Bode's Integral Theorem [8, 9]*
A discrete time SISO and minimum phase LTI system has a stable open loop transfer function $L(e^{j\phi})$. *The sensitivity transfer function of the unity negative feedback system is* $S(e^{j\phi}) = \frac{1}{1+L(e^{j\phi})}$. *If the closed-loop system is stable, then*

$$\int_{-\pi}^{\pi} \ln\ |S(e^{j\phi})|\, d\phi = 2\pi(-\ln |K_z + 1|), \tag{6.18}$$

where $K_z = \lim_{z\to\infty} L(z)$, $\phi = \omega T$, *and* T *is the sampling rate.*

It is worth noting that the transfer functions are periodic about Nyquist frequency $\frac{\pi}{T}$.

Corollary 2 *When* $L(e^{j\phi})$ *is strictly proper, the Discrete Bode's Integral Theorem in (6.18) reduces to*

$$\int_{-\pi}^{\pi} \ln\ |S(e^{j\phi})|\, d\phi = 0. \tag{6.19}$$

This is the waterbed effect in discrete time domain.

When the waterbed effect occurs, the magnitude of the peak of the sensitivity transfer function $||S||_\infty$ is bounded by Theorem 2. Now suppose that $|S(e^{j\phi})| \le \alpha < 1$ and $\phi \in [-\phi_1, \phi_1]$, $\phi_1 < \pi$. From [17], it is straightforward to see that

$$||S||_\infty \ge \left(\frac{1}{\alpha}\right)^{\frac{\phi_1}{\pi-\phi_1}}, \tag{6.20}$$

i.e., when the average magnitude of the sensitivity transfer function at low frequencies is -40 dB and the sampling frequency is 25 kHz, it can be shown that $||S||_\infty \geq 3.5$ dB if the bandwidth of the sensitivity transfer function is set at 1 kHz. As such, lowering the gain of the sensitivity transfer function at low frequencies would result in a larger $||S||_\infty$ at high frequencies (before the Nyquist frequency).

Corollary 3 *When $L(e^{j\phi})$ is proper with $K_z < -2$ or $K_z > 0$, then the Discrete Bode's Integral Theorem in (6.18) becomes*

$$\int_{-\pi}^{\pi} \ln \, |S(e^{j\phi})| \, d\phi < 0. \tag{6.21}$$

This implies that some loop-shaping technique is possible and may not be bounded by the waterbed effect. This property is exploited during integrated servo-mechanical design of the mechanical plant P using the GKYP Lemma [10].

Corollary 4 *When $L(e^{j\phi})$ is proper with $-2 < K_z < 0$, the Discrete Bode's Integral Theorem in (6.18) implies that*

$$\int_{-\pi}^{\pi} \ln \, |S(e^{j\phi})| \, d\phi > 0, \tag{6.22}$$

and feedback control is now degrading sensitivity and performance rather than improving it.

This conclusion is similar to that of non-minimum phase systems.

As a result, the presence of non-minimum zeros in the mechanical plant P and delay from the sampled-data system causes overall positive sensitivity in mechatronic systems. However, this problem can be alleviated with the development of in-phase mechanical actuators, e.g. [18], with possible reduction to Corollary 2. This restricts the overall positive sensitivity area to zero and within the limits of the waterbed effect.

6.3.3 Summary

In this section, the constraints and specifications of future high-performance mechatronic systems have been described from a control theory perspective. Using a systems design methodology [19], the mechatronic system design problem can be handled using both theoretical and graphical approaches. Our future works include development of a comprehensive integrated servo-mechanical framework considering negative-imaginary [20] and distributionally robust [21] properties, with specific applications to flexure-based magnetic levitation motors.

Bibliography

[1] T. Yamaguchi, M. Hirata, and C. K. Pang (eds.), *High-Speed Precision Motion Control*, CRC Press, Taylor and Francis Group, Boca Raton, FL, USA, 2011.

[2] T. Atsumi, T. Arisaka, T. Shimizu, and H. Masuda, "Head-Positioning Control Using Resonant Modes in Hard Disk Drives," *IEEE/ASME Transactions on Mechatronics*, Vol. 10, No. 4, pp. 378–384, August 2005.

[3] A. Yokozuka and M. Hirata, "Determination of the End of Track Seeking of Hard Disk Drives Using Support Vector Machine," in *Proceedings of the 2012 ASME-ISPS/JSME-IIP Joint International Conference on Micromechatronics for Information and Precision Equipment*, pp. 358–360, Santa Clara, CA, USA, June 18–20, 2012.

[4] N. Cristianini and J. Shawe-Taylor, *An Introduction to Support Vector Machines*, Cambridge University Press, Cambridge, UK, 2000.

[5] J. Freudenberg, R. Middleton, and A. Stefanopoulou, "A Survey of Inherent Design Limitations," in *Proceedings of the 2000 American Control Conference*, pp. 2987–3001, Chicago, IL, USA, June 28–30, 2000.

[6] C. K. Pang, D. Wu, G. Guo, T. C. Chong, and Y. Wang, "Suppressing Sensitivity Hump in HDD Dual-Stage Servo Systems," *Microsystem Technologies*, Vol. 11, Nos. 8–10, pp. 653–662, August 2005.

[7] C. K. Pang, S. C. Tam, G. Guo, B. M. Chen, F. L. Lewis, T. H. Lee, and C. Du, "Improved Disturbance Rejection with Online Adaptive Pole-Zero Compensation on a *Phi*-Shaped PZT Active Suspension," *Microsystem Technologies*, Vol. 15, Nos. 10–11, pp. 1499–1508, October 2009.

[8] C. Mohtadi, "Bode's Integral Theorem for Discrete-Time Systems," *IEE Proceedings*, Vol. 137, No. 2, pp. 57–66, March 1999.

[9] B. Wu and E. Jonckheere, "A Simplified Approach to Bode's Theorem for Continuous-Time and Discrete-Time Systems," *IEEE Transactions on Automatic Control*, Vol. 37, No. 11, pp. 1797-1802, November 1992.

[10] Y. Z. Tan, C. K. Pang, F. Hong, and T. H. Lee, "Integrated Servo-Mechanical Design of High-Performance Mechatronics Using Generalized KYP Lemma," *Microsystem Technologies*, in press.

[11] L. Hitz and B. D. O. Anderson "Discrete Positive-Real Functions and Their Application to System Stability," *IEE Proceedings*, Vol. 116, pp. 153–155, January 1969.

[12] M. Kobayashi, S. Nakagawa, and S. Nakamura, "A Phase-Stabilized Servo Controller for Dual-Stage Actuators in Hard-Disk Drives," *IEEE Transactions on Magnetics*, Vol. 39, No. 2, pp. 844–850, March 2003.

[13] D. Wu, G. Guo, and T. C. Chong, "Midfrequency Disturbance Suppression via Micro-Actuator in Dual-Stage HDDs," *IEEE Transactions on Magnetics*, Vol. 38, No. 5, pp. 2189–2191, September 2002.

[14] C. K. Pang, F. Hong, and X. Wang, "Integrated Servo-Mechanical Control Systems Design Using Nyquist Plots for High-Performance Mechatronics," *Microsystem Technologies*, Vol. 18, Nos. 9–10, pp. 1719–1729, October 2012.

[15] Z. Li, G. Guo, B. M. Chen, and T. H. Lee "Optimal Track-Following Design for the Highest Tracks per Inch in Hard Disk Drives," *Journal of Information Storage and Processing Systems*, Vol. 3, Nos. 1–2, pp. 27–41, April 2001.

[16] D. Davison, P. Kabama, and S. Meerkov, "Limitation of Disturbance Rejection in Feedback Systems with Finite Bandwidth," *IEEE Transactions on Automatic Control*, Vol. 44, No. 66, pp. 1132-1144, June 1999.

[17] M. Seron, J. Braaslavsky, and G. Goodwin, *Fundamental Limitations in Filtering and Control*, Springer, London, UK, 1997.

[18] T. Arisaka, T. Shimizu, T. Atsumi, H. Masuda, and T. Yamaguchi, "Development on In-Phase Actuator Mechanism in Hard Disk Drives," in *Proceedings of the 2004 Asia-Pacific Magnetic Recording Conference*, Seoul, Korea, August 16–19, 2004.

[19] C. K. Pang, T. S. Ng, F. L. Lewis, and T. H. Lee, "Managing Complex Mechatronics R&D: A Systems Design Approach," *IEEE Transactions on Systems, Man, and Cybernetics Part A: Systems and Humans*, Vol. 42, No. 1, pp. 57–67, January 2012.

[20] J. Xiong, I. R. Petersen, and A. Lanzon, "Finite Frequency Negative Imaginary Systems," *IEEE Transactions on Automatic Control*, Vol. 57, No. 11, pp. 2917–2922, November 2012.

[21] J. Goh and M. Sim, "Distributionally Robust Optimization and Its Tractable Approximations," *Operations Research*, Vol. 58, No. 4: Part 1, pp. 902–917, July/August 2010.

Index

ENGINEERING/ELECTRICAL

Advances in

High-Performance Motion Control of Mechatronic Systems

Mechatronic systems are used in a range of consumer products from large-scale braking systems in vehicular agents to small-scale integrated sensors in mobile phones. To keep pace in the competitive consumer electronics industry, companies need to continuously improve servo evaluation and position control of these mechatronic systems. ***Advances in High-Performance Motion Control of Mechatronic Systems*** covers advanced control topics for mechatronic applications. In particular, the book examines control systems design for ultra-fast and ultra-precise positioning of mechanical actuators in mechatronic systems.

The book systematically describes motion control design methods for trajectory design, sampled-data precise positioning, transient control using switching control, and dual-stage actuator control. Each method is described in detail, from theoretical aspects to examples of actual industry applications including hard disk drives, optical disk drives, galvano scanners, personal mobility robots, and more. This helps readers better understand how to translate control theories and algorithms from theory to design and implementation in realistic engineering systems. The book also identifies important research directions and advanced control techniques that may provide solutions for the next generation of high-performance mechatronics.

Bridging research and industry, this book presents state-of-the-art control design methodologies that are widely applicable to industries such as manufacturing, robotics, home appliances, automobiles, printers, and optical drives. It guides readers toward more effective solutions for high-performance mechatronic systems in their own products.

K15386

ISBN: 978-1-4665-5570-9

CRC Press
Taylor & Francis Group
an informa business
www.crcpress.com

6000 Broken Sound Parkway, NW
Suite 300, Boca Raton, FL 33487
711 Third Avenue
New York, NY 10017
2 Park Square, Milton Park
Abingdon, Oxon OX14 4RN, UK

www.crcpress.com